
THE UNIVERSITY *of* EDINBURGH

# PHASE CHANGE AND COMPLEX PHENOMENA IN DROPS AND BUBBLES OF PURE AND BINARY FLUIDS

**Dimitrios Mamalis**

Thesis submitted for the degree of

Doctor of Philosophy

at

The University of Edinburgh


March, 2016

# Declaration

The author declares that the work undertaken in this thesis is his own, expect where explicitly stated otherwise in this text. The candidate confirms that appropriate credit has been given where reference had been made to the work of others. This work has not been submitted, in part or in whole, for any other degree or professional qualification.

Dimitrios Mamalis

# Acknowledgments

It would not have been possible to write this doctoral thesis without the paramount help and support of the kind people around me, during my time in Edinburgh, and only some of whom it is possible to mention here.

First and foremost, I would like to express my sincere gratitude to my supervisors Prof. K. Sefiane and Dr. V. Koutsos for their invaluable guidance, patience, motivation and immense knowledge during each step of this research work. Their advices, trust and the opportunity provided to form a part of this project, are truly appreciated. I could not have imagined having better advisors and mentors for my PhD study. The Engineering and Physical Sciences Council (EPSRC) DTA should also be acknowledged for its financial support during these years.

In addition, I would like to thank all the people I have met during my period in Edinburgh; flatmates, colleagues and friends, both inside and outside the university who have been an invaluable source of support and amusement in my everyday life. I would like to acknowledge with special thanks all IMP members for my making the most creative, supportive and cheerful workplace than one could image. To mention some: Ares, Nelly, Sofia, Charithea, Esme, Dani, Alex, Pedro, Dimitris, Rohan, Mike, Alex and Irene.

Last but not least, I would like to specially thank my family, in particular I dedicate this PhD to my parents Fotini and John and to my sister Maria; who despite the distance, they have always been by my side offering unlimited support and love.

# Abstract

Evaporation, wetting and multiphase flows of drops and bubbles are everyday life phenomena with potential impact in many industrial, biological, medical or engineering applications. The understanding and controlling of the physical and chemical mechanisms governing these phenomena have become of paramount importance. This thesis encompasses three topics: evaporation of sessile droplets of polymer solutions, the role of thermocapillarity on self-rewetting fluid dynamics and migration of bubbles in liquid flows.

Firstly, the evaporative behaviour of sessile droplets of aqueous polymer solutions and the effect of different molecular weights on the drying process has been studied. Drop shape analysis allowed monitoring the evolution of all stages during drying and indicating the transitions between stages. The mechanisms taking place during the crucial stages of pinning and depinning were illustrated, revealing the effects of adhesion and contact line friction forces on the final morphology of the dried polymeric deposits. Additionally, the effect of varying substrates from hydrophilic to hydrophobic was examined demonstrating the importance of interfacial interaction phenomena.

The initial spreading dynamics of binary alcohol mixtures (and pure liquids) deposited on different substrates in partially wetting situations, under non-isothermal conditions was systematically investigated. Moreover, the temporal and spatial thermal dynamics within pure droplets and alcohol mixtures using IR thermography revealed the existence of characteristic thermal patterns due to thermal and/or solutal instabilities. The contribution of the Marangoni effect as an important heat transport mechanism within the evaporating droplets was investigated.

The motion of buoyancy-driven bubbles in a vertical microchannel and the significant role of thermocapillarity was reported in this series of experiments. The behaviour of the bubbles in self-rewetting fluid flows departed considerably from that of pure liquids flows. Furthermore, heat transfer coefficient calculations in the single and two phase flows demonstrated that the presence of Marangoni (surface tension) stresses resulted in the enhancement of the heat transfer distribution in the self-rewetting fluid flows compared with the pure ones.

# Contents

# List of Publications

## Journal Articles

Mamalis D., Koutsos V., Sefiane K., Kagkoura A., Kalloudis M., and M.E. R. Shanahan.
Effect of Poly(ethylene oxide) Molecular Weight on the Pinning and Pillar Formation of Evaporating Sessile Droplets: The Role of the Interface
*Langmuir, Volume 31, Pages 5908-5918,* ***2015***. DOI: 10.1021/la504905y

Buffone C., Sefiane K., Minetti C., and D. Mamalis.

Standing wave in evaporating meniscus detected by infrared thermography.

*Applied Physics Letters, Volume 107, Pages 041606-1 to 041606-4,* ***2015***. DOI: 10.1063/1.4927744

## Conferences, Workshops

Non-isothermal spreading dynamics of self-rewetting droplets.

Mamalis D., Sefiane K., Sahu K.C., Karapetsas G., and O.K. Matar.

*American Physical Society, 68th Annual Meeting of the Division of Fluid Dynamics,* Volume 60, Boston, Massachusetts, US (2015).

On the emergence of vortices in irregular evaporating sessile droplets.

Sáenz P. J., Mamalis D., Sefiane K., Valluri P., and O.K. Matar.

*American Physical Society, 67th Annual Meeting of the Division of Fluid Dynamics,* Volume 59, San Francisco, California, US (2014).

Droplet Evaporation: Polymer Pillar Formation and Water-Alcohol Mixture Spreading Dynamics.

Mamalis D., Sefiane K., Koutsos V.

*Institute for Materials and Processes Seminar Series*. University of Edinburgh, Scotland, UK (2014).

Poly(ethylene oxide)-based structures self-assembled on surfaces after evaporation from aqueous solutions.

Koutsos V., Mamalis D., Kalloudis M., and Sefiane K.,

*Workshop "Smart and Green Interfaces 2013 (Prague)*" Prague, Czech Republic (2013).

# List of Figures

# List of Tables

# Chapter 1: Introduction

The ubiquitous nature of wetting, capillarity and phase change phenomena are encountered and observed in everyday life in many ranging and diverse situations. Despite the significant effort of many researchers try to shed light on these highly complex phenomena, many questions still remain unknown and there is still much knowledge to be gained from conducting fundamental research into wetting and phase change phenomena in drops and bubbles.

Essentially, when a liquid droplet contacts a solid surface it will try to minimize its surface energy and reach a thermodynamic equilibrium state between the three phases (solid-liquid-gas) meeting at the triple contact line (TCL). This state is fundamentally governed by the balance between the physicochemical interactions of the three difference phases present in the system: liquid-solid, liquid-gas and solid-gas.

Thomas Young [1] was the first, back in 18$^{th}$ century, who he set out in descriptive terms the principles governing the balance between theses phases with the observed contact angle adopted between a liquid and a solid surface during wetting. This consideration led the author to the concept of surface tension forces acting at the vicinity of these phases. In 1805, Young introduced in his seminal work the famous Young-equation, stating the interface force balance, namely the stress equilibrium where solid, liquid and gas phases meet at the contact line [1]. Since then, many theoretical and experimental studies have been carried out to explain the physical mechanisms present in phenomena such as spreading, dewetting, adsorption (liquid or particles) on solid surfaces etc. In a series of Young's contribution, Dussan [2], de Gennes [3] and Joanny [4] described both statically and dynamically the motion of a liquid front at the contact line. Understanding the physics and chemistry of these interfacial phenomena and interactions during wetting-spreading are of paramount importance for many industrial, biological or pharmaceutical applications such as microfluidics [5], self-cleaning surfaces [6], polymer films [7, 8], coating and deposition processes (herbicides-pesticides) [9].

However, equilibrium states between liquid phases and solid surfaces are hardly present in nature due to the fact that fluids are being sensitive in temperature and pressure condition changes or other physical mechanisms such as evaporation which result in non-equilibrium processes and phase transitions. Evaporation of a liquid phase should occur whenever the liquid molecules at gas-liquid interface have sufficient energy to be subjected to a phase transition from liquid to gas, provided that the surrounding environment near the interface is not saturated with the liquid vapour, as reported from Bourges-Monnier and Shanahan [10]. Although, at first, the nature of liquid evaporation is apparently simple, it is a relatively complex phenomenon to investigate and has received important scientific attention over the past years attempting to understand the underlying complex physical and chemical mechanisms [10-14]. Evaporation of liquids is a complicate transient process where heat and mass are transferred between the phases, by cooling and/or Marangoni (surface tension stresses) effects present in the system. Essentially, crucial parameters affecting this phenomenon such as wettability [10, 15, 16], temperature [17, 18] and pressure [19] have been extensively examined by many authors. Despite all the work which has been conducted in this topic, both experimentally [12, 16, 20] and theoretically [18, 21-24], it is still a very active area of research with many outstanding questions and unexplored problems such as substrate-droplet interactions during drying, the presence or absence of the Marangoni effect and internal flows, the addition of particulates (colloidal or polymeric) within the evaporating liquids.

Another topic that has been extensively studied, for more than a decade now, is the evaporation of fluids containing particles or colloidal suspensions and the deposits left after complete dry-out. Deegan *et al.* was the first to elucidate the main responsible mechanism which leads to accumulation of particles around the edge of a pinned volatile droplet during evaporation [25-27]. An advective (capillary) liquid flow from the bulk of the fluid towards the pinned contact line to replenish the evaporated liquid was observed, namely the coffee ring-stain effect [28-30]. The potential of controlling the patterning process through evaporation exhibits numerous potential applications in different research fields such as ink-jet printing [31], self-assembly [24], crystallography [32], electronics [33], blood diagnosing methods [34, 35], optics or patterning [25].

In addition to single components (pure liquids) and colloids suspensions, a great number of experimental studies have been performed on evaporating droplets of polymer solutions. Most of the work presented in this thesis focuses on the evaporation process of polymer solutions, aiming to the better understanding of the governing transient complex phenomena regarding to a variety of industrial, biological applications etc., involving solvent-assisted polymer processing. Although polymers in solutions can exist in different phases controlled by the temperature and concertation parameters, the final morphology of the dried solute is not always a ring but depends on many experimental factors such as: interactions between solvent, vapour, substrate [36, 37] convection currents within a drop [18, 29], interfacial phenomena and evaporation rate [38, 39]. It is the purpose of this study to present, analyse and discuss how a number of parameters affect the evaporation mechanism of polymer solutions and its resulting dried polymeric final morphology, for the particular case of a water soluble semi-crystalline polymer.

The effectiveness of the surface-tension variations (Marangoni effect) along a liquid-gas interface during droplet evaporation or bubble rise in liquid flows, was another extensive topic of investigation in this thesis. If surface tension deviations i.e. temperature and/or compositional, are present throughout the interface, stress gradients arise including interface flow where fluid is driven from regions of low to high surface tension. Generally, these surface tension driven currents are referred to as Marangoni flow, or as thermocapillary and/or solutal flows, if the stress gradients are due to temperature and/or chemical composition differences. There are two distinct investigative undertakings, the first includes results obtained from the evaporative behaviour of volatile pure liquids droplets (for reference) and binary alcohol mixtures, and are attributed to the wetting dynamics and to the thermal behaviour observed during drying process. Understanding these interplays becomes of great importance for the manipulation and reproducibility of these phenomena. The second set of experiments investigates the bubble motion inside a microchannel and the role of thermocapillarity in the heat transfer performance of these liquid flows. The use of specific binary alcohol mixtures, called self-rewetting fluids, as operating fluids (or drops) with modified physical properties compared to the pure ones results in enhancing thermal conductivity, heat or mass transfer, spreading and wetting of the

systems. In the last decade, numerous studies have suggested these novel binary alcohol fluids for potential applications in boiling [40-42], heat transfer [43, 44], space technology [45-47], heat pipe systems [48], coatings [33, 49].

This thesis compromises eight chapters. Chapter 1 provides the introduction of this thesis and includes a brief overview of the main focus of the research and discussing the scientific interest of the work which has been undertaken. In addition, a quick outline of the format of this thesis is presented and a brief summary of the various areas of research that may be useful is given.

In Chapter 2, a comprehensive literature review and the theory behind the most relevant fundamental theoretical and experimental concepts of this study are presented. This chapter provides the reader with the necessary knowledge required for the understanding of the physics, chemistry and engineering aspects surrounding wetting, evaporation and thermocapillary phenomena, together with the most important findings which have been published. The fundamentals of spreading on solid surfaces are introduced which are associated with the different evaporative modes adopted. The topic of suspension and colloidal droplet evaporation is covered with a review of the up to date experimental and theoretical work. Furthermore, the specific case of polymer solution evaporation is presented and the essential scientific background in this area is elaborated. An overview on the current status regarding interfacial thermal and/or compositional phenomena in drops and bubbles is given, including the most significant discoveries and applications, useful in understanding the results obtained in this thesis. Finally, the concept of fluid flow dynamics in channels with the most relevant theoretical works to the subject of this investigation are presented.

Chapter 3 includes a detailed description of the fluids, solutions, substrates and channels used in this research as well as, the methodology and experimental techniques adopted.

In Chapter 4, the contact line dynamics and the pinning/depinning mechanisms acting at the triple contact line of evaporating polymer, poly(ethylene oxide), aqueous sessile droplets are presented for different molecular weights on substrates varying from hydrophilic to hydrophobic. In detail, the evolution of the evaporation process connected with the final dried polymeric deposits left after complete evaporation were analysed and discussed. In addition, the interface phenomena acting at the vicinity of the contact line and their influence in the bulk fluid dynamics which is able to modify the final morphology of the deposits, were extensively studied.

The work conducted in Chapter 5 consists of an experimental investigation on the early time spreading dynamics of evaporating sessile pure liquid droplets and binary alcohol mixtures (self-rewetting fluids) on solid substrates under non-isothermal conditions. A systematic study of the surface tension of the pure liquids and the alcohol mixtures was conducted in a wide range of temperatures. The anomalous property of the surface tension with the temperature for the self-rewetting fluids in some ranges of concentration was revealed. In addition, to widen our knowledge about the interfacial phenomena, an infrared thermal investigation into the liquids mentioned above, at the short times of spreading at different temperatures, was carried out focusing on the presence of Marangoni effect in the system. The chapter reports on the interesting thermal fluctuations present during the wetting-evaporation process of the self-rewetting fluids and the complicated nature of these observations. Stemming from the above-mentioned findings, the effect of non-circular wetted area on the evaporation process of pure water sessile droplets on different substrate and temperatures was investigated using IR thermography. The singularities of the non-spherical evaporating droplets, due to the irregular three-dimensional shape and the associated strong Marangoni effect (interfacial imbalances), was studied revealing interesting thermal pattern activity which is discussed.

In Chapter 6 the migration of bubbles inside a microchannel filled with different operating fluids under isothermal and non-isothermal conditions was systematically investigated. The various interesting bubble flow dynamics are shown to vary depending on the applied mass flux, temperature conditions and the nature of the

liquid flows used. Additionally, an examination of the subsequent heat transfer performance of these liquids in the single and two phase flows was carried out revealing that surface-driven flows may have a significant contribution in the observed behaviour to both pure and alcohol mixtures liquid flows.

The most important findings and conclusions resulting from the present experimental investigation and suggested future work are summarised in Chapter 7.

# Chapter 2: Theory and Literature Review

## 2.1 Wetting and Spreading Phenomena

Wetting - spreading refers to the behaviour of a liquid which is in contact with a solid surface. Wetting phenomena are ubiquitous in nature and occur whenever a surface is exposed to liquids, Figure 2.1-1. Whenever a liquid droplet is placed on the surface of a substrate, the liquid is expected to spread until it reaches an equilibrium state. This may require the drop to either spread covering the surface or remain as a drop adapting a spherical shape. Such a process depends on properties of the surfaces involved as well as the external conditions such as temperature, pressure, relative humidity etc. Due to the common nature of this phenomenon, understanding the different interactions between liquids and solids can greatly improve our knowledge and becomes crucial for many industrial, biological, agricultural or everyday applications [31, 50-53]. One important property that dictates the degree of wettability is surface tension.

**Figure 2.1-1** Wettability and spreading behaviour in nature [54].

### 2.1.1 Surface tension

Surface tension arises from the cohesive nature of liquid matter. A liquid is a state of matter that exists when the attractive forces of the liquid molecules is larger than the thermal movement due to the effect of heat. Molecules at the liquid/vapour interface experience an energy imbalance caused by the much larger attraction of the neighbouring liquid molecules, compared to the gas molecules. This imbalance tends

to cause a net inward force which minimises the surface area of the liquid surface. The attraction results from the presence of various intermolecular forces (Van der Waals, hydrogen bonds, electrostatic forces etc.) as presented in Figure 2.1-2. Surface tension is temperature and/or composition dependent and for narrow temperature ranges is expected to decrease linearly with temperature for ordinary pure liquids (single component). When plotting the surface tension versus the temperature a fairly straight line can be obtained which has a surface tension of zero at the critical temperature. Equation 2.1 depicts the linear dependence of the surface tension on temperature, ignoring the effects of gas phase, for a fixed non-deformable interface and isolated capillary convection from buoyancy by neglecting gravity, [55].

$$\gamma_T = \gamma_0(1 - k\gamma\, T) \tag{2.1}$$

Where $\gamma$ is the surface tension forces and $T$ is the temperature. The term $k\gamma = \left(\frac{\theta\gamma}{\theta T}\right)$ is temperature coefficient and is a universal constant for almost all known liquids, $k\gamma$ = 2.1 x $10^{-7}$ J/K [56]. An important consequence resulting from equation 2.1 is the presence of convection in the system resulting from local variations in temperature and/or composition, and thus surface tension gradients.

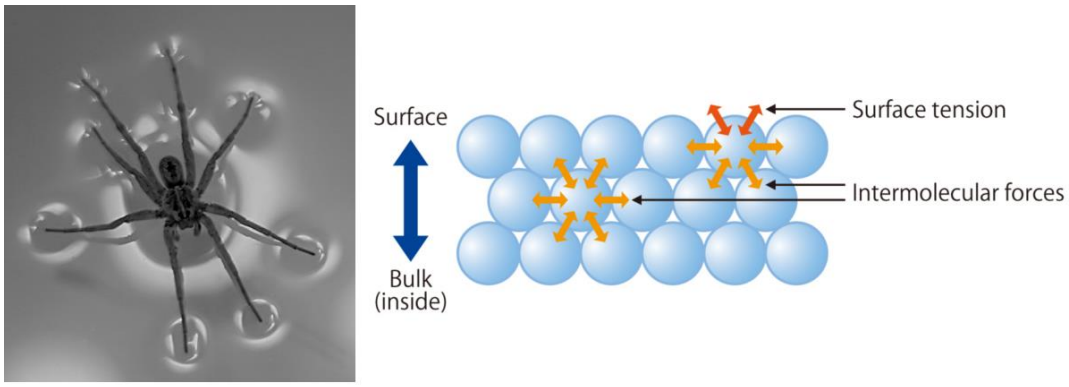


**Figure 2.1-2** Surface tension of a spider on water and a schematic drawing of the intermolecular force between the molecules and the molecules of the liquid try to minimize the surface area of the liquid [57, 58].

## 2.1.2 Young-Laplace equation

In physics, the capillary pressure difference sustained across two static fluids, such as water and air, due to surface tension phenomenon is described by the Young-Laplace equation and is given in equation 2.2 [1]. It is the normal stress balance between two static fluids meeting at an interface, where the interface is treated as a surface with zero thickness.

$$\Delta P = P_{inside} - P_{outside} = \frac{2\gamma}{r_m}$$
$$\frac{1}{r_m} = \gamma\left(\frac{1}{R_1} + \frac{1}{R_2}\right) \quad (2.2)$$

Where $\Delta P$ represents the pressure difference between the two fluid phases, $r_m$ represents the mean radius of curvature, $R_1$ and $R_2$ are the principal radii of curvature, Figure 2.1-3 presents schematically an example of spherical meniscus that forms at the interface between two fluids in a tube, and it is a portion of the surface of a sphere with radius $r_m$.

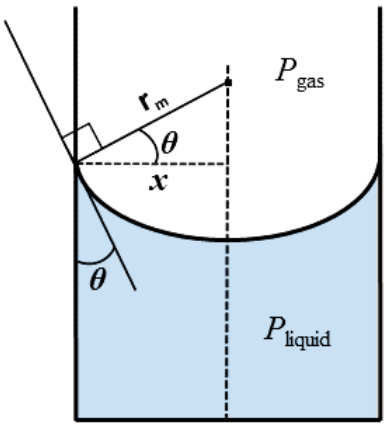


$$r_m = \frac{x}{cos\theta}$$
$$\Delta P = \frac{2\gamma cos\theta}{x}$$

**Figure 2.1-3** Representative example of a spherical meniscus in a tube with wetting angle less than 90°.

### 2.1.3 Wetting modes

Liquids behave differently on different substrates when they come in contact with the latter. For instance, water resting on a silicon substrate will form a spherical droplet, whilst the same droplet when placed on a smooth glass surface will spread completely. The wettability of a liquid phase on a solid phase is defined by the contact angle between the liquid drop and a solid surface. Theoretically, wetting can be described as the motion of a fluid-fluid interface (liquid-gas) over a solid surface [51]. The contact line or wetting line is the regime where the three phases, solid, liquid, gas are meet. In the case of a droplet deposition with negligible inertia forces, the spreading parameter $S$ which measures the surface energy difference between dry and wet surfaces, can be used to predict whether a substrate is wettable or not [51], and this is given in equation 2.3.

$$S = \gamma_{SG} - (\gamma_{SL} + \gamma_{LG}) \tag{2.3}$$

The terms in the equation above represent the interfacial energies, $\gamma$, between the solid/gas, solid/liquid, and gas/liquid, respectively. For $S > 0$, the liquid spreads into a nanometre-thin film which phenomenon called total wetting. For $S < 0$, the drop does not spread completely but reaches an equilibrium spherical shape with an equilibrium contact angle $\theta_{eq}$; which is known as partial wetting.

#### Complete wetting

When the surface energy per unit area of the dry substrate is greater than that of the wetted substrate total wetting occurs. Therefore, the spreading behaviour of liquids is the combination of solid-liquid and liquid vapour surface tensions and, in this case, will not be enough to overcome the solid-vapour surface tension. Liquids with typically low surface tension such as ethanol (~ 22 mN/ m) or butanol (~ 24 mN/ m) etc. tend to spread completely on surfaces, resulting in a thin film of liquid that is depicted on the left of the schematic diagram in Figure 2.1-4.

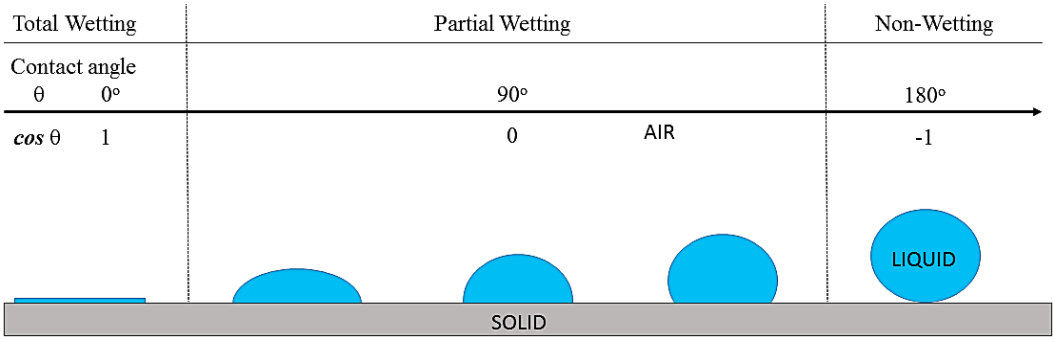


**Figure 2.1-4** Schematic diagram of the spreading regimes depending on the surface, the liquid and the surrounding gas phase.

## Non-wetting

The other extreme case in wetting behaviour occurs when the liquid molecule interactions are stronger than of the fluid-solid interactions. In this case the liquid molecules are packed close together, and liquid would slide like a ball without sticking on the surface due to its strong adhesion and surface tension. The deposited drop forms a globule shape as shown in Figure 2.1-4 (right side). Non wetting liquids are used in thermometry such as mercury (liquid material) which typically behaves in this manner. It can also be observed in water drops resting on hydrophobic surfaces, (Figure 2.1-5). Surfaces which reduce the wetting of a liquid on a surface are useful in many applications, such as self-cleaning applications or as water repellents for textiles and fibres etc.

**Figure 2.1-5** Water drop non-wetting behaviour on a Teflon hydrophobic surface.

## Partial wetting

When the surface energy per unit area of the dry substrate is less than that of the wetted substrate the liquid will not completely spread. The liquid will form an intermediate drop shape, spherical cap, which will have a characteristic non-zero contact angle ($0^o < \theta < 180^o$) at the proximity of the contact line, this is presented in Figure 2.1-5.

## 2.1.4 Young's equilibrium contact angle

It was more than two centuries ago since the seminal work of Thomas Young [1] on wetting was published. Despite all the years, it is still considered as the foundation of modern wetting and capillary phenomena in nature. Young observed the reproducibility of the contact angle obtained between same liquid droplets onto same solid surfaces. More specifically, he was the first to relate the wetting contact angle $\theta$ and the interfacial energies-forces acting at the three phase contact line (solid-liquid-gas), as shown in Figure 2.1-6.

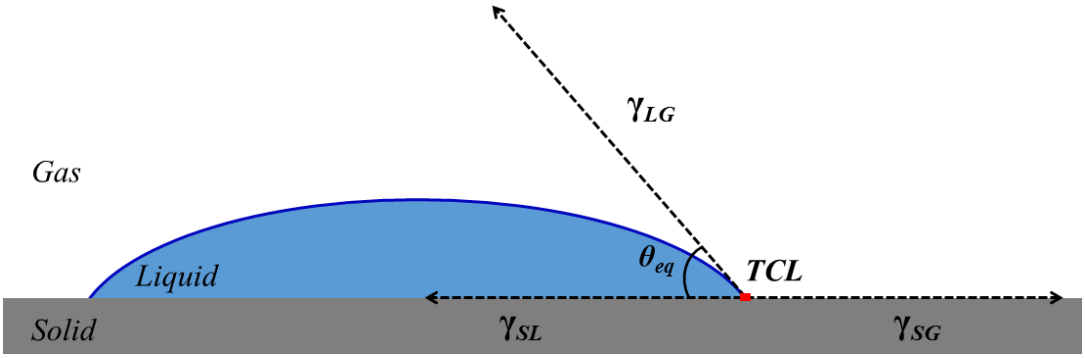


**Figure 2.1-6** Schematic illustration of the Young's force balance at the triple contact line (TLC). A sessile droplet resting on a solid flat surface with the representative three surface tension, $\gamma$, parameters and the equilibrium contact angle, $\theta_{eq}$.

Where $\gamma_{SG}$, $\gamma_{LG}$ and $\gamma_{SL}$ are the different interfacial tensions solid-gas, liquid-gas and solid liquid respectively. $\theta_{\text{eq}}$ is the macroscopically equilibrium contact angle adopted by the droplet between the solid-liquid and the solid-gas interfaces. This force balance proposed by Young [1] and completed by Dupré [59] is still widely used nowadays, in many experimental and numerical studies, as presented in equation 2.4.

$$\gamma_{SG} = \gamma_{SL} + \gamma_{LG} \cdot \cos\theta_{eq} \tag{2.4}$$

The above equation can be obtained either through a force balance near the contact line (CL) or using minimisation of energy potential. This equation, which visualised in Figure 2.1-6, assumes that the system is in thermodynamic equilibrium state. The Young equation is a force balance where surface tension forces, $\gamma$, sum to zero at the three phase contact line, and thus they should dictate the shape of the droplet and the equilibrium contact angle $\theta_{\text{eq}}$. Provided also that the size of the droplet is sufficiently small i.e. radius, *R*, below the capillary length, $l_c = \sqrt{\gamma/\rho g}$ where $\gamma$, $\rho$ and $g$ are surface tension, density and gravitational acceleration, respectively, then gravitational forces can be neglected in the system [50]. Hence, the droplet acquires the shape of an axis-symmetric spherical cap known as a sessile droplet.

### 2.1.5 Contact angle hysteresis

Contact angle hysteresis (CAH) is one of the most important aspect of wetting of liquid droplets on surfaces ranging from centimetre to micrometre scales. In Figure 2.1-7, a characteristic example of a droplets resting on a vertical substrate can easily explain this state. Gravitational forces pull on the droplet to move it down and as a result, the droplet attains an asymmetrical shape. Therefore, the top of the droplet adopts a low contact angle (opposing the driving force of gravity) and the bottom a higher contact angle (in the direction of the driving force, gravity). However, there are many metastable states of a droplet wetting on a solid surface, and the observed contact angles are usually not equal to $\theta_{\text{eq}}$. The phenomenon of wetting is not static

and thus the measurement of a single static contact angle to characterize wetting behaviour is no longer adequate. If the three-phase contact line is in actual motion, the contact angle termed as "dynamic" contact angle. In particular, the contact angles formed by expanding and contracting the liquid phase are referred to as the advancing contact angle $\theta_a$ and the receding contact angle $\theta_r$, respectively, Figure 2.1-7. Dynamic contact angles can be measured at various rates of speed but at a characteristic low speed, it should be close or equal to a properly measured static-equilibrium contact angle. The difference between the advancing angle and the receding angle which is called the hysteresis, it has extensively been studied by many researchers [3, 4, 50, 60-62] and can be estimated as: $H = \theta_a - \theta_r$. The significance of contact angle hysteresis has been extensively investigated and the general conclusion is that it arises from surface roughness and/or heterogeneity [63-68]. Since most solids are never truly homogeneous, the surface defects such as impurities, contaminants etc. interfere (contact line pinning) with the contact line, and thus the determination of the exact value of the contact angle is difficult to be estimated.

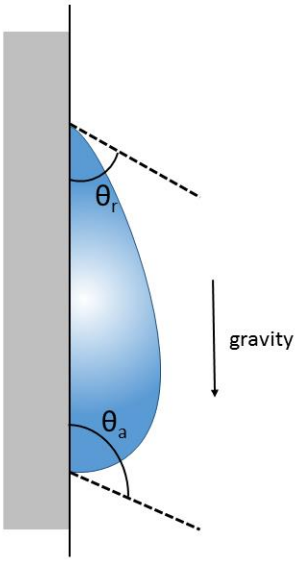


**Figure 2.1-7** Schematic illustration of a drop on a vertical surface, resting at the critical advancing contact angle $\theta_a$ and the critical receding contact angle $\theta_r$, under the gravity effect.

## 2.2 Spreading and Contact Line Dynamics

Spreading behaviour and subsequent evaporation when a droplet is deposited on a solid substrate have attracted the interest because of the influence to a large number of technological applications involved in coating, microfluidics and ink-jet printing technologies [3, 31, 50, 53, 69-72]. The underlying mechanisms for these phenomena are still under investigation and are recognised as crucial in a wide range of biological, natural and industrial processes [26, 28-30]. Droplet wetting and evaporation is a complex phenomenon involving three phases (liquid, vapour, and solid) interactions through coupling by conduction with the substrate, convection/conduction within the drop and convection/diffusion in the vapour phase. When the fluid impacts on a solid surface it is initially in a transient region where the contact line moves until the liquid-solid-vapour system reaches its equilibrium state. The first moments of spreading tend to be rapid and the dynamics on how the drop reaches a stationary condition vary depending on important parameters such as surface chemistry, liquid physicochemical properties and environmental conditions [3, 50, 72].

Many experimental and theoretical studies have been devoted to understanding the evolution of the internal flows generated within a spreading and evaporating liquid drop, and the drastic effect on the wetting. These flows within the drops are affected by liquid viscosity, surface tension, density, and the wettability of the substrate surface and influence the wetting behaviour of the liquid on solids. Moreover, adding heat in the system (by e.g. a heated substrate) induces variations of the physical properties which complicates the system and modifies further the wetting behaviour of the droplet.

In the case of single-component droplets, a characteristic flow is generated within the droplet and it is found to be an outward flow stemming from mass conservation in order to replenish liquid evaporating preferentially at the outer edge of the droplet [25-27]. During the evaporation of volatile liquid droplets thermocapillary instabilities, known as Marangoni instabilities, are developed when a system is subjected to

sufficiently strong surface tension gradients. The origin of this fluid flow instabilities, in volatile liquid droplets, is the Marangoni flow (effect) which is driven by surface tension instabilities along the interface due to temperature gradients [18, 29]. The interests in thermal flows-instabilities commenced at the beginning of the 20$^{th}$ century pioneered by Bénard [73]. He performed experiments, in which horizontal liquid sheets were subjected to a vertical temperature gradient and observed cellular convection patterns, known as Bénard cells. Later investigations [55, 74, 75] showed that the convection cells in shallow liquid layers are due to the presence of surface tension instabilities rather than buoyancy driven. Pearson [55] concluded that these patterns could not be explained by means of density gradients in the system but surface tension gradients are the driving force i.e. Marangoni effect. Ghasemi *et al*. [76] reported that the flow in an evaporating water droplet which is in a reduced pressure environment, is driven mainly by thermocapillary convection i.e. temperature gradients. This study pointed out to the important role of the Marangoni flow in the energy transport mechanism, as the evaporation rate increased in the case of reduced pressure environment. The significant contribution of the Marangoni flow, i.e. intensity and orientation, in a single-component system depends on the relative thermal properties of the substrate and the liquid, and the experimental conditions [77]. Generally, surface-tension-driven flows in single-component volatile droplets, e.g. water, are essentially thermocapillary in nature.

On the other hand, for binary and generally multicomponent droplets the physical behaviour poses many challenges as it can be more complex. Previous studies with droplets formed by binary mixtures of water with alcohol (methanol [49], ethanol [23, 78-81] and 1-propanol [36]) showed a different behaviour compared to those of the pure liquids. The evaporation mechanism of these binary mixtures in particular involves three distinct stages: a first stage, where the more volatile component (alcohol) migrates to the liquid interface and evaporates first; a second stage which is transitional and involves evaporation by both components (mixed stage); and a last stage which mainly consists of the evaporation of the less volatile component of the mixture [23, 49, 78, 81, 82].

Previous studies investigating the first seconds of an evaporating droplet spreading on a solid surface revealed that the underlying mechanisms of the observed behaviour are related to inertia, capillary and viscous forces [3, 50, 72, 83]. More specifically, during spreading the contact line moves radially outwards from the contact point and the droplet wets a circular area of radius $r(t)$. The unbalanced horizontal force: $\gamma(\cos\theta - \cos\theta_{eq})$ drives the droplet to spread on the substrate until it reaches the final equilibrium contact angle $\theta_{eq}$, where $\gamma$ is the liquid-vapour interface surface tension and $\theta$ the instantaneous contact angle. Experimental and theoretical studies of spreading droplets have shown that an inertial regime exists before the viscous regime [84-88]. This rapid early stage of wetting lasts only few milliseconds and, for completely wetting surfaces, it is well described by an exponential power law, $r \sim t^{1/2}$. Here, the characteristic inertia time scale $\tau_\rho$ for the early stage of spreading is $\tau_\rho \sim \sqrt{\rho R^3/\gamma}$, where $R$ is the initial droplet radius before contact and $\rho$ is the liquid density [84, 85, 89, 90]. Bird *et al.* found that the short-time spreading dynamics depends strongly on surface wettability due to capillary wave generation, leading to a non-universal exponent that varies with the equilibrium contact angle $\theta_{eq}$ [85]. Interestingly, more recent investigations for droplets spreading on partially wetting surfaces revealed that the early times dynamics (immediately after initial contact) are independent of the surface wettability, with an exponent ~0.5 (best fit exponent: 0.48) consistent with the inertia-capillary balance [90]. Additionally, in the final stage of spreading, it is well known that the spreading dynamics are governed by the Tanner's law which emerges by balancing capillary and viscous forces and relates the radius of the wetted area with time as $r \sim t^{1/10}$ [50, 91, 92]. The spreading dynamics in this regime is characteristically slow and if the capillary forces driving the flow are primarily hindered by viscosity the natural timescale follows as $\tau_\mu \sim \rho R/\gamma$.

## 2.3 Sessile Droplet Evaporation

Evaporation phenomenon is encountered in several engineering and industrial processes such as spray drying, rapid cooling by drop wise heat exchange, fuel

injection into combustion engines, medical care, controlling the deposition of particles on solid surfaces, nuclear engineering and microelectronics [10-14, 16, 20-22, 24, 26, 27, 30, 93-103]. Understanding the physics of an evaporating sessile drop requires a detailed analysis of heat and mass transfer at various interfaces: liquid-gas, solid-gas and solid-liquid. The evaporation of liquid phase is a natural phenomenon and when the atmosphere in the immediate vicinity of the drop is not saturated with the vapour of the liquid, evaporation occurs i.e. liquid molecules are transferred from liquid to the surrounding atmosphere due to the phase change (liquid-gas). The wetted area of a deposited sessile liquid drop is limited by the contact line and can be characterized by contact angle, contact radius and drop height. The mass loss from the liquid phase due to evaporation results in a changing drop profile; either by a decrease in contact angle or a reduction in base radius or a combination of both. Picknett and Bexon [11], conducted a theoretical and experimental investigation into the evaporation of small drops where gravitational effects were neglected and a spherical cap approximation for the drop shape was applied. The results indicate the presence of three distinct modes of drop evaporation: constant contact radius (CCR), constant contact angle (CCA) or a mixed mode, Figure 2.3-1. A few years after the milestone work of Picknett and Bexon [11], the evaporation modes were related to the wetting behaviour by Birdi *et al.* [13] where different evaporation modes were reported depending on the wettability of the substrate i.e. hydrophilic (contact angle, $\theta < 90^o$) or hydrophobic (contact angle, $\theta > 90^o$). On hydrophilic surfaces, the evaporation proceeds at constant (pinned) radius (CCR) while the contact angle decreases in time leading to a steady evaporation rate (increase) over time. Other works related to the subject of evaporation mechanism are those of Birdi *et al.*[12] and Rowan *et al.* [94] who carried out experiments showing that in CCR mode, the evaporation rate is higher for bigger droplets radii due to the diffusion-driven evaporation. The evaporation rate of droplets at CCR was further investigated and supported by Panwar *et al.* [22] where the evaporating droplet followed a linear decay of mass in time. On the other hand, at CCA mode, the droplet evaporates with a receding contact radius while the contact angle remains fixed, Figure 2.3-1.

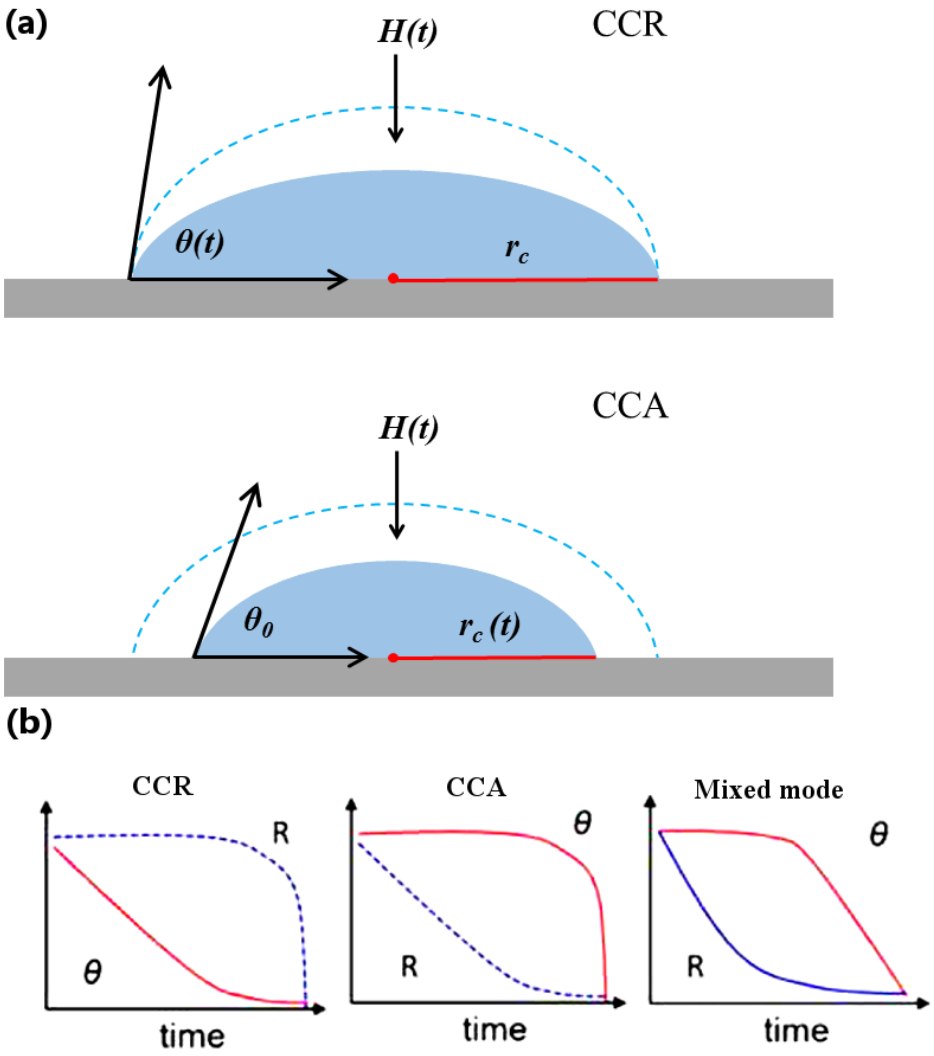


**Figure 2.3-1** Modes of droplet evaporation. (a) Evaporation mechanism with constant contact base radius $r_c$, (CCR) whilst the drop contact angle $\theta$ (t) decreases in time. The droplet evaporates with constant contact angle $\theta_0$, (CCA) and the base radius $r_c$ (t) decreases in time. (b) Representative graphs of the evaporation modes: CCR ($R$ = constant and $\theta \neq$ constant), CCA ($R \neq$ constant and $\theta$ = constant) and mixed mode ($R \neq$ constant and $\theta \neq$ constant).

On (smooth) hydrophobic surfaces at CCA evaporation mode, Mc Hale *et al.* [104] and Erbil [20] found that the contact radius monotonically decreased and the constant contact angle led to a non-linear evolution of mass or volume loss in time. In the mixed mode, evaporation occurs with either or both contact angle and contact radius decreasing in time. However, it was not until the work of Bourgès-Monnier and Shanahan [10] that the evaporation of pure sessile droplets and the impact of the substrate's roughness were extensively investigated. They thoroughly studied the

evaporation behaviour of two different fluids varying the substrate hydrophobicity and four different evaporative regimes were identified. They showed that a droplet could evaporate in a more complicated fashion mixing the CCR and CCA modes. This mechanism is usually referred to as stick-slip (SS) mode. In the first regime the drop was found to evaporate with a constant contact radius. In the second stage of evaporation, the contact angle and drop height decrease to account for the volume loss of the evaporated liquid. Third stage, which occurs on smooth surfaces, drop height and contact angle remain almost stationary, with a corresponding decrease in base radius. Finally, in the fourth stage which corresponds to the drop disappearance, Figure 2.3-2.

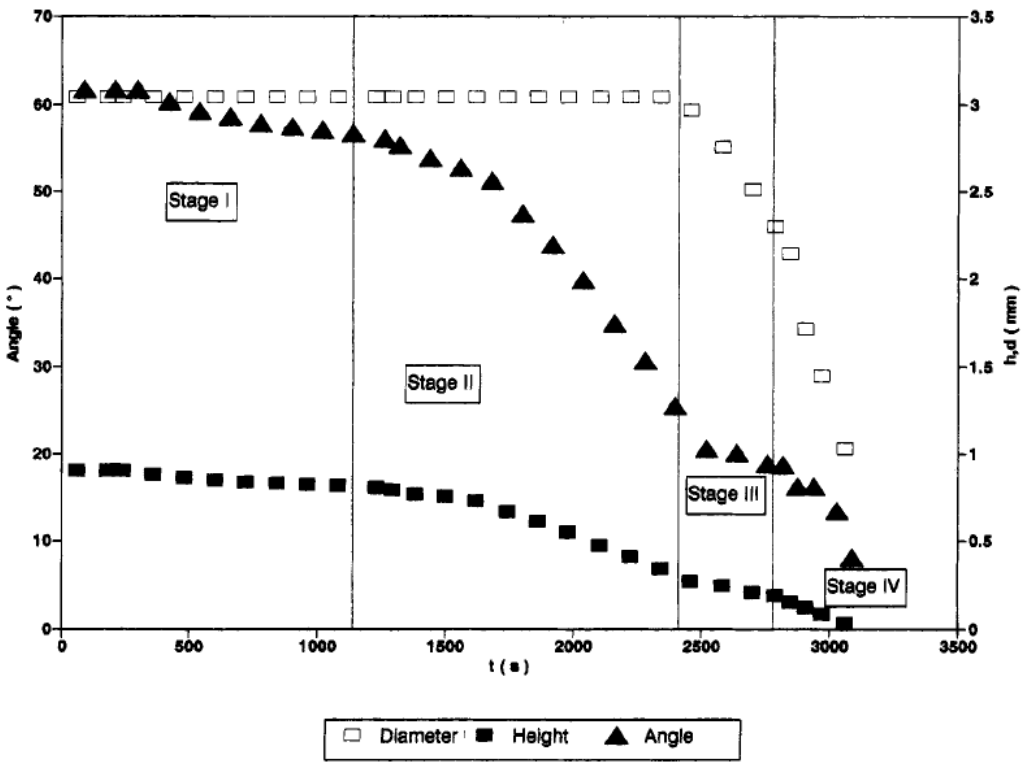


**Figure 2.3-2** Evolution of drop height, *h*, contact diameter, *d*, and contact angle, *θ*, for a water drop (initial volume 4μL) on a polished epoxy surface [10].

Many theoretical investigations have been conducted during this century. Picknett and Bexon [11] proposed a diffusion model based on the Maxwell's [105] equation which

describes the transport of vapour molecules from the surface of a spherical droplet towards an infinite medium analogous to that of heat diffusion

$$-\frac{dm}{dt} = -4\pi RD(c_s - c_\infty) \tag{2.5}$$

where $-\frac{dm}{dt}$ is the rate of mass loss in time of a sphere with radius $R$, $D$ is the molecular diffusion coefficient of the vapour in air, and $c_s$ and $c_\infty$ the vapour concentration of saturation and that of the infinite medium, respectively. Thereafter, Picknett and Bexon [11] using the analogy between diffusive flux and electrostatic potential, attempted to determine the complex problem of an evaporative liquid drop which wets a solid substrate. A decrease in the rate of evaporation was observed due to the lesser liquid-gas interface area sensitive to evaporation when compared to that of a sphere, because of the smaller surface area for the diffusion of vapour molecules. This reduction in evaporation rate was modelled by introducing a factor, $C_x$, the electrostatic capacitance, analogous to the one used for obtaining the electrostatic potential of an equiconvex lens. This factor, $C_x$, is function of both droplet contact angle and radius of curvature [11]:

$$-\frac{dm}{dt} = -4\pi RD(c_s - c_\infty)C_x \tag{2.6}$$

Based on all the latter and bringing together all the findings, understanding the evaporation mechanism and wetting behaviour of liquids becomes crucial for many industrial applications and everyday life events. It is evident that evaporation of sessile droplets depends essentially on the evaporation mode which is dictated by the dynamics at the contact line and hence depends on the nature of the substrate and the fluid, respectively.

## 2.4 Colloidal Droplet Evaporation and Coffee Stain Effect

Colloidal suspensions are found all around in everyday life events such as paints, milk, coffee, blood etc. This term can be defined as a disperse phase of solid particles (micrometre size) which are homogeneously mixed in a bulk fluid or a continuous medium and have been proposed for many industrial sectors such as inject printing technologies [72, 106], pharmaceutical and biological applications [14, 50], self-assembly [33], evaporative cooling technologies [107] etc. In the seminal work of Deegan *et al.* [26] in 1997, the evaporation of colloidal suspensions (containing micro-spheres) and the coffee ring stain left after complete dry-out was investigated, as presented in Figure 2.4-1. In a free evaporative system, the presence of particles in suspension have been reported to have an important impact on the contact line dynamics as well as self-assembly [25, 33, 108]. Because of the preferential evaporation near the CL, suspended particles ‘‘tend’’ to deposit there and form the ‘‘coffee ring’’ stains.

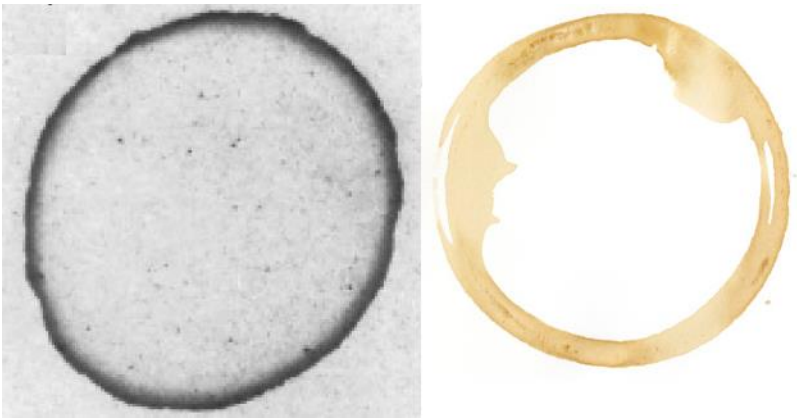

**Figure 2.4-1** (Left) Ring stain effect, after the complete dry-out of an evaporating droplet containing micro-spheres, under the CCR mode [25]. (Right) The well-known coffee ring stain phenomenon.

The phenomenon of “coffee stains” is explained by the outward flow generate within an evaporating droplet [26]. This outward flow, named capillary flow, is a combination of the increased evaporation rate at the droplet edge and the contact line

pinning caused by solute deposition near the contact line [26]. More specifically, since evaporation is greater at the TCL, particles which are homogeneously suspended in the solution, are dragged from the bulk towards the contact line enhancing the accumulation and deposition at the edge. The induced outward capillary flow within the droplet, the migration and the deposition of particles at the droplet edge with the characteristic evaporative flux profile along the liquid interface is presented in Figure 2.4-2. The equation 2.7 describes the radial outward velocity $\bar{v}$ , based on a vertically averaged radial flow [27].

$$\bar{v}(r,t) = -\frac{1}{\rho r h}\int dr \cdot r\left[J(r,t)\sqrt{1+\left(\frac{\theta h}{\theta r}\right)^2}+\rho\frac{\theta h}{\theta t}\right] \qquad (2.7)\ [27]$$

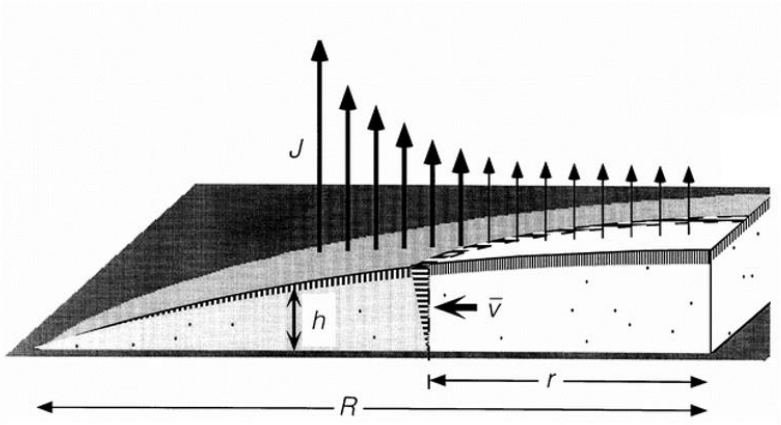


**Figure 2.4-2** Schematic representation of the evaporation mechanism of a droplet containing particles where *J* is the evaporative flux i.e. vapour leaves at a rate per unit area *J*(r), $\bar{v}$ is the outward flow mean velocity. Note that evaporation flux distribution on droplet surface is irregular.

However, Shen *et al.* showed that for evaporating droplets exists a lower limit of droplet size for successful formation of a coffee ring structure (above a concentration threshold) [109]. This is owing to the competition between the liquid evaporation time and particles diffusive motion within the droplet. For suspended particles of size ~100 nm, the minimum diameter of the coffee-ring structure is found to be ~10 μm. Small droplets will dry more quickly, and therefore the suspended particles will not have sufficient time to migrate to the contact-line rim and form the ring stain. Hu and Larsson [14] supported the observations of Deegan *et al.* and proposed an analytical

model for the evaporation of pinned sessile droplets. These authors suggested analytical expressions for the non-uniform distribution of both vapour and evaporative flux at the droplet surface as a function of contact angle $\theta$ (from $0^o$ to $90^o$) during evaporation. In subsequent publications, the same authors Hu and Larsson [18, 99], neglected inertia effects and employed lubrication theory to investigate the velocity flow fields within the droplets, first in absence of Marangoni (thermocapillary) stresses [99] and then taking into account the latter [18]. These Marangoni stresses are due to the surface tension gradient caused by a non-uniform temperature distribution along the droplet interface. Following from these studies Hu and Larsson [29] showed numerically that the ring-formation behaviour can be suspended as a result of the presence of recirculating currents within the evaporating droplet caused by the thermal Marangoni flows. They concluded that the coffee-ring phenomenon requires not only a pinned contact line, where particles adhere to the substrate, but also the suppression of the Marangoni effect which results from surface-tension gradients due to the evaporative cooling [29]. Later Ristenpart *et al.* [77] concluded that the direction of the flow depends on the relative thermal conductivities of the substrate and the liquid.

Crafton & Black investigated the role of the substrate temperature on the wetting and evaporation behaviour of volatile droplets [110], using water and heptane drops on aluminium and copper surfaces. They observed and quantified the evaporation rates of small liquid droplets in order to measure heat transfer rates when droplets evaporate on a horizontal heated surfaces. Mollaret *et al.* [17] investigated the wetting and evaporation mechanism of sessile water drops on heated aluminium and PTFE surfaces. The observed behaviour of the water drops was explained by a force balance at the triple contact line during evaporation. The strong effect of thermal conductivity of various substrates on the evaporation rate of sessile droplets was examined by David *et al.* [111]. Later on, Sobac & Brutin [112] experimentally investigated the influence of the substrate temperature and substrate thermal properties on the evaporation process of pinned water drops into air. They showed that the influence of the substrate thermal properties on the evaporation rate of the system is explained by the thermal diffusivity of the liquid and solid phases. Sefiane *et al.* [30] performed an experimental and theoretical study focused on the effect of atmosphere conditions of an evaporating pinned water drop onto different substrates. They found that by reducing the atmospheric pressure, there is an increase in the diffusion coefficient of

water vapour in the atmosphere and hence increased the evaporation rate. Also, by using different ambient gases they altered the diffusion coefficient and therefore affected the evaporation rate of the system [30]. Very recently Shanahan revised [113] the CCR and CCA modes of evaporation and proposed new analytical expressions to demonstrate the dependence of the lifetime of a volatile (ethanol) droplet on the hydrophobicity of the substrate.

In 1995, Shanahan [95] developed a theory, for stick-slip mode (SS), in order to explain the characteristic jumps of the drops contact line in the last stages of the evaporation process. In the following years, a few number of experimental and theoretical studies have been focused on the complex pinning-depinning behaviour of the triple contact line (SS mode) by Nguyen & Nguyen [114], Moffat *et al.* [102], Orejon *et al.* [115] and Askounis *et al.* [116] . They concluded that the contact line dynamics are governed by the competition between the pinning forces i.e. anchored contact line due to chemical or surface heterogeneities, and the depinning forces due to the resulting deviations of the droplet shape profile [115].

It is clear from the review so far, that the addition of nanoparticles in a bulk liquid changes drastically the contact line dynamics of the system depending on the evaporative mode: constant contact radius (CCR), constant contact angle (CCA) or ‘‘stick-slip’’ (SS). To conclude, the final morphology of the dried solute is not always a ring and depends on many experimental factors, including the interactions among solvent, solute, vapour, and substrate [36, 37], the solvent evaporation rate [117], the shape of suspended particles [118], phase transitions within the droplet [119, 120], self-assembly and organization as mediated by solvent dewetting [25, 33, 121], and the contribution of any convective currents [18, 29] etc.

## 2.5 Polymer Evaporation Stages and Final Morphology

Besides single-component fluids and colloidal suspensions, drying experiments have been performed on drops of polymer solutions and complex fluids. The drying process of composite fluids such as polymer solutions involves a complex evolution which is

related to a large number of microscopic phenomena such as solvent diffusion, transfers at the vapour / liquid / interface, concentration changes, and phase transitions: gelation or glass transition etc. [38, 39, 119, 120, 122-124]. These phenomena are crucial for printing and coating technologies since they give rise to major defects and irregularities in the system such as cracks, debonding and wrinkles, and thus the final material quality. From the fundamental standpoint, interest has grown recently in surface instabilities, crack patterns arising from shrinkage of the solute polymeric material during evaporation process and the final morphology formation.

Pauchard *et al.* [120, 122] reported a number of complicated phenomena that arise as polymer solutions evaporate. In their study, during the evaporation process of dextran (a branched polysaccharide) solutions, the concentration at the droplet's edge increased as a result of the outward capillary flow within the liquid phase. This resulted in a phase change on the surface of the liquid droplet forming a glassy skin with a spherical shape [120, 122, 125, 126]. Further evaporation and loss of water within the droplet led to the glassy cap which was deforming and buckling with different shapes. All of these various complicated structures, including doughnut- and sombrero-like deposits, depend on experimental conditions such as the contact angle, relative humidity, temperature, and polymer concentration [122, 127]. In this study, particular interest was paid to investigate the complete evaporation process of poly(ethylene oxide) (PEO), one of the most extensively studied of all water-soluble synthetic polymers [128-131]. It is a very common and widely used linear (non-branched) polymer [132-135], and precipitates as a solid phase, usually in the form of semi-crystalline termed as spherulites. It dissolves well in water, although at high concentrations or molecular weights polymer solutions can appear cloudy because of micrometre-sized clusters of undissolved polymer [130]. The origin of these clusters is still a point of speculation for many researchers. Previous studies on drying droplets of PEO solutions showed that the deposited solid structures could not be described by either the coffee-ring stain effect or the proposed skin-buckling models but required a four-stage drying process: *pinned drying*; where contact line is stationary, *pseudodewetting*; where the receding contact line is induced by precipitation, *boot-strap growth-building*; during which the liquid droplet is lifted on freshly precipitated solid, and *solid contraction*; late drying stage [123, 127]. In the recent work of

Willmer *et al.* [123] the physical and chemical properties of PEO was extensively discussed. In particular, the amphiphilic nature of PEO in solutions and its tendency to form crystalline spherulites rather than an amorphous glass at high concentrations. They proposed that the four-stage drying process cannot be explained using a skin-buckling model because the surface area of the droplet is shown to increase during the characteristic growth stage [123]. Thereafter, they concluded that a crucial mechanism during the boot-strap stage takes place in which the liquid droplet is lifted above the surface by the newly formed solid deposit, resulting in solid pillars [123]. Later, Baldwin *et al.* [38] performed experiments on the evaporation of aqueous PEO. They focused on a detailed description of each stage and proposed physical models to explain key aspects of the distinct pillar formation. More specifically, they examined several experimental parameters including relative humidity, temperature, pressure, droplet volume, and initial contact angle, revealing their influence on the final morphology of the dried polymeric material i.e. shape of the deposits – puddle or tall pillar [38]. The effects of these parameters are combined into a dimensionless Péclet number, $Pe = \frac{h_0 J}{D_c}$, which is the ratio of advection over diffusive motion of the dissolved polymer, where $J$ is the evaporative flux per unit area, $h_0$ is the initial height, and $D_c$ is the cooperative diffusion coefficient of the polymeric material [38]. The Péclet number is plotted against concentration in a phase diagram revealing that a clear boundary separates pillars and puddles with given initial parameters [38]. The experimental analysis showed that the final deposit of these heterogeneous elevated structures can sometimes be taller than the initial droplet height and all of the dried polymeric material ends up nearly in the centre of the droplet rather than distributed around the edge of the initial triple contact line (TCL), i.e., the typical ring-stain effect as discussed in previous chapters [38]. Recently, Baldwin *et al.* [124] presented a semi quantitative model comparing the opposing effects of advective build-up at the contact line to diffusive flux and used it to calculate a dimensionless number $x$ in order to predict which deposit will form. This ratio $x$ is similar to the Péclet number, but it is constructed for the specific narrow wedge near the triple contact line, comparing the effective motions of flux and diffusion motion in this characteristic region:

$$x \approx [K/(2\pi)][c_0/(1-c_0)][\dot{a}/(D_0\, R\, \sin\theta)] \qquad (2.8)$$

where $K$ is a constant, $D_0$ is the self-diffusion coefficient, $c_0$ is the initial concentration, $\theta$ is the contact angle, and $\dot{\alpha}$ is the overall evaporation rate. By analysing the varying experimental parameters of concentration and flux, they showed that the boundary between flat puddles and pillars (monoliths) is at $x \approx 1.6$ [124]. They concluded that the drying behaviour of these polymer droplets was defined by three critical factors: initial concentration, droplet geometry, and evaporation rate [124]. In the latest work of Baldwin *et al.*, [39] final pillar (monolith) formation was extensively investigated with respect to the molecular weight, evaporation rate, and concentration of the PEO droplets. Through a variety of experiments and measurements, they demonstrated that the pillar (monolith) formation occurs over a limited range of molecular weights. They have also shown that values of $Pe > 1$ lead to a preferential deposition of the PEO solute at the contact line, which can explain pillar formation for intermediate molecular weights [39]. However, the Péclet number argument does not account for the absence of pillars at high molecular weights [39, 136]. They discussed the molecular-weight dependence within various theoretical frameworks (e.g. viscoelasticity and diffusion), and they speculated on the influence of contact line crystallization, viscosity, adhesion, and friction phenomena [136]. However, the variation of the end result dried deposits i.e. puddles or pillars, on different molecular weights still poses many challenges and unexplained questions. It is important to determine how to control the evaporation mechanism and the final shape of the solute dried deposit for different molecular weights for both fundamental and application reasons.

## 2.6 Thermocapillarity in Drops and Bubbles

The term ‘‘thermocapillarity’’ refers to phenomena that arise as a result of interfacial tension gradients at a liquid-liquid or gas-liquid interface caused by temperature differences along the interface. Regularly, gravity is always presents on earth, and when the density of a dispersed liquid phase differs from that of a continuous phase, the dispersed phase will sink or rise if it is denser or less dense than the continuous phase, respectively, e.g. air bubbles in a liquid. Many experimental works have been

carried out in space conditions with the motivation of studying the motion of bubbles, drops or particles due to forces other than gravity. In experiments performed abroad a space vehicle such as an orbiting space laboratory or an outer space probe, gravitational effects acting on these objects suspended in a fluid phase are so small that can be neglected. There are few mechanisms free of gravitational forces that will cause a bubble or a drop in a liquid to move such as an electric or magnetic field. However, the most common mechanism that have been used in many experimental works is the application of a temperature gradient field in a continuous phase. A temperature variation in a liquid phase can be achieved by heating or cooling the system locally.

Thermocapillarity can be considered as a mechanism for driving the motion of drops and bubbles immersed in a second phase. The change in the interfacial tension (formation of surface tension gradients) at the liquid-liquid or gas-liquid interface due to temperature variations induces thermocapillary (tangential) stresses, known as Marangoni stresses (Marangoni effect) and cause a bubble or a drop to move. This mechanism is always present in non-isothermal interfacial flows. Typically, the interfacial tension of pure (ordinary) liquids decreases linearly with increasing temperature which leads to the motion of bubbles or drops toward warmer regions, in the direction of the applied temperature gradient. In practise, drops rarely move at a steady state because the physical and chemical properties vary with temperature. The most important physical property in this case is liquid viscosity. A drop is expected to continue to accelerate as it moves toward the warmer regions due to the decreasing function of viscosity with the temperature. In less common cases where the interfacial tension increases with increasing temperature, a drop or bubble, when released from a steady state would initially accelerate towards to colder regions but then decelerate as it encounters as more viscous liquid. This reverse-anomalous behaviour (reverse Marangoni effect) compared with those of the pure liquids, in the presence of surface tension gradients in the system, is encountered sometimes in the cases of mixtures e.g. binary alcohol mixtures. This kind of alcohol liquid mixtures (self-rewetting) will be investigated extensively in this thesis and will be discussed in Chapters 5 and 6.

The mechanism of thermocapillary stresses is driving interfacial flows and it can be important in a great variety of microfluidics applications as have been reported in previous works [137-141]. In their seminal work, Young *et al.* [142] studied the thermocapillary migration of bubbles for the first time. They performed experiments on air bubbles in a column filled with viscous fluid, silicone oil, heated from below. They showed that under the effect of thermocapillary force, small bubbles was seen to move downwards, whereas larger bubbles moved in the opposite direction due to the fact that buoyancy overcomes the effect of thermocapillarity [142]. Moreover, Young *et al.* provided a theoretical description of the bubble motion under the combined influence of gravity and thermocapillarity, in a downward temperature gradient field, leading the bubbles to almost come to a standstill position as the acting forces are balanced [142]. The governing equation in the linear limit where convective transfer of energy and momentum were negligible in the system, with Reynolds and Marangoni numbers close to zero, were solved by Young *et al.* Following this pioneering work, numerous theoretical and experimental studies have been carried out to investigate the effect of convective heat transfer with varying Reynolds numbers (small-large) [143-147], showed that the results of Young *et al.* were a solution of the momentum equation for an arbitrary Reynolds number, where the convective heat transfer in the system was not taken into account. These authors also reported and calculated the presence of drop deformation from the spherical shape.

The latter studies stemmed from the interest in microgravity applications where buoyancy was considered negligible. Later on, bubble migration under the effect of buoyancy combined with the action of thermocapillarity, was studied by Merrit *et al.*, presenting numerical simulations [148]. Balasubramaniam examined the motion of a gas bubble in a vertical temperature gradient including buoyant contribution to this motion and the influence of temperature on viscosity [149]. The results obtained showed that the steady migration velocity of the bubble, with the largest order of magnitude, is a linear combination of the velocity for solely thermocapillary motion obtained by Balasubramaniam & Subramanian (1996) [143] and the purely buoyancy-driven rise velocity of the bubble in the limiting case of large Reynolds and Marangoni numbers [149]. A great variety also of numerical simulations have been performed taking in account the effect of surface deformation on thermocapillary bubble

migration with varying dimensionless numbers such as Capillary, Marangoni and Reynolds numbers [150-154].

Most of the studies mentioned above have been considered for common (ordinary) fluids such as water, oil, air etc. where the surface tension decreases almost linearly with increasing temperature. However, very recently, Shanahan and Sefiane demonstrated that thermocapillary force may drove bubbles against a liquid flow in a binary alcohol mixture [155]. This previously unreported phenomenon revealed by Shanahan and Sefiane, brought in light a new type behaviour in which bubbles tend to travel against the liquid flow towards colder regions due to the strong effect of thermocapillarity in the system [155]. They concluded that this newly unusual observed behaviour of travelling bubbles corresponded to the ‘‘anomalous’’ property of the alcohol mixtures used in the experiments. Continuing with the efforts to understand the behaviour of bubbles in binary alcohol mixtures, in this present study, we are interested to investigate the thermocapillary migration of bubbles inside a channel filled with a continuous liquid phase that exhibits a non-linear dependence of the surface tension on temperature (self-rewetting fluid), under a controlled temperature gradient field.

### 2.6.1 Dimensionless group numbers

The most common entities that are measured in thermocapillary migration of drops and bubbles, in isothermal and non-isothermal systems, are the trajectory of a bubble or drop. Theoretical models attempted to provide predictions and insights for the velocity profile, size and shape of migrating bubbles or drops, by making idealized assumptions. However, when the governing equations and boundary condition are non-dimensionalized, three important dimensionless groups emerge, termed as Reynolds ($Re$), Marangoni ($Ma$) and Capillary ($Ca$) numbers:

$$Re = \frac{ineria\ forces}{viscous\ forces} = RV/v \tag{2.9}$$

$$Ma = \frac{convective\ energy\ transport}{conduction\ energy\ transport} = RV/a \tag{2.10}$$

$$Ca = \frac{viscous\ forces}{surface\ tension\ forces} = \mu V/\gamma \tag{2.11}$$

Here, $R$ is the drop radius, $v$ is the kinematic viscosity of the continuous phase, $a$ is the thermal diffusivity, $\mu$ is its dynamic viscosity and $\gamma$ is the surface tension between the drop and the continuous phase. The symbol $V$ refers to the characteristic velocity, obtained by balancing the thermocapillary stress at the liquid interface with a specific viscous stress and can be defined as:

$$V = \frac{|\gamma_T|\,|\nabla T_\infty| R}{\mu} \tag{2.12}$$

where $\gamma_T$ is the rate of change of interfacial tension with temperature, $\nabla T_\infty$ is the temperature gradients enforced in the continuous fluid phase. The ratio surface forces to inertia forces is expressed by Kapitza ($Ka$) dimensionless number. The Kapitza number acts as an indicator of the hydrodynamic wave regime in the falling liquid film flows and can be described as:

$$Ka = \frac{\gamma}{\rho(g \sin\theta)^{1/3} v^{4/3}} \tag{2.13}$$

where $\gamma$ is the surface tension force, $g$ is gravitational acceleration, $\rho$ is density, $\theta$ is inclination angle, and $v$ is kinematic viscosity.

Therefore, in the general problem, there are more independent dimensionless numbers such as Prandlt ($Pr$), Weber ($We$), Grasshof ($Gr$), Rayleigh ($Ra$), Nusselt ($Nu$), Bond ($Bo$) which include additional parameters such as ratio of viscosities, thermal conductivities, thermal diffusivities and the densities of the two phases etc.

Prandtl ($Pr$) group is a dimensionless number, named after the German physicist Ludwig Prandtl, defined as the ratio of momentum diffusivity (kinematic viscosity), $v$, to thermal diffusivity, $a$.

$$Pr = \frac{v}{a} = \frac{viscous\ diffusion\ rate}{thermal\ diffusion\ rate} = \frac{\mu/\rho}{k/c_p\rho} \tag{2.14}$$

Where $k$ is the thermal conductivity and $c_p$ is the heat capacity.

Weber ($We$) number is a useful dimensionless number for analysing multiphase flows and it measures the relative importance of fluid's inertia compared to its surface tension:

$$We = \frac{\rho V^2 L}{\gamma} \tag{2.15}$$

$L$ is its characteristic length, usually the droplet or bubble diameter.

For larger Capillary numbers ($Ca$ > 0.02), inertial effects must be considered and hence the researchers suggested an empirical correlation of the dimensionless bubble diameter by considering capillary number ($Ca$) and Weber number ($We$). In fact, Weber number includes Capillary and Reynolds numbers [156] and when inertia effects are important in the system the follows as: $We = Re \cdot Ca = \rho RV^2/\gamma$, and influence deformation.

In fluid dynamics and heat transfer, the Grashof ($Gr$) number is a dimensionless number which approximates the ratio of buoyancy to viscous force on a fluid and for pipes (our study) can be written as:

$$Gr = \frac{g\beta(T_S - T_\infty)D^3}{v^2} \tag{2.16}$$

where $g$ is acceleration due to gravity, $\beta$ is the coefficient of thermal expansion, $T_S$ and $T_\infty$ is the surface and bulk temperatures, respectively and $D$ is the bubble diameter.

Additionally, Rayleigh ($Ra$) number is the dimensionless number associated with buoyancy-driven flow and is used to calculate natural free convection in a system. The Rayleigh number is defined as the product of the Grashof number, which describes the relationship between buoyancy and viscosity within a fluid, and the Prandtl number, which describes the relationship between momentum diffusivity and thermal diffusivity. For a fluid, when the Rayleigh number is below a critical value, heat transfer is primarily in the form of conduction and in the form of convection when it exceeds the critical value. For free convection the $Ra$ is defined as:

$$Ra = Gr_L \cdot Pr = \frac{g\beta(T_S - T_\infty)L^3}{va} \tag{2.17}$$

where $L$ is the characteristic length. Note that for most common cases $Ra$ number is large around $10^6$ to $10^8$. For example, near a vertical surface the transition occurs when $Ra$ is around $10^9$.

In heat transfer situations, the ratio of convective (both advection and diffusion) to conductive heat transfer across the boundary (surface) within a fluid is described by the Nusselt ($Nu$) dimensionless number:

$$Nu = \frac{h_{conv}L}{k} \tag{2.18}$$

where $h_{conv}$ is the convective heat transfer coefficient of the flow and $k$ is the thermal conductivity of the fluid. Examples of characteristic length $L$ could be: the outer diameter of a cylinder in (external) cross flow (perpendicular to the cylinder axis) or the diameter of a sphere.

The Bond ($Bo$) (also called Eötvös number) dimensionless number measures the importance of surface tension forces compared to the body forces and usually is used to characterise the shape of drops and bubbles in a surrounding fluid.

$$Bo = \frac{\Delta\rho g L^2}{\gamma} \tag{2.19}$$

Note that $\Delta\rho$ is the difference in density between the two phases of the system. A low $Bo$ value (typically $Bo < 1$) indicates that surface tension forces dominate and at high $Bo$ values the system is unaffected by surface tension effects.

## 2.7 Self-Rewetting Fluids

In their seminal work of Vochten and Petre [157] reported for the first time that for dilute aqueous solutions of high carbon alcohols (number of carbon atoms ≥ 4), the dependence of the surface tension with the temperature showed to follow non-linear (quasi-parabolic) behaviour with a well-defined minimum. Moreover, the minimum temperature of these curves decreases with the increase in the number of carbon atoms of these aqueous solutions [157]. Experimental work on these anomalous alcohol mixtures was also carried out under reduced gravity conditions by Limbourg-Fontain *et al.* [158]. The unusual behaviour of these binary alcohol mixtures compared to the pure liquids leads to a non-linear thermocapillary effect which was studied by Oron *et al*. [159] and later by Slavtchev and Miladinova [160]. Dilute aqueous solutions of alcohols such as butanol, pentanol, hexanol etc. can be considered ‘‘self-rewetting” fluids because of the anomalous dependency of the surface tension with temperature in a range of concentration, *c* [161, 162]. Due to the presence of thermocapillary stresses, and the characteristic curvature of the surface tension-temperature relationship, these alcohol mixtures ‘‘self-rewet” by spreading rapidly towards the hot regions, thereby preventing dry-out of hot surfaces and enhancing the rate of heat transfer of the system. Self-rewetting fluids have recently been investigated and proposed as new innovative working fluids for advanced heat transfer devices, e.g.

heat pipes or heat spreaders for terrestrial and space applications [43-48, 163]. Figure 2.7-1 gives a plot of the behaviour of ordinary liquids and the particular aqueous alcohol solutions as a function of temperature, *T*. Since these solutions are non-azeotropic for dilute concentrations, the alcohol-rich composition preferentially evaporates in the course of liquid/vapour phase change, which results in a concentration gradient in the liquid/ vapour interface. The formation of gradients at the liquid–vapour interface (concentration and temperature instabilities) lead to surface flows directed from the colder region to the hotter side, at temperatures above the minimum of the surface tension [161, 162], as can be seen in Figure 2.7-1. In this case, the convection mechanism is driven by the reverse Marangoni effect. Thus, Marangoni flows may play an important role in energy transport phenomena [76].

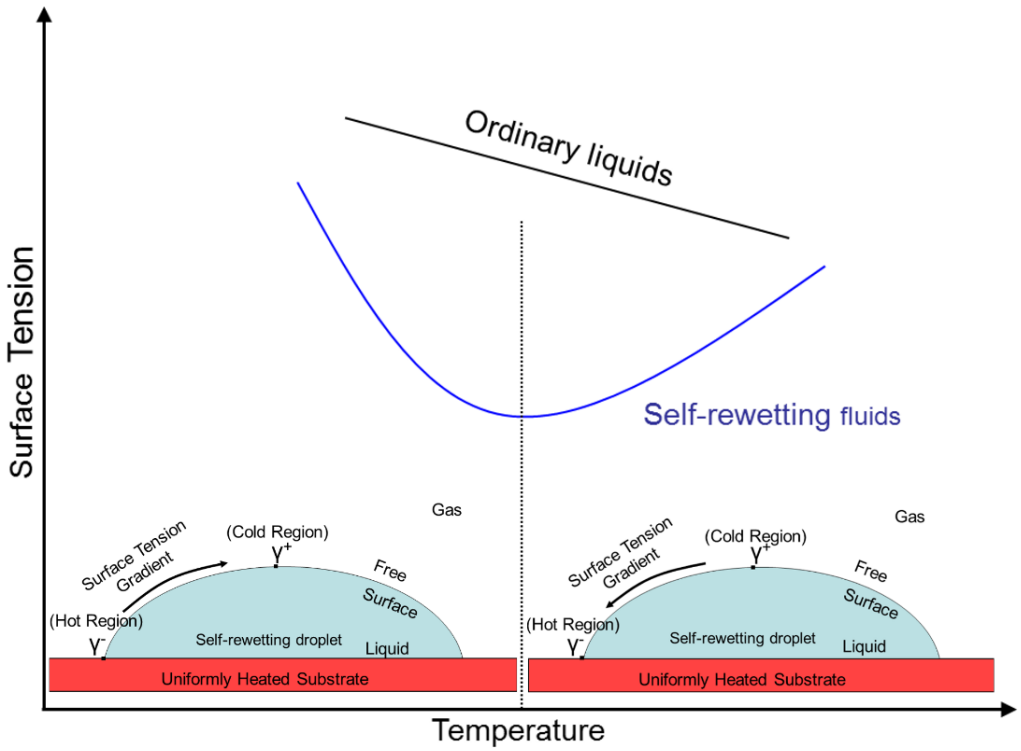


**Figure 2.7-1** Ordinary liquids (black line) and binary alcohol mixtures (blue line) surface tension dependence with temperature and schematic view of the Marangoni effect for self-rewetting droplets on a heated substrate as surface tension gradients are induced at the liquid/vapour interface.

The anomalous property of the self-rewetting fluids was investigated by many authors [42, 48, 164] inside heat pipes using them as working fluids. They reported that this characteristic behaviour of the alcohol solutions was associated with essentially higher critical heat fluxes in heat pipes than for water cases. Moreover, they concluded that the size of vapour slug inside wickless heat pipes was considerably smaller than of those in ordinary operating fluids (water or alcohols). Later on, Karapetsas *et al*. [165] demonstrated the significant influence on the dynamics of the fluid flows and drops migration due to the presence of a minimum in surface tension which can give rise to interesting phenomena, such as thermocapillary-driven spreading, with complex contact line dynamics. Very recently, Shanahan and Sefiane [155] brought to light a new phenomenon in which drifting bubbles migrated against the liquid flow inside a micro-channel due to the strong thermocapillary stresses. They concluded that the observed behaviour of the bubbles can be explained by the non-linear (parabolic) dependence of the surface tension with temperature of these binary alcohol mixture (self-rewetting fluids). They reported that bubbles movement was not only against the liquid flow following an exponential velocity profile but also tend to an equilibrium position where the bubbles finally settle in a stationary position.

The main motivation of the aforementioned studies commenced from the characteristic anomalous property of these binary alcohol solutions and parabolic dependence of the surface tension on temperature. In this work, particular interest was paid to investigate the behaviour of self-rewetting fluids associated with the thermocapillary instabilities generated when a droplet spreads in a non-isothermal system, the internal flows within the spreading droplet and the subsequent contact line phenomena which are discussed in Chapter 5. Furthermore, the behaviour of these interesting binary fluids as working fluids inside a micro-channel in single and two phases flows was extensively examined and analysed. More specifically, we focused on the thermocapillary migration of a buoyancy-driven air bubble and the impact on the enhancement of the heat transfer profile compared with those of the pure liquids situations, Chapter 6.

## 2.8 Fluid Dynamics in Channels

### Multiphase flow

In the last decades, the growing interest in the complete understanding of multiphase flows has led to the development of novel and precise experimental methods and techniques. Multiphase flows occur in many operations in chemical, petroleum and power generation industries. Particular interest also was paid to the rapid progress of microfluidic industry which requires more effective cooling or heating methods and systems, aiming to control the heat transfer mechanisms in smaller scales, including applications such as multiphase flow through porous media [166], cell-biological systems [167, 168], human airways [169] etc. Flows in multiphase systems provide several mechanisms that could enhance the performance of the single-phase ones and it is still of field that poses many challenges [170]. However, the presence of gas e.g. air bubbles in microfluidic systems can generate major problems by disturbing and eventually blocking the fluid flow of the system and in turn affect the heat transfer profile. The boundary interactions between the gas, liquid and solid phases induce non-linearity and instabilities between the components of the system. Comprehensive studies on microchannel single phase and two-phase flows heat transfer can be found in literature [170-175]. More specifically, multiphase systems such as bubbly flow in a channel, are of considerable use in many industrial applications such as column reactors, drug delivery or cardiovascular systems and DNA analysis [41, 176-179]. In multiphase flowing systems, the complicated interplay between gravitational, viscous, inertia and interfacial forces is responsible for different phase distributions and complex flow patterns. Thus, it is of a great importance to categorize the different forces acting in a system in order to predict the multiphase flow behaviour. Figure 2.8-1 shows how the dimensionless numbers i.e. Capillary and Weber numbers, vary with the channel's hydraulic diameter, $d_h$, and the velocity $U$, when they are altered.

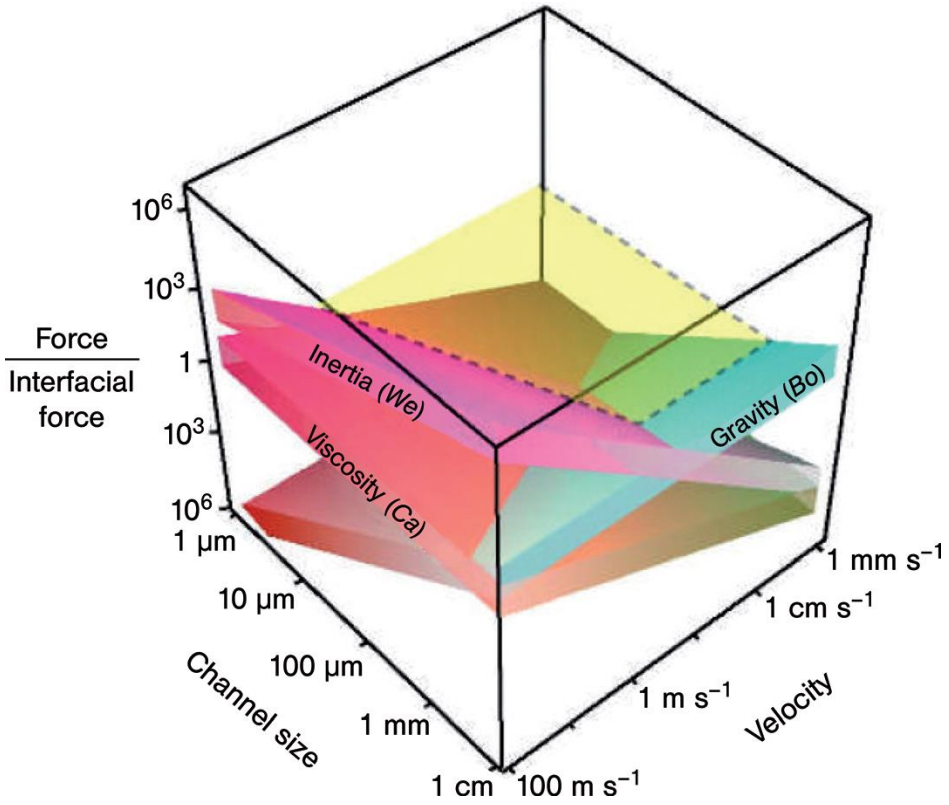


**Figure 2.8-1** Inertia, viscous and gravitational forces, relative to interfacial forces, as a function of the channel size (hydraulic diameter, $d_h$,) and the characteristic velocity ($U$) in a microfluidic multiphase system [180].

Previous studies have shown that different heat transfer profiles were reported depending on various experimental conditions such as gravitational forces [43, 45, 142], channel geometry [181-183], working liquid [44, 155, 184], applied heat flux [185, 186], mass flux [182, 186] etc. Understanding how the presence of bubbles affect the flow resistance in micro-channels is a way of determining the pumping or energy requirement for microfluidic devices where two-phase flow is involved.

## 2.8.1 Multiphase flow regimes

A particular type of geometric distribution of the (liquid – vapour) components is called a *flow pattern* or *flow regime*. In a flow pattern map, the boundaries between the different flow patterns occur because a regime becomes unstable as the boundary

is approached and the growth of this kind of instability causes transition from one to another flow pattern. The flow pattern boundaries are not distinctive lines but are defined more as transition zones. Detailed discussions of these patterns are given by Hewitt (1985) [187], Nedderman (1988) [188] and Dukler (1986) [189]. In the two-phase flow systems, many different flow patterns have been obtained by many researchers under various experimental parameters such as liquid flow rate, channel geometry etc. Although quantitative methods and simulations are under development the last decades, the description and the analysis are often based on qualitative information such as visualizations. In the present work, experiments have been carried out of gas bubbles flowing in a vertical microchannel. Hence, for co-current upward flow of a gas and liquid in a *vertical* channel, depending on the different flow patterns of the liquid and the gas phases, the flow regimes are limited in the following four distinct categories: ***Bubbly flow***, ***Slug flow***, ***Annular flow*** and ***Churn flow***.

The above mentioned about characteristic flow patterns regimes within a vertical microchannel can be seen schematically in Figure 2.8-2.

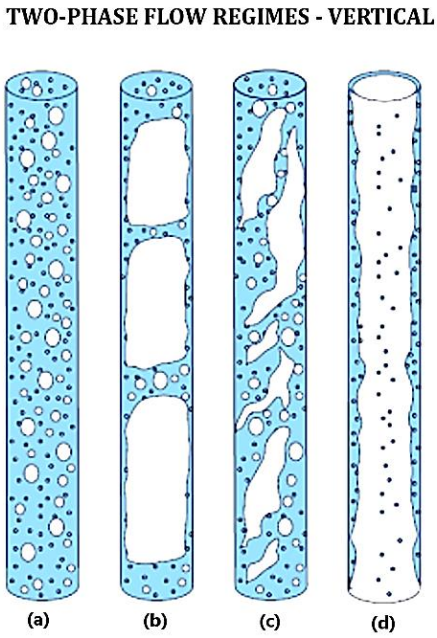


**Figure 2.8-2** The most common flow patterns in a two-phase flow inside a vertical microchannel: (a) Bubbly flow, (b) Slug flow, (c) Churn flow and (d) Annular flow.

In this chapter, the emphasis is on presenting a review the most important investigations and theories to the subject of matter of this thesis. To guide the reader, this has been divided into three sections according to the physical configurations discussed in subsequent chapters namely wetting phenomena and evaporation and thermocapillarity.

The next chapter describes; the fluids studied and preparation methods, experimental setup, procedure, and the different techniques, tools, and approaches, used during this experimental research.

# Chapter 3: Experimental Methodologies and Apparatus

In this chapter, the evaporative behaviour of several volatile liquid droplets was investigated using different experimental methods such as infrared thermography and high speed imaging. Five liquids were tested in these experiments: water, butanol, pentanol, water-butanol, water-pentanol and five different substrates were examined: glass, aluminium (alloy), ceramic (AlN), PTFE (Teflon), and poly(ethylene) oxide (PEO). The effects of applying different substrate temperatures and varying initial liquid temperature were also investigated. Pendant drop, sessile drop, AFM, profilometry and microscopy were techniques used during this thesis, to shed further light on the liquid-solid-gas interactions throughout evaporation process. Droplet shape and contact line dynamics were analysed at macroscale and different evaporative behaviours depending on crucial parameters such as hydrophobicity of the substrate, nature of fluid (pure and mixtures), addition of polymer, nature of the polymeric material and temperature, were identified. Additionally, infrared thermography and high speed imaging were used to record and visualize the motion of travelling air bubbles inside transparent glass micro-channels under different applied liquid phase flows, before and after heating the system. The study of bubbles' motion inside the micro-channels helped to reveal some mechanisms present in the two phase flow systems regarding the heat transfer performance.

## 3.1 Fluids, Substrates and Microchannels

### 3.1.1 Pure fluids

Deionized water, pure ethanol, pure 1-butanol and pure 1-pentanol were used for the preparation of the solutions for this experimental study. Deionized water was obtained from a Barnstead NANOpure© Diamond$^{TM}$ (Thermo Scientific, Waltam, MA) analytical ultrapure water dispensing system with a conductivity of 18.2 × 106 Ω/cm. Analytical grade ethanol (Ethyl alcohol, Pure, 200 proof, ACS reagent, ≥ 99.5%, Sigma-Aldrich Co. LLC. 459844), 1-butanol (Butyl alcohol, ACS reagent, ≥ 99.4%, Sigma-Aldrich Co. LLC. 360465) and 1-pentanol (Pentyl alcohol, ACS reagent,

≥99%, Sigma-Aldrich Co. LLC. 398268) were purchased from Sigma-Aldrich, St. Luis, MI.

### 3.1.2 Aqueous solutions of polymers and alcohols

#### 3.1.2.1 PEO solutions

Aqueous solutions were prepared using polymer poly(ethylene) oxide (PEO) with a variety of molecular weights: $M_w$ = 10 000 g/mol (Sigma-Aldrich 44101), 100 000 g/mol (Sigma-Aldrich 181986), 200 000 g/mol (Sigma-Aldrich 181994), and 300 000 g/mol (Sigma-Aldrich 182001). All solutions with an initial concentration of $c_0$ = 10% by mass. The specific concentration (10% wt.) used corresponds to close to the semi-dilute region for the lowest $M_w$ and well into the semi-dilute region for the rest cases [39]. The prepared solutions were mixed using distilled, deionized water and were left to equilibrate for at least 24 h before use. A roller mixer was used to increase the dissolution rate. Mechanical mixing methods (vortex mixer, centrifuge, or sonicator) were not used to prevent possible molecular damage. After mixing, cloudy undissolved polymer clusters appeared clearly in our samples. These clusters were successfully removed from all samples by driving them through a 0.45 μm filter with an adjustable-speed syringe pump at speed around 0.5 mL/h. Filtering the PEO samples in order to remove undissolved clusters resulted in slightly reducing the overall concentration (and also density $\rho$). A comparison of the concentrations of the solutions was carried out before and after filtering for all molecular weights. It is clearly depicted in the graph (Figure 3.1-1) that filtering did not change drastically the initial concentration (<5%) of these specific PEO solutions, in good agreement with previous works that have been reported in the literature. The method used for the removal of PEO aggregates (clusters) did not damage the polymer molecules [38]. For each measurement, a PEO droplet with an initial concentration of 10% wt. and with volumes ranging from 1 μL to 5 μL was deposited onto a chosen substrate and the whole evaporation process was systematically recorded. The droplets were deposited using a 1 mL syringe with a 0.71-mm-diameter syringe needle. Despite the large shear

rates in the needle (~100 $s^{-1}$), no significant differences in drying behaviour were seen when compared with droplets deposited less controllably by pouring, so we assume that the polymer molecules were undamaged. The PEO sessile droplets temperatures were at 21° ± 1°C, the air temperature and the relative humidity surrounding the substrate were $T$ = 21° ± 1°C and $RH$ = 35 ± 5%, respectively, under ambient pressure conditions.

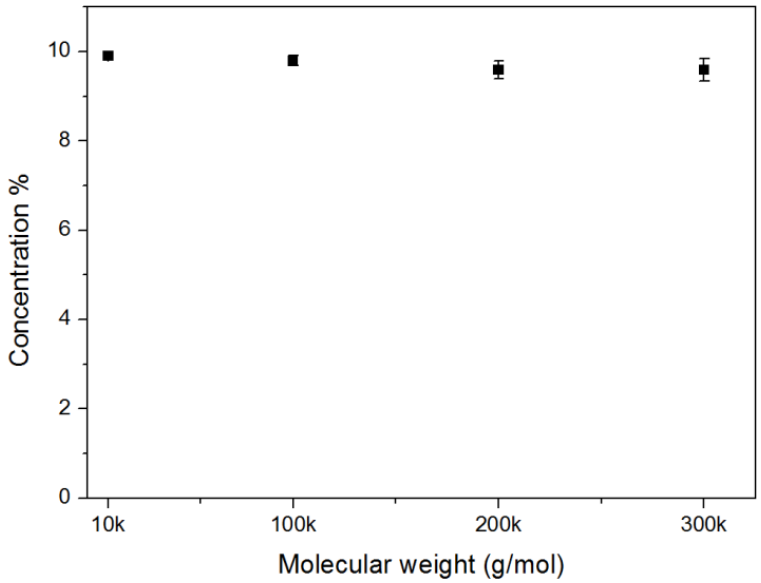


**Figure 3.1-1** Average values obtained from the calculated dried filtered PEO material over the four different molecular weights for the 10% wt. PEO droplets (experimental results up to 5 repetitions for each $M_w$) after complete evaporation process, under controlled ambient experimental conditions. Note that the error bars for the molecular weight of 10k and 100k are smaller than the size of the black squares.

### 3.1.2.2 Binary alcohol mixtures

The first step in this series of experiments was to prepare solutions using pure alcohols: 1-butanol and 1-pentanol with specific concentrations: water – 1-butanol 5% vol. and water – 1-pentanol 2% vol. (namely self-rewetting fluids). For each measurement, a binary droplet with steady concentration, temperature and with a volume in the range from 1 μL to 5 μL was placed onto a chosen substrate and the spreading behaviour was recorded. With a syringe pump set at a constant volume rate

of 1 μL/min, a pendant droplet was grown at the needle tip, until it touched the heated substrate. A flexible silicone rubber heater SRGF-203/5-P-230V (OMEGALUX® Silicone Rubber Fiberglass Insulated Heaters) was placed underneath the substrate in order to heat up uniformly the (glass) substrate. The binary alcohol mixtures temperatures were kept constant at $9^o \pm 1\ ^oC$, the air temperature and the relative humidity surrounding the substrate were $T = 17^o \pm 1\ ^oC$ and $RH = 30 \pm 5\%$, respectively. The atmospheric pressure was assumed to be at $P = 1$ atm.

### 3.1.3 Substrates

Surface defects or chemical heterogeneities are regularly recognised as the main parameters for the presence of contact angle hysteresis. Aiming to minimize these effects ideal, smooth, rigid solid substrates were acquired in our experimental investigation. Substrates with different degrees of hydrophobicity, from hydrophilic to hydrophobic to cover a wide range of wettabilities were used. The hydrophilic substrates were ethanol-cleaned borosilicate glass microscope coverslip (dimensions: 24 mm × 50 mm × 100 μm from TAAB Laboratories Equipment Ltd., England) and aluminium (Al) alloy substrates where (Al) is the predominant metal, with thicknesses around 1 mm and they were provided from the mechanical workshop lab in the University of Edinburgh. Moreover, a corrosion-resistant ceramic (AlN) substrate (StableTemp Ceramic Hot Plate) was used to conduct experiments regarding non-spherical droplets and provided from Core-Parmer®. The hydrophobic substrates were silicon wafers spin coated with a 1-μm-thick poly(tetrafluoroethylene) (PTFE) layer. The wafers were then cut into $1\times 1$ cm$^2$ samples. PTFE substrates were cleaned before use in an ultrasonic bath filled with isopropanol for at least 10 min, then rinsed with deionised water and blow-dried gently using a jet of compressed air. Any contaminates e.g. grease, included in the compressed air supply had a small impact on the cleanliness of the substrates. All the wafers were prepared from our collaborators in the Scottish Microelectronic Centre in the University of Edinburgh. Additionally, experiments were carried out with the borosilicate glass substrates coated with PEO films prepared from 1 or 10 % wt. PEO solutions with two different molecular weights: 10 000 and 100 000 g/mol. Spin coating was used to deposit thin and ultrathin PEO films on the flat smooth glass substrates. A small amount of PEO solution was

applied to the centre of the substrate span at 2000 rpm at a duration of either 90 or 120 s. Moreover, dip coating was used to prepare thicker absorbed PEO films. Topography images and/or height profiles of the PEO films were acquired by surface profilometry and atomic force microscopy (AFM). A surface roughness tester was used to measure the height profiles of the thicker PEO films and an AFM imaging for the thinner ones. The equilibrium contact angles, $\theta_0$, for each substrate used, were determining by averaging data from more than 20 repeats and measured using the FTÅ200 apparatus. The results obtained for the equilibrium contact angles, $\theta_0$, for all the experiments performed, were summarized in Table 3.1-1. Moreover, all the syringes and needles used were washed vigorously with deionised water and dried with nitrogen stream to remove any dust or contaminants.

**Table 3.1-1** Various equilibrium contact angle $\theta_0$, measurements for different substrates and fluids in a volume range from 1 μL to 5 μL, used in this study. Note that deviations in $\theta_0$ for the pure liquids and for the water – 1-butanol 5% vol. mixture droplets on glass and aluminium were due to the temperature range used to perform this series of experiments, from ~20 to ~90 $^{o}$C. Including the instrument and the experimental conditions, the error for the measured contact angles is around ± 2$^{o}$.

| **Substrate** / **Fluid** | Borosilicate glass coverslip | PTFE (Teflon) | PEO films (thin) ~20nm - ~4μm | PEO films (thick) ~30nm - ~280μm | Aluminium (Al) alloy |
|---|---|---|---|---|---|
| Water | 68$^{o}$ - 72$^{o}$ | ~115$^{o}$ | 30$^{o}$ - 35$^{o}$ | 28$^{o}$ - 37$^{o}$ | 58$^{o}$ - 65$^{o}$ (30,60,90 $^{o}$C) |
| 1-Butanol | 12$^{o}$ - 21$^{o}$ (30,60,90 $^{o}$C) | - | - | - | - |
| Water – PEO 10% wt. | 60$^{o}$ - 75$^{o}$ | - | 25$^{o}$ - 35$^{o}$ | 35$^{o}$ - 55$^{o}$ | - |
| Water – 1-Butanol 5% vol. | 55$^{o}$ - 65$^{o}$ (30,60,90 $^{o}$C) | - | - | - | - |

### 3.1.4 Characterization of aluminium surfaces

Scratched rough aluminium (alloy) were the substrates chosen to perform experiments investigating the evaporation mechanism of deformed pure water liquid droplets. In what follows, scanning electron microscopy (SEM) was performed in order to characterise the used aluminium substrates related to the experiments where the non-spherical droplets deposited under non-isothermal conditions. The aluminium substrates were scratched before droplet deposition in order to achieve a non-spherical droplet shape using a thin (diamond) scriber. Electron SEM images at different positions on the surface of the aluminium i.e. at the scratched area and at locations far from it, were acquired, as can be seen in Figure 3.1-2 and 3.1-3 , respectively.

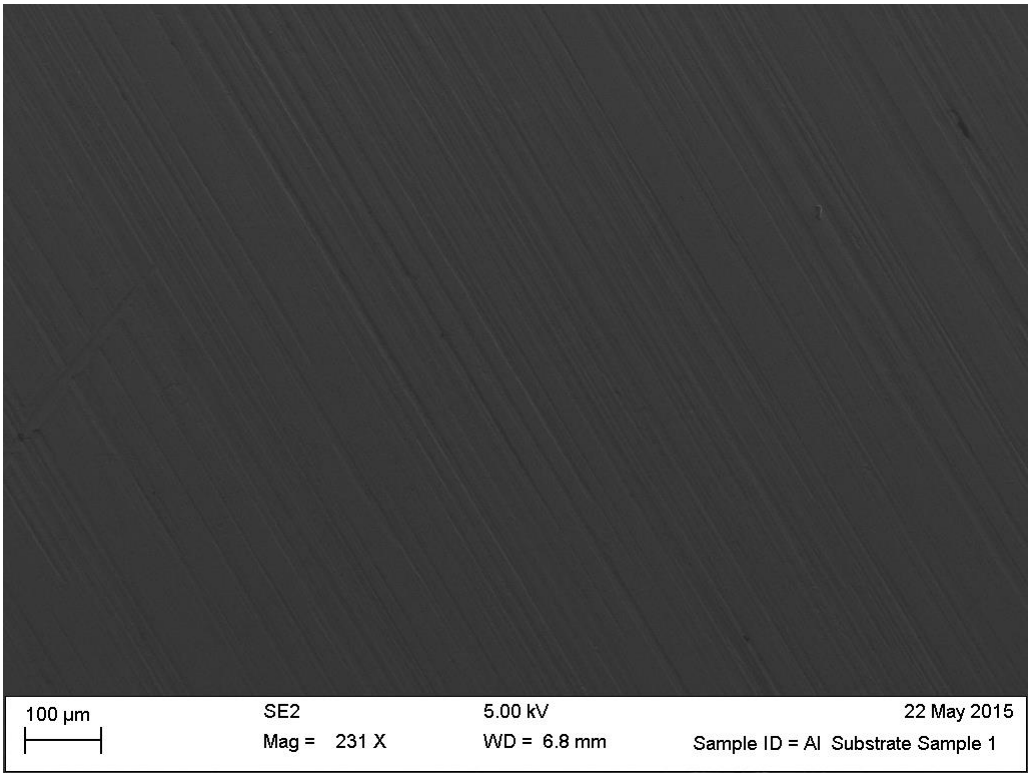


**Figure 3.1-2** Representative electron SEM images of the aluminium substrate used to perform the experiments depositing pure water droplets, under non-isothermal conditions. Note that the images extracted from the SEM apparatus depict locations far from the scratched area.

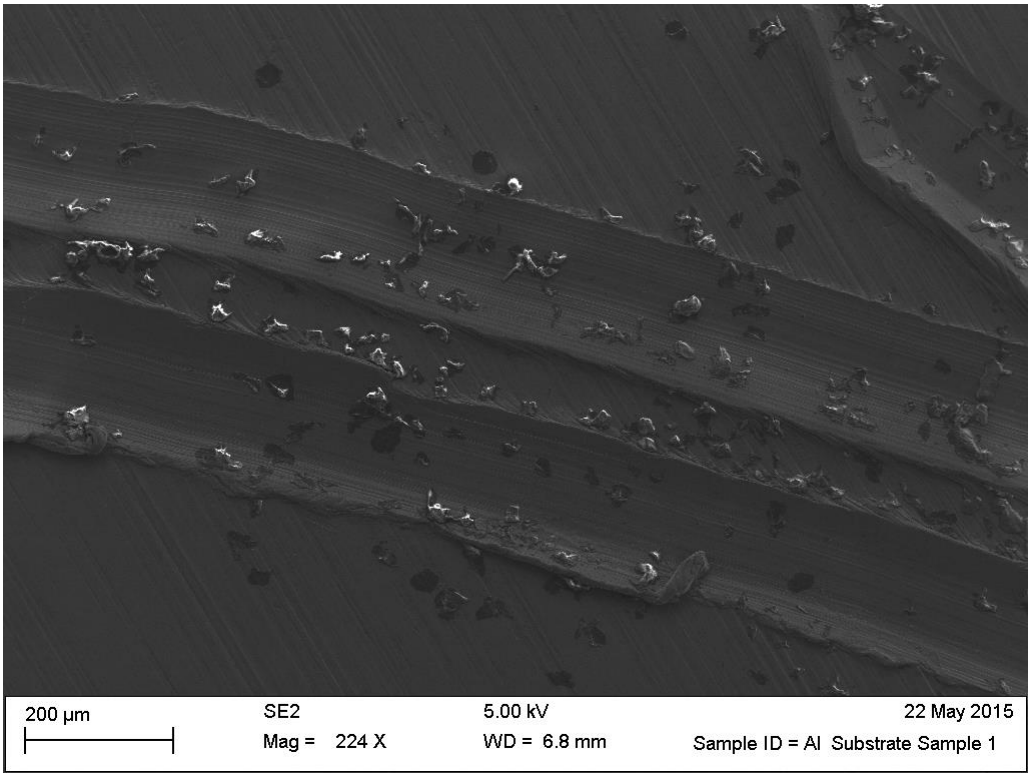


**Figure 3.1-3** Representative electron SEM images of the aluminium substrate used to perform the experiments with pure water droplets, under non-isothermal conditions. Note that the images extracted from the SEM apparatus depict the scratched area of the substrate.

Additionally, chemical characterization using the scanning electron microscope (SEM) (non-destructively) via the energy dispersive X-ray spectrometry analysis (EDS) was performed on the aluminium substrates. In more details, the electron beam stimulates the atoms in the sample with uniform energy and they instantaneously send out X-rays of specific energies for each element. This radiation gives information about the chemical composition of the aluminium samples. The results from the obtained SEM electron images (Figure 3.1-2 and 3.1-3 ) at specific areas and with the accompanied compositional analysis (elemental mapping) at these locations are presented in Figure 3.1-4 and 3.1-5, respectively. The chemical analysis results verified the presence of the aluminium oxide (Al2O3) layer at the interface of the aluminium (alloy) samples.

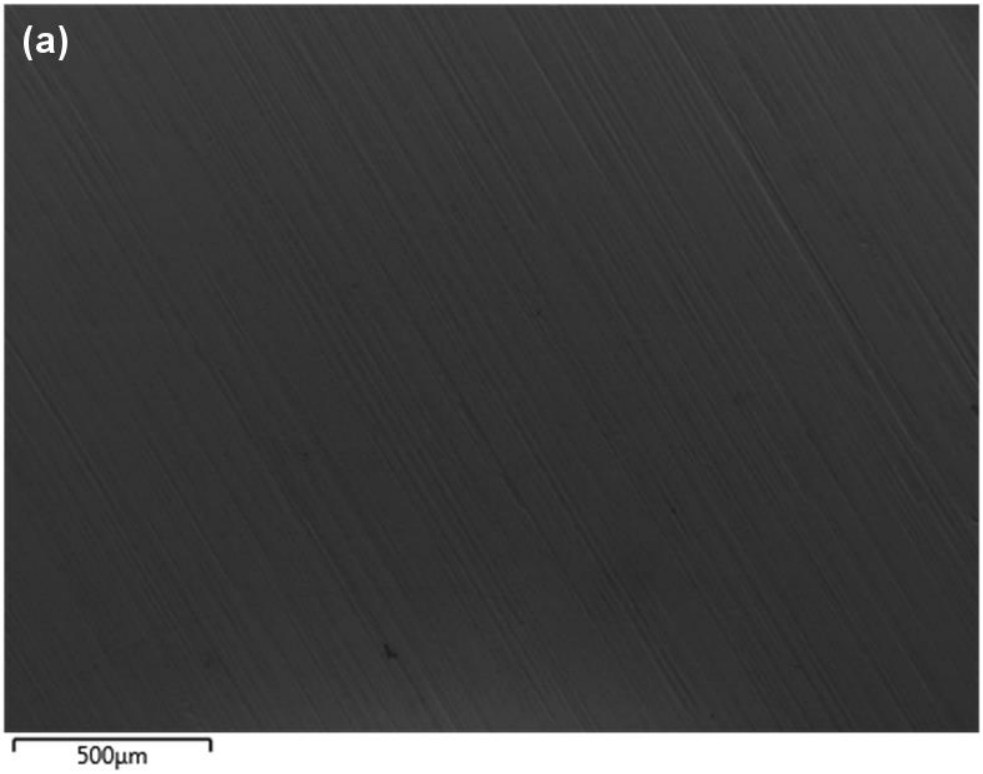
(a)
500µm

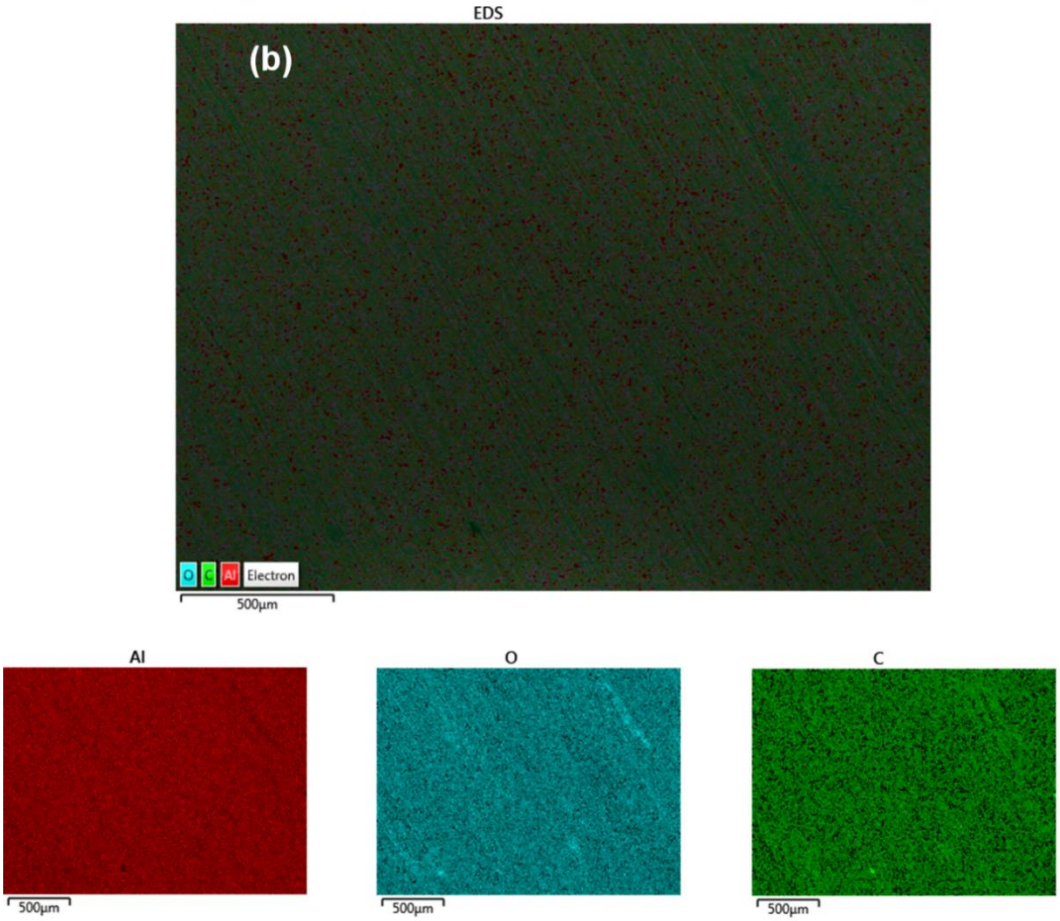


**Figure 3.1-4** (a) Typical electron SEM image of the aluminium substrate at locations far from the scratched area and (b) elemental mapping for the same SEM image obtained using the energy dispersive X-ray spectrometry analysis (EDS).

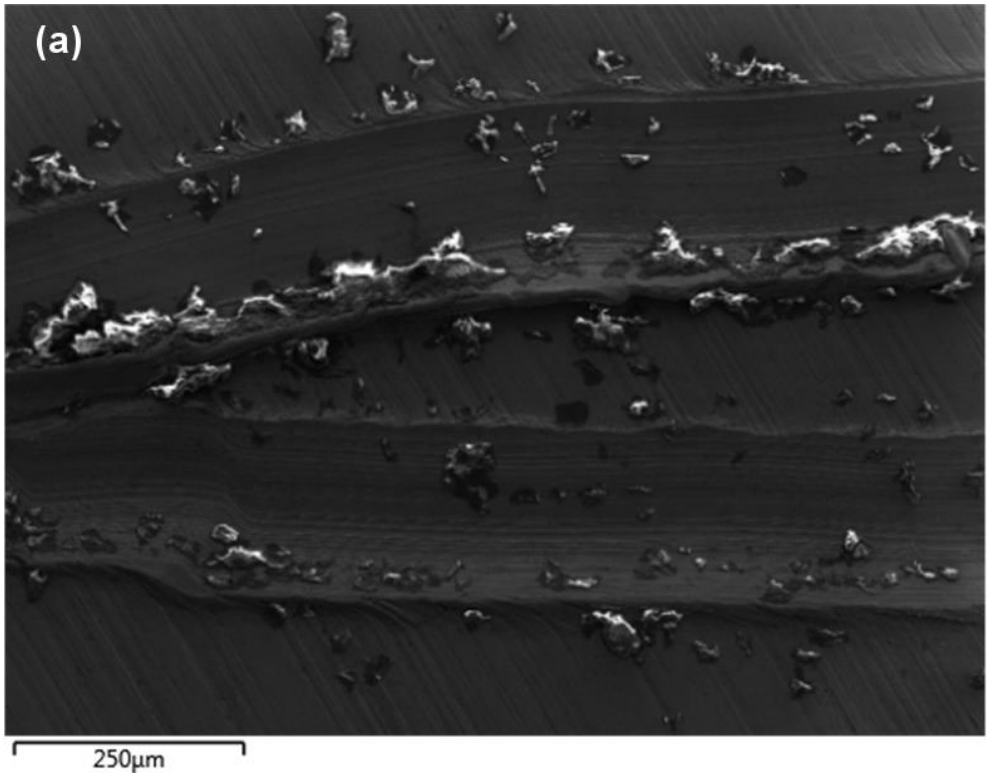
(a)
250µm

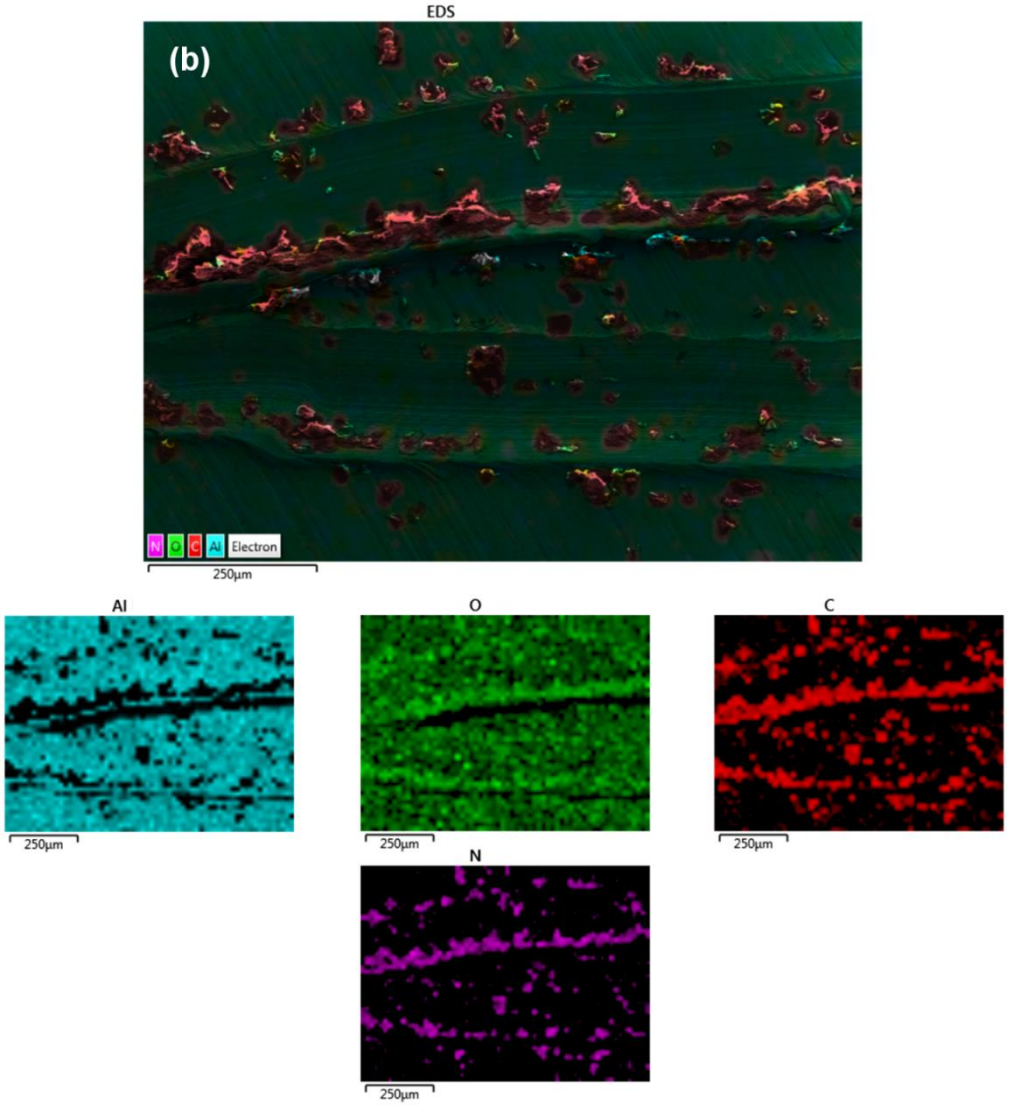


**Figure 3.1-5** (a) Typical electron SEM image of the aluminium substrate at the scratched area and (b) the elemental mapping for the same SEM image obtained using the energy dispersive X-ray spectrometry analysis (EDS).

Continuing with the efforts to further characterise chemically the aluminium samples at positions where the scratched area was located, an EDS spectrum chemical analysis was performed. Figure 3.1-6 show typical electron SEM image at the scratched area i.e. *spectrum 1* and *2*, where the chemical examination was conducted, respectively. The results from EDS analysis of the *spectrum 1*, Figure 3.1-7 (graph on top), showed the presence of an alumina layer (Al2O3), same as presented Figure 3.1-4, regarding substrate areas which were taken far from the scratched region. Furthermore, the EDS analysis of the *spectrum 2* (Figure 3.1-7 graph below) indicated that the chemical

composition of the visible agglomerates on the aluminium surface were carbons (C), probably owing to the diamond pen used, as also seen in Figure 3.1-5.

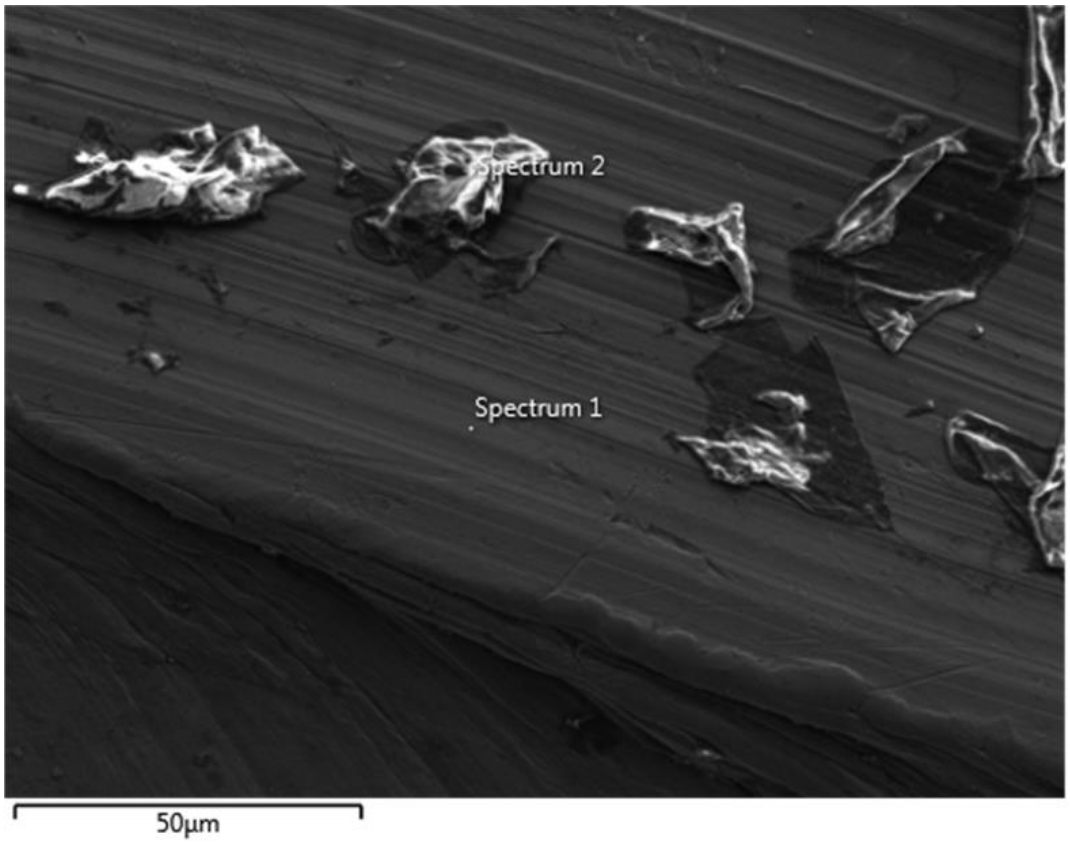


**Figure 3.1-6** Electron SEM image of the aluminium substrate at the scratched area and the specific positions where the EDS spectrum analysis was conducted namely *spectrum 1* and *2*.

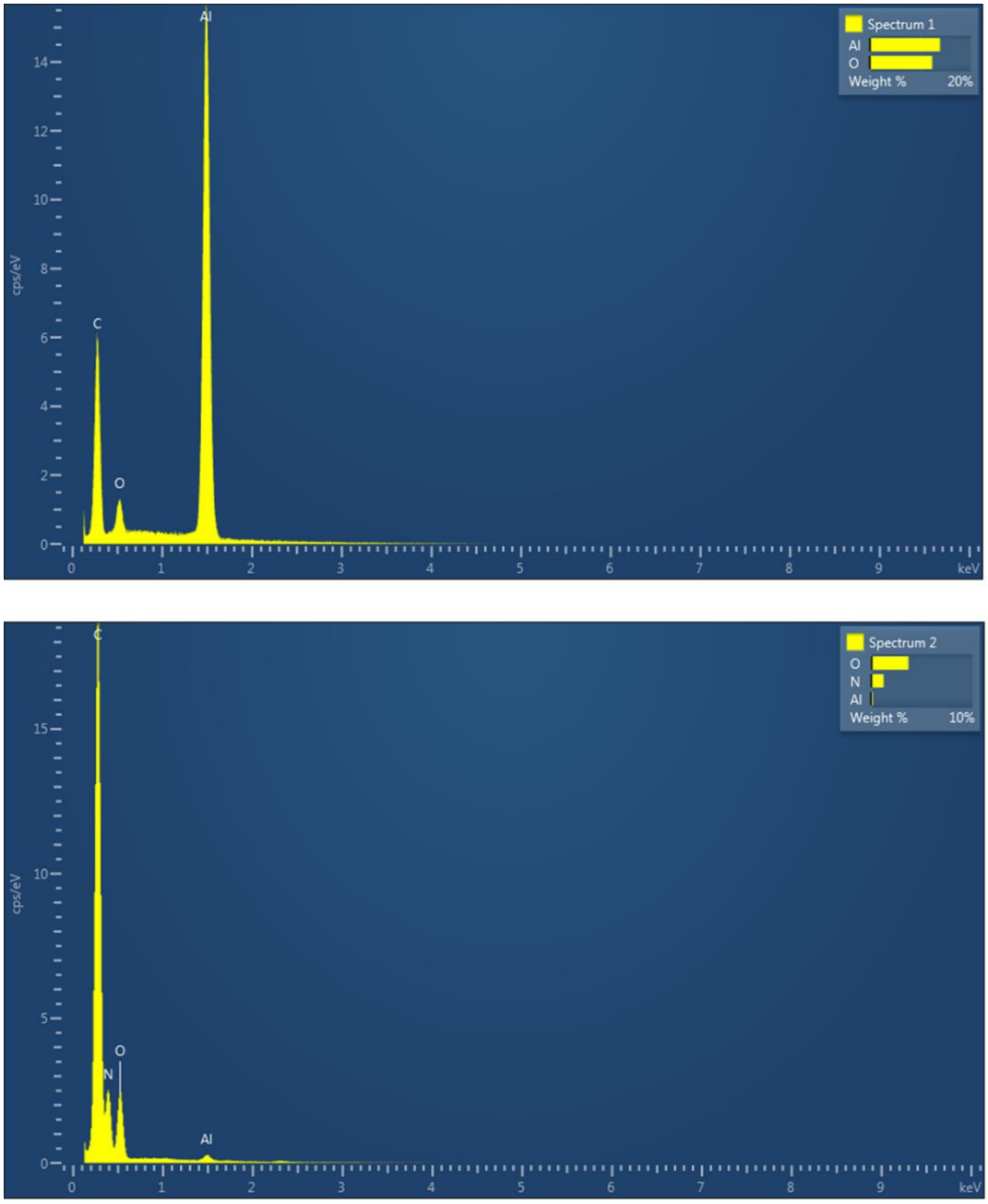


**Figure 3.1-7** EDS spectrum chemical analysis of two positions: *spectrum 1* and *2* (as presented in Figure 3.1-6), at the scratched area of the aluminium sample where the deposition of the pure water droplets occurred.

### 3.1.5 Microchannels

Pure water, pure 1-butanol and aqueous solutions of pure 1-butanol with specific concentration: water – 1-butanol 5% vol. (self-rewetting fluid) were adapted for this experimental section. A heated circular channel with 145 mm length and 4 mm inner diameter was applied, through which the requisite liquid i.e. pure liquids and binary alcohol mixture, was pumped in. The used microchannels were built from borosilicate glass and provided by VitroCom® Inc. manufacturing company. To be able to visualize inside the micro-channel at the same time as applying a controlled heat flux, a transparent, conductive, metallic deposit of tantalum (*Ta*) was applied to the exterior of the microchannel. More specifically, the thickness of the coating, required for suitable heating of the channel and was in the order of tens of nanometres, which was negligible in comparison to the glass thickness of 1 mm. The tantalum deposit was uniformly distributed both across and along sections the microchannel. The microchannel was connected by its ends to a DC power supply, enabling heating of the channel by passing a controlled current through the resistive tantalum coating, thus controlling the wall temperature along the channel. A syringe was placed at the cold side (starting point, bottom of the channel) with a needle of 0.1 mm diameter in order to induce small controlled gas air bubbles in the fluid flow, as can be seen in Figure 3.1-8. The fluid delivery system was combined with a syringe pump to produce the required constant liquid mass flow rate through the system. The syringe pump device was provided by Cole-Palmer Instrument Co, Ltd and was combined with 100 mL borosilicate glass syringe from FORTUNA® Optima. Then, the syringe was connected with the microchannel by a plastic tube which was able to resist corrosion from the alcohol (butanol) mixture and also to operate under high temperatures up to 100$^{o}$C. Liquid was injected through the microchannel where it was subjected in a controlled temperature gradient (from ~18$^{o}$ to ~75$^{o}$ ±1$^{o}$C) and collected at the exit of the microchannel in a glass tank. A National Instruments® system was used for data acquisition, connected to a computer and a LabVIEW® user interface. Inlet and outlet temperature and pressure were monitored using thermocouples, K type, and pressure sensors connected to a data acquisition board on a PC. A high speed camera was set-up to visualise the flow at frame rates up to 2500 fps. A cold light source was used in conjunction with the high speed camera, providing back lighting of the micro-channel.

The high-speed camera employed was a NanoSense® MK III (IDT), with interchangeable macro and micro lenses, used as appropriate. The resolution of the camera allowed for either the entire heated micro-channel length to be captured or for just a particular section of interest to be focussed upon. The rate of the camera was set from 500 fps to 2500 fps depending on different visualization requirements. The records were extracted from the high-speed camera were analysed with the ImageJ® software in order to measure the bubbles size and velocity. A ThermaCamTM infrared thermography system was used to visualise and record the temperature profile at the micro-channel exterior wall.

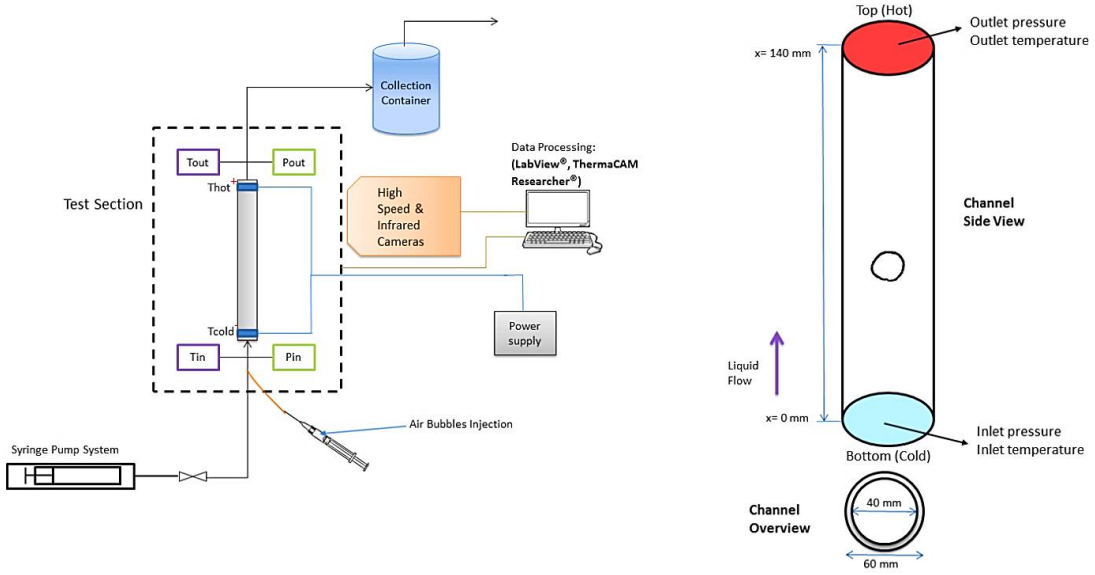


**Figure 3.1-8** (Left) Representative schematic drawing of the setup used to perform the experiments using microchannels and (Right) the tested circular borosilicate glass microchannel adopted in this study.

### 3.1.5.1 Data reduction

## Mass flux

The mass flux was determined from the volume flow rate and the cross-sectional area of the microchannel used in this experimental study:

$$\phi = \frac{\dot{V}\,\rho_L}{A_c} \tag{3.1}$$

where $\dot{V}$ is the volume flow rate set by the pumping device and the syringe (100 ml), $\rho_L$ is the liquid density and $A_c$ is the cross-sectional area.

The three applied mass fluxes in the tested microchannel for the single phase flow under controlled isothermal conditions were: 0.663 $kg \cdot m^{-2} \cdot s^{-1}$, 1.327 $kg \cdot m^{-2} \cdot s^{-1}$ and 1.99 $kg \cdot m^{-2} \cdot s^{-1}$. For the two-phase flow tests the mass flux were used, under non-isothermal conditions and within a controlled temperature gradient field from ~18$^{o}$C to ~75$^{o}$C, were set at 0.263 $kg \cdot m^{-2} \cdot s^{-1}$, 0.663 $kg \cdot m^{-2} \cdot s^{-1}$, 1.327 $kg \cdot m^{-2} \cdot s^{-1}$ and 1.99 $kg \cdot m^{-2} \cdot s^{-1}$. The conditions of low mass flux rates were selected due to the fact that the obtained data for the calculation of heat transfer coefficient profiles were more accurate.

## Channel wall temperature

Efforts have been exerted in order to obtain accurate, reliable and reasonable temperature data from the IR thermographic measurements in terms of post-process analysis and heat transfer calculations. Figure 3.1-9 shows a typical example of the wall temperature map, both inlet and outlet part of the heated microchannel, acquired with the use of an infrared camera. The temperature of the microchannel varies along the surface area and increases in the flow direction as can be seen in Figure 3.1-9. Figure 3.1-10 presents graph of the spatial temperature variation along the inlet and

outlet sides of heated microchannel regarding the IR images portrayed in Figure 3.1-9, respectively.

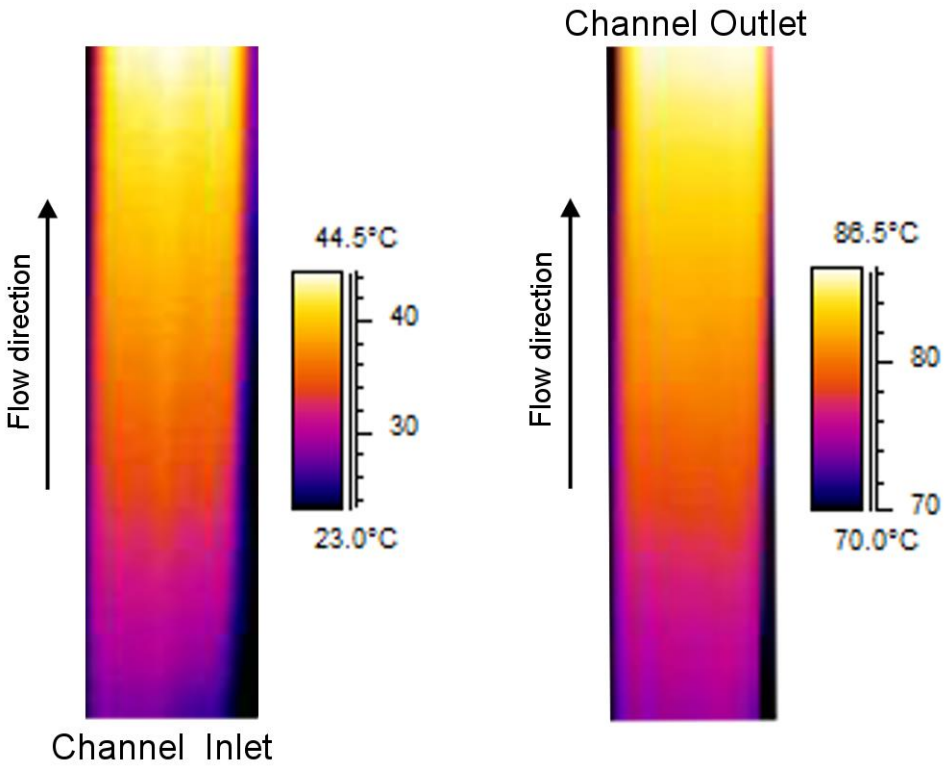


**Figure 3.1-9** Representative IR images of the heated microchannel used in this study, acquired with the use of an infrared camera. Note that the left IR image presents a distance of ~30 mm from the microchannel's inlet and the right IR image depicts a distance of ~30 mm until the outlet part of the microchannel.

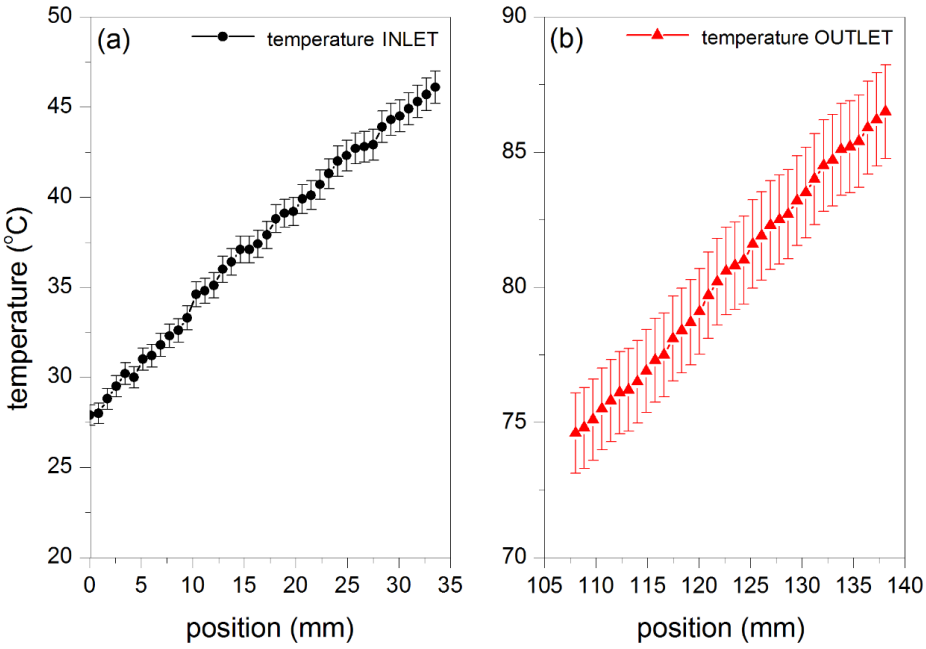


**Figure 3.1-10** Temperature map profile evolution along the surface of the heated microchannel from the (a) inlet and (b) outlet sides, as presented in the IR images in Figure 3.1-9, respectively.

## Heat loss & Heat transfer

For the single phase flow, the effective heat transferred to the liquid was estimated by using:

$$Q_{eff} = C_{p,L}\,(T_{out} - T_{in})\dot{m} \tag{3.1}$$

where $\dot{m}$ is the mass flow rate (kg $s^{-1}$), $C_{p,L}$ is the liquid specific heat capacity, $T_{in}$ and $T_{out}$ are the inlet and outlet liquid temperatures, respectively. Then the heat flux was calculated as $q = Q_{eff}/A$ , where $A$ is the channel's internal surface area.

For the two-phase flow, heat loss was estimated considering the convective loss $Q_{conv}$ and the radiative loss $Q_{rad}$. The convective loss was calculated as:

$$Q_{conv} = h_{conv,AIR} \cdot A_{W,out}(T_{W,avg} - T_{env}) \tag{3.2}$$

where $h_{conv,AIR}$ is the convective heat transfer coefficient of air and was estimated using the empirical correlations of natural convection external flow conditions. Also, $T_{W,avg} - T_{env}$ is the average temperature of the channel wall, $T_{env}$ is the ambient temperature and $A_{W,out}$ is the outer surface area of the tested micro-channel. The radiative loss was calculated by:

$$Q_{rad} = \varepsilon \cdot \omega \cdot A_{W,out}(T_{W,avg}^4 - T_{env}^4) \tag{3.3}$$

where $\varepsilon$ is the total emissivity of the micro-channel deposit, and $\omega$ is the Stefan–Boltzmann constant. The emissivity of tantalum deposit on the borosilicate glass channel was found from literature (Malter and Langmuir [190], Allen *et al*. [191], Miloševic *et al*. [192]). Since $\varepsilon$ increases with increasing temperature and $\varepsilon$ was reported to be 0.136 at 1000 K [190], in the present study, $\varepsilon$ is approximated to be 0.1. Actually, the calculated $Q_{rad}$ was very low compared with the total heat $Q_{eff}$, thus the approximation of $\varepsilon$ and $Q_{rad}$ brings negligible errors to the heat loss calculations. Moreover, the spectral emissivity according to Madding [193] can be determined as:

$$\varepsilon = T_{IR1} - T_{IR2}/T_1 - T_2 \tag{3.4}$$

where $T_{IR1}$ and $T_{IR1}$ are the infrared camera temperature measurements and $T_1$ and $T_2$ the known measured temperatures. In all the tests, emissivity $\varepsilon$ fell in the range of 0.76 – 0.82, therefore a value of 0.78 was set as the channel wall emissivity in this study. Thus, the effective heat transferred in the two-phase flow was given by

$$Q_{eff} = Q - Q_{conv} - Q_{rad} \tag{3.5}$$

and the heat flux was applied on the test section was $q = Q_{eff}/A$ . Each test condition was repeated around 15 times and the characteristic heat transfer coefficient profiles were obtained.

The calibration of the IR video was carried out by measuring the pixels of a known-length within the same view field. The calculation of Biot number ($Bi$) allowed to

study the temperature uniformity within the channel body by comparing the heat conduction resistance to the heat convection resistance:

$$Bi = \frac{h_c d_{wall}}{k_{channel}} \tag{3.6}$$

where $h_c$ is the convective heat transfer coefficient calculated from the Shah and London [194], $d_{wall}$ is the channel wall thickness and $k_{channel}$ is the thermal conductivity of the channel body. Following the above mentioned, a Biot number at around ~0.06 was found in our system. Since $Bi << 1$, the difference between the inner and outer wall temperatures can be neglected [195]. Therefore, the channel outer surface temperature was used to calculate the local heat transfer coefficients. The thermally observed region of the channel was divided into 10 segments, as can be seen in Figure 3.1-11. Thus the time-averaged temperatures at 10 locations were calculated to reveal the local heat transfer coefficient, $h_{T.P.,local}$, in the two-phase flow system, along the channel axial direction using:

$$h_{T.P.,local} = \frac{q}{T_{W,local} - T_{L,local}} \tag{3.7}$$

where $T_{L,local}$ is the local liquid temperature in the micro-channel and $T_{W,local}$ is the local wall temperature of the microchannel. $T_{W,local}$ was increased along with the flow direction. In the present study, inlet and outlet fluid temperatures were acquired by the inserted thermocouples (K-type, accurate to ±0.05°C). The local liquid temperatures in axial direction along channel were not experimentally measured due to the fragility of the channel and the consequent inconvenience of thermocouple installation, which would deteriorate the transparency and also damage the tantalum coated surface of the channel. The local liquid temperature was calculated based on the assumption that all the effective heat flux was used to heat up the liquid. This leads to the following energy balance:

$$2x(d_{in})q = C_p \varphi A_c \left(T_{L,x} - T_{in}\right) \tag{3.8}$$

where $T_{L,x}$ (or $T_{L,local}$) is the local liquid temperature at a distance $x$ (mm) from the channel inlet, and $T_{in}$ is the inlet liquid temperature. So the liquid temperature can be written as:

$$T_{L,x} = \frac{2q(d_{in})}{C_p \varphi A_c} x + T_{in}. \tag{3.9}$$

The experimental uncertainties came from pump velocity, input power, channel dimension and temperature measurements. According to the standard uncertainty analysis of Taylor [196], the maximum uncertainties of channel estimated and summarised in Table 3.1-2.

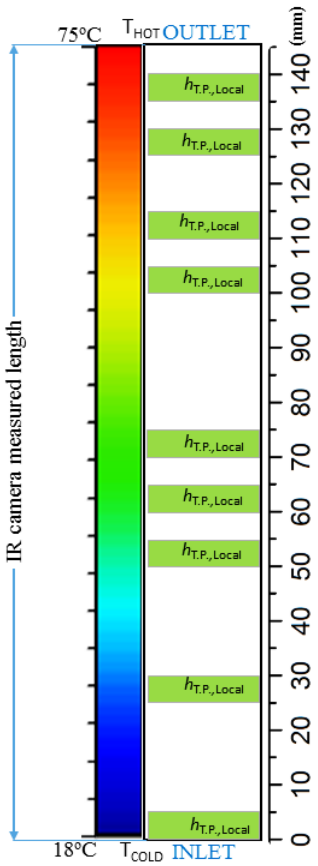


**Figure 3.1-11** Schematic drawing of the liquid temperature along the channel and the local heat transfer calculated areas.

**Table 3.1-2** Experimental measurement uncertainties (absolute error)

| Parameter | Maximum uncertainty (%) |
|---|---|
| Pump volumetric flow rate | 0.5 |
| Voltage | 0.2 |
| Current | 0.5 |
| Pressure | 0.25 |
| Channel depth and thickness | 10 |
| Channel width and length | 2 |
| IR camera measured temperature | 2 |
| Flow velocity | 12.5 |
| Channel surface area | 5 |
| Mass flux | 10 |
| Heat flux | 5 |
| Heat transfer coefficient | 17 |
| Local liquid temperature | 16.3 |
| Bubble aspect ratio | 6 |
| Bubble equivalent radius | 6 |

## 3.2 Experimental Techniques

### 3.2.1 Drop shape analysis

A FTÅ200 (First Ten Ångstroms, Inc., Portsmouth, OH) droplet shape and dynamic contact angle analyser was the apparatus used to deposit droplets of controlled volume and to record the droplet profile evolution over time until completed the evaporation mechanism. The FTÅ200 was equipped with: an adjustable sample table, a back and front light source to provide better contrast. A precise controlled dosing system and a CCD camera with a video-digitalized board capable of transferring a sequence of images (up to 100 fps) to the PC. Digital images of the evaporating sessile droplets

were recorded and analysed using the dynamic contact angle analyser software, FTÅ v2.0. Special, care was taken to place the substrates horizontally (a spirit level was used) and to reduce convective air currents around the droplet due to the light source. A previously well-cleaned substrate was placed on the adjustable sample table, and sessile droplets with volumes ranging from 1 μL to 5 μL were gently deposited on a chosen substrate using a syringe adjusted to the FTÅ200 dosing system. Different recording options used depending on the volume of the drying sessile droplets. At early times, in the evaporation process when the droplet was adopting a spherical cap shape, the profile was fitted using the Young−Laplace equation [197], and values for the droplet base radius *r*, height *h*, volume *V*, surface area *A*, and contact angle $\theta$ were extracted over time *t*, and plotted using OriginLab® (a data analysis and graphic software). However, in the experiments where were used liquid droplets of polymer solution poly(ethylene oxide) (PEO), once the deposition and the growth of the polymeric material began and the liquid droplet was resting on the solid deposit, the Young−Laplace equation could no longer be used to model the entire surface (polymeric phase). Instead, the two dimensional droplet profile was extracted from the recorded images using ImageJ (image processing and analysis in java) version 1.46m (2011, U.S. National Institutes of Health) and the surface area *A* and volume *V* of (the profile) rotation were calculated numerically with PCO − Pictures (DocSchneider Engineering & Technical Software CH-8308 Illnau, Switzerland). Values of the deposit base radius *r*, height *h*, and volume *V* were calculated by numerically integrating the digitized PEO deposit profiles. The contact line dynamics of the evaporating pure and binary alcohol sessile droplets were also investigated using the FTÅ200 instrument. Moreover, in some experiments in order to examine the wetting behaviour of the liquid droplets (pure and binary alcohol mixtures) under the effect of varying temperatures, a flexible silicone rubber heater SRGF-203/5-P-230V (OMEGALUX® Silicone Rubber Fiberglass Insulated Heaters) was placed underneath the moveable sample table in order to heat up uniformly the chosen substrate.

All experiments were carried out under ambient experimental conditions of temperature, relative humidity and pressure. Figure 3.2-1 depicts the experimental apparatus, and besides that a snapshot of the FTÅ200 v2.0 software to illustrate the optimum sharpness, brightness and contrast required between the drying sessile droplets and the surroundings.

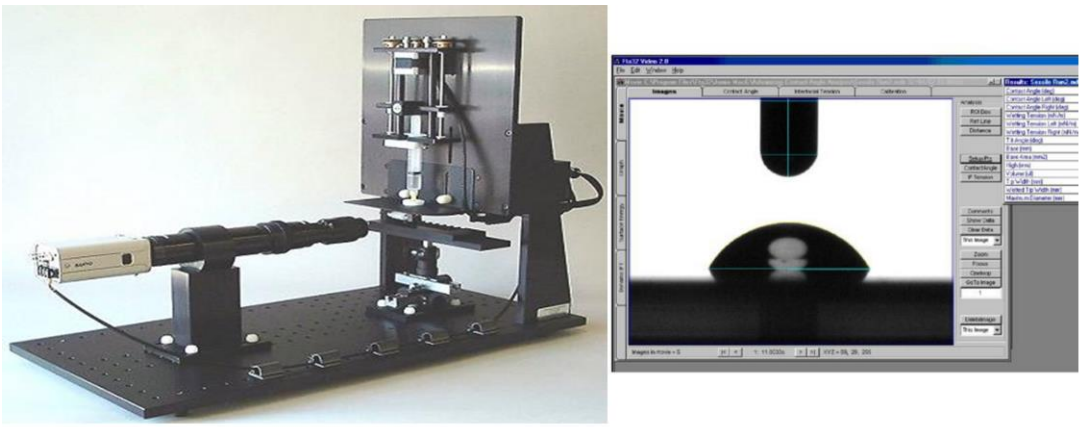

**Figure 3.2-1** (Left) FTÅ200 apparatus consist of: movable sample table, front-back light sources, a CCD camera and a pumping - dosing system. (Right) FTA v2.0 software snapshot of the fitted droplet profile using Young's equation.

### 3.2.2 High speed camera

The droplets spreading dynamics of the advancing/ receding contact base lines and the bubbles motion (shape geometry and velocity profiles) inside a microchannel were also investigated by using high speed visualizations. The high-speed camera employed was a NanoSense® MK III (IDT), with interchangeable macro and micro lenses, used as appropriate. The resolution of the camera allowed for either the entire heated micro-channel length to be captured or for just a particular section of interest to be focussed upon. The rate of the camera was set from 500 fps to 2500 fps depending on different visualization requirements and experimental conditions. The recorded images were extracted from the high-speed camera were analysed with the ImageJ® (image processing and analysis in java) version 1.46m (2011, U.S. National Institutes of Health) software in order to measure the droplets' spreading profiles. The migrating bubbles' motion (shape geometry and velocity profiles) was analysed with the X-Vision (acquisition and image processing) software provided from Integrated Design Tools, Inc. (IDT). A led back light source to achieve the optimum contrast for the processing of the images was also implemented in this experimental setup.

### 3.2.3 Infrared thermography

A ThermaCam™ infrared thermography system (SC3000 Series, FLIR Infrared Systems, 2005) was also used to analyse the surface temperature profiles of evaporating droplets of the same range size and concentration and was also used to visualise and record the temperature profile at the micro-channel exterior wall. The ThermaCam™ SC3000 offers ultra-high thermal sensitivity, broad dynamic range and revolutionary long-wave imaging. It is characterized by a measurement in the 8 – 9 μm band of the infrared spectrum with a high resolution of 320 x 240 pixels, thermal sensitivity of 20 mK at 30°C, an accuracy of ±1°C for temperature up to 150°C, and is Stirling cooled. The images were recorded at 50 frames/s using a camera fitted with a microscope lens with 10 × 7.5 $mm^2$ field of view and a minimum focal length of 26 mm. The infrared system provides for automatic transmission correction of temperature, based on atmospheric temperature, relative humidity, input distance from the object and emissivity of the object i.e. droplet or (surface) microchannel. The IR camera was used with a dedicated PC for acquisition, with specialised software (ThermaCAM Researcher Professional v2.9®) for image post-processing and analysis. The emissivity of the binary mixtures (alcohol solutions) was close to that of pure water (~0.95) and it is a stored parameter to accurately measure the surface temperatures. The droplets were manually injected onto a chosen substrate which was heated-up uniformly in the same way as with the experiments with the FTÅ200 apparatus using a flexible silicone rubber heater SRGF-203/5-P-230V. Before doing the experiment, it was checked that the substrate temperature homogeneity was stable at ± 0.5°C. The thermal imaging camera was vertically assembled at the top of the droplet. The infrared camera recorded radiation coming from the fluid volume and the heated substrate. The spatial and temporal temperature data that was acquired of the droplets and the microchannel surface field was transferred to the PC with the built-in ThermaCam software.

### 3.2.4 Pendant drop technique

Pendant drop method analysis was used to measure interfacial tension of the fluids i.e. the gas-liquid, $\gamma_{GL}$, surface tension. This method involves the determination of the profile of a drop of one liquid suspended in another liquid or fluid at mechanical equilibrium. More specifically, during this process, a liquid droplet is formed at the tip of a syringe which is connected with the pumping system and the size of the droplet is slowly increased until dropping off. The profile of the investigated droplets is determined by the balance interplay between the interfacial forces (keeping the droplet attached on a syringe) and the gravitational forces (pulling the droplet down). The surface tension of the ordinary liquids (pure water and pure butanol) and the binary alcohol mixtures (self-rewetting fluids) have been measured in the temperature range from ~10$^o$ to ~90$^o$ C, using the pendant drop method (FTÅ apparatus) and the results will be discussed in Chapter 5. An average value of ~50 measurements was conducted for each solution at controlled experimental conditions: $T$ = 19$^o$ ± 1$^o$ C, relative humidity $RH$ = 35 ± 5% and pressure $P$ = 1 atm. Figure 3.2-2 presents a typical snapshot of a pendant drop extracted from the FTA v2.0 software.

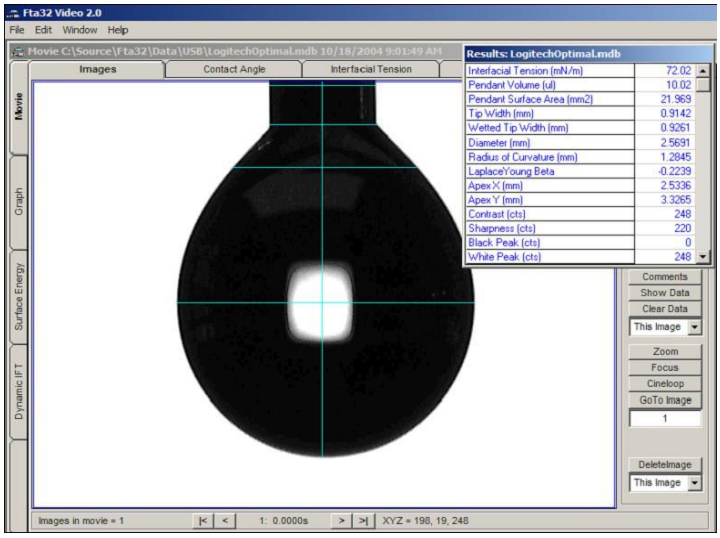


**Figure 3.2-2** Screen capture from FTÅ200 software shows a pure water droplet analysed with sessile drop method.

### 3.2.5 Atomic force microscopy

Atomic force microscopy (AFM) technique was adapted to characterise the substrates used during experimental research carried out in Chapter 4. This method was used to obtain information about the surface homogeneity, whether may be topographical or compositional. AFM was selected to image the features of the deposits left of the aqueous poly(ethylene) oxide droplets after the complete evaporation process. In addition, this same imaging technique was used to visualise and measure the thickness and structure of the polymers (PEO) films-layers were used in Chapter 4. The great resolution down to the atomic scale (sub-nanometres) both vertically and laterally planes offered the AFM, was the motivation for using this technique. The equipment used was a Bruker Multimode/ Nanoscope IIIa AFM (Bruker AXS, Santa Barbara, CA), equipped with a J scanner (x−y scan range of ∼140 μm) and with 8 nm radius LTESP Bruker cantilevers with a nominal spring constant of 48 N/m and resonance frequency of 190 kHz. A typical snapshot of the AFM equipment can be seen in Figure 3.2-3. The samples were imaged in tapping mode (tip in intermediate contact with the surface), in air and at room temperature conditions. Acquired images were post-processed by levelling and analysis (including height profiles) using Gwyddion software [198], a modular program for scanning probe microscopy (SPM) data visualization and analysis. The thickness was measured by taking profiles and/or images at the edge of the films and/or over areas where we scratched the polymer layer with a thin scriber. The results obtained will be presented and discussed in Chapter 4. It is worth noting that AFM experiments were carried out under the supervision of Dr. Michael Kalloudis, graduated PhD student at the Institute of Material and Processes at the University of Edinburgh.

**Figure 3.2-3** Typical snapshot of the Bruker Multimode/ Nanoscope IIIa AFM used in this experimental research to characterise the height profiles of the PEO films (thin).

## 3.2.6 Surface profilometry

A portable surface roughness tester, SURFTEST SJ-410 series (Mitutoyo Corporation, Japan), was used to characterise and measure the height profiles of the thicker PEO films and deposits after the complete of the evaporation process, Figure 3.2-4. The surface profilometer consisted of a large colour graphic LCD touch-screen that ensures both intuitive control and accurate advanced readability and operability and a stylus tip detector with enhanced measuring functions. The wide-range (800 μm), high resolution (0.000125 μm, at 8 μm range) detector and a drive unit provided high accuracy measurement in its class. The surface tester was also equipped with a high speed printer which prints out the results of the measurements.


**Figure 3.2-4** Snapshot of the portable surface roughness tester, SURFTEST SJ-410 series, used in this experimental research to characterise the height profiles of the PEO deposits and films (thick).

### 3.2.7 Scanning electron microscopy

Scanning electron microscopy (SEM) experiments were conducted to characterise the aluminium substrates regarding the experiments were carried out for the non-spherical droplets, discussed in Chapter 5. SEM produced images of the aluminium substrate by scanning it with a focused beam of electrons. The electrons interact with atoms in the sample, producing various signals that can be detected and that contain information about the sample's surface topography and composition. The equipment used was a Carl Zeiss SIGMA HD VP Field Emission SEM equipped with Oxford AZtec ED X-ray analysis and Electron Backscatter Diffraction (EBSD) systems as displayed in Figure 3.2-5. Experiments were undertaken in collaboration with Dr. Nicola Cayzer, from the school of Geoscience, in the University of Edinburgh.


**Figure 3.2-5** Snapshot of the Carl Zeiss SIGMA HD VP Field Emission SEM was adapted to characterise the aluminium (alloy) substrates used in this experimental research.

# Chapter 4: Effect of Molecular Weight on PEO Droplets and Pillar Formation

In this chapter, we attempt to shed light on the drying mechanism of sessile droplets of aqueous poly(ethylene oxide) 10% wt. (PEO) solutions. Contact angle analysis was used to examine the four stage dying mechanism i.e. *pinned drying* (stage I), *pseudodewetting* (stage II), *boot-strap growth-building* (stage III), and *solid contraction* (stage IV) by monitoring the base radius $r$, height $h$, volume $V$, surface area $A$, and contact angle $\theta$, of the PEO droplet over time $t$, at constant temperature, humidity, and pressure throughout the whole drying process. Polymeric residues were formed with either a disklike puddle or a distinctive tall conical pillar shape. The use of contact angle analysis technique allowed us to systematically capture all the stages of the evaporating mechanism and consider the transitions between the characteristic stages for the different molecular weights. We focused to illustrate the effect of adhesion and contact line friction during the crucial stages of pinning and depinning for the high molecular weights and its influence on the final morphology of the dried polymeric material (PEO). In the second part of this chapter, we performed an experimental investigation on PEO droplet evaporation on PEO and PTFE (Teflon) films demonstrating the importance of interfacial interactions phenomena taking place in the vicinity of the contact line and the crucial impact on the final morphology of the PEO dried deposits. This experimental technique, for the first time, provided valuable insights and revealed the differences in the underlying mechanisms that govern each stage of the drying process for each molecular weight used, on different surfaces which varying in hydrophobicity. It is important to determine how to control the evaporation mechanism and the final shape of the solute polymeric deposit for different molecular weights for both fundamental and application reasons.

## 4.1 Experimental Method

Aqueous solutions of polyethylene oxide (PEO) were prepared using with various molecular weights: $M_w$ = 10 000 g/mol, 100 000 g/mol, 200 000 g/mol and 300 000 g/mol. All solutions which were prepared with an initial concentration of $c_0$ = 10% by mass (which corresponds to close to the semi-dilute region for the lowest $M_w$ and well into the semi-dilute region for the rest) [39] were mixed using distilled, deionized water and were left to equilibrate for at least 24 h before use. A roller mixer was used

to increase the dissolution rate. After mixing process, cloudy undissolved polymer clusters appeared in our samples. These clusters were successfully removed from all samples by driving them through a 0.45 μm filter with an adjustable-speed syringe pump at around 0.5 mL/h. Filtering samples in order to remove undissolved clusters resulted in slightly reducing the overall concentration and also density ρ (see also Figure 3.1-1). The method used for the removal of aggregates does not damage the polymer molecules [38]. For each measurement, a droplet with an initial concentration of 10% and with a volume in the range from 1 to 5 μL was placed on an ethanol-cleaned borosilicate glass microscope. Furthermore, silicon wafers spin coated with a 1-μm-thick poly(tetrafluoroethylene) (PTFE) layer were used in this work. PTFE substrates were cleaned before use in an ultrasonic bath of isopropanol for at least 10 min. The droplets were deposited using a 1 mL syringe with a 0.71-mm-diameter syringe needle. Despite the large shear rates in the needle (∼100 s−1), no significant differences in drying behaviour were seen when compared with droplets deposited less controllably by pouring, so we assume that the polymer molecules are undamaged. A digital camera and a diffuse light source placed on either side of the droplet were used to record the whole evaporation process. Digital images of the drying droplets were recorded at about 10 s intervals and analysed using the dynamic contact angle analyser namely FTÅ200 (First Ten Ångstroms, Inc., Portsmouth, OH) software. At early times in the evaporation process when the droplet was a spherical cap, the profile was fitted using the Young−Laplace equation [197] and values for the droplet base radius *r*, height *h*, volume *V*, surface area *A*, and contact angle θ were extracted. However, once the deposition growth of the polymeric material began and the liquid droplet was resting on the solid deposit, the Young−Laplace equation could no longer be used to model the entire surface. Instead, the two-dimensional droplet profile was extracted from the recorded images using ImageJ version 1.46m (2011, U.S. National Institutes of Health) and the surface area *A* and volume *V* of (the profile) rotation were calculated numerically with PCO − Pictures (DocSchneider Engineering & Technical Software CH-8308 Illnau, Switzerland). Values of the deposit base radius *r*, height *h*, and volume *V* were calculated by numerically integrating the digitized deposit profiles. The measurements were taken under ambient conditions i.e. relative humidity $RH = 35 \pm 5\%$, temperature $T = 22 \pm 1$ °C, and pressure $P = 1$ atm). After the initial deposition of the droplet on the bare glass coverslip, the contact line became pinned between approximately 60° and 75°, with the vast majority between 65° and

70°. Additional experiments were carried out with glass substrates coated with PEO films prepared from 1 or 10 wt. % PEO solutions with two different molecular weights: 10 000 and 100 000 g/mol. Spin coating was used to deposit thin and ultrathin PEO films on the flat glass substrates. A small amount of PEO solution was applied to the centre of the substrate span at 2000 rpm at a duration of either 90 or 120 s. Moreover, dip coating was used to prepare thicker absorbed PEO films. Topography images and/or height profiles of the PEO films were acquired by surface profilometry and atomic force microscopy (AFM). A surface roughness tester, SURFTEST SJ-410 series (Mitutoyo Corporation, Japan), was used for the height profiles of the thicker films. AFM imaging for the thin PEO films was conducted using a Bruker MultiMode Nanoscope IIIa AFM (Bruker, Santa Barbara, CA), equipped with a J scanner (x−y scan range of ~140 μm). The samples were imaged in tapping mode (tip in intermediate contact with the surface). Acquired images were post-processed by levelling and analysis (including height profiles) using Gwyddion software [198]. The thickness was measured by taking profiles and/or images at the edge of the films and/or over areas where we scratched the polymer layer with a thin scriber. The films were continuous apart from the very thin ones (~20 nm thickness) where in some areas the film broke and the substrate was revealed. The substrates, PEO solution droplets preparation procedure as well as the experimental techniques used in order to extract and analyse the data followed were fully described in the previous chapter (Chapter 3). Additionally, details about the characterisation of the PEO films will be presented in Chapter 4.5.

## 4.2 Four Stage Evaporative Behaviour of PEO Droplets

Results concerning the evaporative behaviour of aqueous PEO sessile droplets on ethanol-cleaned borosilicate glass substrates and the resulted solute dried PEO deposit for four different molecular weights are presented next.

Liquid PEO samples were prepared with the same initial concentration of four different molecular weights, $M_w$, of PEO. Droplets with initial volumes ranging

between 1 and 5 μL were left to evaporate until complete drying. Figure 4.2-1 presents typical final images obtained from the complete drying process of the 10% wt. PEO sessile droplets with an initial volume of 3 μL for the four different molecular weights i.e. $M_w$ = 10 000, 100 000, 200 000, 300 000 g/mol. Their free evaporation was captured using a FTÅ200 apparatus (drop contact angle analysis, section 3.2) and analysed with the accompanying software. It can be seen clearly from the images that there are obvious differences in the evaporation mechanism and the final morphology of the dried PEO deposits for the four different molecular weights used. More than ~25 repetitions of each droplet volume and molecular weight were carried out showing very good reproducibility.

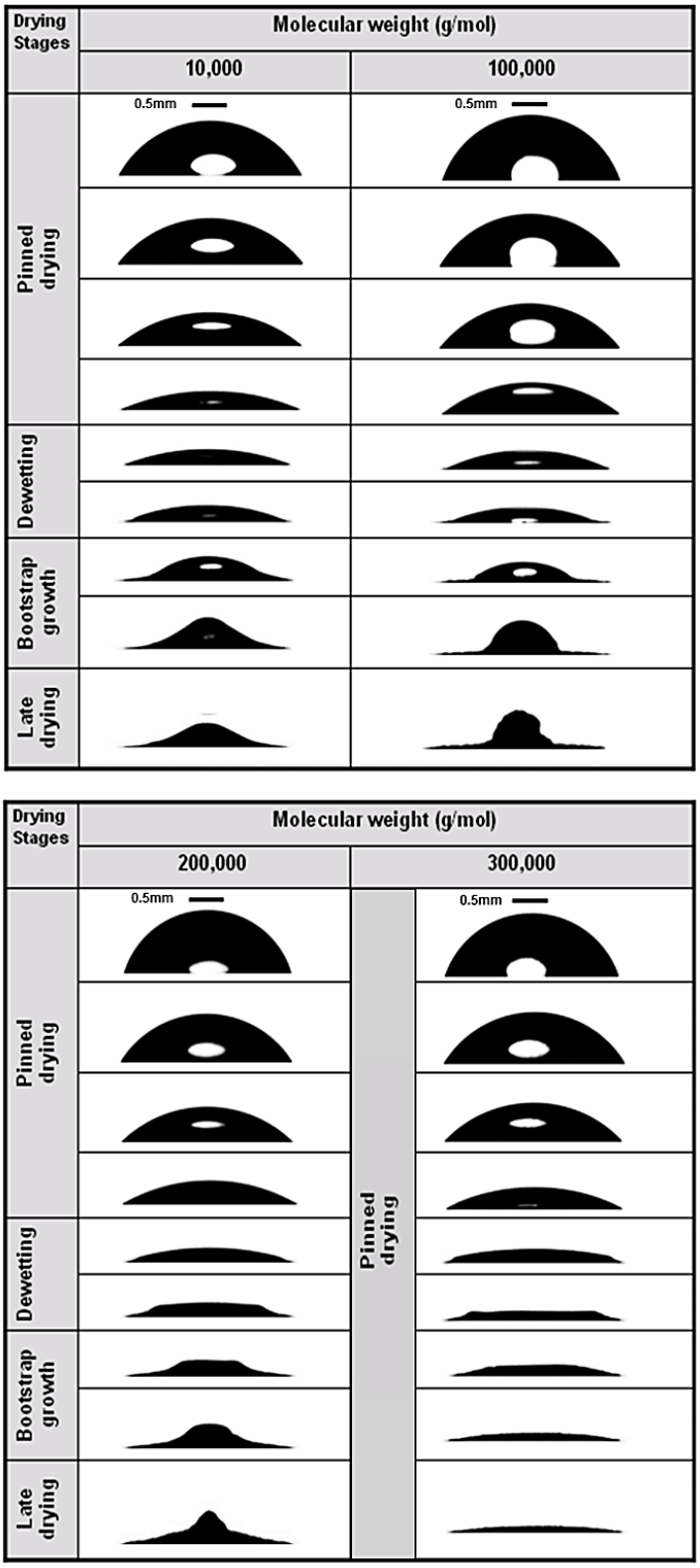


**Figure 4.2-1** Typical examples of the evaporation process for 10 wt. % PEO droplets with volumes of 3 μL for the four different molecular weights $M_w$ via the characteristic four-stage drying mechanism: Stage I, pinned drying; stage II, dewetting; stage III, bootstrap growth; and stage IV, late drying under controlled ambient conditions. Note that the scale bar represents 0.5 mm.

Figure 4.2-2 and 4.2-3, shows representative PEO droplets examples showing the whole evolution of the evaporation process over time *t*. In more details, each graph presents the time sequence of contact angle $\theta$ and contact base radius *r* extracted profiles of 10% wt. PEO droplets of volumes 1, 3, and 5 μL. At the beginning of the drying mechanism, pinned contact line behaviour is shown during stage I, with the droplet having a constant base radius *r*. The contact angle $\theta$ and height *h* both decreased in order to compensate for the reduced volume of the evaporating droplet. As the evaporation rate is greater at the triple contact line (TCL), the liquid flows radially outward in order to sustain the pinned droplet profile [26]. By the time the polymer concentration *c* at the vicinity of the contact line becomes sufficiently high (locally TCL more polymeric material than water), the precipitation of solid, semicrystalline spherulites of PEO will occur [38]. This should correspond to the (local) saturation $c_{sat}$ (*ca.* $c_{sat} \approx 0.6$ by mass and is approximately independent of $M_w$) [39]. Hypothetically, at this point, the resulting deposit hinders radial, liquid flow by the creation of a "wall" of solid polymer separating evaporation flux and liquid (water) replenishment. As a result of this behaviour the evaporation/flow continuity shifts radially inward. While this process continues during the second stage of drying (pseudodewetting), the results will be a thin "carpet" of polymeric material left behind at the same time as the contact line steadily recedes. It can be seen in Figure 4.2-2 and 4.2-3, the pinning stage takes considerably various times for the different molecular weights. The lowest duration of stage I was observed in the case of 100 000 g/mol, whereas in the case of 300 000 g/mol the droplet remained pinned until finish the whole evaporation mechanism.

As mentioned above, during stage II the contact line recedes (base radius *r* decreases) and a thin layer of the polymer was left behind. Regularly, the contact angle $\theta$ and height *h* continue to decrease, but more slowly than in the previous stage (I). This effect may be expected on geometric grounds if the evaporation rate of the system remained essentially unchanged. Interestingly, in the case of 10 000 g/mol, the contact angle showed a plateau or a small increase for a short time period after the depinning of the contact line. Stage III (bootstrap growth-building) commences when the droplet (at concentration $c_{sat}$) started to be lifted upward by the solid PEO precipitate. During this stage, the apparent contact angle $\theta$ and height *h* increased, as displayed in Figure 4.2-2 and 4.2-3. However, base radius *r* decreased as the contact line recedes until the

solvent is completely evaporated. During this stage, the droplet seemed to push itself upward [123]. This is most obvious in the case of 100 000 g/ mol, where the highest pillars were obtained after complete evaporation of the PEO liquid droplets. Note that in the case of 300 000 g/mol, no pillars were observed. This stage ends when the overall polymeric structure reached its maximum height and all of the polymeric phase has precipitated as semicrystalline spherulites. Water may still be trapped within the polymeric solid phase which lead to the last stage of drying process (stage IV) where the remaining liquid was fully encapsulated by solid PEO and the evaporation rate in the system decreased considerably. However, as this specific phase of drying can be essentially very slow, we were not completely sure about its duration but the opacity of the final dry deposit gives an indication of its desiccation. It is worth noting that the forces generated during stage IV by the shrinking structure adhering to the coverslip (glass in our experiments) can be strong enough to cause upward bending of the underlying substrate [199-201]. Remarkably, droplets with the highest-molecular-weight PEO, $M_w$ = 300 000 g/mol, never reached the stage III as depicted in Figure 4.2-2 and 4.2-3. The height $h$ of the PEO liquid droplets steadily decreased, and the final deposit is a flat disklike "puddle", with a quite constant thickness. Interestingly, for these droplets there was some evidence of a slight reduction or decrease in base radius $r$ and simultaneously a small increase (a trivial jump) in contact angle $\theta$, but this was not sustained and the system remained pinned followed by solid contraction; late drying stage occurring to some extent simultaneously.

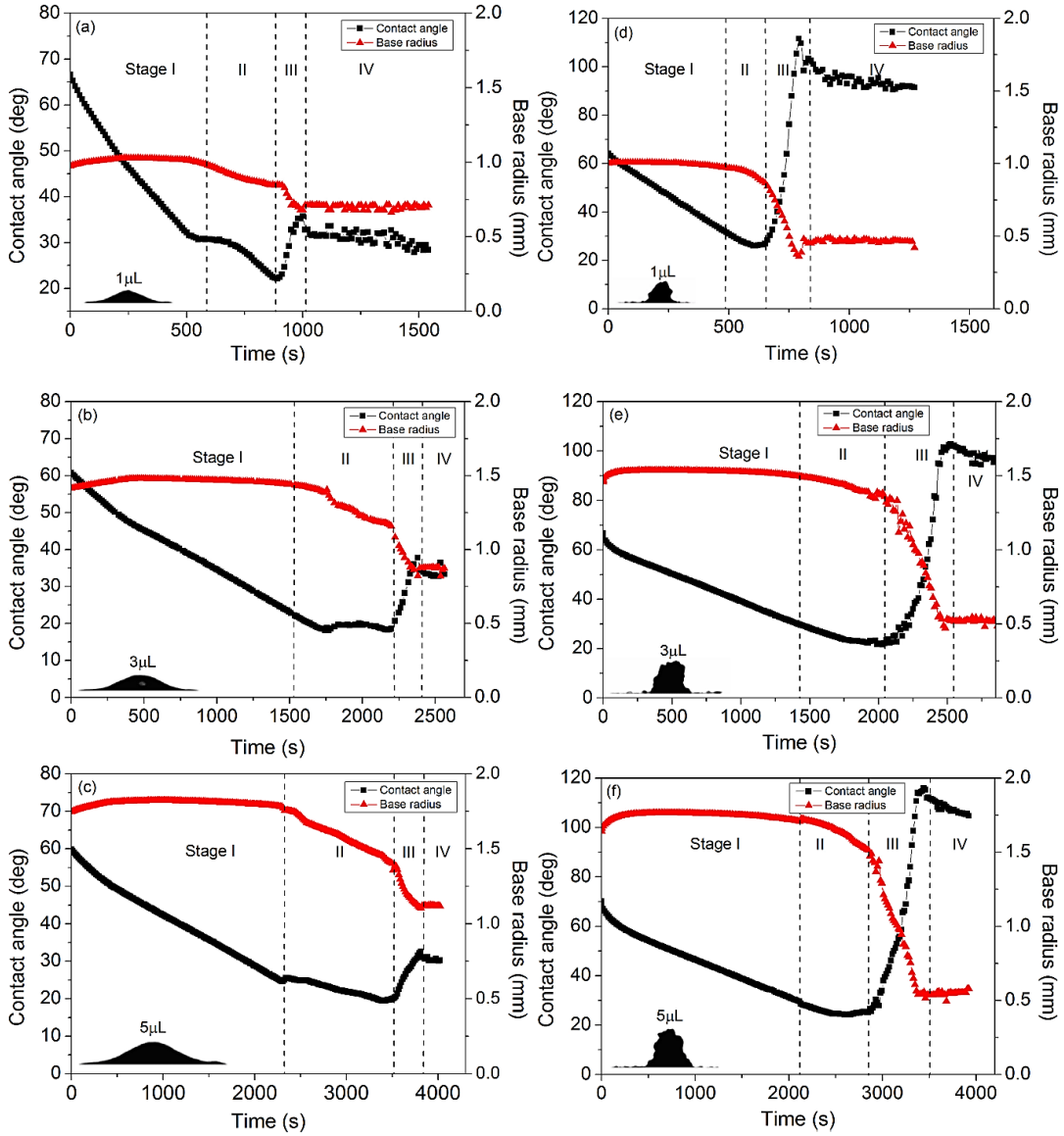


**Figure 4.2-2** Contact angle, $\theta$ (degrees), and base radius, $r$ (mm), versus time (s) (a, 1; b, 3; c, 5 μL) for 10 000 g/mol and (d, 1; e, 3; f, 5 μL) 100 000 g/mol during the evolution of the whole evaporation process (representative examples from ~25 repetitions for each $M_w$). Black squares correspond to contact angle measurements, and red triangles depict base radius measurements. Uncertainties, at later times, in base radius $r$ and contact angle $\theta$ are due to deviations in the shape of the droplet as the polymeric material is deposited. Insets depict the final PEO deposits.

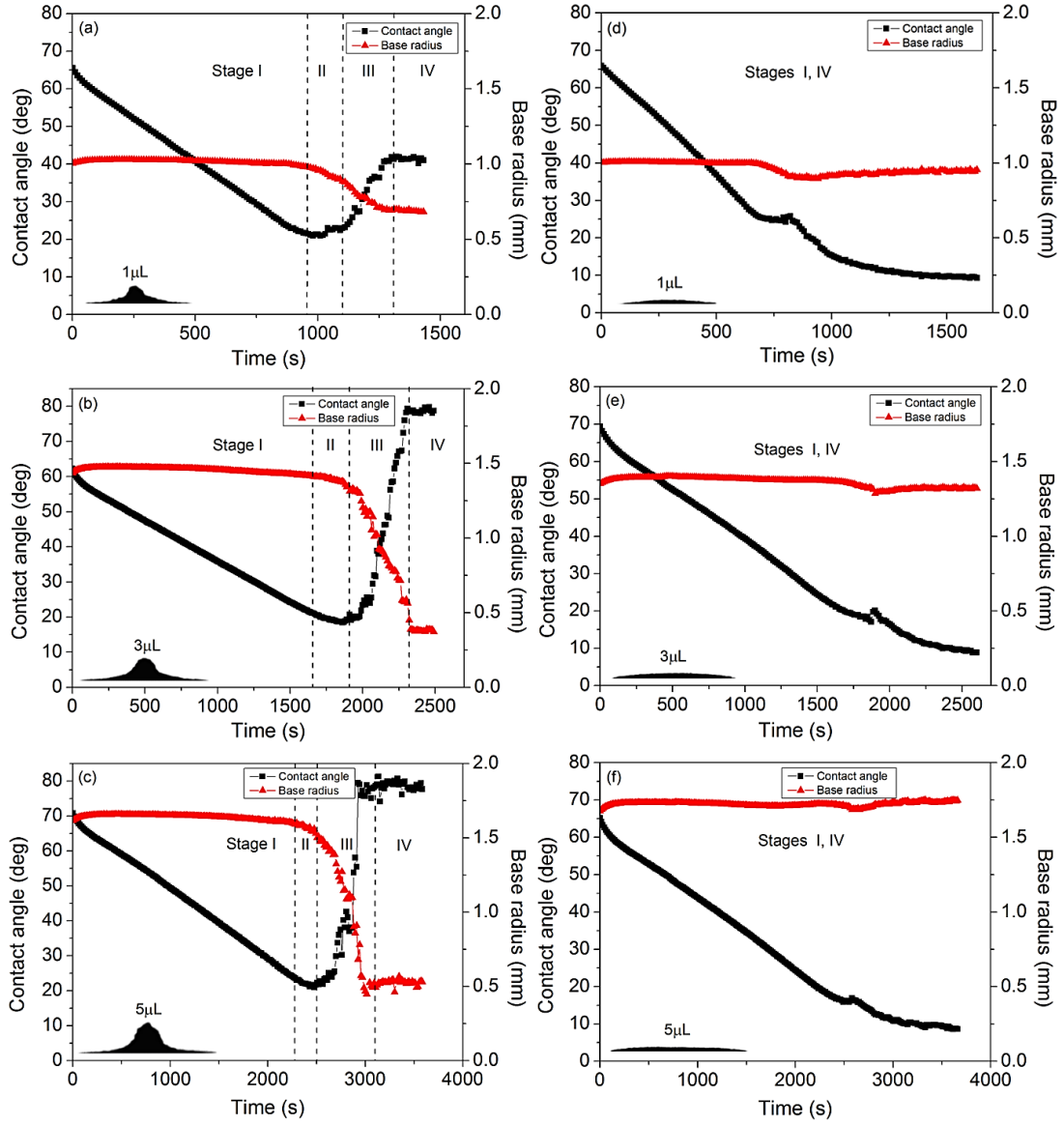


**Figure 4.2-3** Contact angle, $\theta$ (degrees), and base radius, $r$ (mm), versus time (s) (a, 1; b, 3; c, 5 μL) for 200 000 g/mol and (d, 1; e, 3; f, 5 μL) 300 000 g/mol during the evolution of the whole evaporation process (representative examples from ~25 repetitions for each $M_w$). Black squares correspond to contact angle measurements, and red triangles depict base radius measurements. Uncertainties, at later times, in base radius $r$ and contact angle θ are due to deviations of the shape of the droplet as polymeric material is deposited. Insets depict the final PEO deposits (pillars or puddles).

## 4.3 Pinning - Depinning Mechanisms

Figure 4.3-1 (a) presents the average duration of the pinning stages during the drying process. The results obtained for this drying stage are plotted against the four different values of $M_w$ for drop volumes ranging from 1 to 5 μL where ~25 individual repeats were carried out for each $M_w$. Remarkably, the pinning-time period (stick time) for $M_w$ = 10 000 g/mol was longer than for $M_w$ = 100 000 g/mol, suggesting that a different mechanism was taking place in the vicinity of the contact line. The pinning period increased from $M_w$ = 100 000 g/mol to $M_w$ = 200 000 g/mol (Figure 4.3-1) and resulted in different final pillar formation morphology. It is worth noting that the 200 000 g/mol case behaved similarly to the 10 000 g/mol case in terms of the pinning time periods (almost the same) leading to relatively low pillars of similar shape. Contrary to all previous observations, PEO droplets with $M_w$ = 300 000 g/mol were maintain to pinned contact line behaviour and no pillar formation occurred as seen in Figure 4.2-3 (d−f). The droplets with $M_w$ = 300 000 g/mol were pinned throughout the whole evaporation mechanism, and thus the corresponding times in Figure 4.3-1 (a) are total evaporation times. The variations of the normalized pinning times i.e. pinning time/total evaporation time, for the four different molecular weights are plotted in Figure 4.3-1 (b). The values of the pinning -time for the five different volumes cluster (especially for the higher molecular weights) and showed more clearly the nonlinear dependence against the $M_w$ and the local minimum at 100 000 g/mol for all volumes used in this experimental study. The depinning mechanism seemed to be an essential phase in pillar (monolith) formation while the solid polymeric material must follow the trace of the droplet inward to the centre of the droplet. In contrast to this behaviour, if the droplet contact line remains stationary (pinned), then pillar formation was suppressed and a puddle appeared after complete evaporation. As the pinning stage (stick time) increased, it discouraged pillar formation. The origins of these complex phenomena at the triple-phase contact line were extensively discussed in the discussion Chapter 4.6.

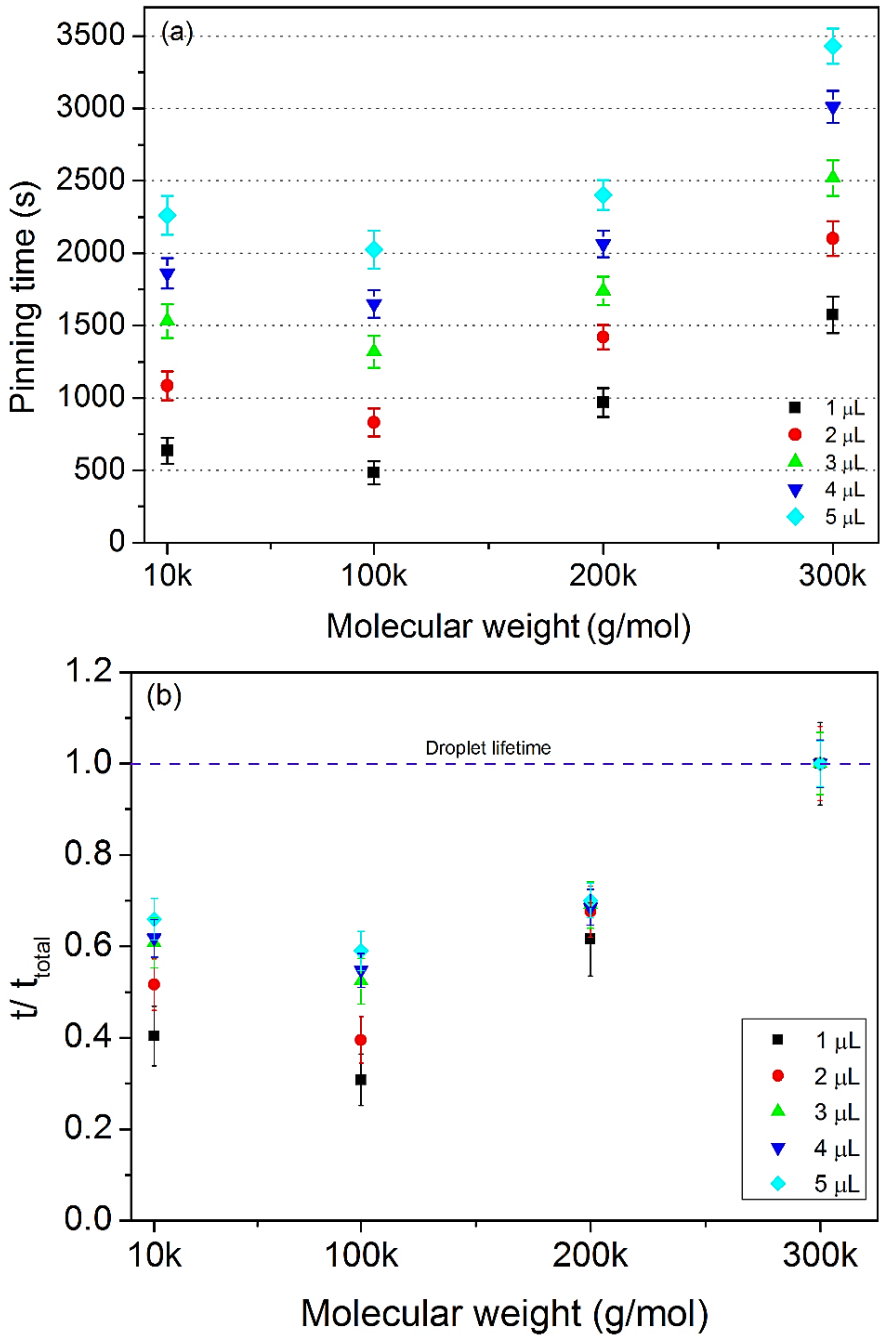


**Figure 4.3-1** (a) Average times values of the pinning stage against the four different molecular weights $M_w$ for the 10% wt. PEO droplets in a range of initial volumes: from ~1 to ~5 µL, and (b) the normalized pinning-time values for the four different $M_w$.

## 4.4 Final Morphology of PEO Deposits

Following the above finding in Chapter 4.2 – 4.3, Figure 4.4-1 shows typical final morphology images of the PEO deposits for the different $M_w$ and all the volumes used, approximately five or six repetitions for each case. It can be observed that the final dried polymeric material exhibited a variety of shapes and final volumes depending on the $M_w$ and droplet volume, from ~1 to ~5 μL, respectively. A low, smooth conical pillar (monolith) was obtained for the final morphology of the dried solutes PEO droplets with $M_w$ = 10 000 g/mol, as presented in Figure 4.4-1. Furthermore, droplets with $M_w$ = 100 000 g/mol displayed final deposits formed as solid, tall, steep, and rough pillars (monoliths), several millimetres in height which sometimes reached twice the initial height $h_0$ of the PEO droplet. The PEO pillars (monoliths) were located usually at or near the centre of the glass substrate. The profile of these droplets exhibited characteristic steep, rough surfaces. Final solid precipitates for droplets with $M_w$ = 200 000 g/mol, were again tall and in the form of rough pillars (monoliths), reaching a maximum height of $h_{max}$, lower than in the previous case of $M_w$ = 100 000 g/mol. The edge of the dried PEO solute deposits extended almost to the initial base radius $r_0$. Finally, for $M_w$ = 300 000 g/mol, smooth, disklike puddle formations where the final base radius was approximately equal to the initial droplet base radius $r_0$ and can be seen in Figure 4.4-1.

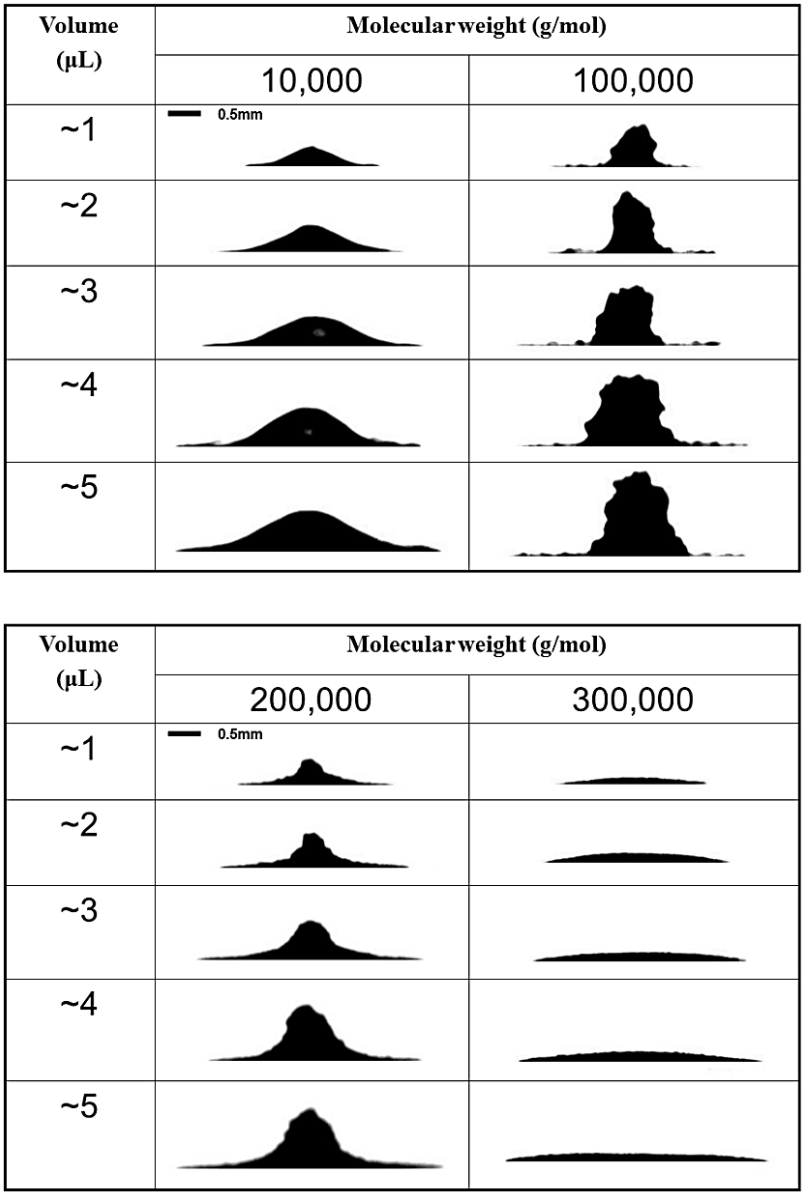


**Figure 4.4-1** Representative examples of the final morphology of the deposits: pillars or puddles, from around 1 to 5 µL droplets containing 10% wt. PEO with $M_w$ = 10, 100, 200, and 300 kg/ mol; characteristic samples from approximately five to six repetitions for each case (molecular weight and volume). Note the preferential formation of high pillars at $M_w$ = 100 000 g/mol and the formation of a flat puddle for droplets with $M_w$ = 300 000 g/mol. The scale bar depicts a width of 0.5 mm.

Figure 4.4-2 (a−d) depicts the results obtained for the aspect ratio measurements (final height over the base diameter) of either pillar or puddle formation of the final PEO solute deposits against the initial volumes of the PEO droplets, for the four different molecular weights. It can be noticed in the graphs that altering the initial volume of the droplet did not drastically influence the behaviour of the dried PEO solute after the complete of the evaporation mechanism over a range from around 1 to 5 μL. Furthermore, Figure 4.4-2 (e) presents the averages of the aspect ratio for each case of the four molecular weights. It is clearly illustrated, Figure 4.4-2 (e), that for higher final pillar formation i.e. droplets with $M_w$ = 100 000 g/mol, the measured average aspect ratios were much higher than the other cases. The reverse result was shown for PEO droplets with the highest molecular weight $M_w$ = 300 000 g/mol, where the final shape was nothing else but flat disks.

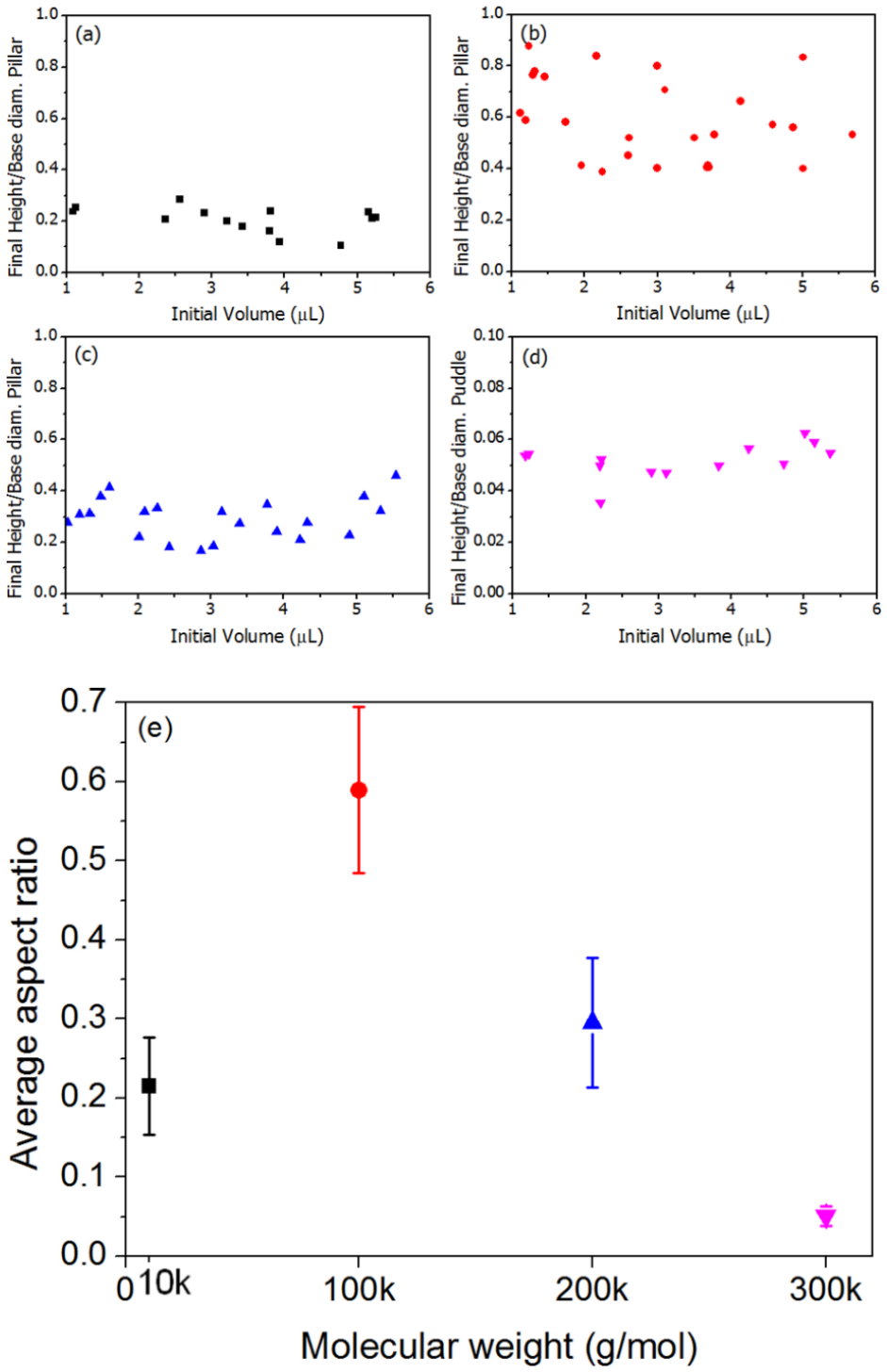


**Figure 4.4-2** Aspect ratio measurements: final height of pillar or puddle formation (mm)/base diameter of pillar or puddle (mm) formation, of the PEO solution samples plotted against the four different molecular weights (a, 10k; b, 100k; c, 200k; d, 300k g/mol). Note that aspect ratio measurements for the case of $M_w$ = 300 kg/mol are plotted on a different scale due to the very low disklike "puddle" shape of the final PEO deposits. (e) Average aspect ratio measurements of PEO solution samples for each $M_w$ used.

Additionally, an estimation of the void fraction i.e. fraction of the volume of voids in a material over the solid volume of the material, was conducted for the final PEO deposits. In more details, the difference between the measured final volume of the deposit and the volume of the solid deposit based on the 10% wt. concentration of PEO, was calculated for every PEO droplet case and the volumes of the droplets, divided by the solid volume of the deposits $[(V_m/V_S) - 1]$, where $V_m$ was the measured final volume of the deposits and $V_s$ is the calculated solid volume. Figure 4.4-3 depicts all the results of the void fraction calculations as a function of the initial volume of the droplets. Void fraction measurements (Figure 4.4-3) clearly showed that only in the case of PEO droplets with $M_w$ = 100 000 g/mol the obtained values significantly deviating from zero (higher void fraction for these deposits), in contrast to the other molecular weights used in this study that were quite close to the zero line and related with the presence low void fraction. The occurrence of voids inside the solid final deposits, for droplets with $M_w$ = 100 000 g/mol with higher pillar formation, could be explained by the frequent appearance of a hollow region at the proximity region of the pillar base (near the substrate) when viewed from underneath the final polymeric dried deposits. Following the previous observations of Willmer *et al*. [123] our experiments were shown to be consistent and could be explained by the presence of low interfacial adhesion between the liquid droplet and the substrate, particularly for the higher $M_w$ that produced final deposits with high pillar formation.

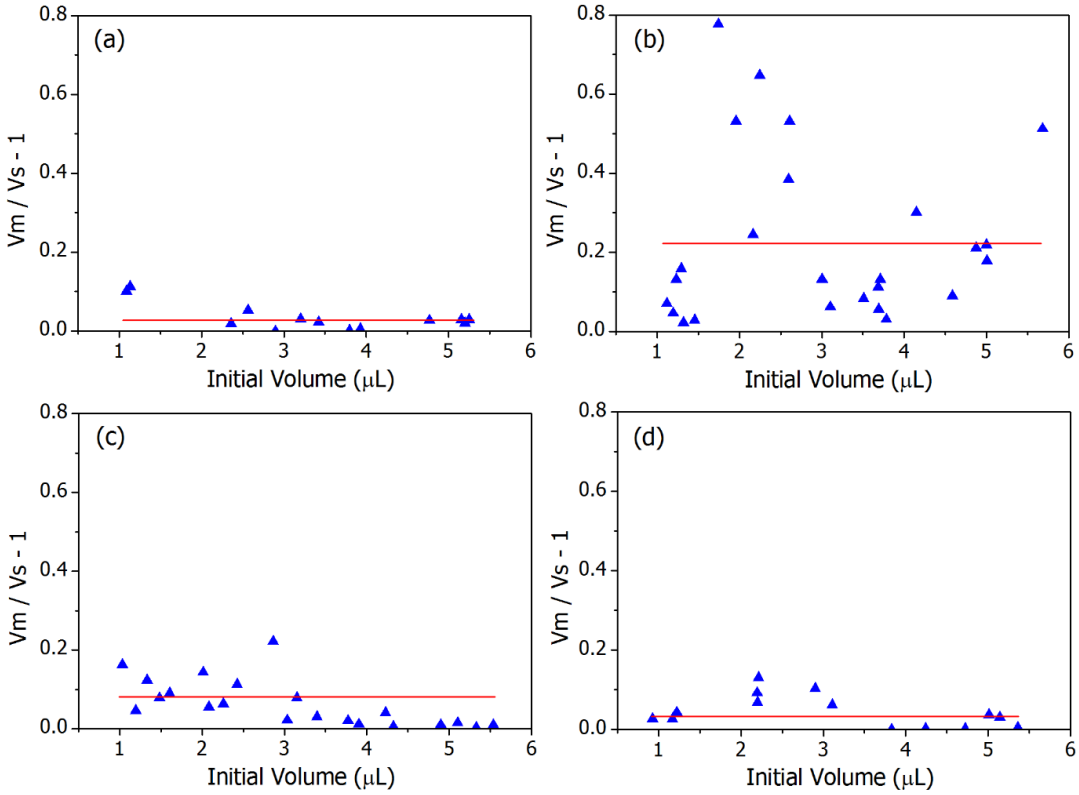


**Figure 4.4-3** Void fraction calculations for the four different molecular weights (a, 10k; b, 100k; c, 200k; and d, 300k g/mol) of the 10% wt. PEO droplets plotted as a function of the initial droplet volume (μL). Note that the values which are closer to the zero line indicate fewer voids than in other cases. The horizontal red line signifies the average value for each molecular weight.

## 4.5 PEO Droplet Evaporation on PEO Films

### 4.5.1 Characterization of PEO films

A series of additional experiments were carried out to investigate the effect of interfacial interactions at the vicinity of the contact line for the characteristic case of the highest molecular weight: $M_w$ = 300 000 g/mol, as it was observed to produce only puddle-shaped final deposits. PEO films were prepared by casting PEO solutions 10% by mass and left to dry out onto the borosilicate glass coverslips. The molecular weights used to prepare the 10% wt. PEO films were 10 000 and 100 000 g/mol and with a wide range of PEO thicknesses from ~20 nm to ~280 μm, respectively. The thickness of the films was measured by taking profiles and/or images at the edge of the films and/or over areas where the polymer layer was scratched using a thin scriber. The films were continuous apart from the very thin ones (~20 nm thickness) where in some areas the film broke and the substrate (glass our case) was revealed. Acquired PEO film images were post-processed and analysed using Gwyddion software [198] (discussed in Chapter 3.2). It is worthwhile noting that in the case of the PEO solution droplet deposition on the PEO films, there was an initial spreading time period, for a few tens or hundreds of seconds depending on the two molecular weight used, until pinning at about 25−55°. For the thinner PEO films, the thickness range was found to be from ~20 nm to ~4 μm and this was associated with the observed lower pinned contact angles at about 25−35°. On the other hand, the thicker films thickness was in a range from ~30 to ~280 μm and the obtained pinned contact angles were at about 35−55°.

Figure 4.5-1 shows experimental results obtained from the surface profilometry tester which point out characteristic measurements for the thickness of the PEO films were used in this experimental work. The first row of the graph refers to 10% wt. PEO absorbed films with 10k (g/mol) molecular weight and the second presents 10% wt. PEO films with 100k (g/mol) molecular weight. The thickness ranges that PEO droplets with 300k (g/mol) $M_w$ form pillars were above ~130 to ~290 microns on the 10k (g/mol) PEO films and for the PEO films with 100k (g/mol) the limit was from around 30 to 220 microns height.

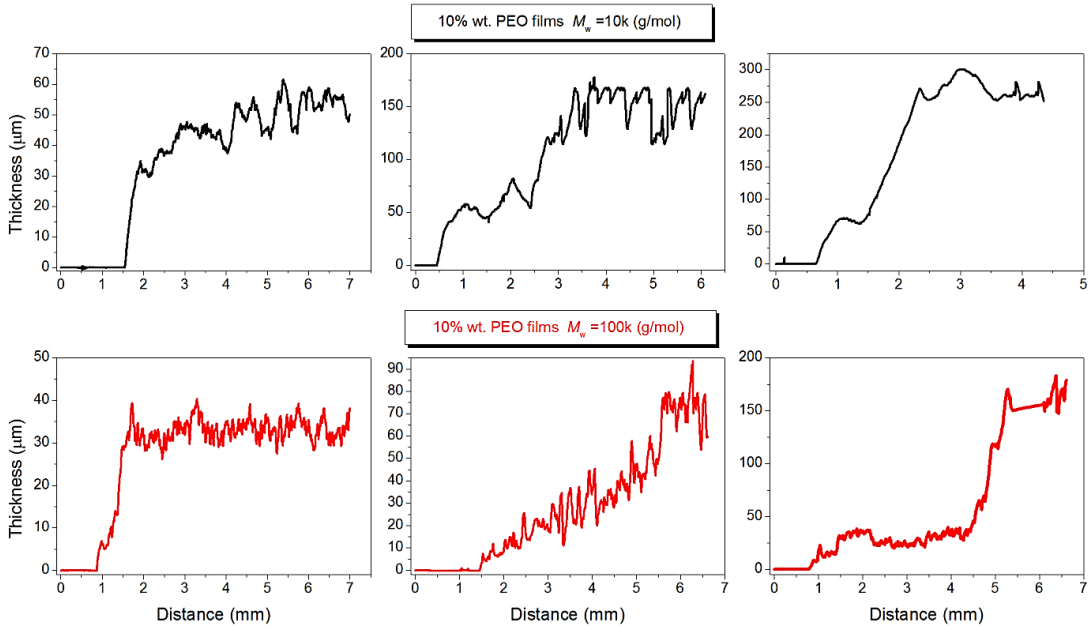


**Figure 4.5-1** Plot of representative 10% wt. PEO films thicknesses ranges (μm) (~15 repetitions of each $M_w$) of 10k (black curves) and 100k (red curves) (g/mol) molecular weight over a scan distance (mm), under ambient experimental conditions.

Figure 4.5-2 and 4.5-3 depict representative results i.e. images and measurements, obtained for the various 10K (g/mol) PEO films with initial concentration $c_0$ = 0.1 and 0.01 (by mass) that were used in ours experiments, respectively. The thickness of the 1% wt. PEO films (Figure 4.5-2) was found to be around ~20 nanometres and for the case of 10% wt. PEO films (Figure 4.5-3), the height of the film was measured around 2.5 microns.

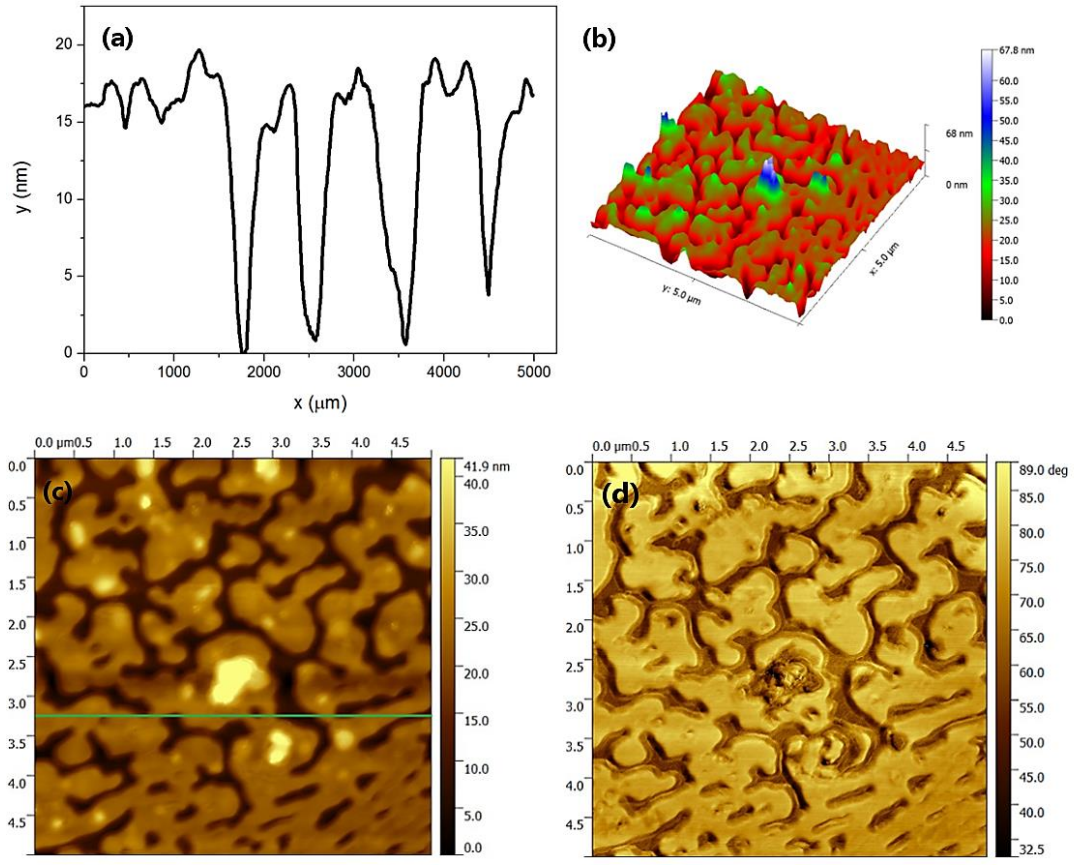


**Figure 4.5-2** Typical example of PEO 1% wt. film with 10k (g/mol) molecular weight: (a) height profile, (b) 3D view image topography, (c) topography image and (d) phase image.

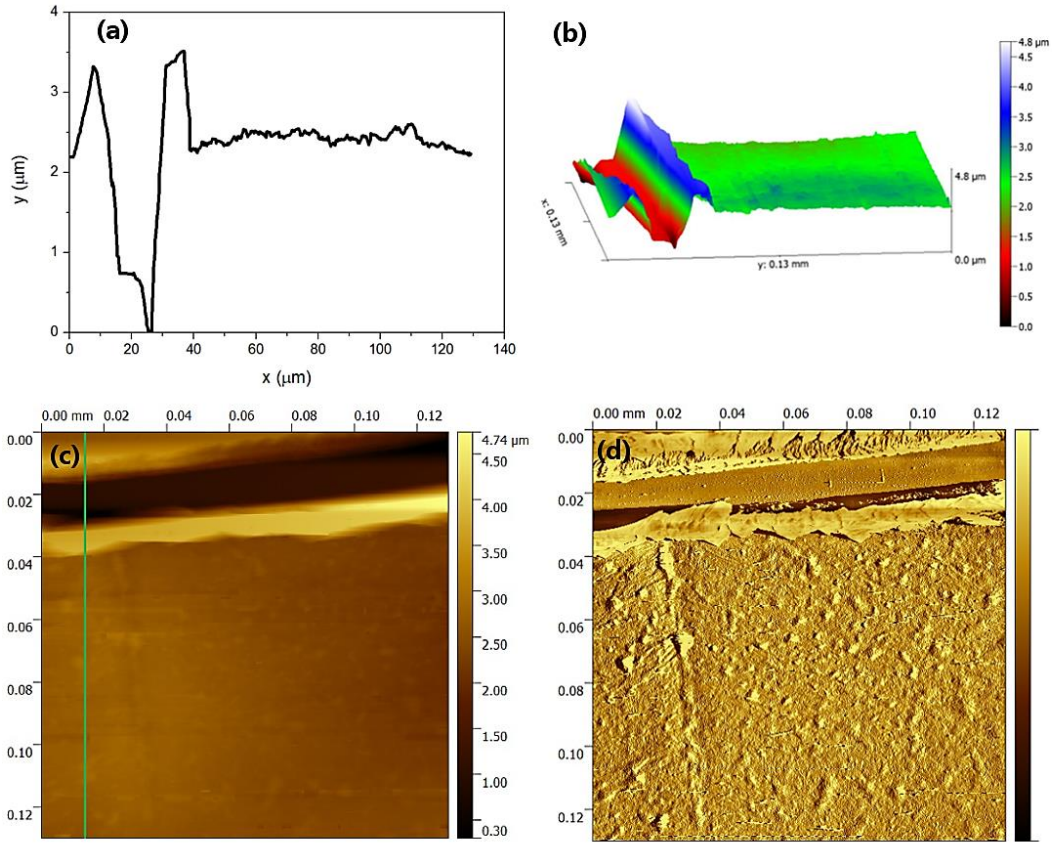


**Figure 4.5-3** Representative example of PEO 10% wt. film with 10k (g/mol) molecular weight: (a) height profile, (b) 3D view image topography, (c) topography image and (d) amplitude image.

Figure 4.5-4 shows characteristic topography surface images which were extracted from the AFM apparatus, for the 10% wt. PEO films with 100k $M_w$ deposited onto the glass slides. It is clearly depicted the formation and the grain boundaries of the PEO spherulites after complete evaporation (Figure 4.5-4).

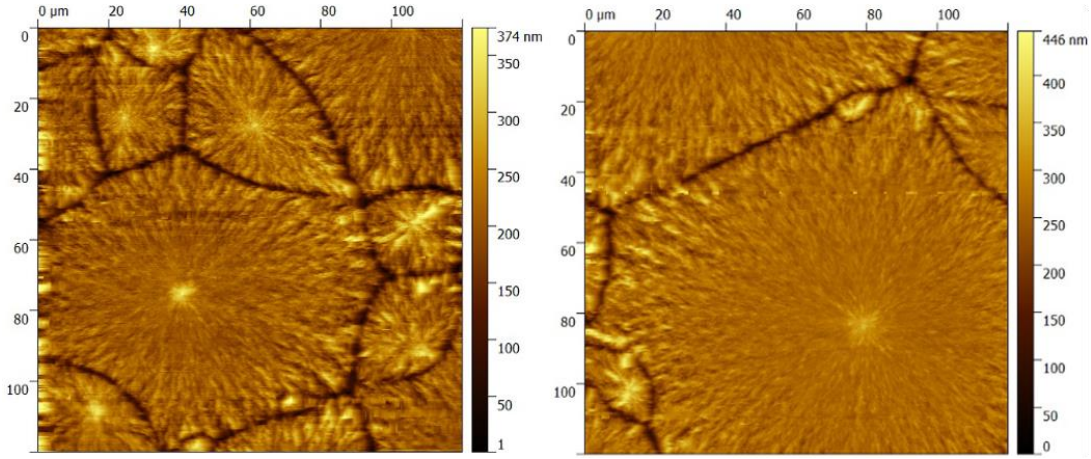


**Figure 4.5-4** Representative topography film surface images where the presence of the PEO semi-crystalline spherulites can be clearly observed of the 10% wt. PEO film with $M_w$ = 100k.

In what follows, typical examples of PEO films with 100k $M_w$ absorbed onto the glass slides can be seen in Figure 4.5-5 and 4.5-6 . The results obtained from AFM apparatus for the 1% wt. PEO films with 100k $M_w$ (Figure 4.5-5) gave thickness ranges around ~1 µm and for the case of 10% wt. PEO films (Figure 4.5-6) the thickness was measured around ~ 4 microns.

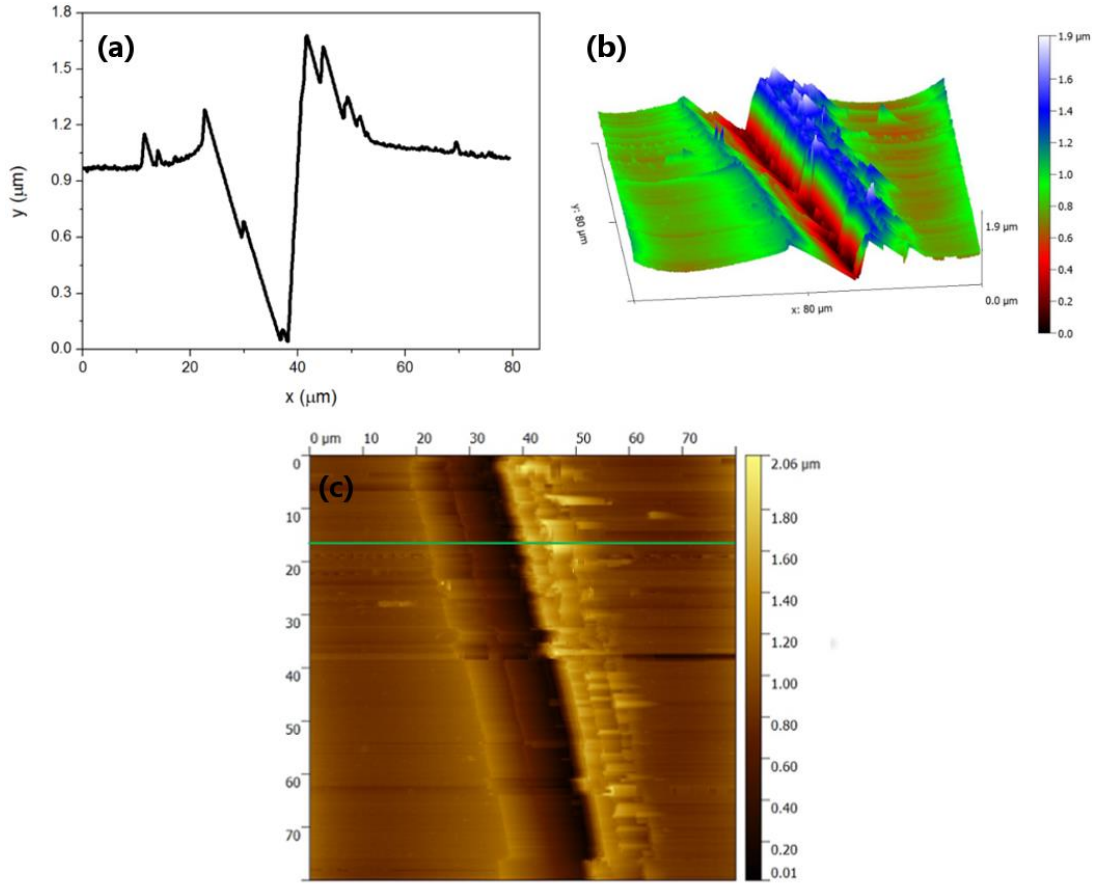


**Figure 4.5-5** Typical example of PEO 10% wt. film with 100k (g/mol) molecular weight: (a) height profile, (b) 3D view image topography, (c) topography image.

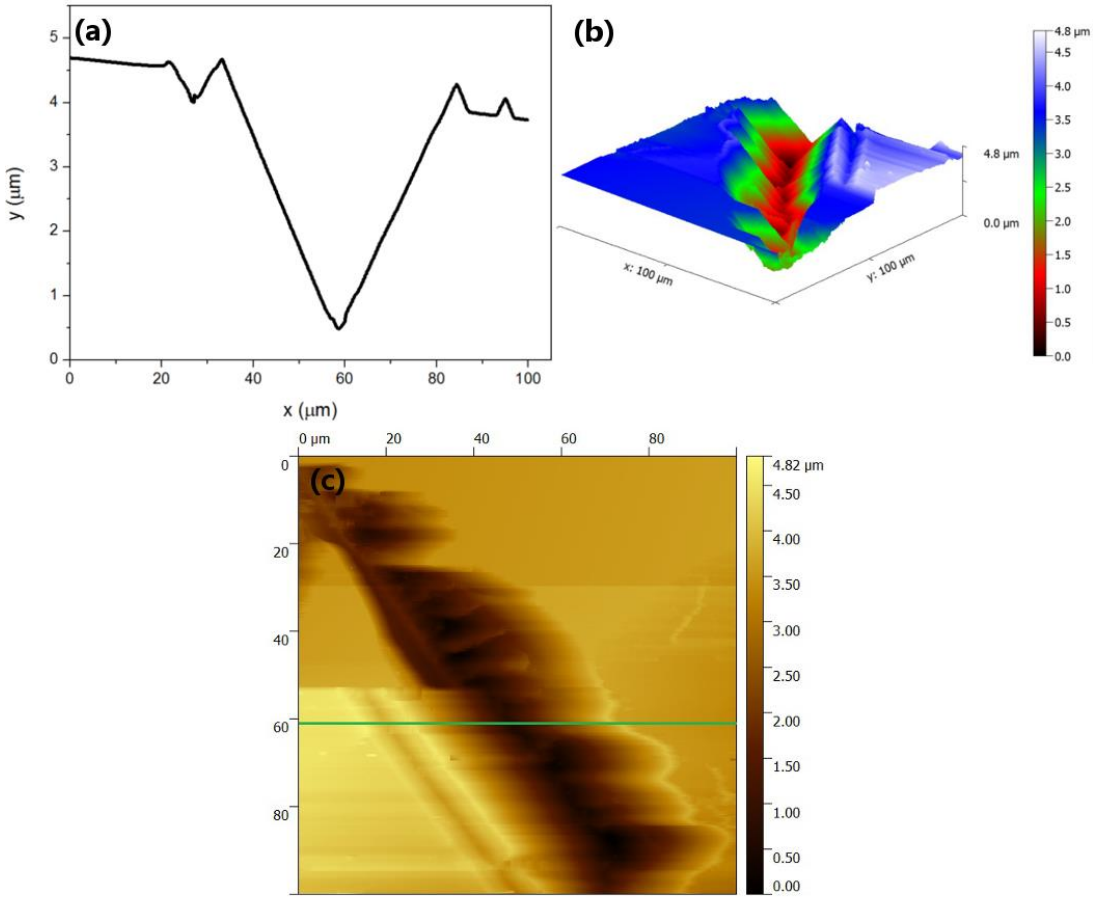


**Figure 4.5-6** Representative example of PEO 10% wt. film with 10k (g/mol) molecular weight: (a) height profile, (b) 3D view image topography, (c) topography image.

## 4.5.2 Pillar formation on PEO films

Following the above finding about the characterization of the prepared PEO films on glass slides, Figure 4.5-7 shows typical examples obtained for the 300 000 g/mol 10% wt. PEO droplet case with volumes ranging from around 4 to 5 µL (more than five experiments were performed for each thickness) after the complete evaporation process on substrates covered with a PEO film. Note that the PEO films were casted by 10% by mass PEO solutions and dried out on borosilicate glass coverslips. The molecular weights used to prepare the 10% wt. PEO films were 10 000 and 100 000 g/mol $M_w$ and thicknesses from 200 - 250 microns. Interestingly, in both case, the 300 000 g/mol (10% wt.) PEO sessile droplet dried out on the (10% wt.) PEO films,

resulting in pillar formation final morphology. The acquired aspect ratios for these experiments were in the range from 0.2 to 0.4.

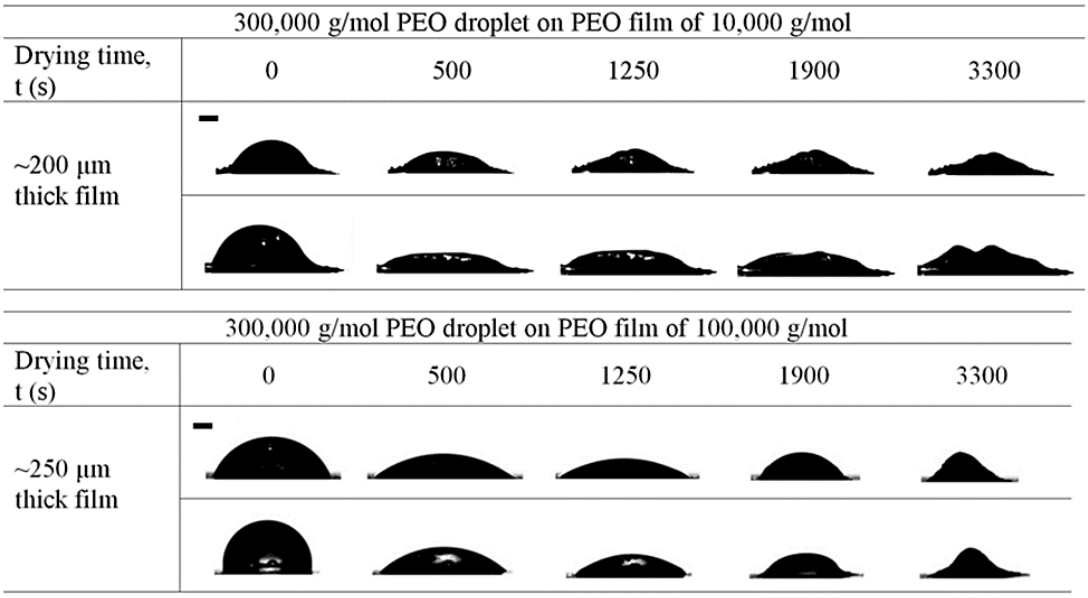


**Figure 4.5-7** Representative examples of time lapse drying profile images of 300 000 g/mol PEO droplets, from ~4 µL to ~5 µL volumes, with initial concentration $c_0$ = 0.1 by mass, placed on PEO films of 10 000 g/mol (above) and 100 000 g/mol (below), during the whole drying process under ambient controlled experimental conditions. The scale bar depicts a width of 0.5 mm. Note that the times presented are approximate.

Figure 4.5-8 shows contact angle $\theta$ and base radius $r$ droplet evolution profiles during the whole evaporation process, for the two cases, presented in Figure 4.5-7. Initially, when the sessile droplet contacted the PEO film there was a spreading time period, and following this, there was a time interval where the PEO droplet adapted an approximately pinned contact line behaviour. This prior stage of spreading was more pronounced for the case of PEO films with $M_w$ = 100 000 g/mol as displayed in Figure 4.5-8 (b). Remarkably, the depinning (II) and the bootstrap growth (III) drying stages took place at the same time (both cases) with a receding contact line and an increasing contact angle $\theta$ (and height $h$), respectively. In the previous work of Baldwin *et al.* reported that pillar formation was inhibited by characteristic low equilibrium contact angles $\theta_0$, even for favourable case with $M_w$ = 100 000 g/mol, where high pillar

formation of the 10% wt. PEO material occurred [38]. It is worth noting that in our experiments using PEO films, the pinned contact angles were greater (35−55°) for thicker films, from around 30 − 280 μm. Furthermore, additional experiments have been done with lower thicknesses of the 10 000 and 100 000 g/mol PEO films from ∼20 nm to ∼4 μm. However, in all cases, the samples either ended up in a disklike ‘‘puddle’’ formation or the resulting peaks had a much lower aspect ratio. It should be noted, though, that for such thinner films, the droplets spread more and become pinned at much smaller contact angles (25−35°) compared to both the droplets placed directly on glass slides (60−75°) and to thicker dip-coated PEO films (35−55°). Thus, the absence of pillars in these cases can be associated clearly with the presence of low contact angles, as reported from Baldwin *et al*. [38].

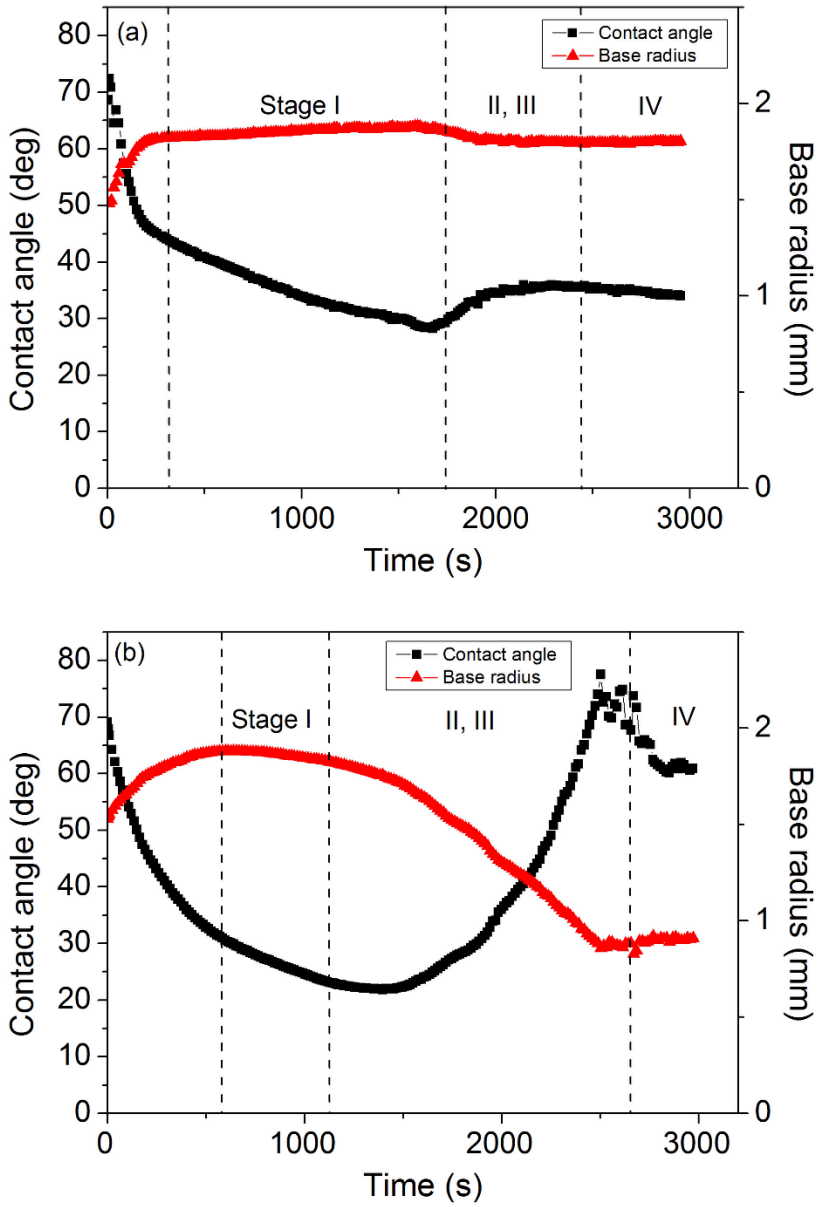


**Figure 4.5-8** Contact angle, $\theta$ (degrees), and base radius profiles, $r$ (mm), against time $t$ (s), for 300 000 g/mol PEO droplets (volumes from ~4 µL to ~5 µL) placed on (a) 10 000 and (b) 100 000 g/mol PEO films, during the evolution of the whole evaporation process (representative examples from approximately five repetitions for each $M_w$). Black squares correspond to contact angle $\theta$ measurements, and red triangles depict base radius $r$ measurements. Note that uncertainties at later times in base radius and contact angle are due to deviations in the shape of the droplet as PEO material is deposited.

## 4.6 Evaporation of PEO Sessile Droplet on PTFE Substrates

To further investigate the role of adhesion and frictions interactions of the PEO droplets with high molecular weight ($M_w$ = 300k g/mol) in the proximity of the contact line, another set of experiments was carried out in this study. In more details, the use of poly(tetrafluoroethylene) (PTFE) substrates to minimize the work of adhesion and friction phenomena was conducted [202, 203]. Figure 4.6-1 presents a typical example of a 10% wt. PEO sessile droplet with $M_w$ = 300k g/mol (performed around 15 repetitions for this substrate) showing the whole evaporation mechanism. The graph shows the time sequence of contact angle $\theta$ and base radius $r$ profiles of a 3 μL PEO droplet. In the beginning, the PEO droplet followed pinned contact line behaviour (stage I) for a small time period. The second stage of drying i.e. depinning, occurred by the decrease in the contact radius, as can be clearly seen in Figure 4.6-1. Stage III (bootstrap growth) followed, with the characteristic increase in the contact angle $\theta$ and height $h$. Finally, the late drying stage occurred, resulting in pillar structure formation of the polymeric material. It is worth observing that the vast majority of the PEO material was dragged toward the centre of the liquid droplet leaving behind a thin trace of PEO material, as can be observed in Figure 4.6-1 (bottom-view image).

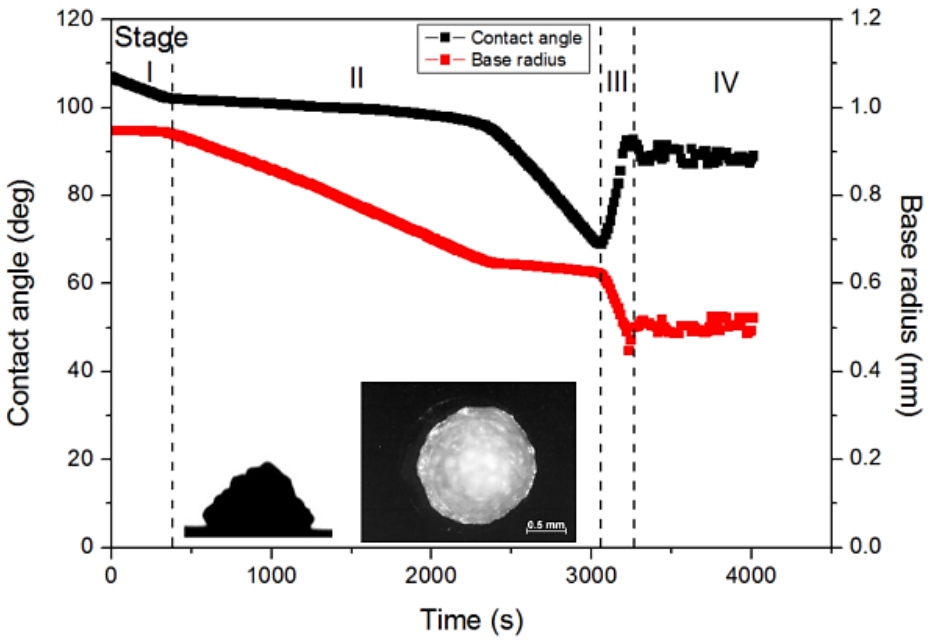


**Figure 4.6-1** Contact angle, $\theta$ (degrees), and base radius profiles, $r$ (mm), versus time (s) for a 3 μL PEO 10% wt. solution droplet of 300 kg/mol molecular weight on a PTFE substrate during the whole evaporation process under ambient conditions. Black squares correspond to the contact angle, and red triangles correspond to base radius measurements. Uncertainties at later times $t$ in the contact angle and base radius are due to deviations in the shape of the droplet as PEO material is deposited. The inset depicts the final PEO deposit extracted from FTA software (side view) and from a stereomicroscope (top view).

## 4.7 Discussion

### 4.7.1 Effect of the molecular weight on PEO deposits

The evaporation of droplets on hydrophilic substrates occurs mainly at the triple contact line (TCL) as stated in the seminal work of Deegan *et al.* [26]. During stage I of the drying process, the local, higher evaporation flux near the pinned contact line, $j$, induces an outward, radial flow to replace the reducing volume of the remaining liquid droplet. Thus, this increases the PEO concentration (ultimately) to $c_{sat}$ locally at TCL. Once the first spherulites have been deposited, the evaporation at the contact line was disturbed, as discussed in Chapter 2, which in turn impeded radial flow and hence depinning occurred. However, diffusion mechanism in the bulk of the fluid opposed this motion which tended to drive the polymer solution to homogeneity. For

this reason, the outward liquid capillary flow, induced by the effect of evaporative flux at the triple contact line, must be greater than the effect of polymer diffusion in order to occur a build-up of polymeric material at the TCL. Previous studies from Baldwin *et al*. [38] showed that the Péclet number: $Pe = \frac{h_0 J}{D_G}$ where $D_G$ is the gradient diffusion coefficient of the polymeric material, and can be used to explain the competition between these opposing trends. A low Péclet number would lead to characteristically small concentration gradients, without preferential deposition at the edge of TCL, and the result would be a puddle-like final PEO deposit [38]. On the other hand, a high Péclet number would result in early crystallization of the polymer at the contact line and would cause a final pillar shaped deposit to occur [38]. The time until $c_{sat}$ was reached at the specific region of the TCL and the liquid droplet depins depends on how quickly polymer chains can move away and accumulate at the contact line and hence depended drastically on the $M_w$ used (polymer chain length). The value of the gradient diffusion coefficient includes a concentration-dependent term [204] which is correlated to $M_w$: $D_G \approx D_0(c^*/c)^{1/2} \approx {M_w}^{-1}$ (for semi-dilute entangled solutions), where $c^* \left(\sim M_w/{R_g}^3 \approx {M_W}^{-4/5}\right)$ is the overlap concentration of the solution, $R_g$ is the radius of gyration, and $D_0$ is the self-diffusion coefficient. Thus, for droplets with low molecular weight in our cases: $M_w$ = 10k g/mol, polymer chains diffused away from the TCL region more quickly and were unable to reach the precipitation concentration sufficiently quickly. They remained pinned for longer time-periods than those with 100 000 g/mol molecular weight (Figure 4.3-1), thus prevented the formation of high pillar. On the other hand, in higher-molecular weight polymers: $M_w$ = 100k g/mol, a drastic decrease in diffusion lead to an earlier accumulation of the polymer chains at the contact line, resulting in early depinning and hence high pillar formation. By extrapolation the latter, one would expect that PEO droplets with $M_w$ = 200k and 300k g/mol would result in easier accumulation at the contact line due to the further decrease in polymer chain diffusion in the bulk of the fluid, leading to even earlier crystallization of the polymeric material and depinning. In turn higher pillar final morphology was expected to occur. Remarkably, this was not seen in our cases; on the contrary, an increase in the pinning times was observed for these droplets, leading to characteristic lower pillars for 200k g/mol and very flat puddles for the case of 300k g/mol. Therefore, another mechanism must have

become dominant in these cases and it is clear from our experimental results that the critical experimental parameter that determined the final morphology was the time period until depinning occurred i.e. the duration of the pinning stage, with a stationary contact line.

### 4.7.2 Surface interactions of the evaporating PEO droplets

Regarding the experiments involving the deposition of PEO droplets with 300 000 g/mol molecular weight on 10 000 or 100 000 g/mol and on PTFE films showed significant differences compared to results obtained on glass slides. These results indicated that the phenomena were taking place at the interface during the evaporation process were of great importance and influenced drastically the final dried morphology of the polymeric material phase. The force balance for fluid−solid systems under dynamic conditions consists of capillary forces, as mentioned above, which were opposed by the friction of the substrate as the fluid advances or recedes during evaporation process. It is well known that for the general case of a solid−liquid−vapour system, the contact line friction was found to increase linearly with liquid viscosity and exponentially with the work of adhesion [205]. As the polymer chain length is a parameter which could essentially modify the adherence energy of the fluid with the substrate and the interfacial dissipation phenomena acting at the contact line. Polymer chains were attracted by the substrate (van der Waals, hydrogen bonds, etc.) and tended to increase the number of monomers in contact with the surface in order to gain adsorption energy, but they were confined and thus lost (conformational) entropy [204, 206]. Therefore, as experimentally verified for the PEO/glass system in particular from previous studies [207-210], large polymer chains adsorb more strongly on solids [211, 212]. When polymers contact a solid surface, an adsorbed layer is formed fairly quickly, even if the bulk solution is dilute [211]. The adsorbed polymer layer thickness depends on the molecular weight and is characterized by a small number of long loops and tails [213, 214] that can extend into the solution and modify the interfacial energy of the system [209, 215, 216]. The loops and tails were more prominent and longer for higher molecular weights used in this study. The frictional stress and the energy of adhesion of a polymer network with an

adsorbed polymer layer were found to increase both with the $M_w$ of the adsorbed layer and the $M_w$ of the chains between the (generated physical and/or chemical) cross-links (with the exception of high grafting densities) [217-221]. The loops and tail ends of the absorbed high- molecular weight polymer chains intertwine with the interconnected polymer network, increasing the (interfacial) adhesion energy of the system [212, 215, 216, 219]. Hence, for sufficiently high molecular weights ($M_w$ = 200k and 300k g/mol), a significant part of the energy of the system is dissipated within this region (contact line) as a result of cohesive interactions and chain entanglements [219]. In our system, for high-$M_w$ PEO liquid droplets, a polymer film with long loops and tails forms fairly quickly on the substrate (glass) and interlaces into the dense polymer network formed within the bulk of the droplet during the evaporation of water. Interestingly, this adhesive effect between the chain network (gel in our case) and the absorbed polymer film inhibits the polymer chain network from moving, and thus depinning could not readily occurred because the dense polymer solution droplet was fixed by the loops and tails of the strongly adsorbed layer. Previous works reported that PEO can adsorb fairly strongly on the glass by hydrogen bonding as already experimentally measured [207-209]. The latter ideas provided us with insight into the possible phenomena in terms of friction, generated at the contact line in our system. These could explain the behaviour of droplets with $M_w$ = 200k and 300k g/mol on glass, where the work of adhesion and the contact line friction was governing the system and control the drying mechanism. The energy dissipation of the system through the enhancement of the frictional resistance at the contact line and the work of adhesion of high molecular weight polymer chains led the system to follow typical pinned behaviour for long times and in particular for the highest $M_w$ = 300k g/mol of this study during the whole evaporation process. Opposing to this motion, for droplets with $M_w$ = 10k and 100k g/mol, these interface phenomena were not pronounced enough to influence drastically the crucial pinning stage and hence the depinning transition due to the relatively small molecular weight. Presumably, in our experiments for the droplets on glass, the minimum in the pinning time exists around $M_w$ = 100k g/ mol (Figure 4.3-1) where the two effects i.e. bulk diffusion and interface adhesion, were becoming less prominent and final pillar formation morphology could easily occur. Contrary to the behaviour presented and explained on glass substrates, in the experiments concerning the deposition of the

300k g/mol droplets on 10k or 100k g/mol PEO films, the already preformed film of lower-molecular-weight PEO prevented the adsorption of the long 300k g/mol chains. Thus, interfacial interactions and friction forces were much weaker in these cases. This was further established by the case of the deposition of the 300k g/mol droplets on PTFE films where the interfacial interactions and friction were characteristically lower due to the chemical nature of the PTFE substrate used and was clearly observed the transition from the pinning to depinning and pillar formation to occur.

An another interesting point that demands some attention was the situation of precipitation-induced depinning, as described in previous works [38, 39, 123, 124], in combination with evidence that the precipitation of the higher -molecular weight droplet started first (Figure 4 in ref [39]). Consecutively, this mechanism was not unexpected as there was less diffusion and $c_{sat}$ (~0.6 for all molecular weights) could be reached faster. However, there was no doubt after our study that for higher molecular weights (particularly case of 300k g/mol) the depinning - dewetting (on glass) did not happen. In view of our results and analysis, we can now conclude that precipitation was not a sufficient condition for depinning and dewetting. In addition, the polymer droplet needed to have the necessary "freedom" to move/slide laterally toward the centre of the evaporating droplet. The interdigitation-induced adhesion with the adsorbed polymer layer inhibited the depinning, although precipitation at the contact line occurred earlier. However, for PEO droplets with lower molecular weight (deposited on glass), this interface effect was absent, chains were short and the adsorbed polymer layer did not interdigitate so much with the polymer gel above, and precipitation, although coming later, induced depinning and dewetting stages.

## 4.8 Conclusions

The evaporation mechanism of aqueous semi-dilute (10% wt.) PEO sessile droplets for four different molecular weights has been extensively studied on various substrates varying from hydrophilic to hydrophobic i.e. solid surface of glass coverslips, planar PEO films (formed on glass substrates) and PTFE (formed on a silicon wafer) films. Interestingly, the shape of the final solid PEO deposits on glass slides was found to

depend strongly on the molecular weight, with high pillars favoured for intermediate molecular weights (100k and 200k g/mol) whereas higher molecular weights (300k g/mol) formed flat disklike puddles. In more details, it was further verified that the duration of the pinning stage was crucial to the final morphology of the polymeric deposits. Long pinning times were associated with puddles or low-aspect-ratio final pillar formation. The competition of the phenomena acting at the contact line and in the bulk of the fluid determined the duration of the pinning stage. Diffusion-based arguments, Péclet number, could account for the absence of high pillars for low molecular weights but could not explain puddle formation for high molecular weights.

Our experiments involving high-$M_w$ PEO droplet evaporation on lower-$M_w$ PEO and PTFE films showed pillar formation and demonstrated that interface (polymer/substrate) phenomena could play a major role in the drying mechanism. For high $M_w$, intertwining between the long loops and tails of an adsorbed polymer layer and the polymer gel network in the droplet could induce strong adhesion which retained the droplet in the pinning stage for the entire drying period. This interfacial phenomenon could clearly explain the formation of puddles for the case of high-$M_w$ droplets on glass and might be an important contribution to the physics of the overall behaviour in addition to the Péclet number arguments discussed in previous studies. It seemed particularly crucial to interpreting the results obtained for the case using high-$M_w$ PEO droplets.

# Chapter 5: Non-Isothermal Wetting Dynamics of Self-Rewetting Droplets

Droplet wetting is frequently encountered in our everyday lives but is also relevant to a wide range of applications. Not surprisingly a large number of studies have been devoted to understand the wetting mechanism of droplets in various settings and configurations (e.g. substrate or conditions). In the previous chapters, we focused on examining the drying behaviour of aqueous PEO sessile droplets with varying molecular weights and the role of interface phenomena that have a drastic effect on the final morphology of the PEO dried deposits. In this chapter, we experimentally investigate the initial spreading dynamics of pure liquids and binary alcohol mixtures (self-rewetting fluids), under controlled non-isothermal conditions of the liquids and the substrates. More specifically, we show that the spreading mechanism of an evaporating droplet exhibit a power law growth with early-stage exponents that depend strongly and non-monotonically on substrate temperature (heated). Moreover, an analysis on the temporal and spatial thermal dynamics at the interface of spreading-evaporating droplet was carried out. Using infrared thermography, the existence of characteristic thermal patterns due to thermal and/or solutal instabilities which lead to surface tension gradients (Marangoni effect) was observed and analysed. The temperature of the substrate was found to drastically affect the early-stage inertial-capillary spreading regime in connection with the anomalous surface tension/temperature dependence of the self-rewetting liquids (discussed in Chapter 2.7). Continuing the efforts to understand the short-time contact line dynamics of a droplet when contacts on a solid surface and the contribution of the surface tension forces generate in the system, a number of experiments on an inclined solid substrate were performed. In more details, we investigated the thermocapillary (Marangoni effect) migration of a self-rewetting droplet on an inclined heated substrate under non-isothermal conditions which was sliding ‘‘freely’’ on silicone oil layer. The importance of strong surface tension gradients and the contribution of Marangoni effect accompanied with the deformation the sliding-spreading droplets was examined. The underlying mechanisms for these phenomena, at contact line and internal flows generate within the evaporating-spreading droplets are still under investigation and are recognised as crucial in a wide range of biological, natural and industrial applications.

## 5.1 Spreading of Liquids and Surface Tension Dependence

The first step in our experiments was to compare the complete spreading behaviour of the pure liquids: (a) pure water and (b) pure 1-butanol, with those of the dilute aqueous solutions of high carbon number alcohols: (c) water – 1-butanol 5% vol. and (d) water – 1-pentanol 2% vol., deposited onto a borosilicate glass coverslip, under controlled experimental conditions. Their wetting mechanism evolution was captured using a FTÅ200 apparatus (drop shape analysis, Chapter 3.2) and post-processed with the accompanying software. Figure 5.1-1 presents the sessile droplet contact base radius $r$ changes i.e. the difference between the final, $r_{max}$ (at equilibrium contact angle, $\theta_{eq}$) and initial value, $r_0$, for three different temperatures: 30, 60 and 90 $^{o}$C, in a volume range from ~1 to ~5.5 μL, onto the uniformly heated glass substrate. Note that the obtained values represent typical examples i.e. among six or more repetitions for each droplet volume and for each temperature, of all measurements were carried out. Pure liquids base radius changes followed a linear increase with temperature (Figure 5.1-1 a, b), contrary to the alcohol binary mixtures where the anomalous (non-linear) dependence of the wetted contact radius with the temperature was clearly revealed in our results as can be observed in Figure 5.1-1 (c) and (d).

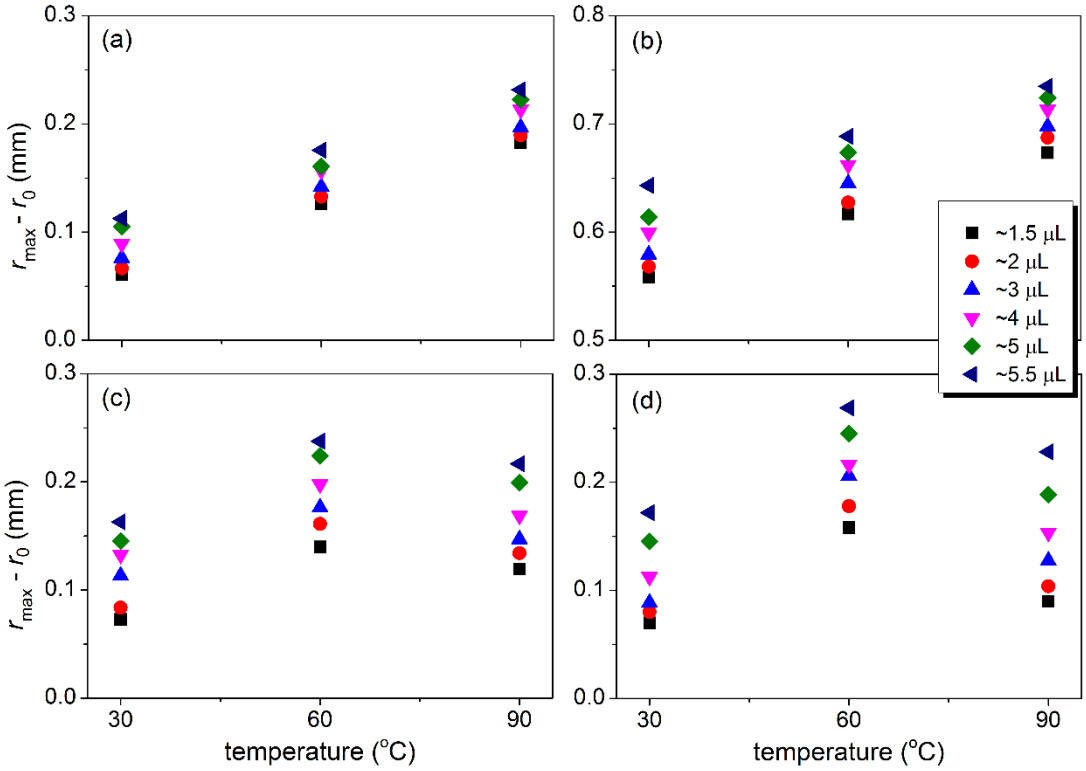


**Figure 5.1-1** Droplet contact radius change (difference between the final, $r_{max}$, and initial, $r_0$, contact base radius for pure liquids, five or more repetitions for each case: (a) pure water, (b) pure butanol and binary mixtures: (c) water – 1-butanol 5% vol. and (d) water – 1-pentanol 2% vol., with volumes: ~1(■), ~2(●), ~3(▲), ~4(▼), ~5(◆) and ~5.5(◀) µL, against the three different temperatures: 30, 60 and 90 °C, on a uniformly heated glass substrate, under ambient experimental conditions.

The surface tension of the ordinary liquids: pure water and pure 1-butanol, and the self-rewetting fluids (i.e. water – 1-butanol 5% vol. and water – 1-pentanol 2% vol.) have been measured in the temperature range from ~10° to ~90° C, using the pendant drop method analysis, FTÅ apparatus. Typical results obtained from the measurements are shown in Figure 5.1-2 where it is clearly depicted the linear decrease of the surface tension of the pure liquids with increasing temperature (Figure 5.1-2 a). However, the non-linear (parabolic) dependence of the surface tension of the self-rewetting droplets with the temperature in a range from ~10 to ~90 °C, as displayed in Figure 5.1-2 b. The minimum of the surface tension was measured at around 63 ±1 °C and the unusual temperature dependence which turns out to be increasing in the higher temperature region beyond the minimum for these self-rewetting solutions was revealed. Consequently, the surface tension measurements

showed good agreement with previous work that have been reported from previous experimental studies using these binary alcohol mixtures [45, 48].

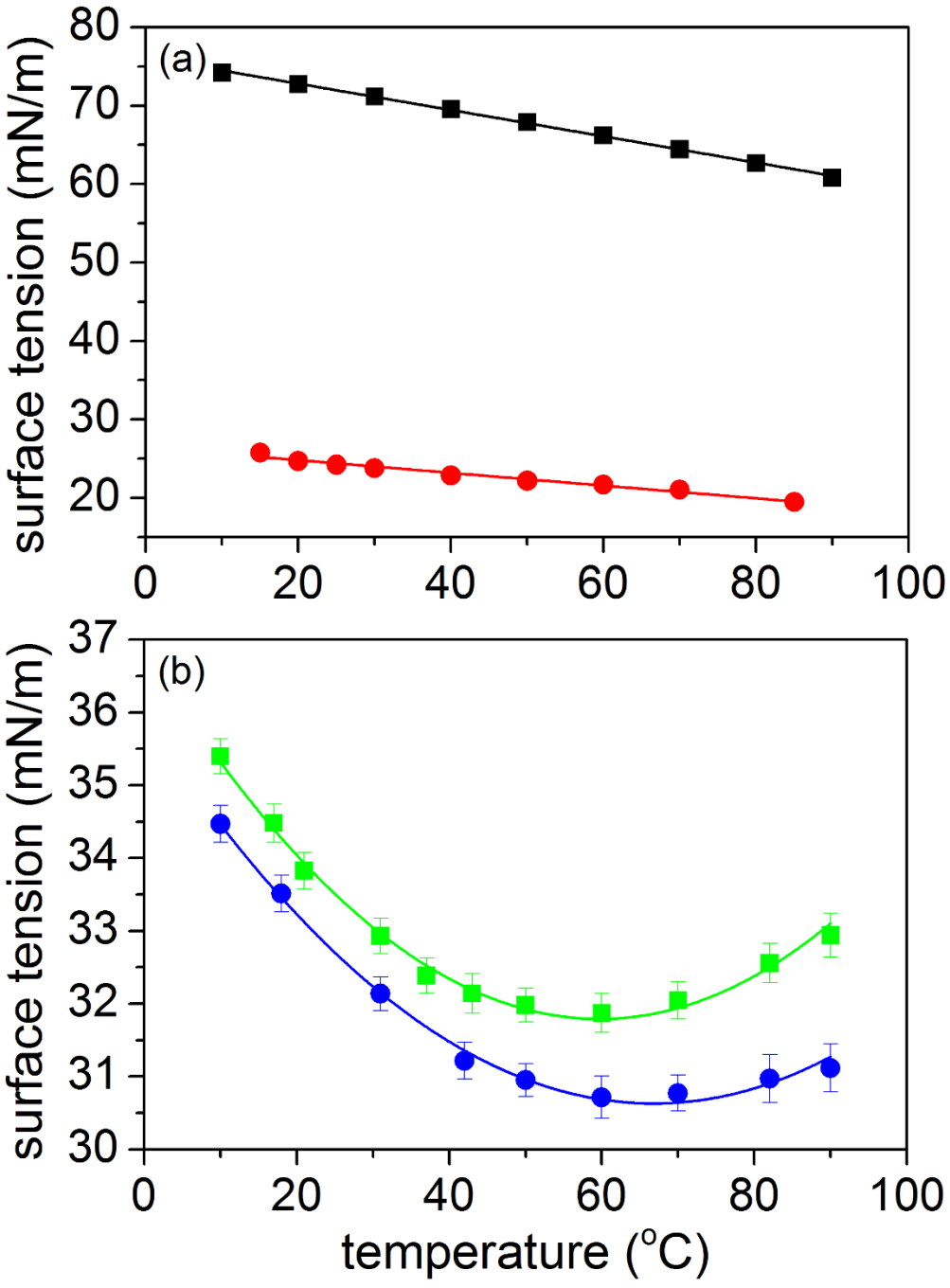


**Figure 5.1-2** Surface tension measurements (mN/m) of the (a) pure liquids: pure water (■) and pure 1-butanol (●) and for the (b) self-rewetting fluids: water – 1-butanol 5% vol. (■) and water – 1-pentanol 2% vol. (●), in the temperature range from 10 – 90 °C, under controlled experimental conditions. Note that the curves represent average values with obtained errors (among six or more repetitions for each temperature) of all measurements were carried out.

## 5.2 Wetting Stages and Spreading Exponents

The spreading contact base radius *r* (t) of the binary alcohol sessile droplets at the early stage (tenths of second) of spreading for a range of volumes from ~1 to ~5 μL was systematically measured using contact angle and shape analyser (FTÅ apparatus). Representative results of the wetting dynamics onto a glass slides of the binary self-rewetting droplets with volumes: 2 and 4 μL, for three different temperatures 30, 60 and 90 $^{o}$C (on the uniformly heated substrate), are presented in Figure 5.2-1. These results showed how the wetted radius *r* of the alcohol mixtures grows over time *t*, once a self-rewetting sessile droplet contacted onto the uniformly heated substrate; this early stage regime is usually dominated by inertia-viscous contributions. The results demonstrated that for each temperature of the (glass) substrate, alcohol binary droplets spread in a different speed rate. In particular, for 90$^{o}$C, alcohol droplets show increased wetting kinetics reaching a maximum radius much quicker than other cases. At around 60$^{o}$C, the binary droplets spread much more than at other substrate temperatures which was consistent with the surface tension minimum (about 63±1 $^{o}$C) shown previously in Figure 5.1-2. It was clear that during this early-time-period of droplet spreading the dominance of the surface tension forces in the system, as reported in previous studies [85, 86, 88]

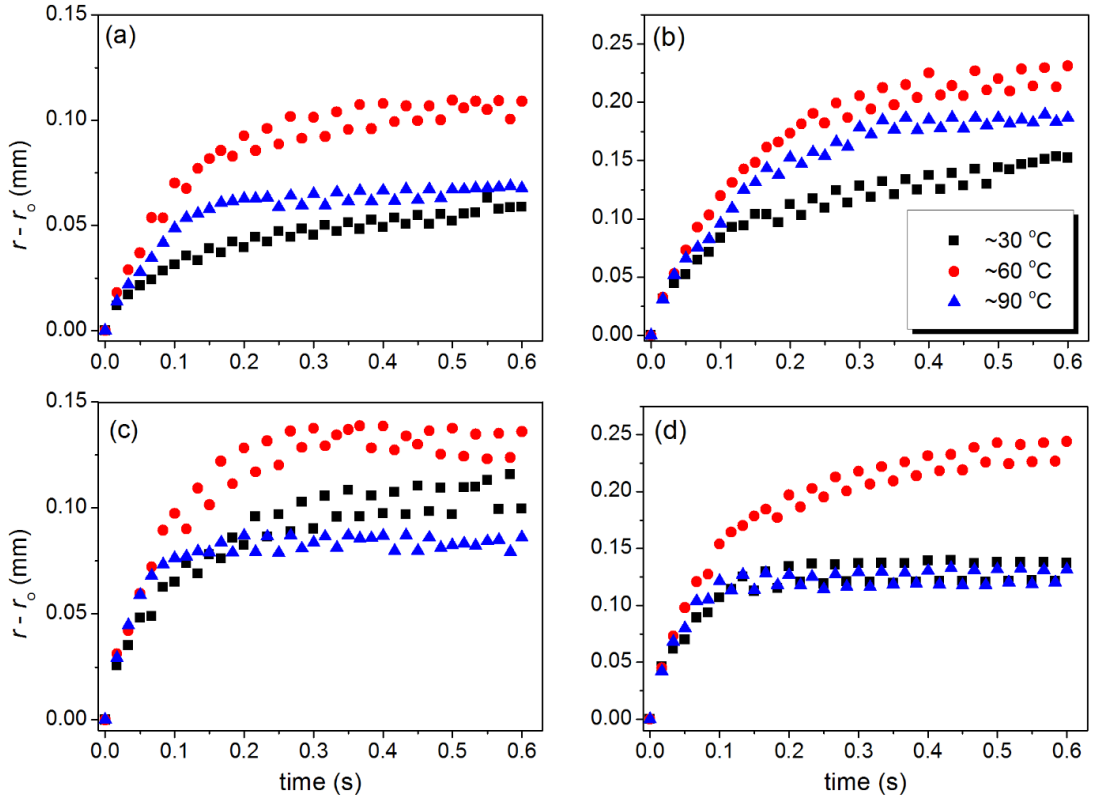


**Figure 5.2-1** Evolution of the contact radius $r$ (mm) of the wetted area for water – 1-butanol 5% vol. droplets: (a) ~2 μL, (b) ~4 μL and for water – 1-pentanol 2% vol. (c) ~2 μL and (d) ~4 μL as a function of time $t$ (s), for the three different temperatures: 30 (■), 60 (●) and 90 °C (▲). Note that the obtained curves represent typical examples (among six or more repetitions for each droplet volume and for each temperature) of all measurements were carried out. Fluctuations observed in wetted radius $r$ measurements are due to the FTÅ apparatus errors, around 2%.

Following the above finding about the wetting behaviour of the self-rewetting droplets on glass slides and the underlying spreading stages, a further analysis focusing on the profile of each stage of wetting was conducted in this experimental work. Figure 5.2-2 depicts log-log plots (both binary alcohol mixtures used, for four temperatures) of the contact line dynamics showing that the spreading occurred in two characteristic stages i.e. inertia and viscous spreading regimes [84-88]. The unbalanced horizontal force: $\gamma(\cos\theta - \cos\theta_{eq})$ drives the droplet to spread on the substrate until it reaches the final equilibrium contact angle $\theta_{eq}$, where $\gamma$ is the liquid-vapour interface surface tension (at specific temperature) and $\theta$ the instantaneous contact angle [84-88]. It can

be clearly seen that once the liquid droplet has established contact with the surface, the extension of the contact line radius $r(t)$ follows an exponential power-law ($r - r_o \sim t^n$) of rapid growth, for all the experiments have been performed. In both graphs, Figure 5.2-2 (a) and (b), the power law-growth had an exponent $n$ which depended on the substrate temperature $T$ (see insets in Figure 5.2-2). These spreading exponents $n$ demonstrated the spreading droplet kinetics on the heated substrate at the early times of wetting. The inertia regime lasts only few milliseconds and the characteristic inertia time scale is $\tau_\rho \sim \sqrt{\rho R^3/\gamma}$, where $R$ is the initial droplet radius before contact and $\rho$ is the liquid density [84, 85, 89, 90]. In this first inertial-capillary dominated stage of wetting, for water-butanol 5% vol. droplets the obtained exponent $\boldsymbol{n_{1st}}$ (first stage) varied as (see also inset in Figure 5.2-2 (a)):

| **exponent $n_{1st}$** | **temperature** |
|---|---|
| ~0.48 | ~20°C |
| ~0.52 | ~30°C |
| ~0.71 | ~60°C |
| ~0.69 | ~90°C |

For the water-pentanol 2% vol. mixtures the power law exponent $\boldsymbol{n_{1st}}$ varied as (see also inset in Figure 5.2-2 (b)):

| **exponent $n_{1st}$** | **temperature** |
|---|---|
| ~0.48 | ~20°C |
| ~0.51 | ~30°C |
| ~0.62 | ~60°C |
| ~0.58 | ~90°C |

It is worthwhile noting the existence of a local maximum in the $\boldsymbol{n_{1st}}$ exponent, in both the binary alcohol mixtures at temperature around 61°C (Figure 5.1-2). Our experiments showed that these early-stage spreading-exponents dependence on temperature to be robust and consistent with the surface tension dependence on temperature (Figure 5.1-2) in agreement with previous studies for pure liquid droplets [89, 90]. Furthermore, it is clearly depicted that at the later times of spreading, characteristic slow wetting dynamics, the $\boldsymbol{n_{2nd}}$ (second stage) power-law exponent was

approximately 0.1 as the system was dominated by viscous-capillary forces and followed the well-known Tanner's law following as: $r - r_o \sim t^{1/10}$ [92]. Another important feature was the presence of a transition regime in the spreading profile of the droplets between the first and second stage and corresponded to the shift from inertial to viscous spreading which lasted as long as the capillary wave, generated at contact, became pronounced over the liquid droplet.

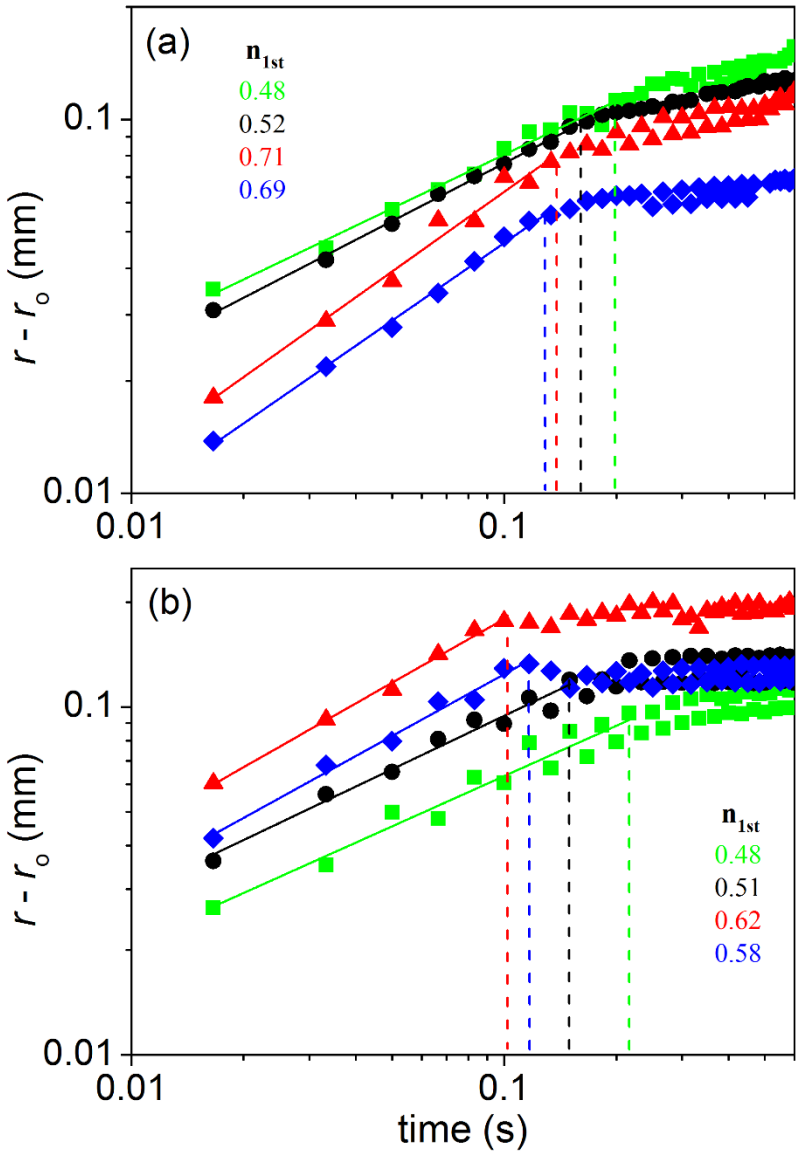


**Figure 5.2-2** log-log plot measurements of the contact radius *r* (mm) plotted as a function of time *t* (s) (volumes ~3 μL) for the four different substrate temperature cases: 20°C (■), 30°C (●), 60°C (▲) and 90°C (◆) for the (a) water – 1-butanol 5% vol. and (b) water – 1-pentanol 2% vol. droplet solutions, respectively. The spreading behaviour follows a power-law (growth) over time ($r - r_o \sim t^n$) with different exponents *n* ($n_{1st}$ for the first stage which

lasts for a period until the dashed lines in each curve). Note that at the later times of spreading (second stage of spreading), slow dynamics with exponent, $n_{2nd} \approx 0.1$, dominates the behaviour and the Tanner's law ($r - r_o \sim t^{0.1}$) governs the wetting mechanism of the self-rewetting droplets. Fluctuations observed in wetted radius *r* measurements are due to the FTÅ apparatus errors, around 2%.

Figure 5.2-3 shows the averages values i.e. five or more repetitions for each case, of the spreading exponents for the pure liquids and the binary alcohol mixtures against the three characteristic substrate temperatures (range of volumes from ~1 to ~5 μL), under controlled non-isothermal conditions, on the uniformly heated glass surfaces. The spreading exponent *n* for the pure liquids increased weakly (and linearly) with increasing temperature in both of the two characteristic stages of spreading, as can be seen in Figure 5.2-3. The behaviour of the exponents of the pure wetting droplets was consistent with the dependence of the surface tension on the temperature and with the argument that surface tension governed and dominated on the short-time wetting dynamics. Binary solutions of alcohols, on the other hand, showed a non-linear dependence with a maximum at around 60±1 $^{o}$C of the spreading exponent *n* with increasing temperature, in the first spontaneous stage of wetting. In the second stage of wetting (Figure 5.2-3 d) alcohol mixture droplets were characterised by slow dynamics (viscous-capillary region) with the characteristic small spreading exponents *n* (~0.1).

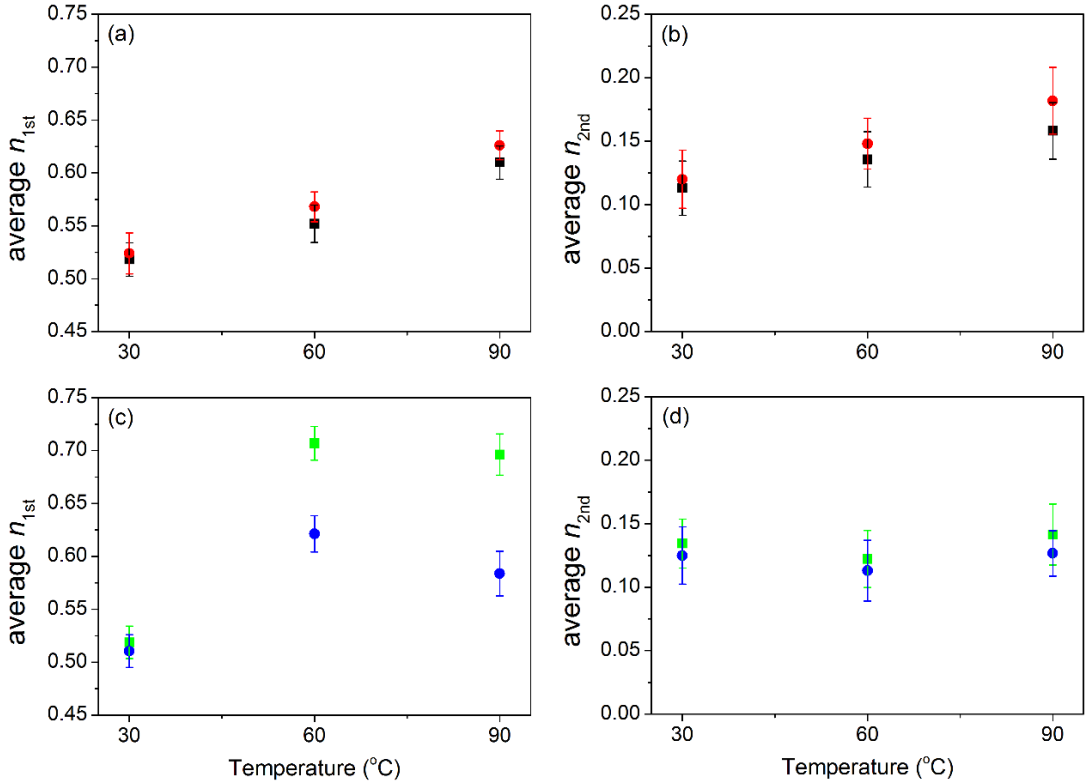


**Figure 5.2-3** Average values (at least five or more repetitions for each case) of the spreading exponents, *n* for the two characteristic stages of wetting versus the three typical substrate temperatures: 30, 60 and 90 °C, for the pure droplets: water (■) and butanol (●) and binary alcohol droplets: water – 1-butanol 5% vol. (■) and water – 1-pentanol 2% (●), under non-isothermal experimental conditions. Note that the error bars obtained among six or more repetitions for each droplet volume and for each temperature of all measurements were performed.

## 5.3 Contact Line Dynamics on the Thermocapillary Motion of a Droplet on an Inclined Substrate

In this section, a systematic study on the motion of sessile self-rewetting droplets over an inclined solid substrate was carried out. The migration of binary alcohol droplets (water-1-butanol 5% vol.) on an inclined heated substrate due to the presence of thermocapillary effects was examined. Experiments consist of depositing droplets of controlled volume (~3 μL) on an inclined (~5 degrees) uniformly heated (around 61 ±1 °C) borosilicate glass substrate which was covered with silicon oil in order to

minimize the contact friction of the substrate before droplet deposition. The droplets should not 'feel' the solid surface, avoiding any chemical inhomogeneities and substrate roughness, and without the pinning behaviour to occur.

Figure 5.3-1 presents time sequence images using a FTÅ200 apparatus (section 3.2) with the accompanying software showing the motion of the sliding sessile droplet on the heated glass slide covered with a silicon oil layer (around 0.2 mm thickness). Interestingly, it can be seen from the obtained images in Figure 5.3-1 that initially the sessile droplet slides and spreads (minimum contact friction, silicone oil layer) due to the action of the gravitational forces. Remarkably, at around $t$ = 0.335 s the sliding-spreading droplet stopped the downward movement and started to climb the inclined heated substrate (some millimetres), against gravity, until $t$ = 0.536 s, where the wetting mechanism of the binary alcohol droplet became more pronounced and the droplet came to a terminal position, as displayed in the sequence images in Figure 5.3-1.

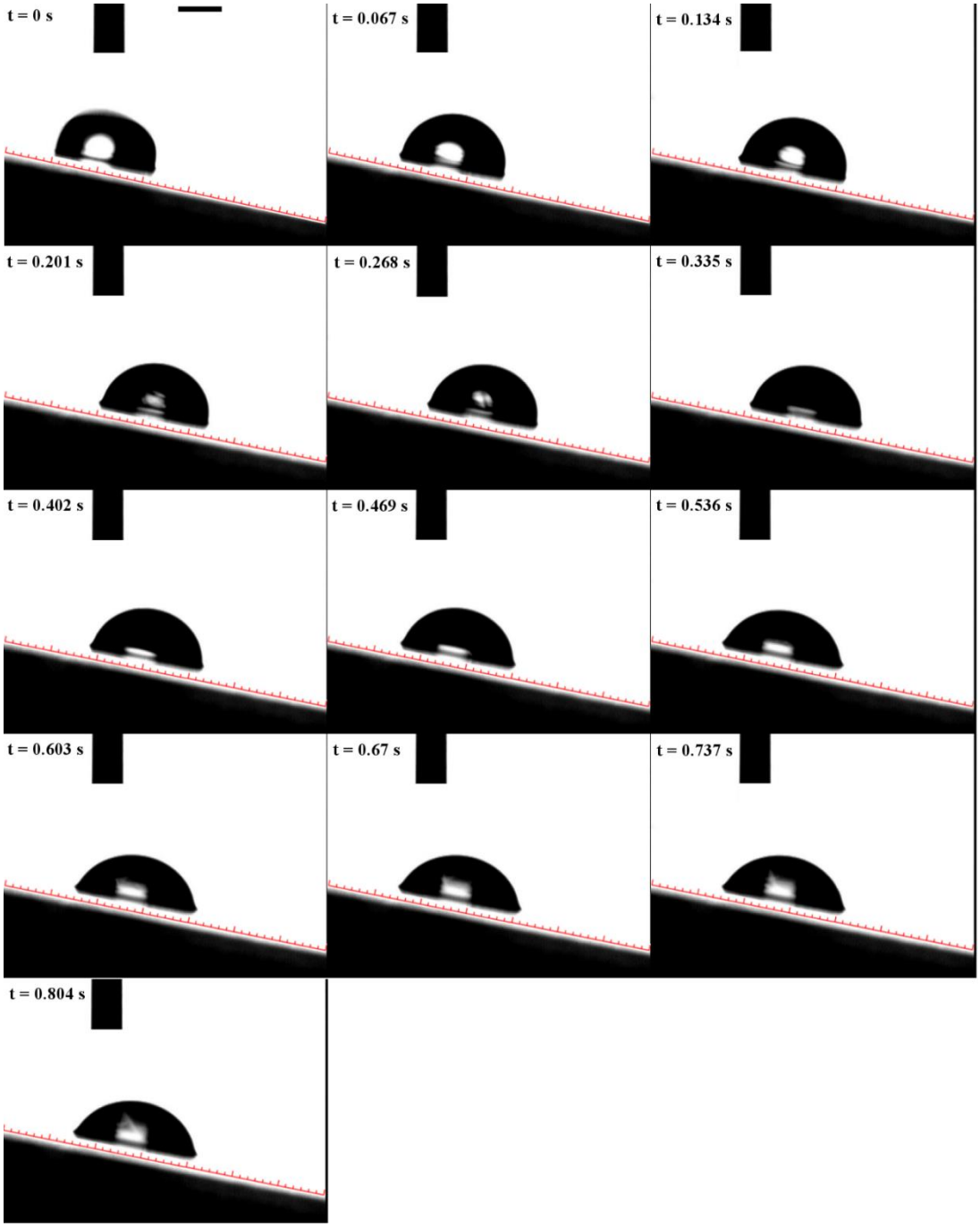


**Figure 5.3-1** Representative time sequence images of a water-1-butanol 5% vol. sliding-spreading sessile droplet (around ~15 repetitions), volume ~4 μL, on an inclined (~5 degrees) uniformly heated (around 61±1 $^{o}$C) borosilicate glass substrate covered with a silicon oil layer (around 0.2 mm thickness) before droplet deposition. The scale bar depicts a width of 1mm, for all images presented.

Following the above finding about the visualization of the binary alcohol sessile droplets motion on an inclined uniformly heated substrate, covered with a silicon oil layer before droplet deposition, results for the spatiotemporal evolution of the droplet shape, the dynamics of the contact lines, and contact angles were generated and analysed using the FTÅ apparatus. Figure 5.3-2 (a) depicts the evolution of the droplet advancing $\theta_a$ and receding $\theta_r$ contact angles against time (see also top view image in Figure 5.3-2). The presence of contact angle hysteresis ($H$) of the droplet was clear and raises the importance of droplet deformation during sliding-spreading behaviour. Additionally, important features that attracted the attention in this study were the velocity and base diameter profiles of the sliding-spreading self-rewetting droplet versus the time, on the heated substrate at temperature of 61±1 $^{o}$C. Figure 5.3-2 (b) presents the velocity and base diameter evolution of the sessile droplet (behaviour as shown in Figure 5.2-1) onto the inclined uniformly heated glass substrate over time, until the droplet reaches a standstill position ($U$ = 0). In more details, the droplet dynamics of each side (2-d profile) i.e. velocity of the right edge (advancing $\theta_a$) and left edge (receding $\theta_r$) of the droplet were individually analysed as it can be seen in Figure 5.3-2 (b). It was clear that the velocity of the right edge ($\theta_a$) was different than the left edge ($\theta_r$) of the droplet and both sides were drastically influenced by the presence of Marangoni stresses (surface tension gradients) during the evolution of the wetting mechanism i.e. inertia regime. Furthermore, in Figure 5.3-2 (b) the plotted evolution of the base diameter of the droplet exhibited a slight spreading behaviour during the downward motion, until $t$ = 0.335 s where the droplet stopped and started to move upward against gravity. After a small oscillation period (~0.1 s) of the base diameter, the droplet spread significantly (during upward motion) until $t$ = 0.536 s (stationary position). The self-rewetting droplet continued to spread at the standstill position until around $t$ = 0.9 s, but clearly with a smaller spreading rate than previously. Figure 5.3-2 (c) depicts log-log plots of the contact line dynamics (wetted area: $r - r_o$) over time $t$, showing that the spreading occurred in three characteristic stages. It is worthwhile noting that the complex behaviour of the deformed self-rewetting droplets, with three distinct stages both sliding and spreading, was clearly associated with the generation of strong surface tension gradients combined with the gravity.

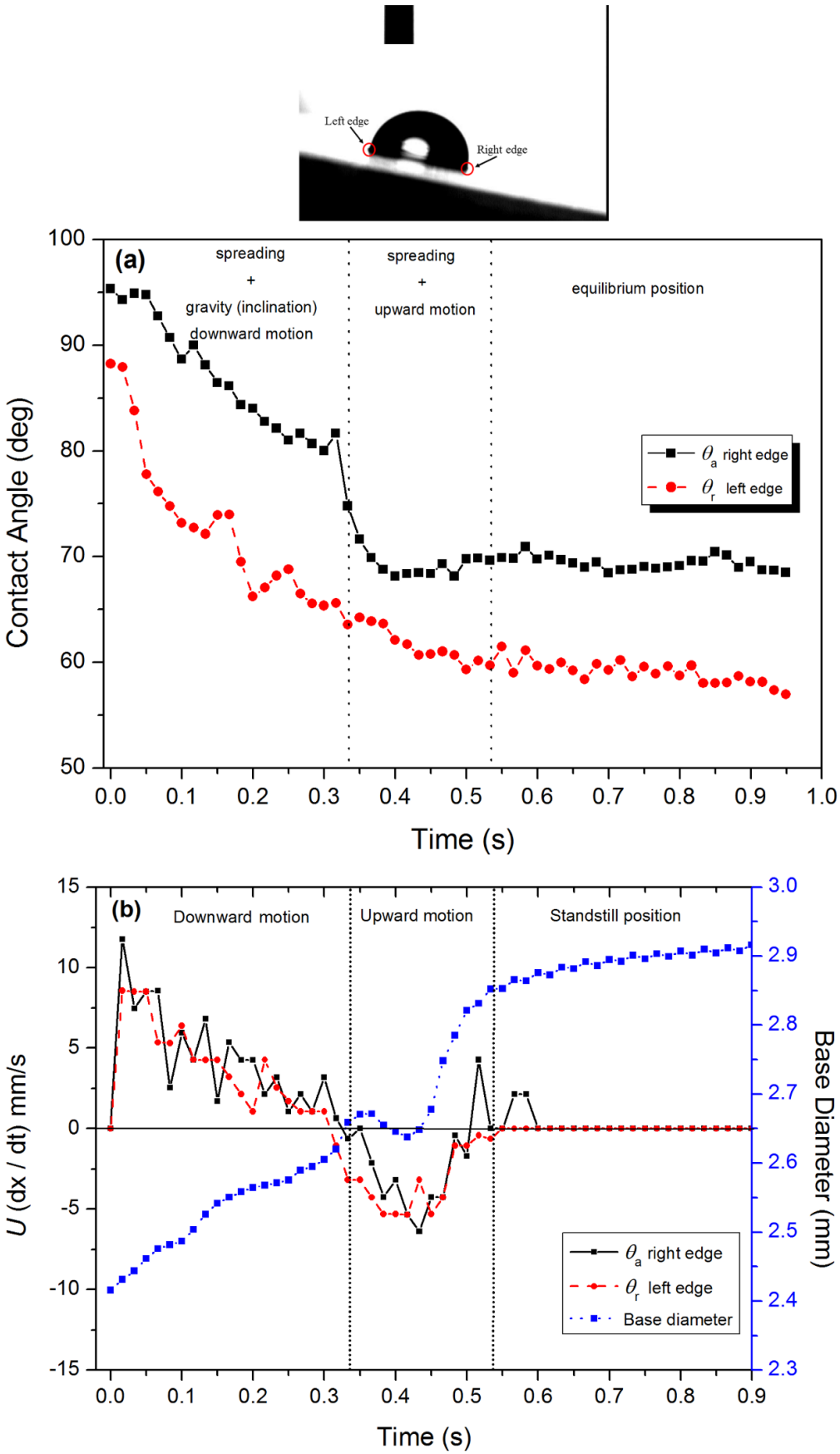
Left edge
Right edge
(a)
spreading
+
gravity (inclination)
downward motion
spreading
+
upward motion
equilibrium position
θa right edge
θr left edge
Contact Angle (deg)
Time (s)
(b)
Downward motion
Upward motion
Standstill position
θa right edge
θr left edge
Base diameter
U (dx / dt) mm/s
Base Diameter (mm)
Time (s)

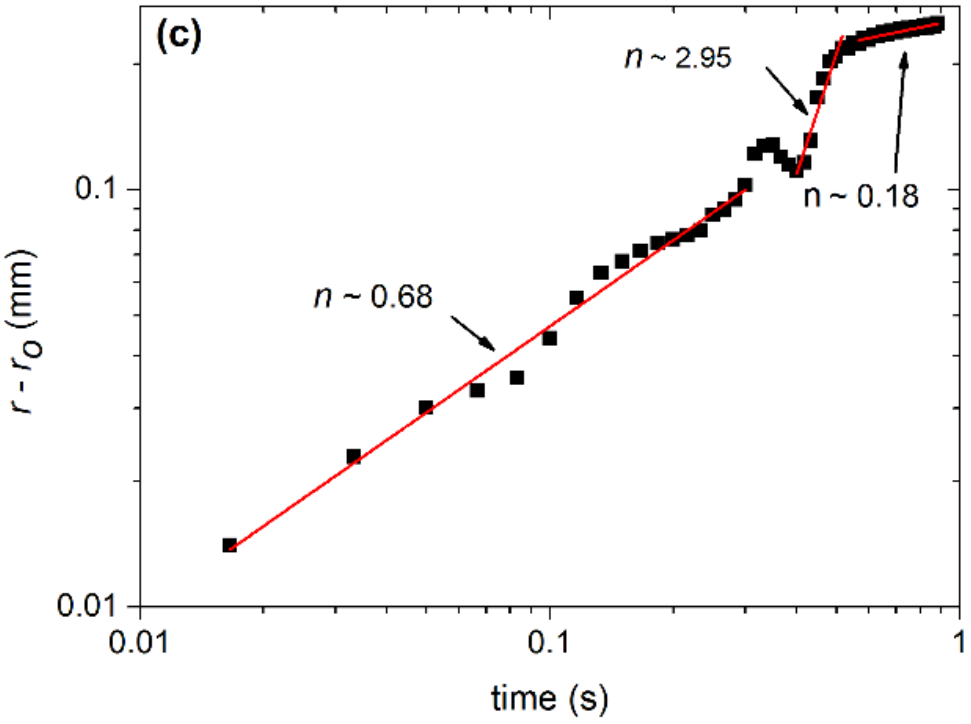


**Figure 5.3-2** Typical example (~13 repetitions) (a) of the advancing $\theta_a$ and receding $\theta_r$ contact angles evolution (b) velocity of the two edges and base diameter profiles over time t, of a water – 1-butanol 5% vol. sliding-spreading sessile droplet (with volume ~4 μL) on an inclined (~5 degrees) uniformly heated (~61±1 ºC) borosilicate glass substrate covered with a silicon oil layer (around 0.2 mm thickness) before droplet deposition. (c) log-log plot measurements of the contact radius *r* (mm) plotted as a function of time *t* (s) and the obtained spreading exponents exponents ( $r - r_o \sim t^n$). Note the schematic drawing on top of the image representing the measured areas (right and left edges of the droplet, respectively). Deviations observed in wetted radius r measurements are due to the FTÅ apparatus errors, around 2%.

## 5.4 Thermal patterns of pure and binary alcohol evaporating droplets

The temperature profiles of the volatile pure (water and 1-butanol) and binary (water-1-butanol) liquid sessile droplets on glass substrates, at various temperatures, were also investigated using IR thermography. The series of experiments consist of depositing droplets of a known volume (from ~1 to ~5 μL) and initial temperature (*T* = 9±1 ºC) on the uniformly heated substrate and recording the interface temperature map profile of the evaporating droplets. Representative infrared temperature profile

images of pure water and pure butanol at substrate temperatures of ~30, ~60 and ~90 $^{o}$C, are presented in Figure 5.4-1 (a) and (b), respectively. In the case of the water droplets the thermal activity was found to be comparatively weaker than those of the pure 1-butanol droplets, as presented in Figure 5.4-1 (a) and (b). This was due to the different physical properties of the liquids, namely the surface tension.

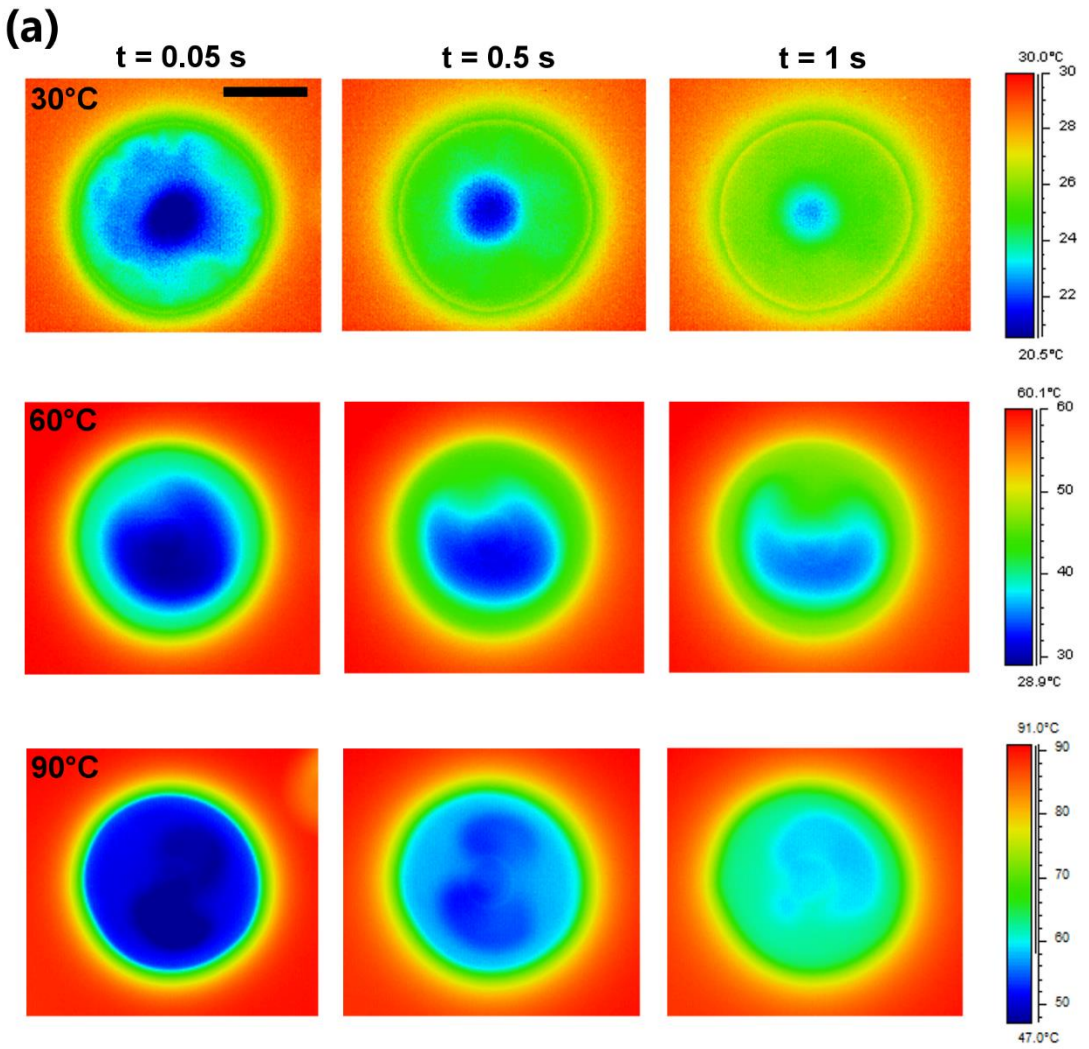

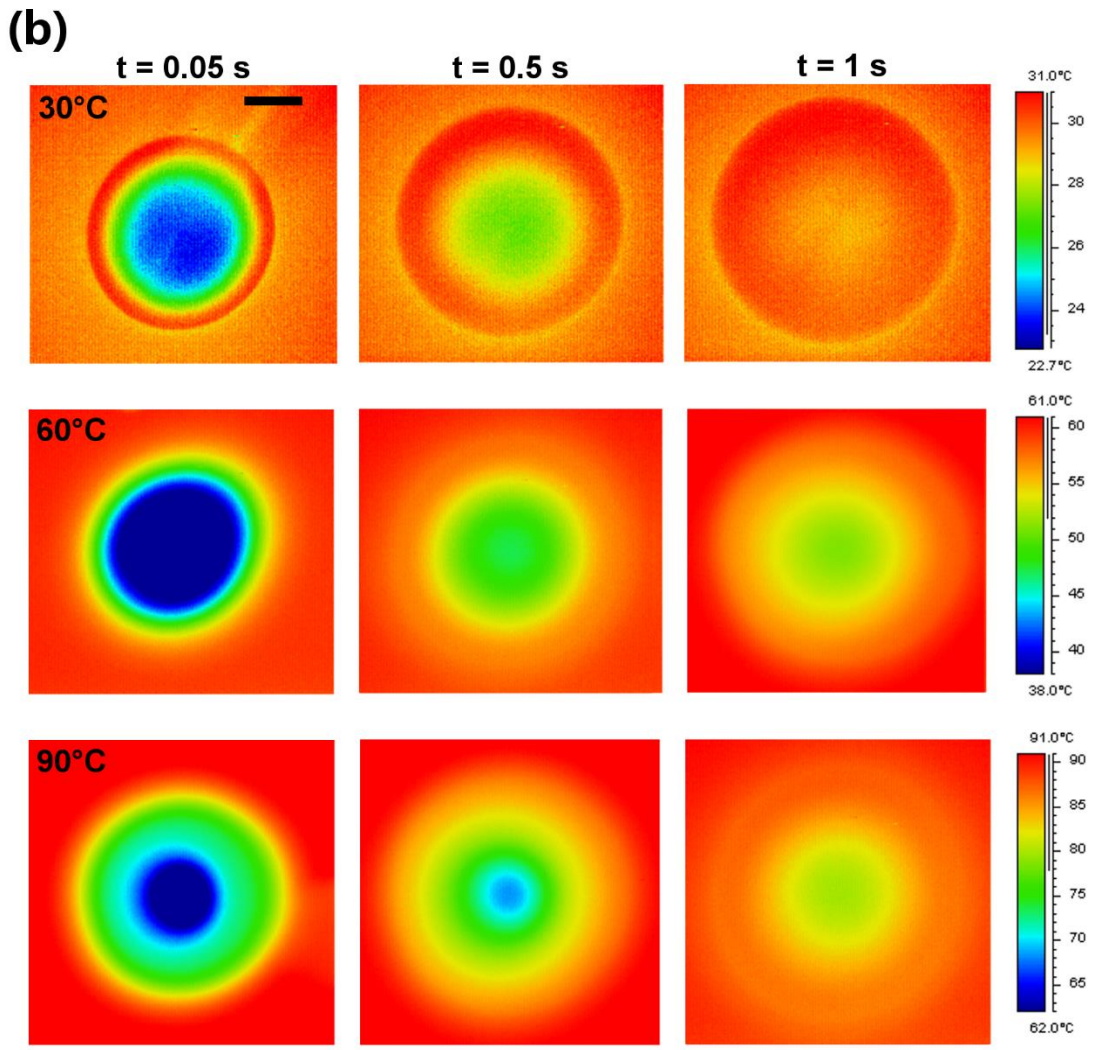


**Figure 5.4-1** IR thermography visualizations of the temperature profile of sessile droplets (top view) of (a) pure water and (b) pure 1-butanol (volumes of 4 ± 0.2 μL) on a uniformly heated glass substrate at three different temperatures of ~30, ~60 and ~90 $^{o}$C, immediately after deposition (0.05 s), after 0.5 and 1 s. Note that the contrast in IR images at substrate temperature of 30$^{o}$C is not as sharp due to the lower temperature differences between the liquid droplets (interface) and the substrate. The scale bars depict a width of 1.5 mm, for each liquid cases.

Figure 5.4-2 depicts the obtained IR images for the water – 1-butanol 5% vol. sessile droplets with volumes of 4 ±0.2 μL and initial temperature 9±1 $^{o}$C, at the three substrate temperatures: 30, 60 and 90 $^{o}$C. The generation of characteristic thermal patterns (heat convection from the edges toward to the centre) at the interface of the binary alcohol droplets can be clearly observed which indicated that these droplets

were in a transient phase with complex mixing, flows and boundary conditions between the two evaporating components (water and butanol). The thermal patterns observed at the substrate temperatures of 60$^{o}$C and 90$^{o}$C were similar to each other, resembling a wave-train motion of alternating warm/cool regions, which travelled in the direction towards the centre of the droplet. The generated thermal patterns were characterised by relatively darker, spoke-like bands, with a preferential direction of propagation waves towards the centre of the droplet. It is worthwhile noting that the development of these thermal patterns occurred spontaneously, upon the deposition of the binary droplets on the heated substrate and were more pronounced at higher temperature differences between the droplet and the substrate. These patterns were organised radially and circle around the apex, in the region where the most of evaporation occurred (mainly from the alcohol component as addressed in Chapter 2.7). Moreover, Figure 5.4-3 and 5.4-4 depicts further infrared visualization images for typical examples of the water – 1-butanol evaporating droplets at temperatures of 60$^{o}$C and 90$^{o}$C, immediately after contact (~0.05 s), 0.5, 1 s and after 3 s, where the generation of theses characteristic thermal instabilities within the evaporating self-rewetting droplets was further verified, respectively. Temperature differences-imbalances (Figure 5.4-2 – 5.4-4) on the free fluid interface are known to generate Marangoni stress and a velocity flow that will drag the fluid from warm regions where the surface tension is small, to cold regions where the surface tension is higher. The latter induced heat convective phenomena inside the evaporating droplet. Additionally, whatever was the evaporation stage of the droplets (both pure and binary liquids), the infrared visualization emphasized the fact that the temperature of the droplet was clearly hotter near the triple contact line (TLC) and colder in the centre, in all the experiments performed.

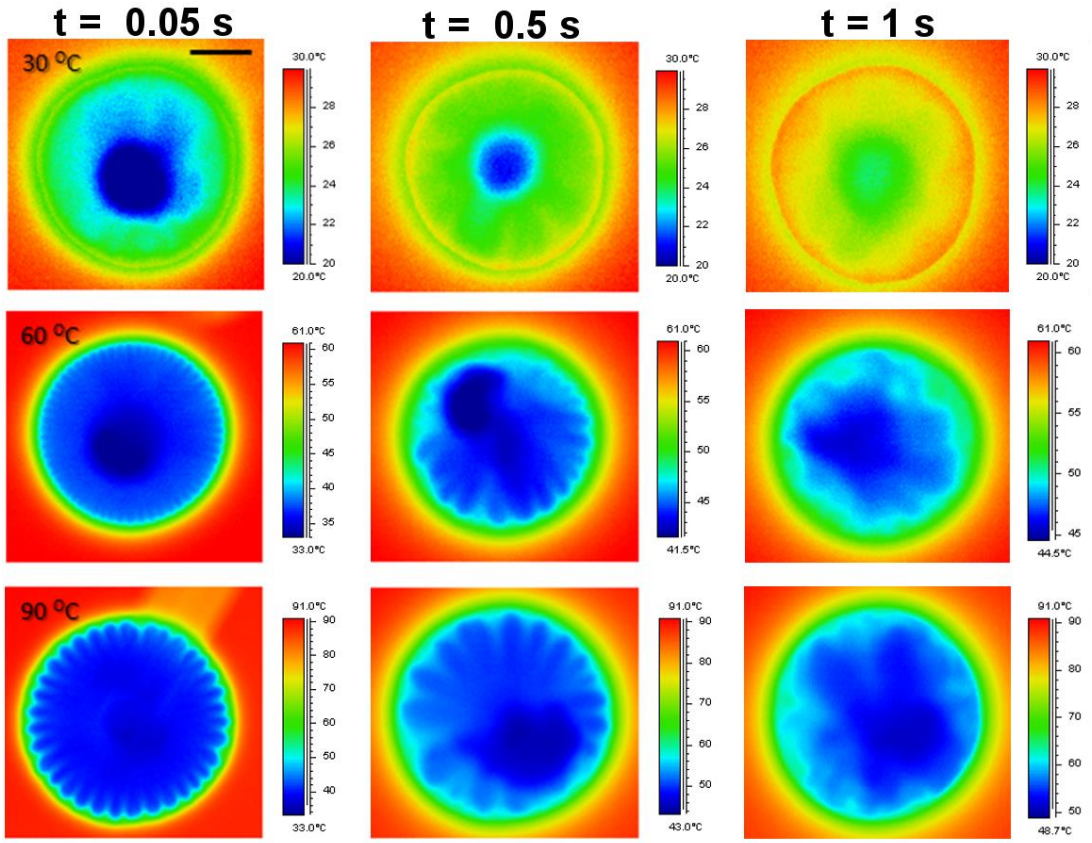


**Figure 5.4-2** IR thermography visualization images of the temperature profile of sessile droplets (top view) of water - 1-butanol 5% vol. (volume of 4 ± 0.2 μL) on a uniformly heated glass substrate at three different temperatures: 30, 60 and 90 °C, immediately after deposition (0.05 s), after 0.5 and 1 s. Note that the contrast in the obtained IR images at substrate temperature of ~30°C is not as sharp due to the lower temperature differences between the liquid droplets and the substrate. The scale bar depicts a width of 1 mm, for all IR images.

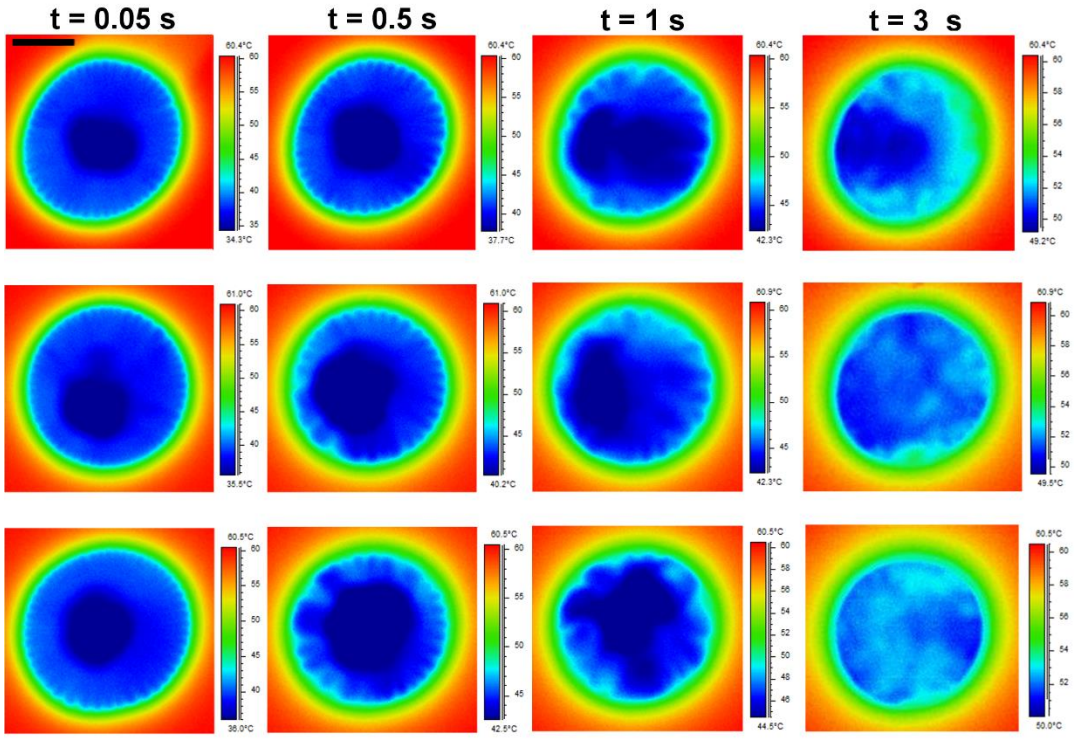


**Figure 5.4-3** Infrared visualization images of the temperature profile of three sessile droplets (top view) of water – 1-butanol 5% vol. (volumes 4.5 ± 0.2 μL) on a uniformly heated glass substrate at temperatures of ~60°C, immediately after contact (~0.05 s) and 0.5, 1 and 3 s. The scale bar depicts a width of 1.5 mm, for all images.

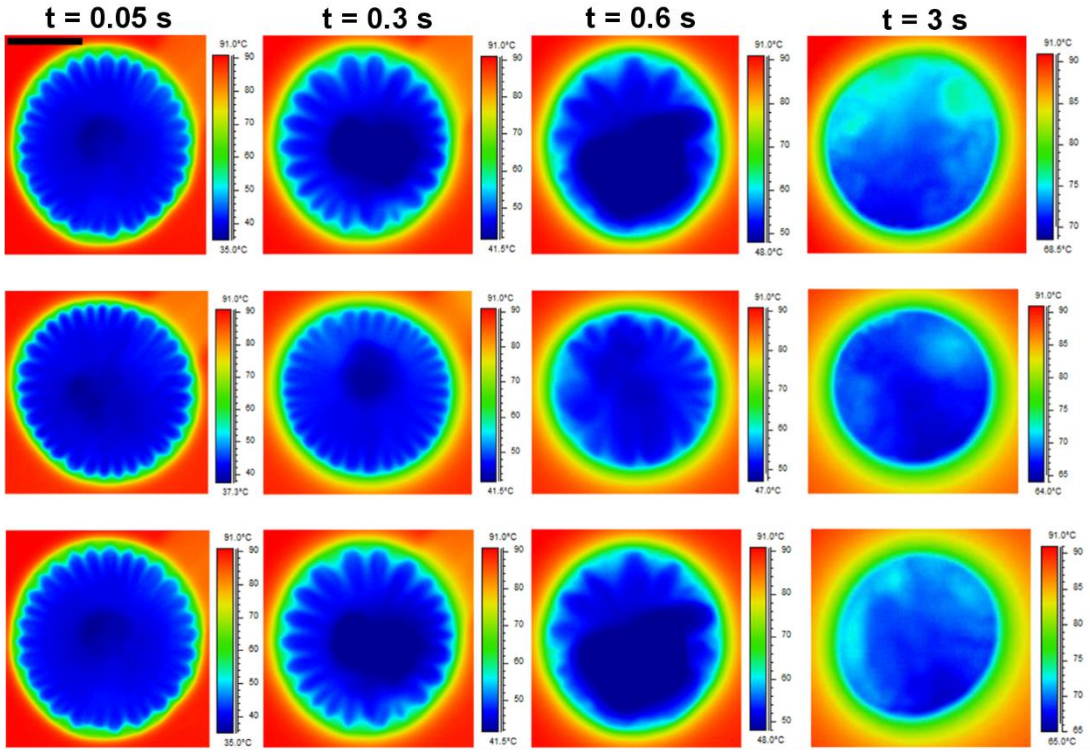


**Figure 5.4-4** Infrared visualization images of the temperature profile of three sessile droplets (top view) of water – 1-butanol 5% vol. (volumes 4.6 ± 0.2 μL) on a uniformly heated glass substrate at temperatures of 90°C, immediately after contact (~0.05 s) and 0.3, 1 and 3 s. The scale bar depicts a width of 1.5 mm, for all images.

The heat-waves on the surface of the water-butanol droplets (with volumes from ~4 to ~4.5 μL) at two different temperatures: ~60°C and ~90°C, corresponding to the number of warmer (or cooler) spoke-like regions, were visually counted and reported as a function of the dimensionless time $t/t_{tot}$, as shown in Figure 5.4-5, where $t_{tot}$ is the duration of the thermal wave phenomena (time until the disappearance of the thermal waves). Detailed inspection of these figures revealed that the number of waves depends drastically on the temperature of the substrate on which the binary droplets were deposited and also on the initial volume of the binary droplets. It is clear that the number of waves associated with the evaporation of the water-butanol droplet deposited on the ~60°C (glass) substrate was larger than that of the droplet deposited on the heated (glass) substrate at around 90°C. As the evaporative mechanism proceeded, the number of waves showed to follow an approximately linear decrease with the time and was consistent with the driving mechanism of these thermal patterns. As the binary sessile droplet evaporated and heated up by the substrate, the

concentration and temperature gradients along the free surface decreased which led to a decrease of the driving force of these patterns, namely the Marangoni effect. It is worth noting that IR thermography visualizations of the temperature profile for water-1-pentanol sessile droplets gave similar results to water-1-butanol droplets, as displayed in Figure 5.4-5.

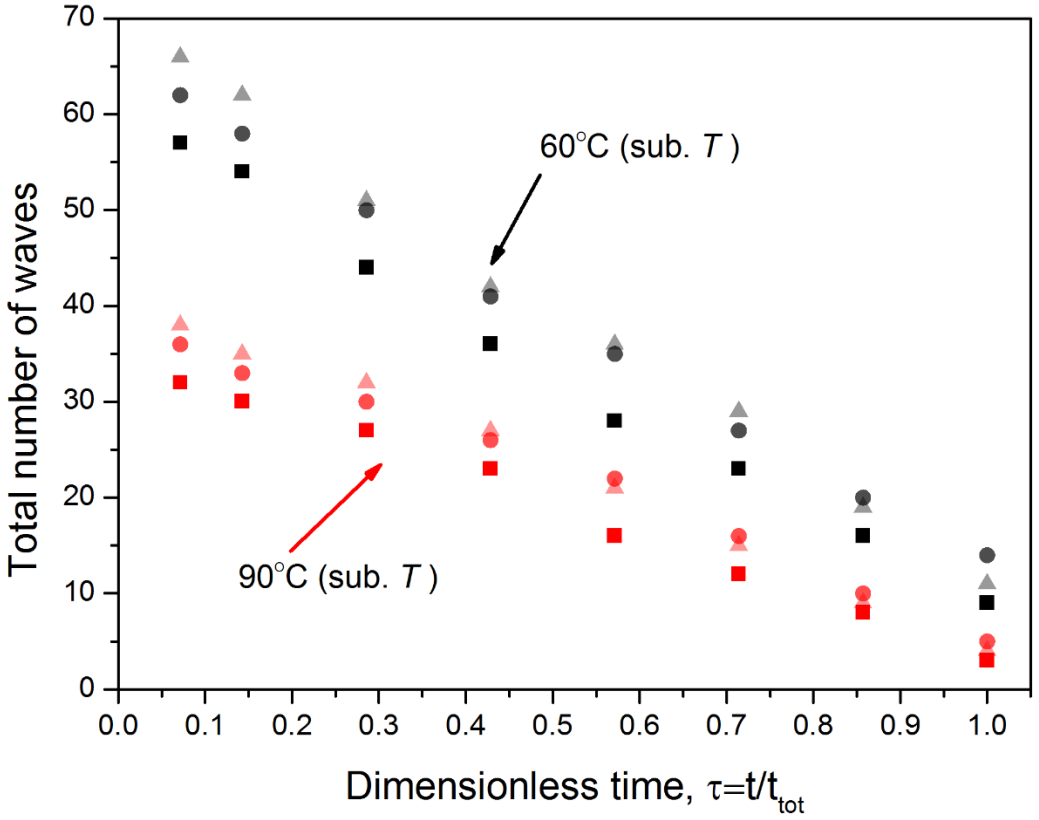


**Figure 5.4-5** Temporal evolution of the number of the observed thermal waves-patterns of six typical examples for water-1-butanol droplets with volumes: 4 (■), 4.3 (●), 4.5 (▲) μL at around 60ºC and 4 (■), 4.3 (●) and 4.5 μL (▲) at ~90ºC substrate temperatures (glass slide), respectively.

Additionally, the thermal activity of self-rewetting droplets on a different heated hydrophilic substrate was examined. Experiments consist of depositing spherical binary alcohol droplets on a heated ceramic (AlN) substrate (different thermal conductivity compared to glass substrate, ~100 times higher [222]) with volumes from ~3 to ~5 μL and initial temperature 9±1 ºC, at two different substrate temperatures: 60ºC and 90ºC. The generation of characteristic thermal patterns (heat convection

from the edges toward to the centre) at the interface of the binary alcohol droplets, with volumes of 4 ±0.2 μL, at substrate temperatures of 60$^{o}$C and 90$^{o}$C, can be clearly observed in Figure 5.4-6 (a) and (b), respectively. The thermal patterns observed, on the ceramic substrate, at 60$^{o}$C and 90$^{o}$C, were similar to each other, resembling a wave-train motion of alternating warm/cool regions, which travelled towards the centre of the evaporating droplet, similar behaviour as seen in the case of glass substrate. The development of these thermal patterns occurred spontaneously, upon the deposition on the heated substrate and were more pronounced at higher temperature differences i.e. between the droplet and substrate. The generated thermal patterns were characterised by relatively darker curved-bands, with a preferential direction of propagation waves towards the centre of the droplet and were organised radially and circle around the apex, in the region where the most of evaporation occurred. Moreover, the wavelength of self-rewetting droplets was seen to increase when the substrate temperature was increased from 60$^{o}$C to 90$^{o}$C (same feature observed for both substrates examined). However, the wavelength of droplets depositing on the ceramic substrate compared to glass changed as the thermal conductivity of the ceramic is higher [222]. The thermal activity and the generation-presence of characteristic thermal patterns i.e. number of waves, wavelength and intensity, at the interface of evaporating self-rewetting droplets was clearly affected from the substrate properties and the applied temperature.

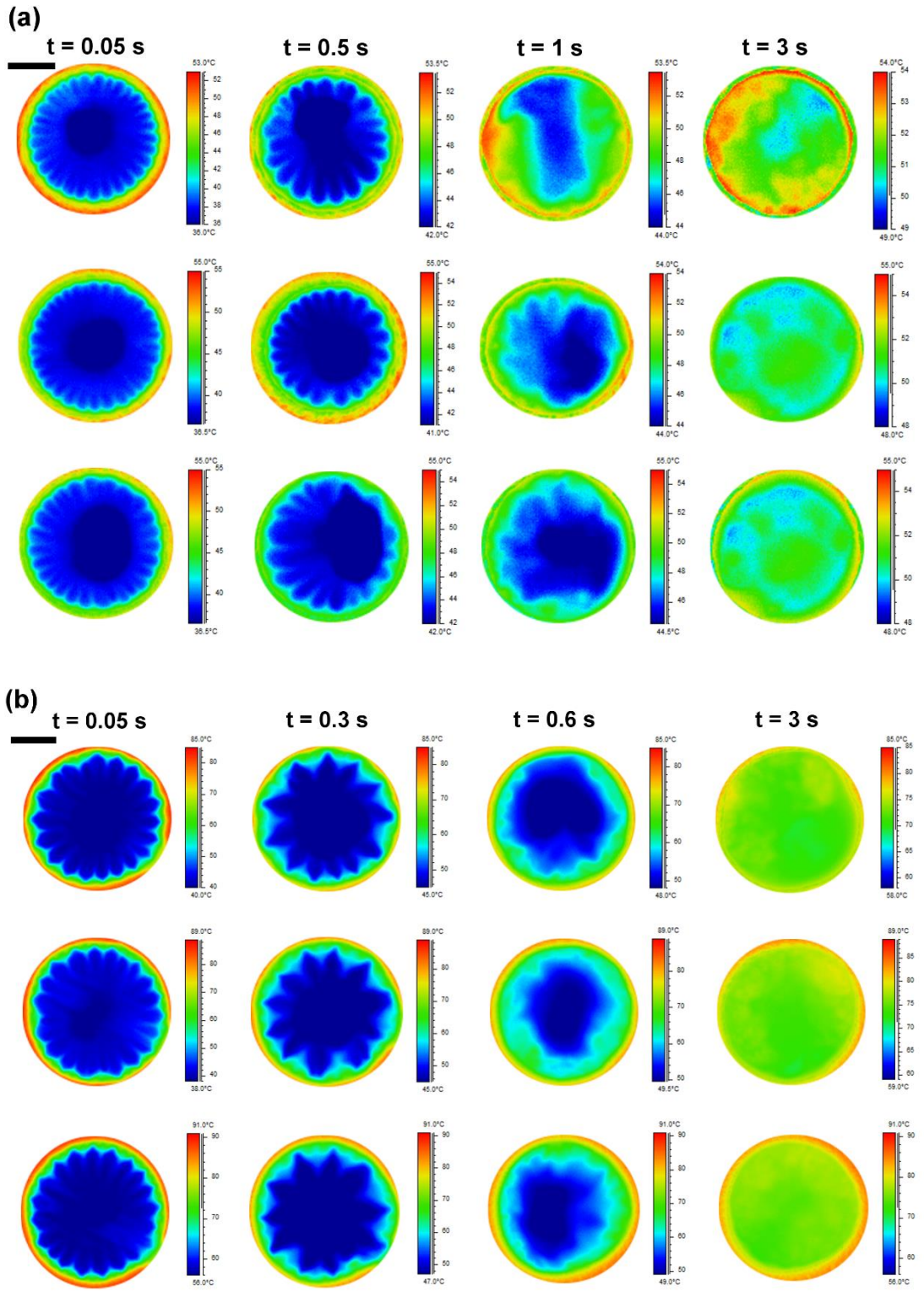


**Figure 5.4-6** Infrared visualization images of the temperature profile of three sessile self-rewetting droplets (top view) with volumes 4.5 ± 0.2 μL, on a uniformly heated ceramic substrate at temperatures of (a) 60°C and (b) 90°C, immediately after contact (~0.05 s) and 0.5 (at 60°C) or 0.3 (at 90°C), 1 and 3 s. The scale bar depicts a width of 1.5 mm, for all images.

## 5.5 Thermocapillary Instabilities of an Evaporating Non-Spherical Droplet

In the previous chapter we systematically examined the spreading mechanism of pure liquids and self-rewetting fluids (binary alcohol mixtures), under non-isothermal conditions and the effect of thermocapillarity on the contact line dynamics, deposited on solid glass substrates. Continuing with the efforts to further expand the understanding of the thermocapillary instabilities (internal flows) present during non-isothermal droplet spreading-evaporation, in this chapter we probe this relationship further. A systematic study on the behaviour of non-spherical pure water droplets under non-isothermal experimental conditions at different substrate temperatures was carried out. The temperature profile and the generation of thermal patterns at the interface of non-spherical pure liquid droplets was examined using IR thermography. In this investigation, we try to address the more complex case of deformed evaporating (cold) droplet placed on a heated solid substrate. The formation of thermal patterns was attributed to the presence of Marangoni stresses in the system and the irregularity of the droplet's shape. The Marangoni effect is of primary importance in our investigation accompanied with the irregular shape of the droplets. To the best of our knowledge, this is the first study of its kind in the literature. Scratched rough aluminium (alloy) was the substrate chosen since its surface heterogeneities ensure the complete pinning of the contact line and the deformed shape of the evaporating liquid droplets.

In what follows, a new series of experiments to investigate the generation of thermal patterns (internal flows) of a *non-spherical* evaporating droplet on a heated surface due to the formation of thermocapillary instabilities within the liquid system was conducted. The interfacial thermal activity of non-spherical pure water droplets at the first seconds of contact with the solid substrate was recorded using IR thermography. Experiments consist of depositing (manually) non-spherical droplets of a known volume from 3 – 5.5 ± 0.2 μL, initial temperature of 2 ±1 $^{o}$C onto a uniformly heated ethanol-cleaned aluminium (alloy) substrate and recording the droplet temperature map profile (Figure 5.5-1 – 5.5-3). In more details, representative infrared temperature profile images at ~40, ~70 and ~90 ± 1 $^{o}$C, for non-spherical pure water liquid droplets over the time of 4 secs, can be seen in Figure 5.5-1 – 5.5-3, respectively. As the

evaporation is not uniform along the interface, being higher near the contact line, this created large temperature gradients between the interface of the droplet (apex) and the substrate (contact line) leading to characteristic convective thermal patterns, *vortices*. The thermal activity of the water droplets at temperature of ~40$^{o}$C was comparatively weaker than those at temperature of ~70$^{o}$C, as displayed in Figure 5.5-1 and 5.5-2. The same feature revealed regarding the thermal activity from ~70$^{o}$C to ~90$^{o}$C, as seen in Figure 5.5-2 and 5.5-3. As expected, the higher temperature difference between the droplet and substrate, the more vigorous the generation of thermal patterns at the interface of the evaporating droplets. Another important feature, in the cases of the deformable pure water droplets at 90$^{o}$C, was the convective ‘‘fingering’’ thermal patterns observed at around 0.05 s. This was followed by the generation of convection vortices. At ~70$^{o}$C, no ‘‘fingering’’ thermal patterns were observed and immediately the formation of vortices occurred, within the evaporating non-spherical droplets. Note that at ~40$^{o}$C, the formation of vortices, within the evaporating droplets, lasted for shorter time as the temperature difference between the droplet and the heated substrate were relatively small compared to the other cases. These observations point to the fact that during the first tenths of seconds of droplet contact i.e. inertia-capillary regime, the Marangoni flow (thermocapillary effect – surface tension forces) contribution became the most significant energy transport mechanism as the substrate temperature was increased from 40$^{o}$ to 70$^{o}$ and then to 90$^{o}$ C, and so evaporation rates were drastically increased in the system.

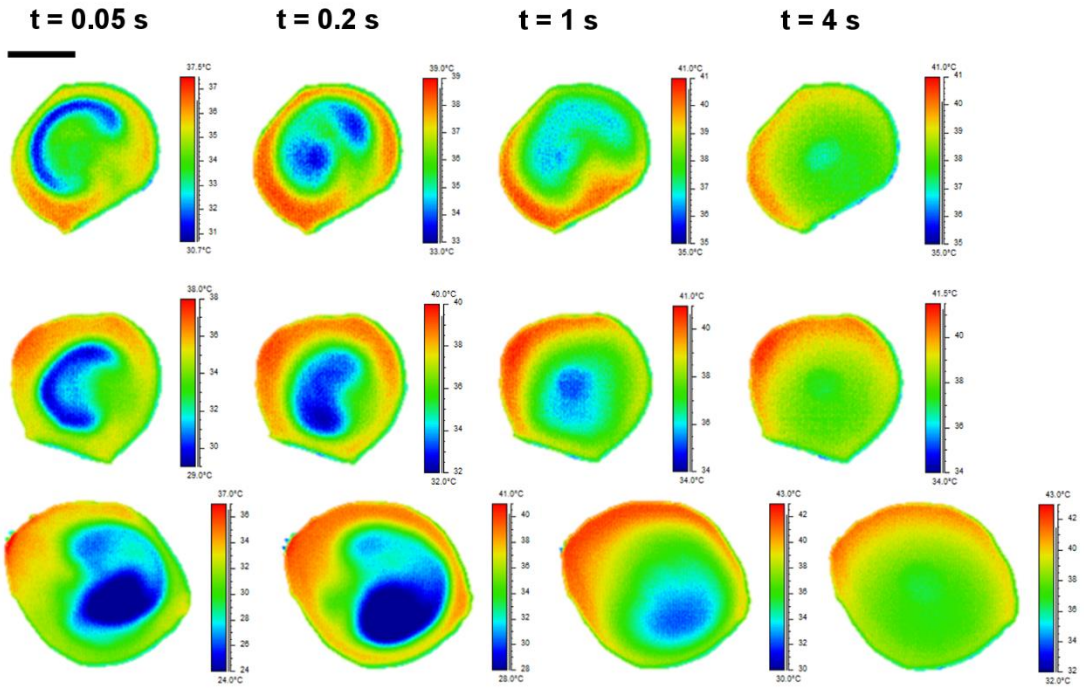


**Figure 5.5-1** Infrared visualization images of the temperature profile of three non-spherical pure water sessile droplets (top view), with volumes from 4 to 5.5 ± 0.2 μL, on a uniformly heated glass substrate at temperatures of 40°C, immediately after contact (~0.05 s), 0.2, 1 and 4 s. The scale bar depicts a width of 1.5 mm, for all IR images.

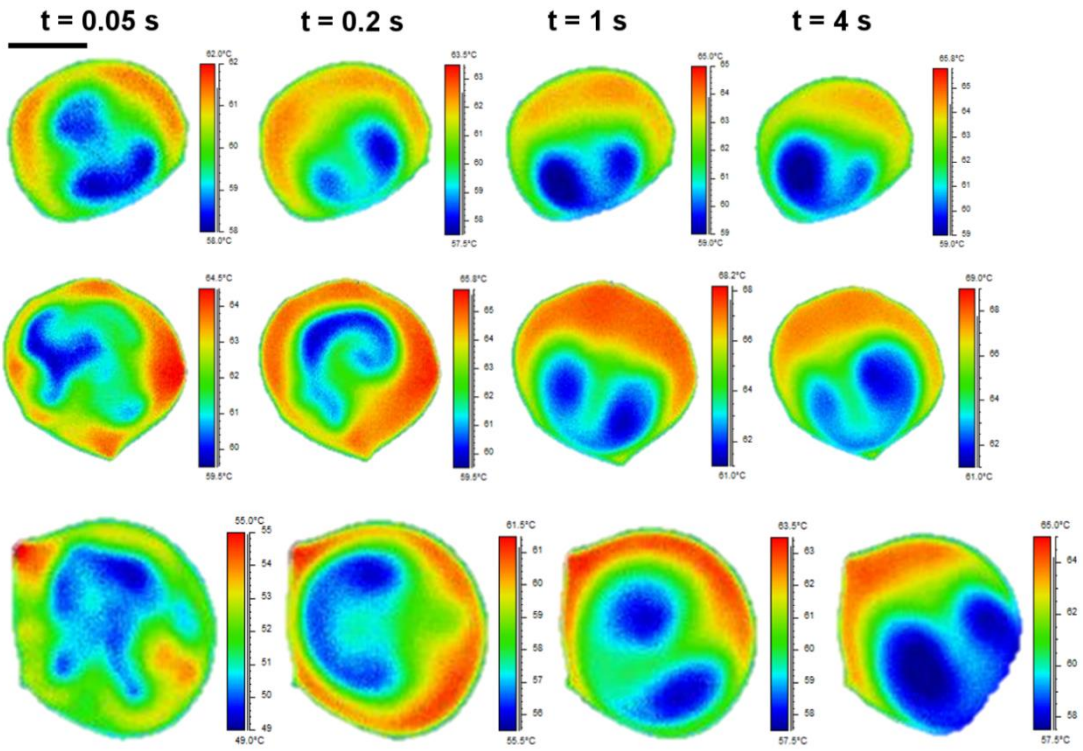


**Figure 5.5-2** Typical infrared visualization images of the temperature profile of three non-spherical pure water sessile droplets (top view), with volumes from 4 to 5.5 ± 0.2 μL, on a uniformly heated glass substrate at temperatures of 60°C, immediately after contact (~0.05 s), 0.2, 1 and 4 s. The scale bar depicts a width of 1.5 mm, for all IR images.

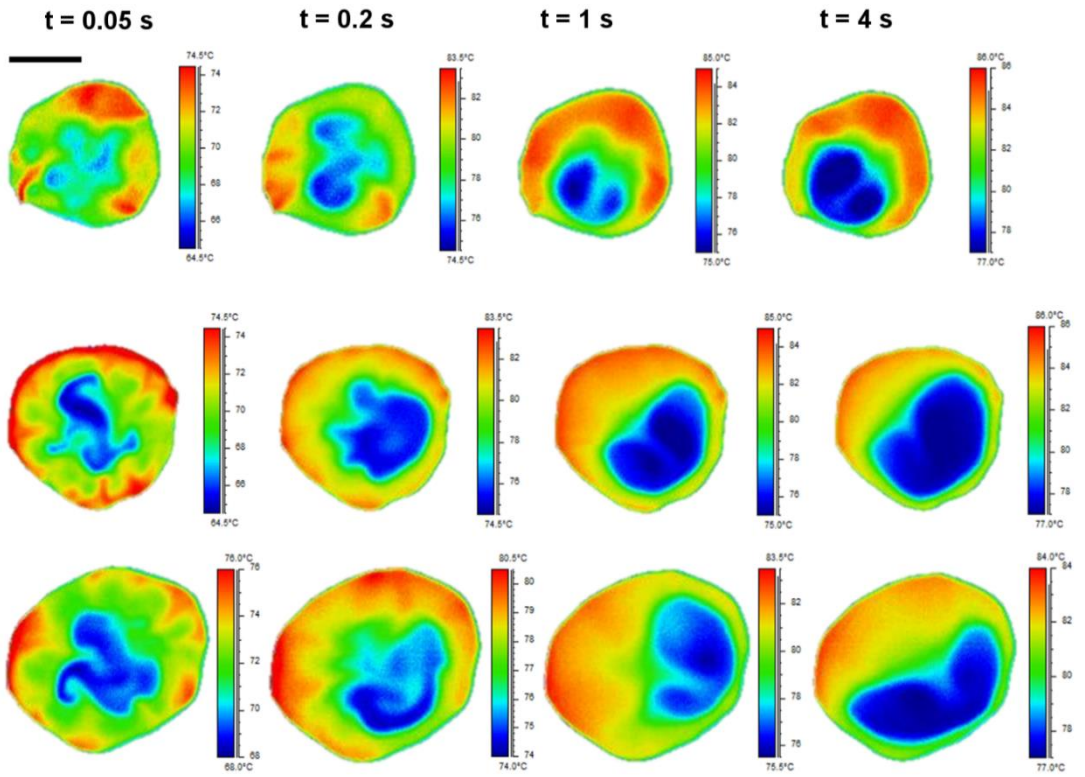


**Figure 5.5-3** Representative thermography images of the temperature profile of three non-spherical pure water sessile droplets (top view), with volumes from 3 to 5.5 ± 0.2 μL, on a uniformly heated glass substrate at temperatures of 90°C, immediately after contact (~0.05 s), 0.2, 1 and 4 s. The scale bar depicts a width of 1.5 mm, for all IR images.

## 5.6 Discussion

### 5.6.1 Surface-tension-driven contact line dynamics and thermocapillary flows

Regularly, convection for volatile small drops, can be either gravity or surface tension (Marangoni effect driven). The capillary length is given by $l_c = \sqrt{\frac{\gamma}{\rho g}}$ ($g$ is the acceleration of gravity) and therefore, for sessile droplets with height $h < l_c$ (small droplets) Benard-Marangoni convection dominates. In this experimental study, the water-alcohol droplets were examined which lead to a capillary length, $l_c$ of around 1.9 mm. Thus, the convection mechanism at the early stages of spreading was unlikely

to be buoyancy driven since the initial sizes of the droplets were small, from ~0.5 mm to ~1 mm, i.e. below capillary length. This implied that the droplets would not be deformed by gravity and would adopt spherical-cap shape. In turn, convection within the evaporating self-rewetting droplets, at the early stage of wetting, was the result of surface-tension-driven flows (Marangoni effect) either thermocapillary (temperature gradients) and/or solutal (concentration gradients) in nature, and could not be described simply by evaporative flux, outward flow as suggested by Deegan in 1997 [26].

The spreading exponent of the early stage growth ($n_{1st}$) which determined the initial spreading speed rate was found to depend on the substrate temperature for all the liquids used. It is well-established that in evaporating sessile droplets, there is continuous outward flow driven by mass conservation [26] because of the higher evaporation rate in the triple contact line (TCL) which leads to small temperature differences. More importantly in our experiments with the uniformly heated substrate, at early stages the temperature differences between the substrate-liquid interface and the rest of the droplet could be very large especially for the high temperature heated substrate cases, as can be visualized in the IR thermography images (Figure 5.4-1 – 5.4-4). These temperature differences led to surface tension imbalances-gradients and thus to the generation of thermocapillary flows (Marangoni effect) within the evaporating self-rewetting droplets.

It has to be mentioned, the evaporation of binary mixture droplets introduced a new additional effect in the system compared with those of the single-component droplets (Chapter 2). As butanol (or pentanol) was more volatile than water and migrated to the liquid-air interface led to local concentration gradients along and across the interface of the droplet, resulting to surface tension stresses inducing additional solutal Marangoni flows which leads to characteristic thermal waves as seen by IR thermography (Figure 5.4-2 – 5.4-4). In fact, any imposed temperature difference across the liquid-vapour interface of these binary mixtures created also local surface concentration gradients. These Marangoni instabilities induced flow away from regions with low surface tension in the direction of increasing surface tension (Figure

5.1-2) resulting in complex thermal patterns. The patterns were more prominent for the higher temperature substrates (90$^{o}$C) leading to more clearly formed curved-bands as presented in Figure 5.4-2 – 5.4-4.

It is only later, when the droplets entered in Tanner's regime and the contact line viscous dissipation controlled the spreading dynamics of the system that the exponent changed to lower values (Figure 5.2-3 b and d). This stage of wetting, at a later phase of evaporation, was characterized by progressively fewer heat waves (until they disappeared) and the presence of slow dynamics (viscous-capillary regime) where the apparent exponent $n$ reached a plateaux with values $0.1 < n < 0.2$ in agreement with other studies reported on other liquids for this specific regime of spreading [89, 90].

The characteristic thermal patterns observed (Chapter 5.4) in our experiments confirmed that the Marangoni instabilities induced characteristic heat travelling waves and showed that the evaporation rate of these sessile water-alcohol droplets could not be described by a vapour diffusion mechanism alone. The fact that the thermal patterns were more prominent for higher substrate temperatures indicated that the Marangoni-induced flows contributed more significantly to energy transport phenomena as the temperature differences were higher at the contact line and in the liquid bulk. By the end of the first stage (inertia-capillary region), most (if not all) of the alcohol phase (butanol or pentanol) would have evaporated and also the temperature differences over the droplet would have become smaller, as the capillary waves propagated within the droplet. Thus, concentration and temperature gradients became really weak to sustain the flow and the solutal - thermacapilllary Marangoni effects became sub-critical. Thus, the frequency of these thermal wave decreased as the droplets heating and evaporation proceeded (Figure 5.4-5).

Additionally, for short chain alcohol molecules (such as butanol and pentanol used in this study) the alcohol-rich phase has a tendency to completely wet the air-water interface; this tendency is more pronounced for shorter alkyl chain lengths and at higher temperatures [223]. This might explain the different spreading exponents was

seen between the two binary spreading mixtures (Figure 5.2-3 c) for higher substrate temperatures.

### 5.6.2 Marangoni driven convection on sliding droplet

The dynamics of a self-rewetting droplet moving on an isothermal (uniformly heated, 61±1 ºC), inclined solid substrate (around 5 degrees) covered with a layer of silicone oil (~0.2 mm thickness), was systematically examined (around 15 repetitions). The droplet motion was driven by gravity (inclination), capillarity (evaporation), and Marangoni stresses arising from the dependence of surface tension on the temperature of the substrate. Initially, immediately after contact, the droplet spread in both directions and at the same time the gravitational forces were responsible for the downward movement of the sliding droplet on the silicone oil layer. The temporal evolution of the wetted length and wetted area were shown to change the sliding-spreading droplet morphology (three-dimensional shape), irrespective of the surface wettability due to the deposited oil layer (minimum contact line friction) [224-227]. As the droplet slid and spread with different velocities (and so contact angles), as seen in Figure 5.3-2, it was expected to deform steadily adapting a contact line area with a corner regime at the rear side, from the initial round (spherical cap) shape (just after contact), schematic drawing in Figure 5.6-1 [224-226]. In Figure 5.6-1 (a) the red dot presents the centre mass of the droplet and the blue vectors the surface tension forces acting at the vicinity of the contact line related to wetted area changes using WOLFRAM MATHEMATICA software and MATLAB R2016a (MathWorks®) software, respectively. The droplet's centre of mass is constantly changing and irregularities in the body forces are expected to be present within the droplet during sliding. Additionally, the temperature variations between the contact line (hot) and the apex (cold) of the sliding-spreading self-rewetting droplet arose surface tension gradients (temperature and concentration) at the droplet interface, as presented in Figure 5.6-1 (b). Furthermore, the droplet deformation generated non-uniform surface tension gradients between the two side (right-left) of the heated contact line and the apex of the droplet.

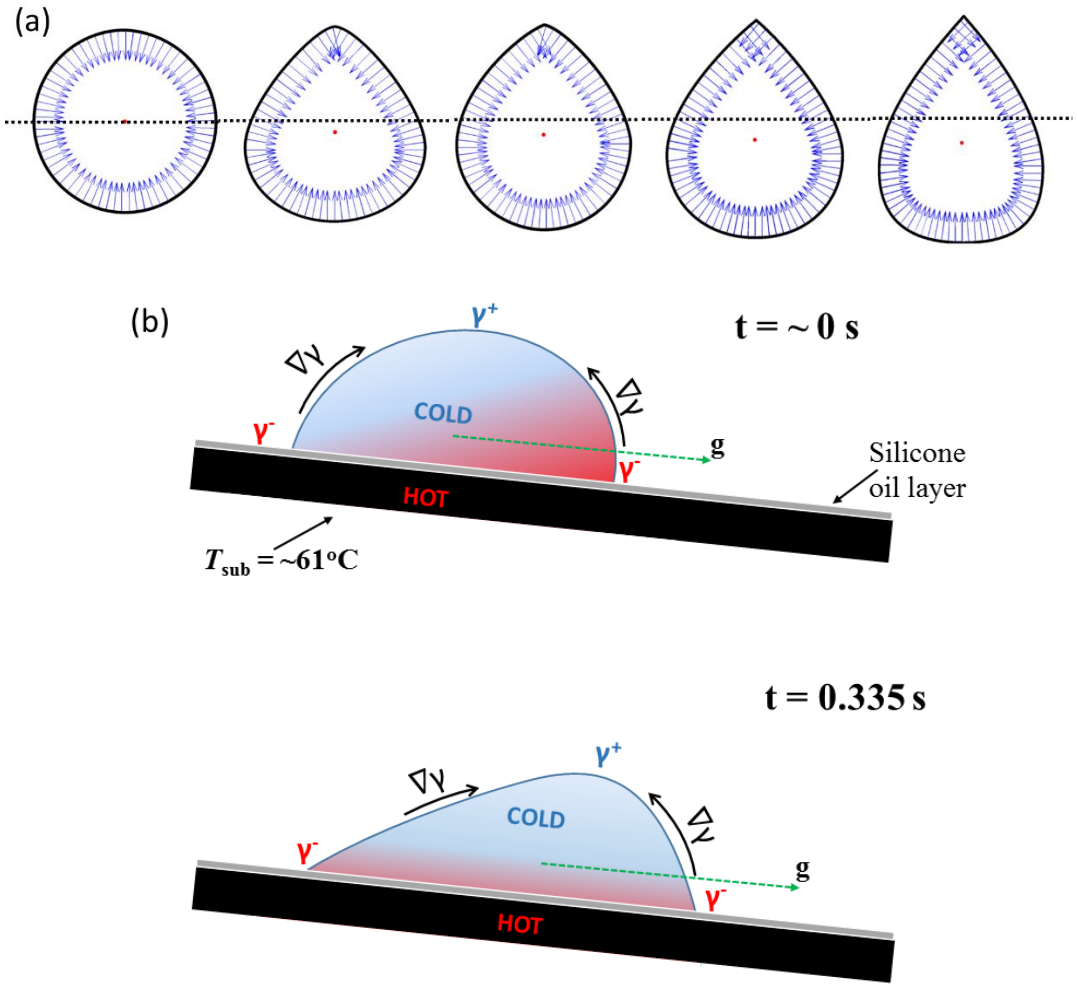


**Figure 5.6-1** (a) Schematic drawing of the droplet deformation during sliding-spreading behaviour where red dots present droplet's centre of mass and blue vectors the surface tension forces acting at the contact line of the deformed droplet (b) schematic presentation of the surface tension gradients (Marangoni effect) presented at the interface of the self-rewetting droplet on the inclined substrate at $t$ = ~0 s and 0.335 s, respectively.

IR thermography on a horizontal glass substrate to demonstrate the existence of Marangoni stresses was conducted. The IR camera used in this study is an infrared (FLIR) ThermaCAMSC3000 (see Chapter 3). Figure 5.6-2 depicts the temperature profiles of the binary (water – 1-butanol 5% vol.) sessile droplets (9±1 $^{o}$C) on silicone oil layer, at ~60$^{o}$C. Figure 5.6-2 (a) and (b), the generation of characteristic thermal patterns (heat convection from the edges toward to the centre) at the interface of the binary alcohol droplets at $t$ = ~0 s and $t$ = ~0.3 s, can be clearly observed, respectively. This indicated that the droplet was in a transient phase with complex mixing, flows and boundary conditions between the two evaporating components (water and

butanol). The generated thermal patterns (Marangoni effect as discussed in Chapter 5.4) were characterised by relatively darker curved-bands, with a preferential direction of propagation waves towards the centre of the droplet. The development of these thermal patterns occurred spontaneously, upon the deposition of the binary droplets on the heated substrate and they were organised radially and circled around the apex, in the region where the most of evaporation occurred. Figure 5.6-2 (c) presents the temperature distribution along the interface of the droplet at two characteristic moments i.e. around 0 s and ~0.3 s. It can be seen from the temperature profile in Figure 5.6-2 (c) that the centre of the inclined droplet was changed due to contact angle hysteresis. The presence of the Marangoni effect (surface tension imbalances) along the liquid interface combined with contact angle hysteresis give arise to complex droplet behaviour.

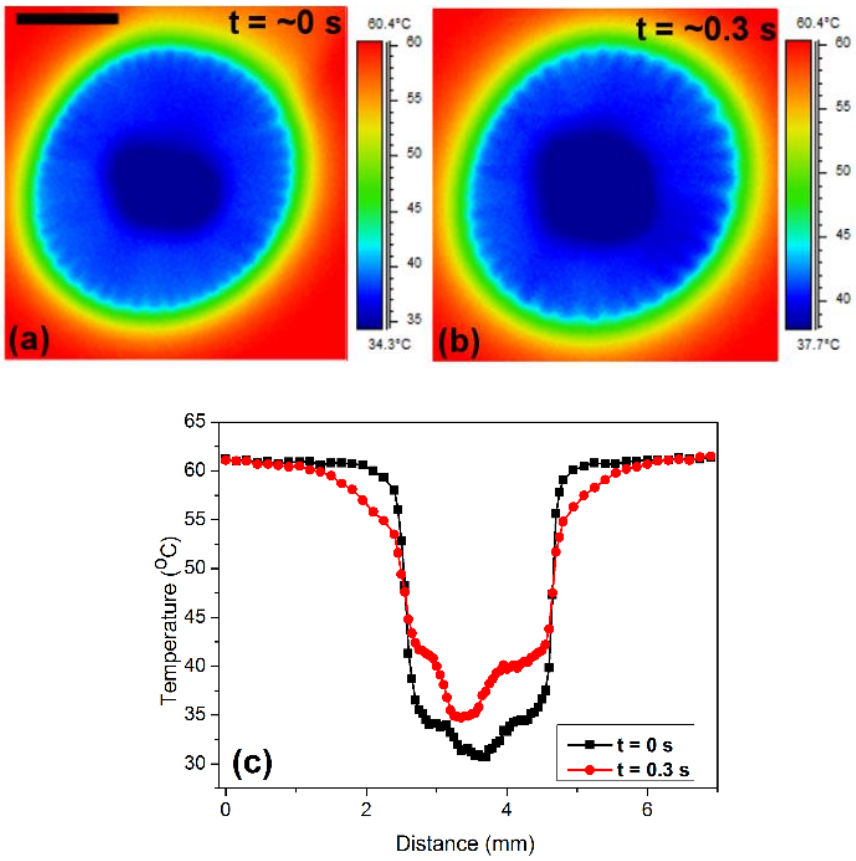


**Figure 5.6-2** IR thermography visualization images of the temperature profile of sessile droplets (top view) of water - 1-butanol 5% vol. (volume of 4 ± 0.2 μL) on a uniformly heated inclined glass substrate, immediately after deposition around 0 s (a), and 0.3 s (b), respectively. Graph (c) depicts temperature profiles along the interface of the sessile

evaporating droplets for the two moments i.e. 0 s and 0.3 s. The scale bar depicts a width of 1 mm, for all IR images.

The surface tension of the self-rewetting fluid i.e. water -1-butanol 5% vol., have been measured in the temperature range from ~10 to ~90°C, using the pendant drop method analysis (FTÅ apparatus), as seen in Figure 5.1-2. The non-linear (parabolic) dependence of the surface tension of the self-rewetting droplets on temperature was clear. The minimum of the surface tension was measured around 63°C and the unusual temperature dependence which turns out to be increasing in the higher temperature region beyond the minimum for these fluids was revealed. At $t$ = ~0 s, Figure 5.6-3, the surface tension gradients at the left side ($\theta_r = 87^o$) of the contact line (hot,) and the apex (cold) was calculated to be roughly: $\nabla\gamma_{LEFT} \approx 0.9\frac{\mathrm{mN}}{\mathrm{m}}$ and at the right side ($\theta_a = 95^o$) was: $\nabla\gamma_{RIGHT} \approx 0.13\frac{\mathrm{mN}}{\mathrm{m}}$. The gravity (strong effect) and the Marangoni stresses (small effect) are acting in the same direction enhancing the downward motion of the self-rewetting droplet, as seen in Figure 5.6-3. Interestingly, at $t$ = 0.355 s, just before the droplet started the upward motion, the calculated overall surface tension gradients between the contact line (hot) and the apex (cold) for the two side of the droplet were: $\nabla\gamma_{LEFT} \approx 0.28\frac{\mathrm{mN}}{\mathrm{m}}$ ($\theta_r = 75^o$), and $\nabla\gamma_{RIGHT} \approx 0.42\frac{\mathrm{mN}}{\mathrm{m}}$ ($\theta_a = 65^o$), respectively. The deformed droplet's motion was influenced by gravity and the presence of strong Marangoni stresses, but were acting in the opposite direction than at $t$ = 0 s, Figure 5.6-3. In details, at the right side (edge) of the droplet, the surface tension gradient was found almost two times higher than the left side resulting in the upward movement against gravity. Another clear feature revealed, from this series of experiments, in the absence of contact line friction forces (silicone oil) and the presence of strong Marangoni stresses (surface-tension-temperature-concentration gradients) in the system, was the drastically enhanced spreading rates (exponents) of the self-rewetting droplets as presented in Figure 5.3-2 (c); almost four times higher spreading rates than the ones observed of the self-rewetting droplets on glass (Chapter 5.2). In summary, it was observed that the inclination of the surface which caused the droplet deformation combined with the presence of strong thermocapillary (and solutal) stresses and gravity played a significant role on droplet's complicated contact line dynamics.

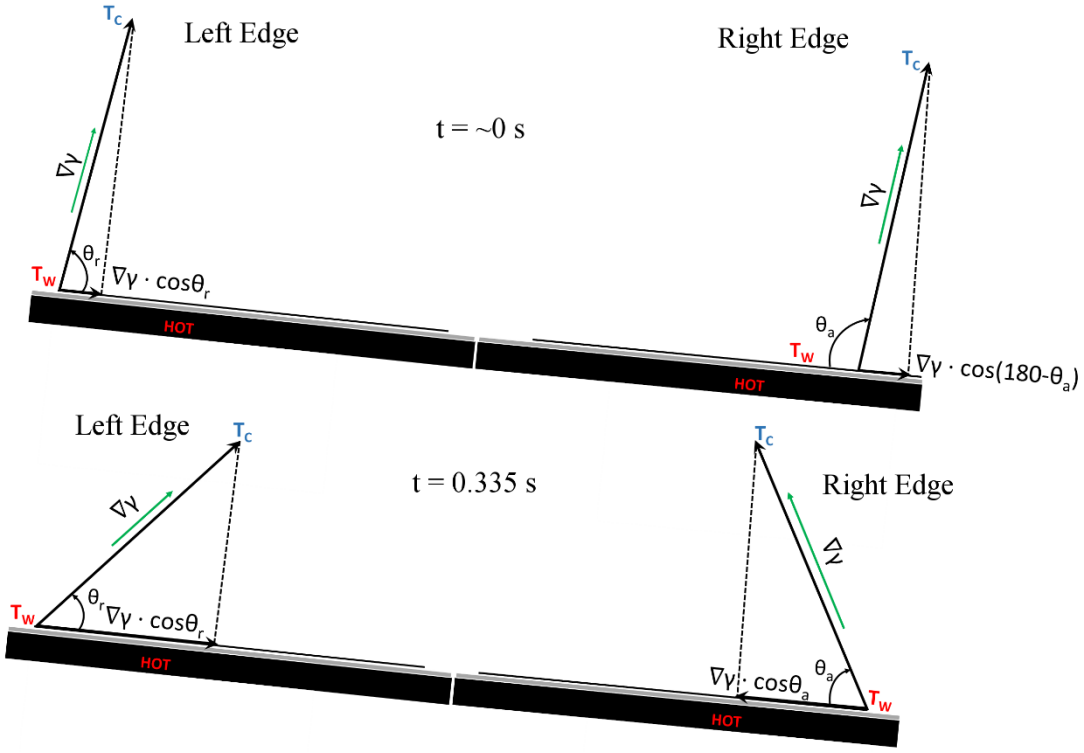


**Figure 5.6-3** Schematic drawing of the surface tension force acting at the vicinity of the contact line of the self-rewetting droplet at two different times: $t$ = ~0 s (immediately after contact) and $t$ = 0.335 s (when the droplet started the upward motion).

## 5.6.3 Thermocapillary actuation and Thermal Patterns of a non-spherical droplet

In this investigation, we tried to address the more complex case of deformed evaporating (cold) droplet placed on a heated solid substrate under controlled non-isothermal experimental conditions. Convection in such water droplets (volatile drops), can be induced by either gravity or surface tension (Marangoni effect) driven. The heat convection revealed from our experiments, at the first seconds of droplet's contact on the heated substrate, was unlikely to be buoyance driven since the sizes of the droplets (height, $h$) were small and below capillary length $l_c = \sqrt{\frac{\gamma}{\rho g}}$, i.e. $h < l_c$, where $h = \sim 1.3$ mm, $l_c = \sim 1.9\, mm$, in our experiments. In turn, in our single component system the remaining mechanism for convection is surface-tension-driven flows, namely Marangoni instabilities. The generation of theses distinctive thermal

patterns, vortices, at the surface of the liquid droplets suggested that the internal flows, at this stage, were driven mainly by temperature differences between the contact line (hot) and the apex of the droplet (cold) and not simply by evaporative flux, outward flow (Deegan, 1997) [26]. Higher temperature differences between the contact line and the apex induced stronger Marangoni flows, vortices, and thus promoted radial mixing in our system. Additionally, the non-spherical shape of the droplet made the system even more complicated. The temperature differences between the apex and the contact line were not uniformly distributed along the interface due to deformable wetted area of the droplet which might explained the generation of theses characteristic thermal patterns at 40$^{o}$C, 70$^{o}$C and 90$^{o}$C, respectively. It was shown that the characteristic vortices emerged more vigorously and persisted for longer times at temperature of 90$^{o}$C. Moreover, at 90$^{o}$C substrate temperature, the generation of characteristic convective ‘‘fingering’’ thermal patterns just before the development of the convection vortices, pointed out significant contribution of the Marangoni effect as a crucial energy transport mechanism within the evaporating droplets (Figure 5.5-3). The imposed irregular droplet geometry resulting in an unsteady mass transfer was very complex and its interface thermal distribution led to the emergence of Marangoni stresses. These stresses induced a pair of self-excited counter rotating vortices with preferential direction within the droplet. It should be also noted that the irregularity in the contact-line area also entailed a significant redistribution of droplet’s thermal field, along with a change in the direction and strength of the Marangoni thermal patterns. The evaporation of non-axisymmetric sessile drops was recently studied by Saenz *et al.* conducting three-dimensional direct numerical simulations (DNS) [228]. The authors reported the presence of azimuthal currents and pairs of counter-rotating vortices in the liquid bulk flow in drops with non-circular wetted area SAENZ [228]. These phenomena were found to play a critical role in the transient liquid flow dynamics associated with the heat transfer performance of the non-spherical evaporating droplets.

## 5.7 Conclusions

The fluid contact line dynamics combined with infrared thermography imaging of evaporating sessile droplets of pure liquids and self-rewetting fluids under isothermal and non-isothermal conditions were extensively investigated. It was shown that the early stage of spreading on partially wetting substrates depends strongly on the substrate temperature. The spreading exponents *n* (wetted area) of the very first initial stage (inertia-capillary regime) of spreading were close to 0.52 at substrate temperature of 30$^{o}$C and increased monotonically at higher temperatures for the pure liquids and non-monotonically for the binary alcohol mixtures. This was consistent with the anomalous surface tension behaviour (at a particular range of temperatures) of these self-rewetting liquids. For all the fluid used in this work, the second stage exponent of spreading mechanism was around 0.1 as expected for the viscous-capillary balance regime following the Tanner's law. Additionally, the spontaneous appearance of characteristic thermal travelling waves during the evaporation process was observed for the cases of self-rewetting fluids. These surface-tension-driven (Marangoni effect) thermal patterns were due to the temperature and/or concentration gradients which were developed along and across the free surface of the evaporating droplets and influenced drastically the early-times spreading behaviour.

Regarding the experiments conducted using self-rewetting droplets sliding on an inclined heated glass substrate covered with a silicone oil layer before deposition; the contact line dynamics was examined. The results have shown that the droplet motion was driven by gravity, capillarity, and the induced Marangoni stresses due to the non-isothermal conditions. Our experiments did not account the contact line friction due to the silicone oil layer which covered the heated substrate before droplet deposition. In the presence of surface tension-temperature-concentration induced gradients along the interface of the droplet, the contact line dynamics of the system were rather complex. The droplet deformation with a changing centre of mass (inclination of the substrate) and the presence of strong Marangoni stresses acting at the interface of the droplet resulted in an enhancement of the spreading rates (compared to the

experiments on solids glass substrates) and the remarkable upward movement of the droplet overcoming the gravity effect.

In most real-life applications evaporating sessile drops are non-spherical or display numerous three-dimensional phenomena, such as the thermocapillary instabilities recently reported by Sefiane *et al*. [49]. Here we considered the case of a pure water droplet that was deformed at its inception onto a heated substrate which the drop's contact wetted area was approximately elliptical. The geometry of the droplet was very complex and its interface thermal distribution led to the emergence of Marangoni stresses perpendicular to the radial direction across the apex of the droplet. The Marangoni convection adopted a preferential direction, which induced a pair of self-excited counter-rotating vortices within the droplet (Figure 5.5-1 – 5.5-3). These thermal patterns drove liquid to the centres (corresponding to the immediate stage of evaporation) of recirculation vortices across the longest ellipse's axis. These vortices might play a prominent role in the bulk velocity field and the heat transfer mechanism. The strong Marangoni stresses (thermocapillary instabilities) combined with droplet shape deformations led to an even more complex fluid dynamic behaviour.

# Chapter 6: Bubble Rise in Self-Rewetting Fluid and the Role of Thermocapillarity

In this chapter, we report on the motion of a buoyancy-driven bubble in a vertical micro-channel and the significant role of thermocapillarity in the system. A series of experiments have been carried out using a circular micro-channel filled with pure liquids (pure water and pure 1-butanol) and a self-rewetting fluid (water – 1-butanol 5% vol.) under isothermal and non-isothermal controlled conditions. In both cases, different mass fluxes and heat fluxes were applied on the micro-channel within the same temperature gradient field (from 18 to $75 \pm 1$ $^{o}$C, inlet-outlet liquid temperatures, respectively) which was increasing linearly in the same direction with the liquid flow. We have shown that the behaviour of the bubbles in a self-rewetting fluid departed considerably from that of pure liquids. The anomalous property of the alcohol mixture i.e. the non-monotonic dependence of the surface tension with the temperature, drastically modified the movement (promote or inhibit) and the shape (spherical or deformed) of the migrating air bubbles. These phenomena were explained in terms of the location of the bubble associated with the well-defined surface tension minimum, and as a function of dimensionless group numbers. Heat transfer coefficient calculations in the single and two phase flows (locally) were acquired for the different experimental conditions (mass fluxes) and all the liquids used in this study. We demonstrated that the presence of Marangoni stresses resulted in the enhancement of the heat transfer distribution in the self-rewetting fluid flows compared with the pure liquids. Promising results have been published with the use of self-rewetting fluids in pool boiling, heat pipes applications and microchannel flow boiling, whereas the purpose of this research is the implementation of a self-rewetting aqueous 1-butanol solution in a temperature gradient field and the investigation of two-phase heat transfer phenomena.

## 6.1 Bubble Motion in a Vertical Microchannel

The use of transparent micro-channels allowed for visualization of the motion (movement and shape geometry) of the induced travelling air bubbles in a continuous liquid phase flow, before and after applying heat on a circular micro-channel. With the use of high speed camera, different flowing patterns were observed within the micro-channel. Bubbly flow and in some specific cases slug flow were recorded

depending on the applied experimental conditions and the working fluids were used in this study. Different operating fluids: pure water, pure 1-butanol and water – 1-butanol 5% vol., at same controlled experimental conditions (mass flux and temperature distribution), demonstrated different activity of the flowing bubbles inside the microchannel. Note that details regarding the experimental apparatus, methodology, calculations and (absolute) errors were extensively discussed in Chapter 3.1.5.

In the case of the pure liquids an experimental investigation with three different volume flow rates: $\dot{V}$ = 0.5, 1, 1.5 mL/ min, in isothermal conditions (~18$^{o}$C) and in a temperature gradient field from, 18 to 75 ±1 $^{o}$C (inlet-outlet liquid temperatures), were systematically performed, around ~15 repetitions for each case, respectively. In Figure 6.1-1, typical sequence of images with bubbles flowing vertically in a heated micro-channel containing two different working fluids: (a) pure water and (b) pure 1-butanol, against time, *t*, at volume flow rate of $\dot{V}$ = 0.5 mL/ min, were presented. In these cases, the induced bubbles were migrating from below (inlet) towards the upper part (outlet) of the channel and with the temperature increasing in the same direction as the liquid flow. In Figure 6.1-1 (a), the migrating air bubble in pure water was shown to follow steady shape geometry along the heated microchannel. In the case of the pure 1-butanol working fluid, Figure 6.1-1 (b), the bubble geometry appeared slightly to fluctuate, adopting a disk-like shape rather than spherical shape, at $\dot{V}$ = 0.5 mL/ min. It is worthwhile noting that for the isothermal cases using the pure liquids as operating fluids not remarkable differences were recorded in bubbles' geometry compared to the different volume flow rates ($\dot{V} = 1, 1.5$ mL/ min) were applied in the microchannel.

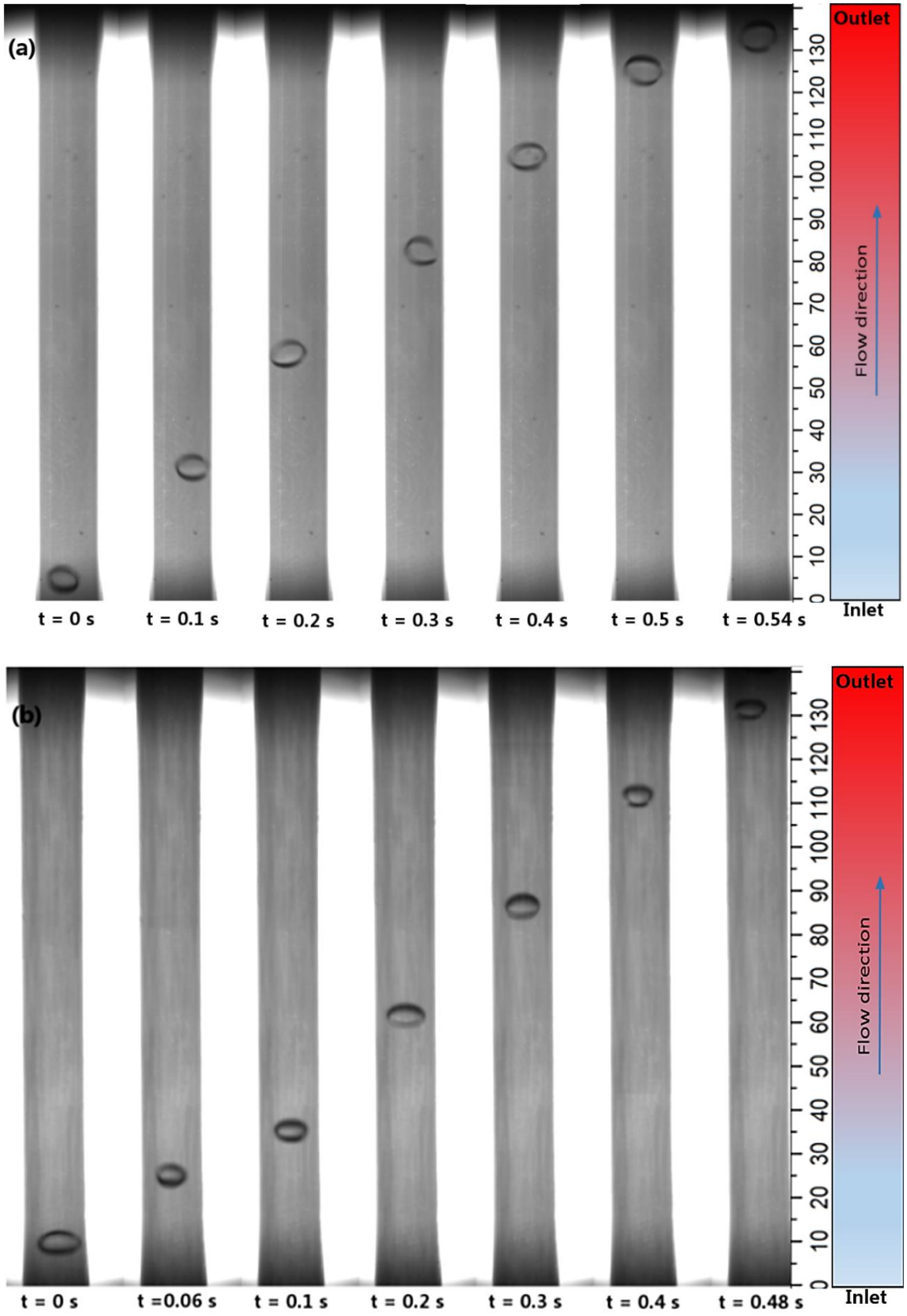


**Figure 6.1-1** Typical image sequence of the manually induced travelling air bubbles (diameters: from ~1.8 to ~3 mm) along the vertical uniformly heated micro-channel, against the time, *t*. Graphs depict bubble images travelling in (a) pure water and (b) pure 1-butanol

working fluids, at volume flow rate of $\dot{V}$ = 0.5 mL/ min, in a temperature gradient field from ~18 to ~75 $^{o}$C (inlet-outlet liquid temperatures), respectively.

In Figure 6.1-2 – 6.1-5 , subsequent images of migrating bubbles in the water – 1-butanol 5% vol. mixture (self-rewetting fluid), versus the time, *t*, at four different volume flow rates: $\dot{V} = 0.2, 0.5, 1, 1.5$ mL/ min, in the same controlled temperature gradient field, from ~18 to ~75 $^{o}$C (inlet-outlet liquid temperatures), were presented, respectively. It can be observed clearly that using the binary alcohol mixture different flow patterns were observed depending on the volume flow rates applied on the operating liquids. Initially, at volume flow rate of $\dot{V} = 0.2$ mL/ min, bubbly flow was observed, then it changed to slug (within some seconds) at around 73 mm from channel's inlet and back again to bubbly flow just before the bubble reached the outlet side of the channel (at ~122 mm from channel's inlet), as can be seen in Figure 6.1-2. Interestingly, at flow rate of $\dot{V} = 0.5$ mL/ min, Figure 6.1-3, the migrating bubble was shown to behave differently and a characteristic periodically increase in bubble size was clearly observed. More specifically, in the proximity of the middle part of the heated channel the bubble was seen to increase in size (visible growth) and this phenomenon was even more pronounced at the outlet side of channel. The same occurrence but with a lower bubble growth can be seen in Figure 6.1-4 where the bubble was flowing in the self-rewetting fluid at $\dot{V} = 1$ mL/ min. In contrast to all the previous case mentioned, bubble shape was not affected at flow rate of $\dot{V} = 1.5$ mL/ min in the binary alcohol mixture, as presented in Figure 6.1-5; the bubble followed steady geometry without visible fluctuations in size. It is clear that at different volume flow rates in the binary alcohol mixture and in the same controlled temperature gradient field, the induced travelling air bubbles behaved differently; thus, altering the heat transfer distribution in the micro-channel.

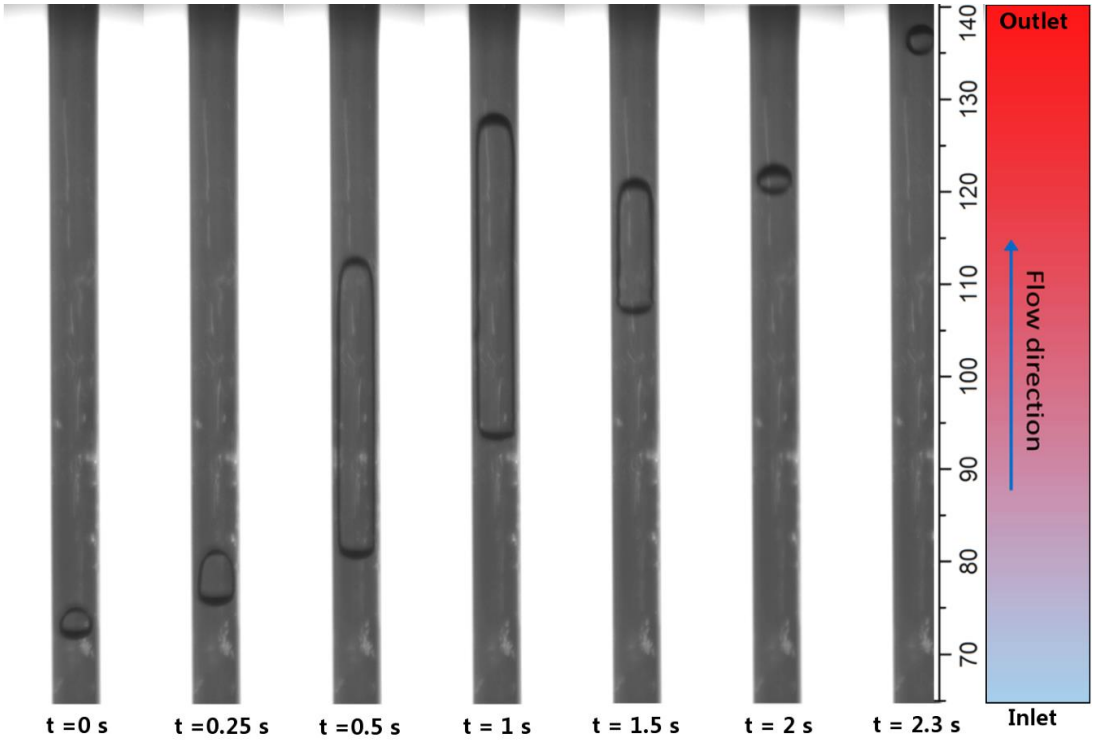


**Figure 6.1-2** Typical image sequence of the induced travelling air bubble (diameters: from ~2.3 mm to ~3.9 mm) along the (vertical) heated micro-channel containing water – 1-butanol 5% vol. mixture, versus the time, *t*. Bubble is flowing vertically in the binary alcohol mixture following the fluid flow, at flow rate of $\dot{V} = 0.2\ \mathrm{mL/min}$ , in a temperature gradient field, from ~18 to ~75 $^{o}$C (inlet-outlet liquid temperatures). Note that the bubbly-slug-bubbly flow transition observed at around 73 mm from microchannel's inlet part until the outlet.

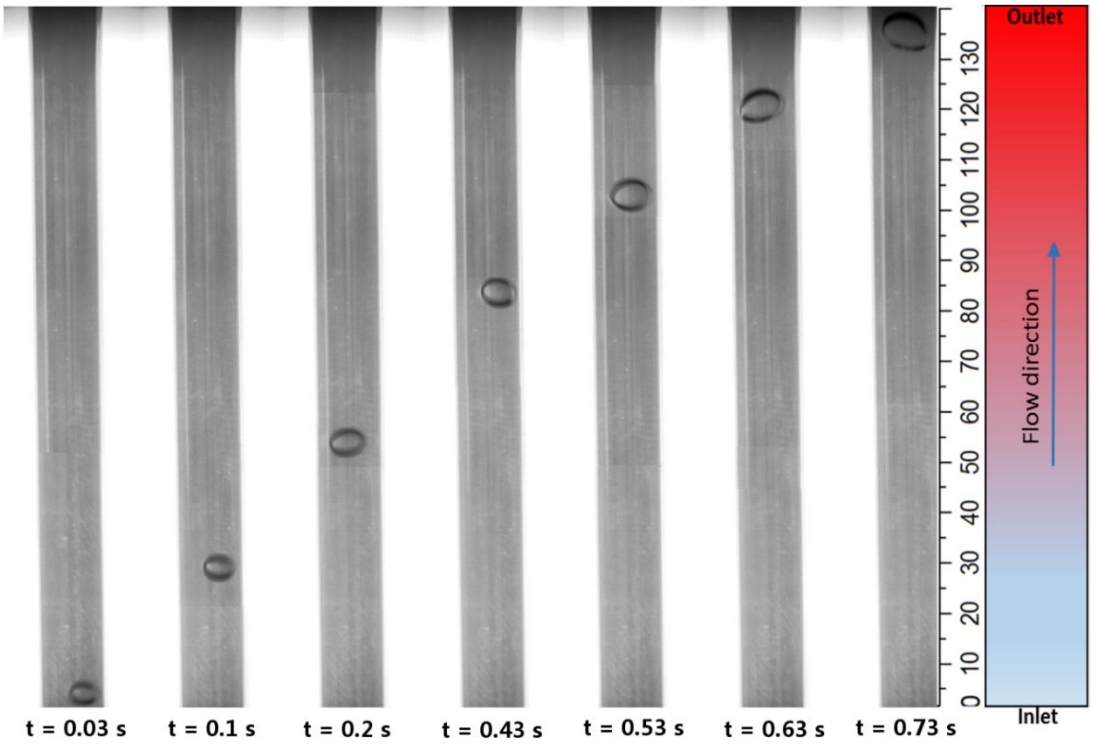


**Figure 6.1-3** Representative image sequence of the induced travelling air bubble (diameters: from ~1.2 mm to ~3.3 mm) along the (vertical) heated micro-channel containing water – 1-butanol 5% vol. as working fluid, against the time, *t*. Bubble is flowing vertically in the mixture following the fluid flow, at flow rate of $\dot{V} = 0.5\ \mathrm{mL/min}$, in a temperature gradient field, from ~18 to ~75 $^{o}$C (inlet-outlet liquid temperatures). Note that the bubble was increased in size (visual bubble growth).

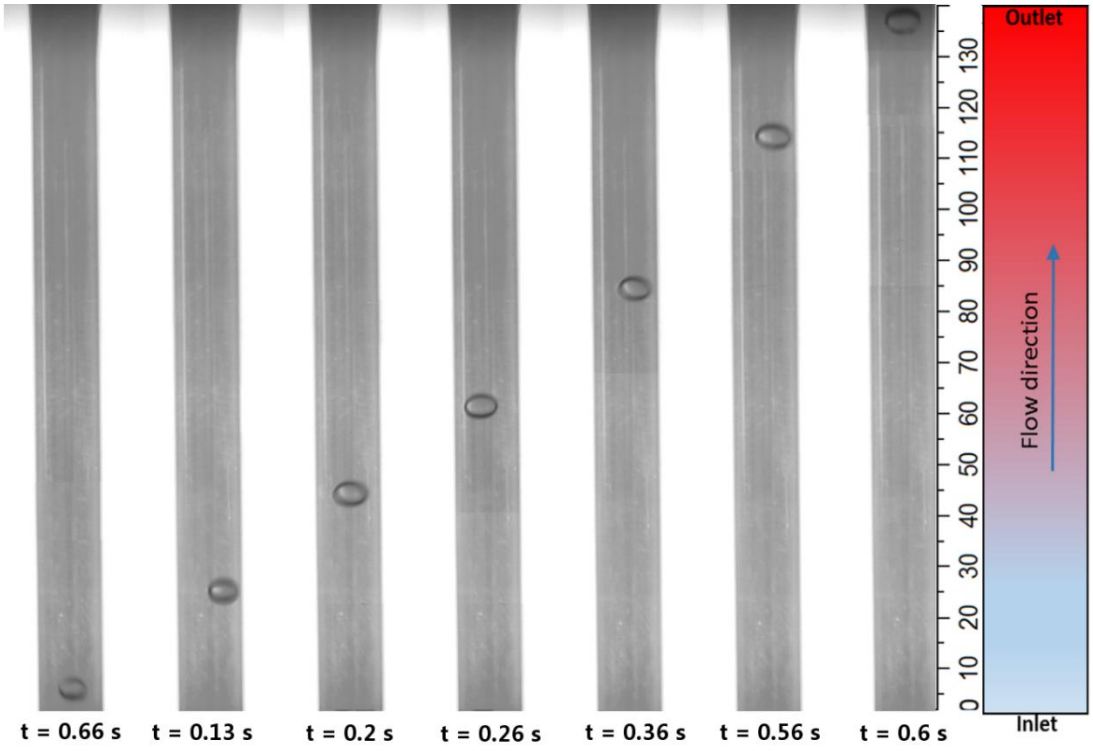


**Figure 6.1-4** Representative image sequence of the induced travelling air bubble (diameters: from ~1.5 mm to ~2.7 mm) along the (vertical) heated micro-channel containing water – 1-butanol 5% vol. as working fluid, over the time, *t*. Note that the bubble is flowing vertically in the mixture in the same direction with the fluid flow, at flow rate of $\dot{V} = 1\ \mathrm{mL/min}$ , in a temperature gradient field, from ~18 to ~75 $^{o}$C (inlet-outlet liquid temperatures).

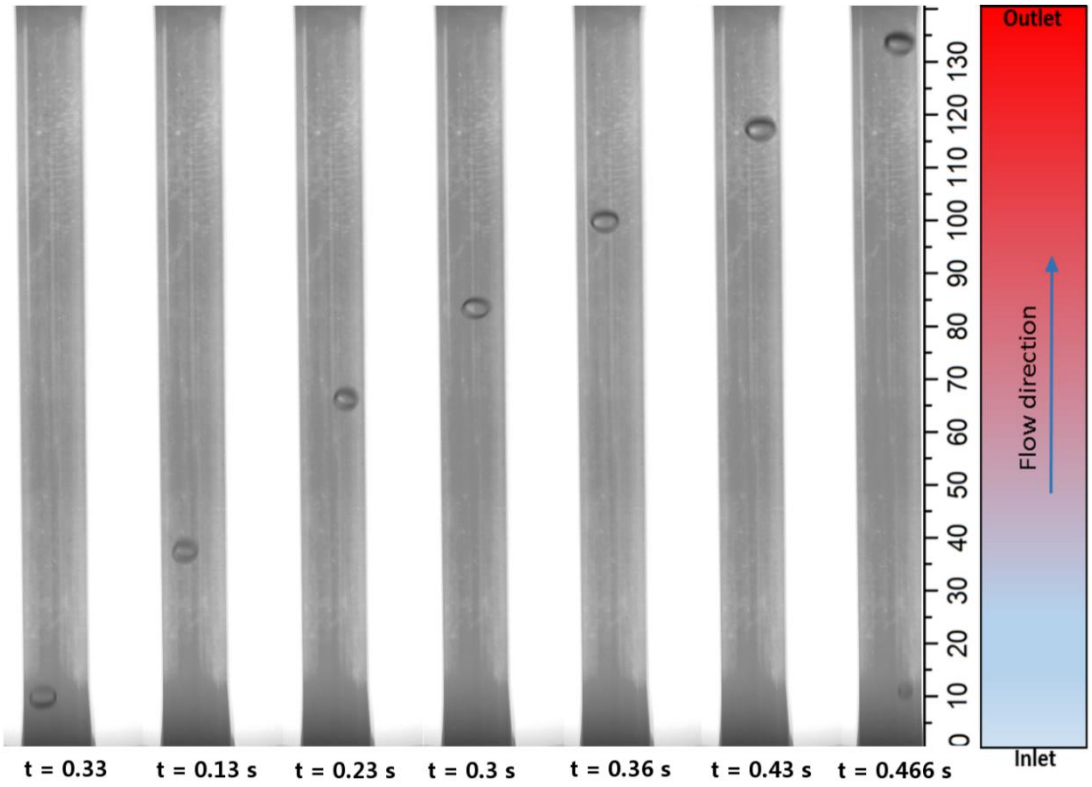


**Figure 6.1-5** Typical image sequence of the induced travelling air bubble (diameters: from ~1.6 mm to ~1.1 mm) along the (vertical) heated micro-channel containing water – 1-butanol 5% vol. as working fluid, over the time, *t*. Note that the bubble is flowing vertically in the mixture in the same direction with the fluid flow, at flow rate of $\dot{V} = 1.5\ \mathrm{mL/min}$ , in a temperature gradient field, from ~18 to ~75 $^{o}$C (inlet-outlet liquid temperatures).

The results of the bubbles position, *x*, travelling in pure water and in pure 1-butanol as operating fluids, along the circular micro-channel, versus the time, *t*, at three different volumetric flow rates: $\dot{V} = 0.2, 0.5, 1, 1.5\ \mathrm{mL/min}$, both in isothermal and non-isothermal conditions (temperature gradient cases), were presented in Figure 6.1-6, respectively. The data in Figure 6.1-6 (a) and (b) shows the migration of the manually induced bubbles under isothermal conditions of the pure liquids i.e. pure water and pure 1-butanol, at constant liquid temperature of ~18$^{o}$C, and with the characteristic obtained velocities, $\upsilon$, acquired from the visualization analysis, respectively. Graphs (c) & (d) depict the non-isothermal cases for the pure liquids, where the bubbles travelled from the cold side (bottom of the channel) to the hot side (top of the channel) in a controlled temperature gradient field, from ~18 to ~75 $^{o}$C (inlet-outlet liquid temperatures). Note that the characteristic velocities $\upsilon$, presented

in the graphs in Figure 6.1-6, for each case, were obtained after a linear fitting. It is clear from the results obtained in the pure liquids that the bubbles travelled for longer time-period i.e. lower bubble velocities, in the non-isothermal cases compared with those in the isothermal ones.

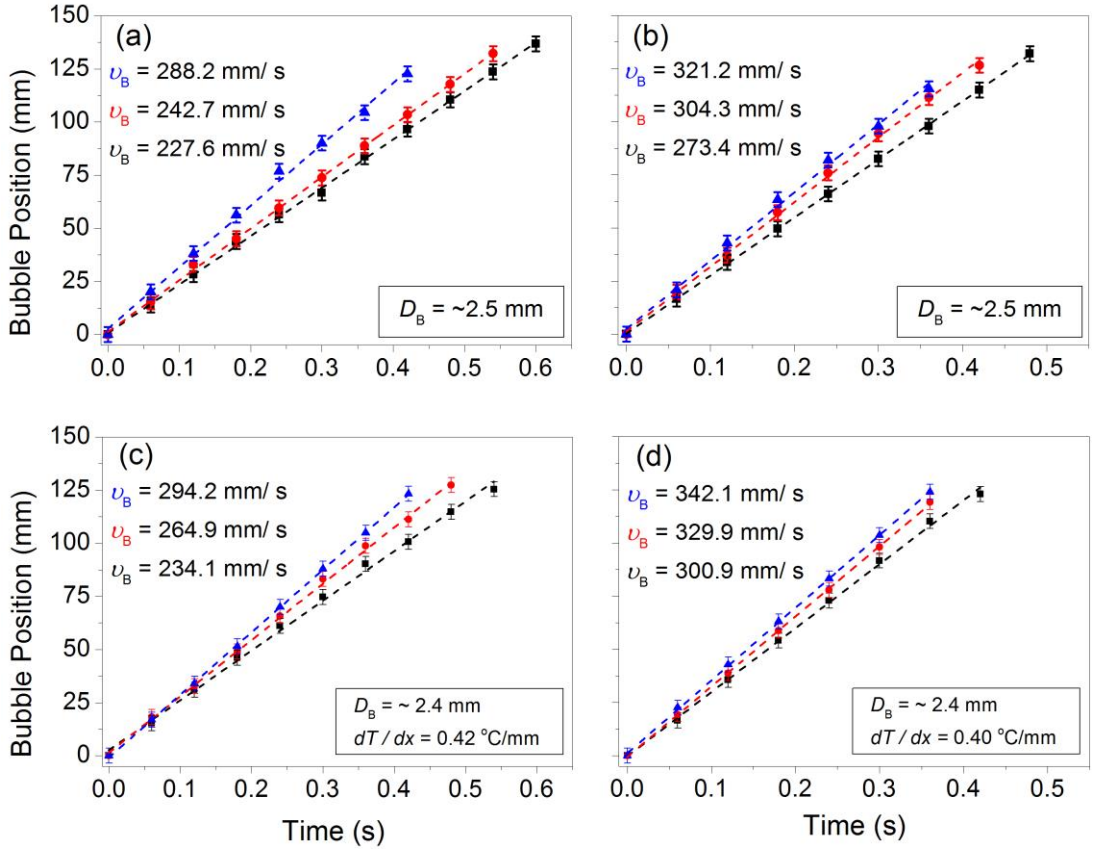


**Figure 6.1-6** Typical examples of the air bubbles positon, *x*, along the circular channel in pure water and pure 1-butanol, both in isothermal and temperature gradients cases, for three different volumetric flow rates: $\dot{V}$= 0.5 (■), 1 (●), 1.5 (▲) mL/ min, against time. More specifically, graphs (a) pure water and (b) pure 1-butanol depict calculations for the isothermal case, at temperature of ~18°C, and with the characteristic velocities, $\upsilon$, for each flow rate. Graphs (c) and (d) present examples of migrating bubbles in pure water and pure 1-butanol, in temperature gradient field, from ~18 to ~75 °C (inlet-outlet liquid temperatures), and the characteristic bubble velocities, $\upsilon$, for each volume flow rate, respectively. Note that in all cases, the velocities were obtained after a linear fitting. Errors regarding the bubble measurements are presented in the Table 3.1-2, bubble radius error around 6%.

In what follows, similar experiments using a self-rewetting fluid as a flowing liquid were conducted. The results of the air bubbles position, *x*, travelling in the circular micro-channel containing a water – 1-butanol 5% vol. mixture, versus time, at three different volumetric flow rates: $\dot{V} = 0.2, 0.5, 1, 1.5\ \mathrm{mL/\ min}$, are presented in Figure 6.1-7. The data, in Figure 6.1-7 (a), depicts the isothermal case of the flowing liquid mixture, at liquid temperature of ~18$^{o}$C, with the obtained characteristic velocities $\upsilon$ of the vertically air bubbles migrating from the inlet to the outlet of the channel, for each flow rate, respectively. Furthermore, the results of the bubbles movement in the alcohol mixture, from the gold (down) to the hot side (upper) of the channel, in a temperature gradient field from ~18 to ~75 $^{o}$C (inlet-outlet liquid temperatures), versus the time, *t*, at the same three volume flow rates as discussed above, presented in the graph (b) of the Figure 6.1-7. It is worth noting, that in all cases bubble velocities, $\upsilon$, were estimated by using linear fitting with the exception for the two cases at $\dot{V} = 0.2, 0.5\ \mathrm{mL/\ min}$, Figure 6.1-7 (b). In these distinct cases (volume flow rates), the bubbles were seen to flow non-linearly (algorithmic behaviour) along the channel and the acquired bubbles velocities were the average speeds, $\bar{\upsilon}$. Another feature was that in the non-isothermal cases the bubbles were travelling for longer time-period in the mixture compared to those in the isothermal cases. This might have pointed out the importance of the thermocapillary forces (Marangoni effect) acting in our system. This complicated behaviour of the migrating bubbles along the heated micro-channel was clearly associated with the anomalous (non-linear) dependence of the surface tension with the temperature of this binary alcohol mixture, the well-defined minimum and this will be explained in the discussion Chapter 6.3.

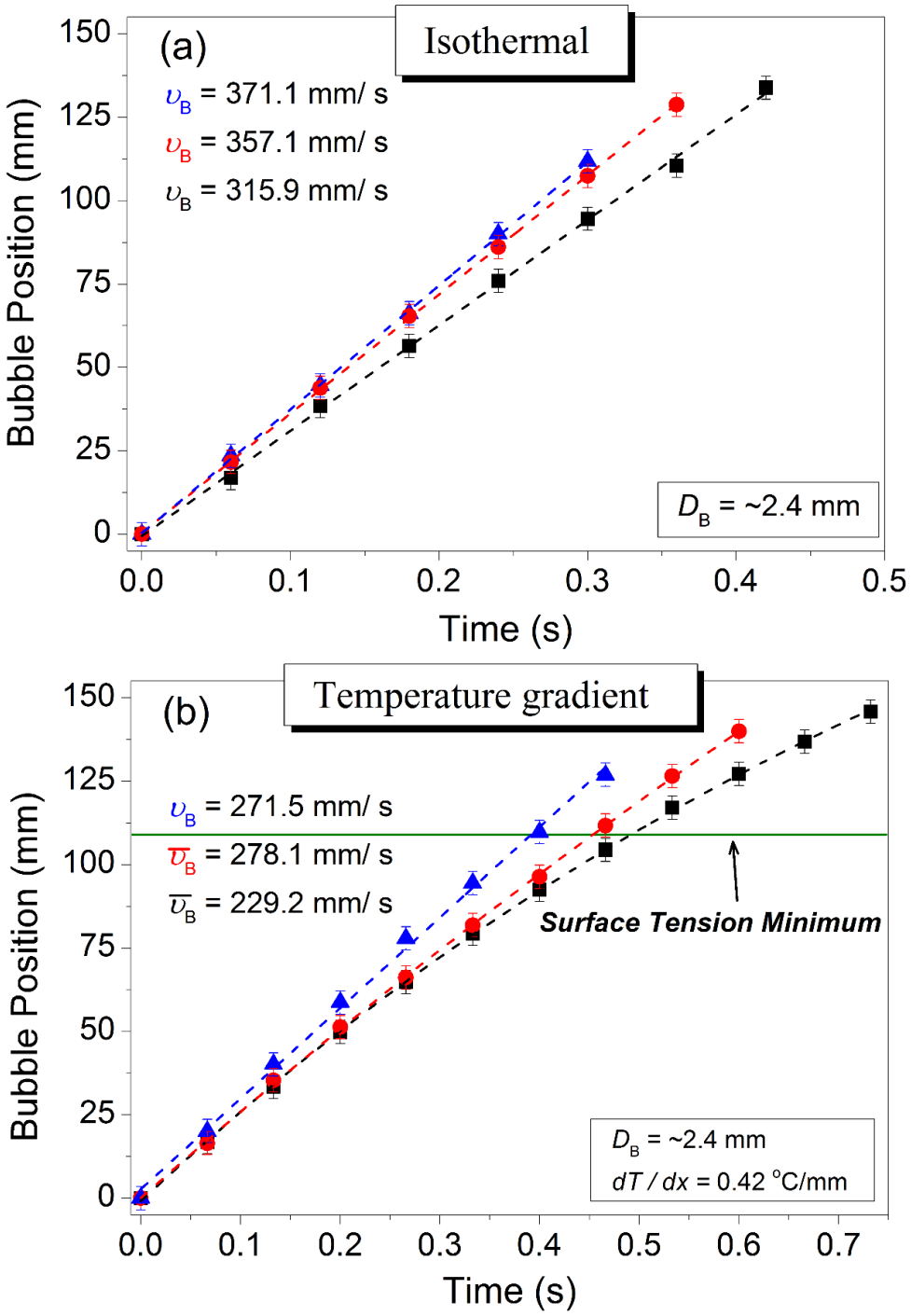


**Figure 6.1-7** Representative examples of the induced air bubbles position, *x*, along the channel filled with the water - 1-butanol 5% vol. mixture, versus the time, *t*, both in isothermal and temperature gradient cases, for three different volumetric flow rates: $\dot{V}$= 0.5 (■), 1 (●), 1.5 (▲) mL/ min. In more details, graph (a) depicts results in the isothermal case, at liquid temperature of 18 ±1 °C, and with the calculated velocities, $\upsilon$, for each flow rate. In graph (b) the data shows examples of bubbles in the binary mixture, subjected in a temperature gradient, from 18 to 75 ±1 °C, versus time, for each volume flow rate, respectively. Note that in graph (b), at $\dot{V}$= 0.5 (■) and 1 (●) mL/ min, the velocities presented are averages $\bar{\upsilon}$, for each case

and were obtained after a non-linear approach (algorithmic shape). Errors regarding the bubble measurements are presented in the Table 3.1-2, bubble radius error around 6%.

In this fashion, the case of the induced bubble travelling in the binary alcohol mixture at $\dot{V} = 0.2$ mL/ min, was analysed separately. In Figure 6.1-8 (a), the distance, *x*, of the travelling bubble, as shown in Figure 6.1-2, was plotted against time and the temperature, *T*. In contrast to all examples presented above i.e. in pure liquids and in binary mixture fluid flows under non-isothermal conditions, for this case, at $\dot{V} = 0.2$ mL/ min , a rather different picture was revealed regarding the bubble behaviour. At the beginning, bubbly flow was observed, then changed to slug flow and before the outlet part of channel the fluid flow was changed back to bubbly. Figure 6.1-2 (b) presents the velocity profile of this characteristic case versus time. During the slug flow, the velocity profiles of the bottom and the upper part of the slug were analysed individually, as displayed in Figure 6.1-2 (b).

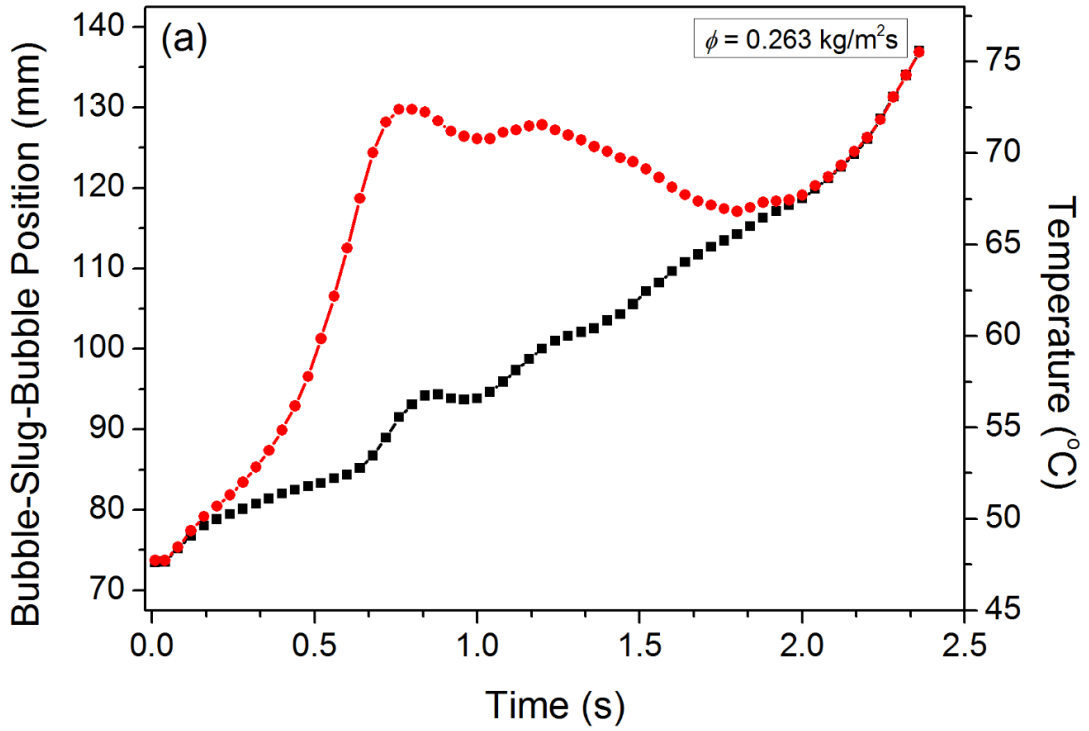

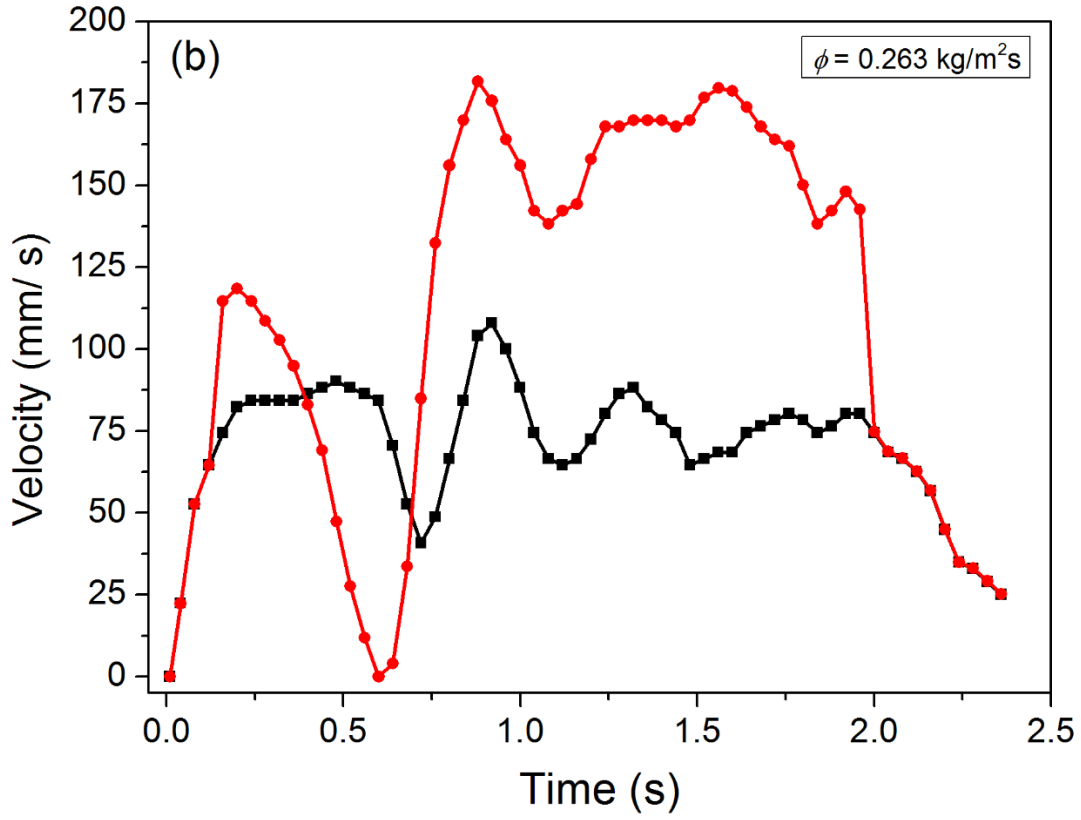


**Figure 6.1-8** (a) Portrayed behaviour (■) bottom side and (●) upper side of the migrating bubble, as shown in Figure 6.1-2, of the observed bubbly-slug-bubbly flow transition as distance, *x*, at ~73 mm, from inlet (cold) to outlet (hot) side of the channel, versus time and the temperature, *T*, at 0.2 mL/ min volume flow rate. Graph (b) shows the velocity profile for this case versus time along the channel where (■) is velocity of the bottom and (●) is velocity of the upper side. Errors regarding the bubbly-slug-bubbly flow measurements are presented in the Table 3.1-2, bubble radius error around 6%.

Furthermore, particular attention was paid to further examine the bubble geometry evolution under different experimental conditions. A methodical examination of the travelling bubbles aspect ratios (bubble *width* / *length*) were visually conducted, along the micro-channel containing the pure liquids and the binary alcohol mixture, both in isothermal and non-isothermal cases. In Figure 6.1-9 and 6.1-10, the aspect ratio measurements of the induced travelling air bubbles along the micro-channel in pure water and in pure 1-butanol, versus time and the position, *x*, at three different mass fluxes, $\phi$, and average heat fluxes, $q_{avg}$, (temperature gradient cases), were presented, respectively. More specifically, in Figure 6.1-9 the graphs (a) – (c) depict the bubble aspect ratios in the isothermal cases (at ~18$^o$C), and graphs (d) – (e) show the

temperature gradient cases aspect ratios (from ~18 to ~75 °C, inlet-outlet liquid temperatures, respectively). The green curves in Figure 6.1-9 depict the average aspect ratios for each case, respectively. Similarly, in Figure 6.1-10 (a) – (c), bubble aspect ratio measurements in the isothermal conditions and graphs (d) – (e) depict the non-isothermal cases (from ~18 to ~75 °C) of pure 1-butanol as working fluid, at three different mass fluxes, $\phi$, and average heat fluxes, $q_{avg}$, (temperature gradient cases), were displayed, respectively. Note that in the cases of the bubbles travelling in pure water, both in isothermal and temperature gradient cases, aspect ratio values showed slight size fluctuations. Interestingly, these fluctuations were a bit stronger (as it can be seen in graphs (c) and (f) in Figure 6.1-9), and were associated with the highest mass fluxes applied for these cases. This might be the point that the bubbles geometry was affected by the applied liquid flow. Similar behaviour was revealed in all the temperature gradient cases in the pure 1-butanol fluid flow where the induced travelling bubbles were seen to deform adapting a disklike shape and thus to fluctuate the bubbles' aspect ratios, as displayed in Figure 6.1-10.

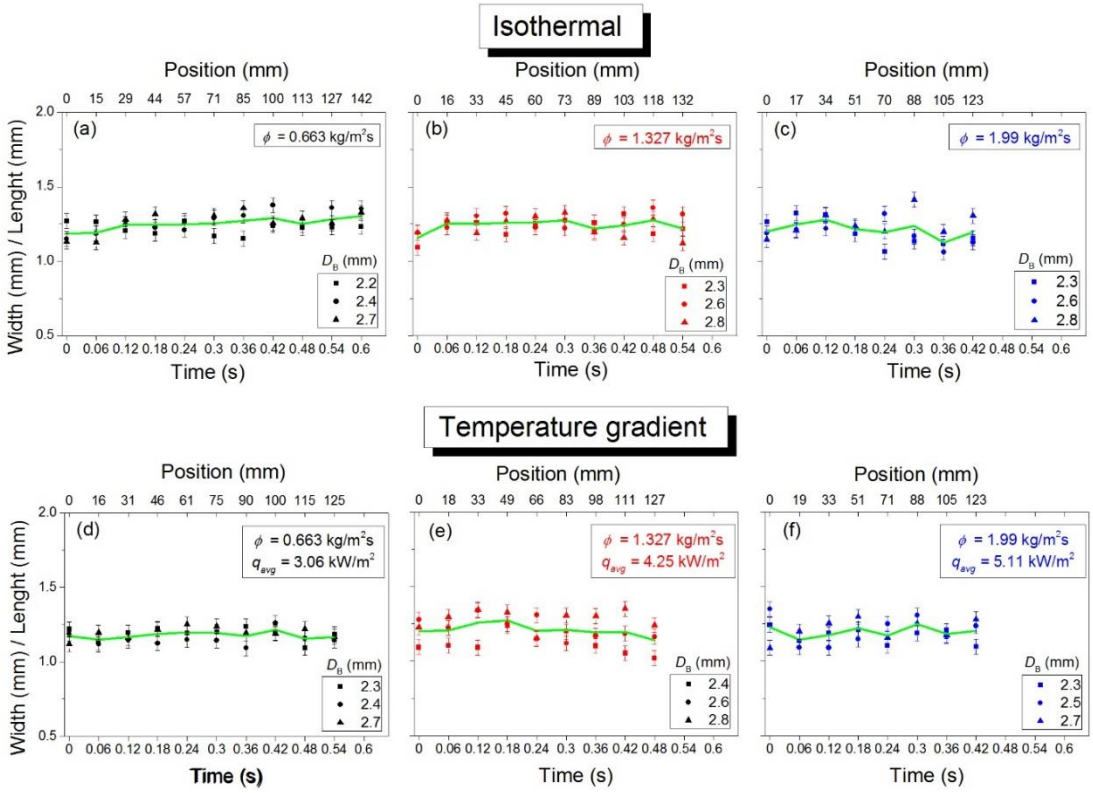


**Figure 6.1-9** Aspect ratio (bubble width / length) calculations of the migrating air bubbles along the circular microchannel in pure water (working fluid), over time and the position, *x*,

at three typical mass fluxes, $\phi$, and at three different average heat fluxes, $q_{avg}$, (temperature gradient cases). Graphs (a) – (c) present characteristic bubble aspect ratios in the isothermal case of pure water fluid flow with the calculated averages (green curve), for each case. Similarly, graphs (d) – (e) show aspect ratio calculations in a temperature gradient field, from ~18 to ~75 ºC (inlet-outlet liquid temperatures), for three different mass fluxes, $\phi$, the (average) heat fluxes, $q_{avg}$, and the average aspect ratios (green curve), respectively. Absolute errors related to bubble aspect ratios measurements are presented in the Table 3.1-2, error around 6%.

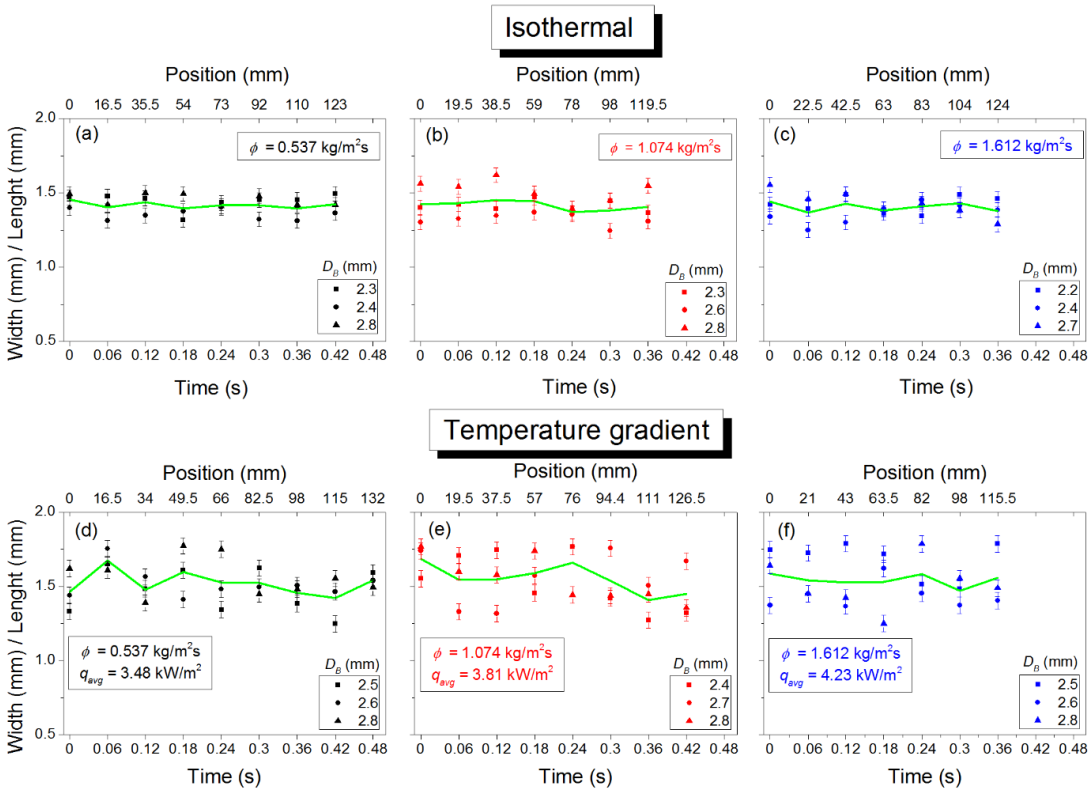


**Figure 6.1-10** Aspect ratio (bubble width / length) calculations of the travelling air bubbles along the circular micro-channel in pure 1-butanol, against time and the position, *x*, at three typical mass fluxes, $\phi$, and at three different average heat fluxes, $q_{avg}$, (temperature gradient cases). More specifically, graphs (a) – (c) present characteristic bubble aspect ratios in the isothermal case of pure 1-butanol operating fluid with the calculated averages, for each case. Graphs (d) – (e) show aspect ratio values in a temperature gradient case, from ~18 to ~75 ºC (inlet-outlet liquid temperatures), at the three typical cases with the obtained averages aspect ratios (green curve). Absolute errors related to bubble aspect ratios measurements are presented in the Table 3.1-2, error around 6%.

In what follows, the aspect ratio calculations of the induced travelling air bubbles in the water – 1-butanol 5% vol. mixture (self-rewetting fluid), versus time and the position, *x*, in the isothermal case, flowing liquid temperature at around 18°C, and in non-isothermal case from ~18 to ~75 °C, at three different mass fluxes, $\phi$, and average heat fluxes, $q_{avg}$, (for the temperature gradient cases), were presented in Figure 6.1-11, respectively. In more details, graphs (a) – (c) depict aspect ratios in the isothermal cases and graphs (d) – (e) refer to the temperature gradient cases in the binary alcohol mixture. Interestingly, it can be seen in Figure 6.1-11 (d) and (e) that the aspect ratio (bubble *width*/ *length*) showed a peculiar increase. A characteristic bubble ratio growth up to ~25% of the initial size was observed in graph (d), at $\dot{V} = 0.5\ \mathrm{mL/min}$, where bubbles were travelling along the channel in the upward temperature gradient, from the cold towards the hot side of the channel. In the case of bubble migrating at $\dot{V} = 1\ \mathrm{mL/min}$, an increase in bubble ratio of up to ~10% can be seen in Figure 6.1-11 (e). These observations were clearly associated with the anomalous (non-linear) dependence of the surface tension with the temperature for this binary alcohol mixture used (discussed in Chapter 2.7). In contrast to the previous cases, bubbles travelling in the alcohol mixture at $\dot{V} = 1.5\ \mathrm{mL/min}$ were not affected by the temperature gradient field due to the high mass flux applied in these series of experiments.

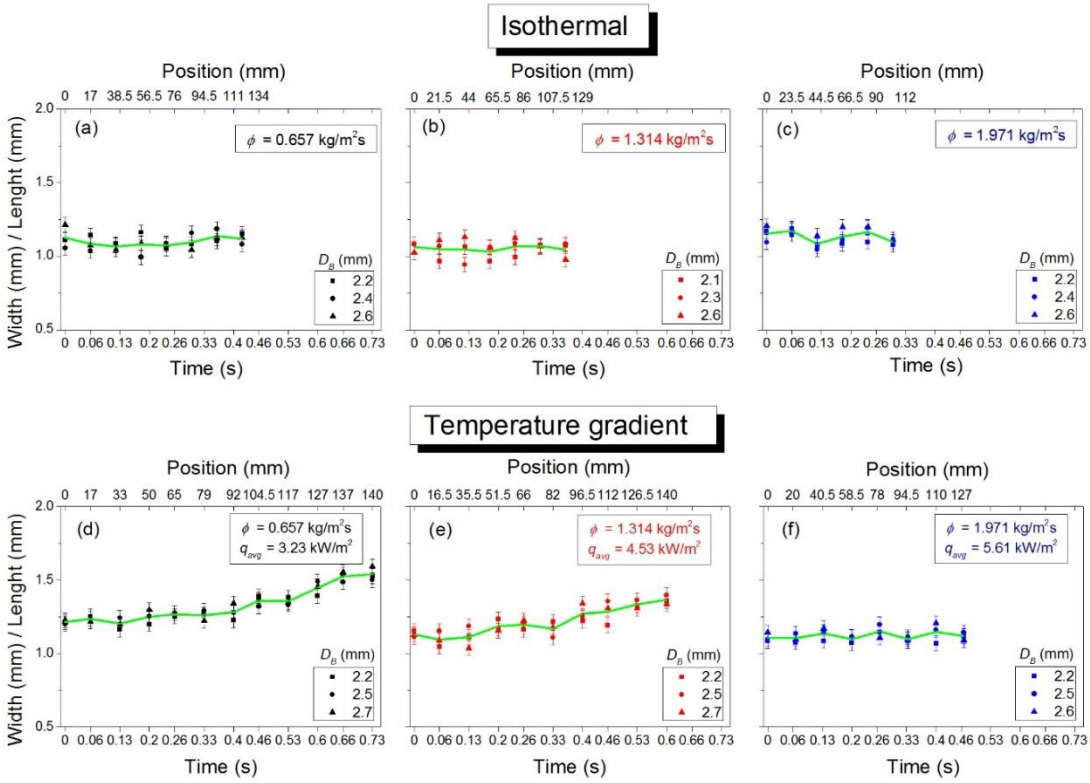


**Figure 6.1-11** Representative aspect ratio (bubble width / length) measurements of the migrating air bubbles along the circular micro-channel filled with water – 1-butanol 5% vol. mixture, over time and the position, $x$, at three typical mass fluxes, $\phi$, and at three average heat fluxes (temperature gradient cases), $q_{\text{avg}}$. More specifically, graphs (a) – (c) present typical bubble aspect ratio calculations in the isothermal case with the calculated averages, for each case, respectively. Graphs (d) – (e) show aspect ratio calculations in a temperature gradient field, from ~18 to ~75 $^{o}$C (inlet-outlet liquid temperatures), at the three different cases. The green curves depict the average aspect ratios for all cases. Absolute errors related to bubble aspect ratio measurements are presented in the Table 3.1-2, error around 6%.

In Figure 6.1-12, the size i.e. *width* and *length*, of the characteristic bubble-slug-bubble case, which was visually presented in Figure 6.1-2, was plotted against the position, $x$, and the temperature, $T$, in the alcohol mixture, in a temperature gradient field, from ~18$^{o}$C (inlet) to ~75$^{o}$C (outlet), at $\dot{V} = 0.2$ mL/ min. At around 77 mm from the channel's inlet, the bubble showed a significant increase in length at the time that the bubble width reached the size of the channel's diameter (close to ~3.9 mm); then the characteristic slug (flow transition) was observed to occur. Interestingly, the slug flow was changed back to bubbly flow at ~ 118 mm from channel's inlet until

the outlet side. It is clear that the behaviour of the bubble in the alcohol mixture, at this applied (lowest) volume flow rate ($\dot{V} = 0.2$ mL/ min), was drastically affected by the temperature gradient field (surface tension dependence with temperature) and the generated strong thermocapillary forces-flows (Marangoni effect) acted and deformed the travelling bubble.

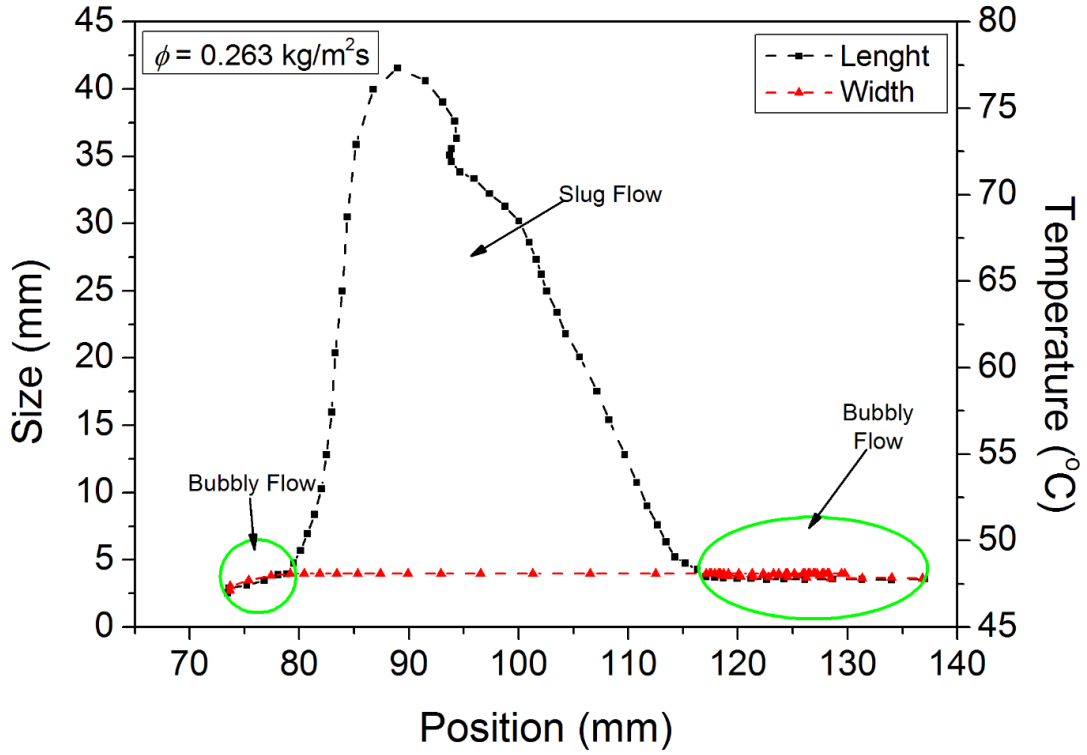


**Figure 6.1-12** Typical example of the bubble-slug-bubble case (start at ~ 73 mm from the channel's inlet) containing water-1-butanol 5% vol. mixture versus the position, *x*, and the temperature, *T*, along the heated micro-channel, at $\dot{V} = 0.2$ mL/ min liquid volume flow rate. Errors related to the size i.e. *width* and *length* measurements of the characteristic bubble-slug-bubble case are presented in the Table 3.1-2, error around 6%.

The relative importance of the momentum forces (inertia resistance) to the viscous forces for the different flow conditions applied in our experiments was calculated using the dimensionless Reynolds number, $Re = \frac{inertia\ forces}{viscous\ forces} = \frac{\rho VL}{\mu} = \frac{VL}{\nu}$ where $\rho$ is the density of the fluid (kg/m$^3$), $V$ is the maximum velocity of the object relative to the fluid (m/s), $L$ is the characteristic linear dimension of the channel (travel length of

the of the fluid) (m), $\mu$ is the dynamic viscosity of the fluid (Pa·s or N·s/m$^2$ or kg/(m·s)) and $v$ is the kinematic viscosity of the fluid ($v = \frac{\mu}{\rho}$) (m$^2$/s). The obtained Reynold numbers for the pure liquids (pure water and pure 1-butanol) and the binary alcohol mixture (self-rewetting fluid) under different experimental conditions are presented in Figure 6.1-13. The characteristic low values of the calculated Reynold numbers indicated that the behaviour of all the operating fluids were depended mostly on its viscosity and also the applied liquid flows were steady and smooth, in agreement with previous reported studies [174, 175, 229].

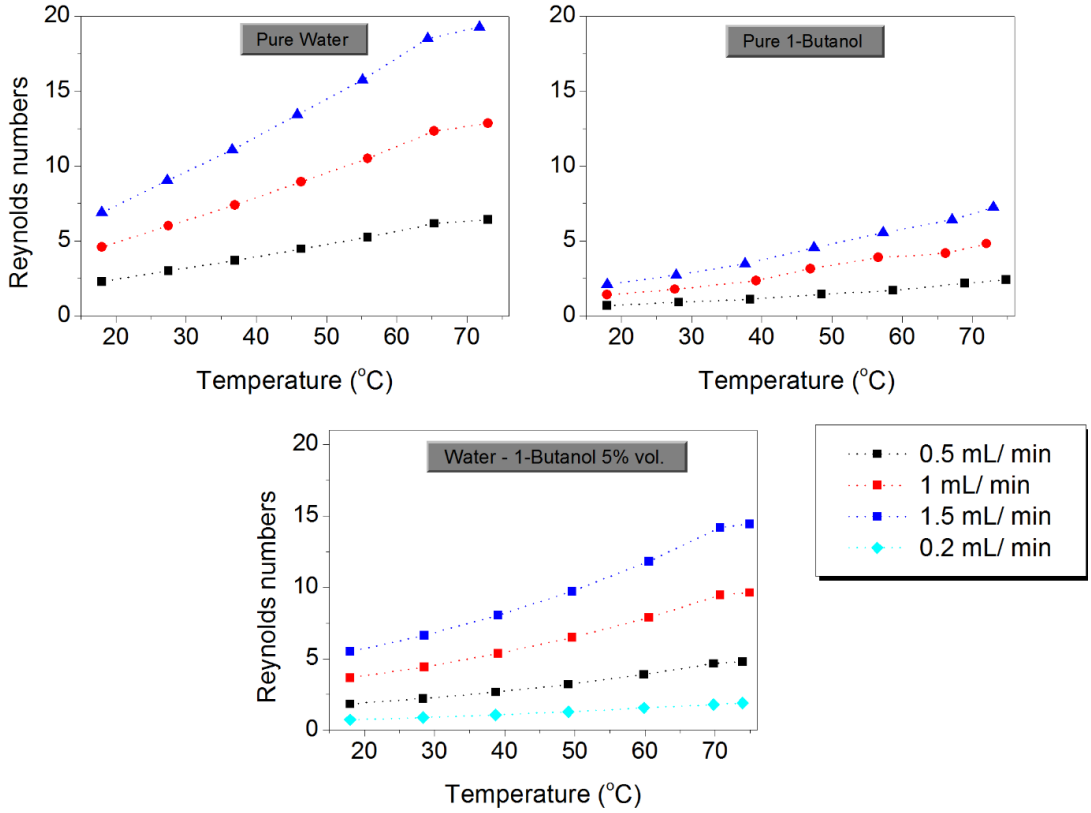


**Figure 6.1-13** Reynold numbers calculation of the pure liquids: pure water and pure 1-butanol, and the binary alcohol mixture (water-1-butanol 5% vol.), versus the temperature along the heated channel, for different volume flow rates, in the same controlled temperature gradient field, from 18 to 75 ±1 °C, respectively. Absolute errors related to Reynolds number calculations are presented in the Table 3.1-2.

## 6.2 Heat Transfer Coefficient

Continuing with the efforts to investigate the motion of air bubbles travelling vertically in a micro-channel filled with pure liquids and a self-rewetting fluid, under isothermal and non-isothermal conditions, using different mass fluxes and heat fluxes, another series of calculations was conducted regarding the heat transfer distribution along the channel in the single phase and two-phase flows. Details regarding the experimental apparatus, methodology, data reduction (heat loss and heat transfer) and absolute errors were extensively discussed in Chapter 3.1.5. The dependency of the heat transfer coefficient,$h_{S.P.}$, in the single phase flow, on the different applied heat fluxes, at ten different mass fluxes, $\phi$ (eq. 3.1), containing the ordinary liquids (pure water and pure 1-butanol) and the water – 1-butanol 5% vol. mixture, in a temperature gradient field from ~18$^o$C (inlet) to ~75$^o$C (outlet), was presented in Figure 6.2-1. Note that heat transfer coefficients in the single phase flows were estimated by using: $h_{S.P.} = \frac{q}{T_W - T_L}$ where $q$ is the heat flux, $T_W$ is the wall temperature of the channel (IR thermography images) and $T_L$ is the liquid temperature, see also Chapter 3.1.5.1. As the higher flow rate strengthens the convective heat transfer, the corresponding channel wall temperature becomes lower. Therefore, higher heat flux was required to keep uniform the temperature gradient field along the channel. It can be clearly seen that heat transfer coefficient values were found to increase as heat flux was increased (also mass flux $\phi$ was increased in the same temperature gradient field) leading to a better heat transfer performance, for all the cases examined in our system, as displayed in Figure 6.2-1, in good agreement with previous studies [172, 175, 229-231].

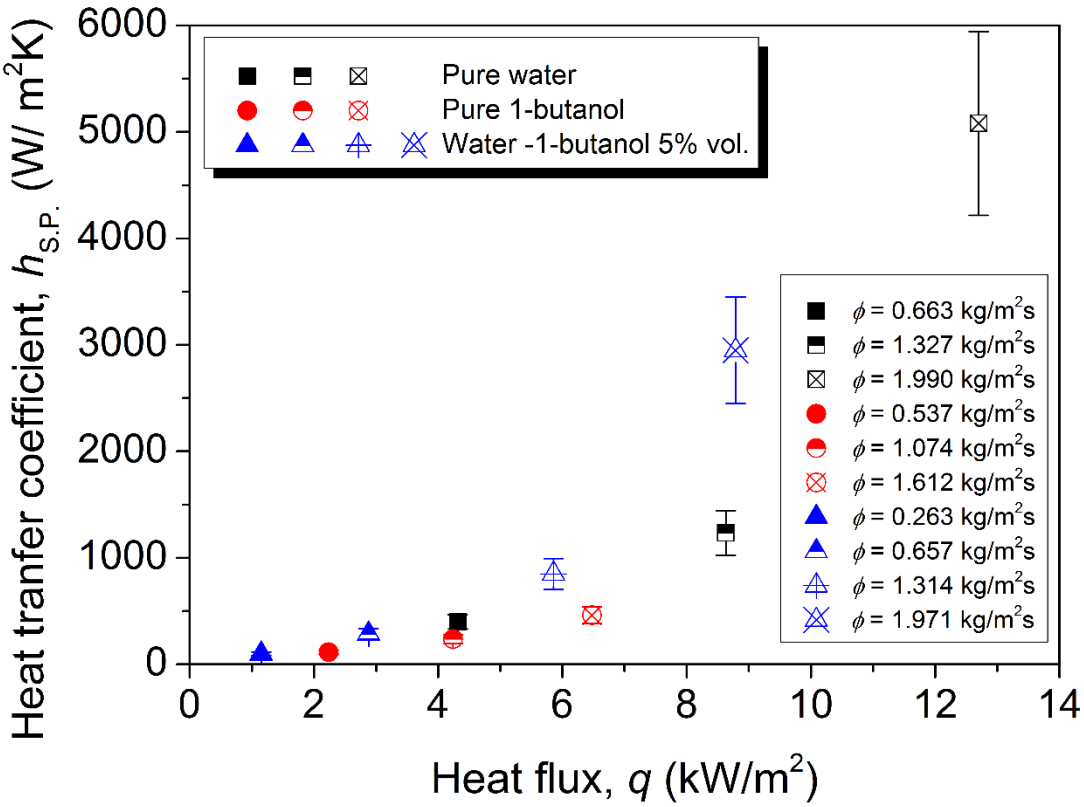


**Figure 6.2-1** Calculated heat transfer coefficient values, $h_{S.P.}$, in the single phase flow versus the heat flux, $q$, at ten different mass fluxes, $\phi$, in the same circular heated micro-channel, for all the working fluids were used in our experimental work. Absolute errors related to single phase heat transfer coefficient calculations are presented in the Table 3.1-2, error around 17%.

Additionally, local heat transfer coefficient calculations, $h_{T.P.,local}$, in the two phase flow were performed along the channel, at seven specific locations as can be seen in Figure 6.2-2 and 6.2-3 (see also schematic drawing in Figure 3.1-11 ), filled with the pure liquids: pure water and pure 1-butanol, in a controlled temperature gradient field, from ~18°C to ~75°C, respectively. The time-averaged temperatures at seven locations were calculated to reveal the local heat transfer coefficient, $h_{T.P.,local}$, in the two-phase flow system by using: $h_{T.P.,local} = \frac{q}{T_{W,local} - T_{L,local}}$ (eq. 3.7). In details, Figure 6.2-2 shows the obtained local heat transfer coefficient values of the migrating bubble in pure water, versus the position, $x$, and temperature, $T$, along the heated channel, at three different mass fluxes, $\phi$, respectively. Moreover, Figure 6.2-3 presents the dependency of local heat transfer coefficient,. $h_{T.P.,local}$, in the two phase flow on the position, $x$, and on temperature, $T$, containing pure 1-butanol, at three different $\phi$, in

the same temperature gradient field, from ~18°C to ~75°C (inlet-outlet liquid temperatures). In addition, a comparison regarding the three different mass fluxes applied on both pure liquids was presented in Figure 6.2-2 (d) and 6.2-3 (d), respectively. It was shown that the higher mass flux applied, the better heat transfer performance was revealed in both pure working fluid cases. Another clear feature is that the bubbles were seen to follow the same trend in terms of the position, *x*, along the channel, in the same operating fluid, but the calculated heat transfer coefficient values were higher for the higher mass fluxes, as stated in both Figure 6.2-2 and 6.2-3.

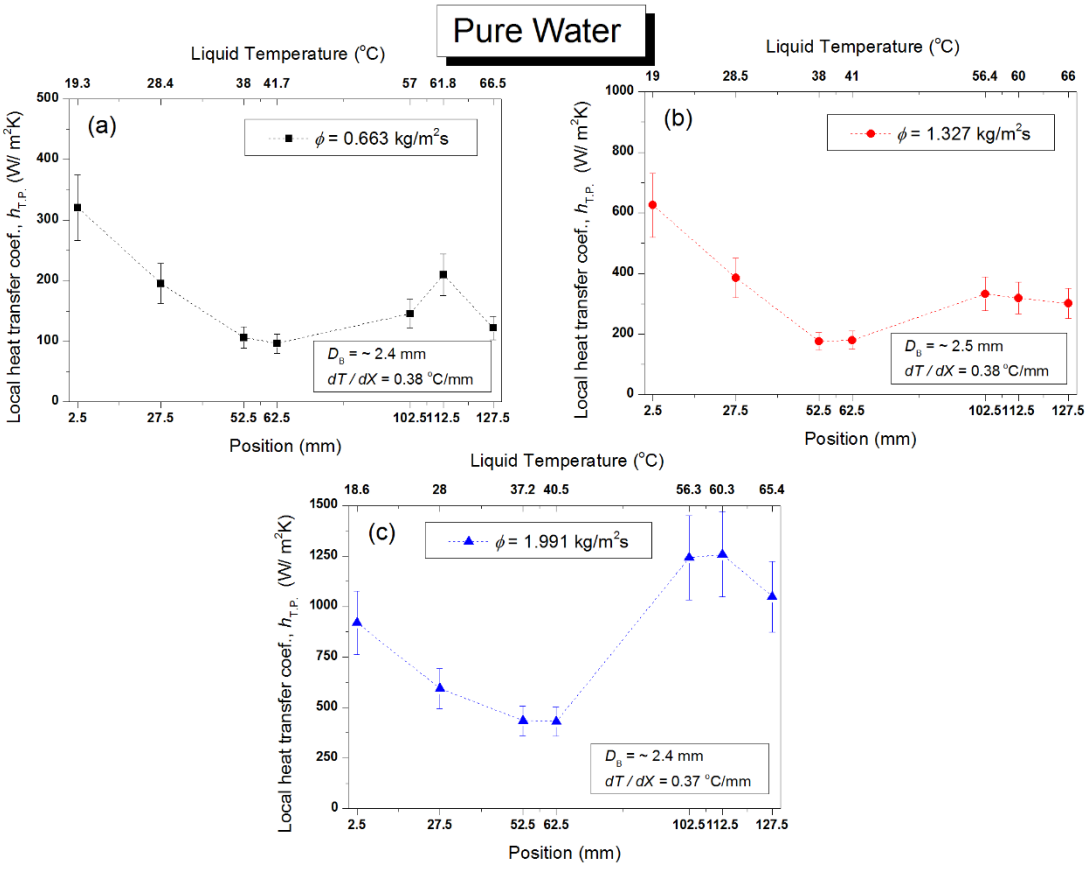

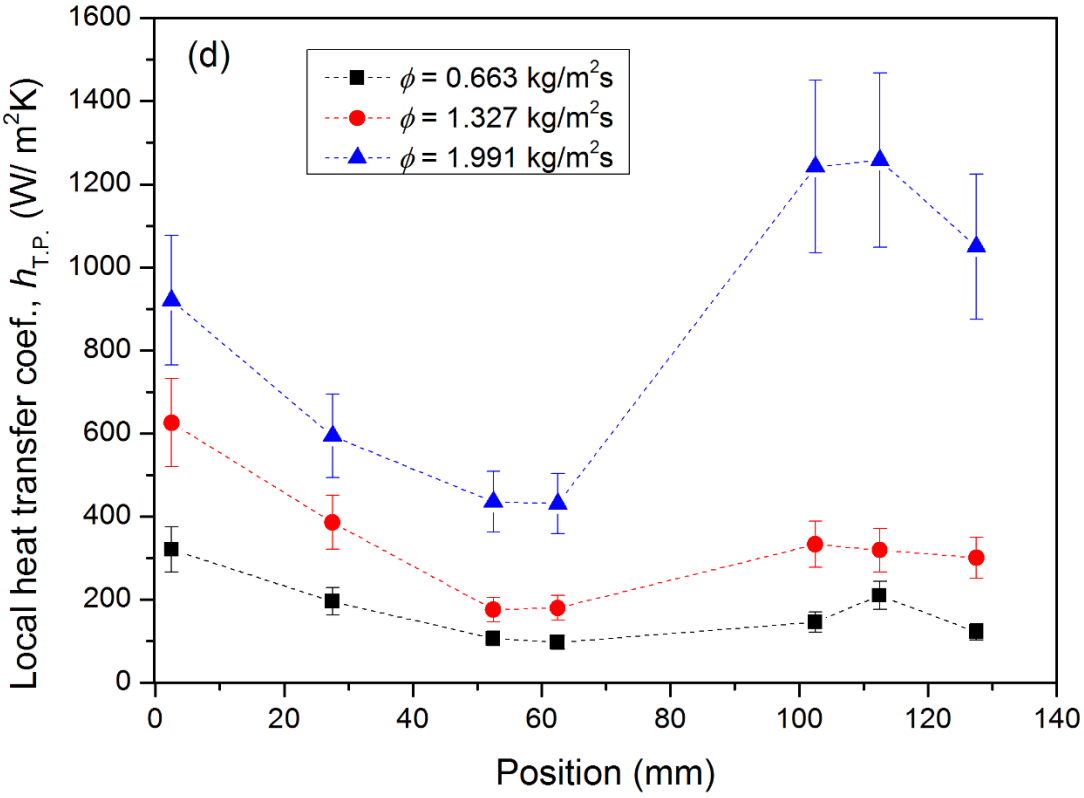


**Figure 6.2-2** Local heat transfer coefficient, $h_{T.P.,local}$, calculations in the two phase flow versus the position, $x$, and the temperature, $T$, at three different mass fluxes, $\phi$, in the same temperature gradient field, from ~18°C to ~75°C (inlet-outlet liquid temperatures), filled with pure water as working fluid. Absolute errors regarding two-phase heat transfer coefficient calculations are presented in the Table 3.1-2, error around 17%.

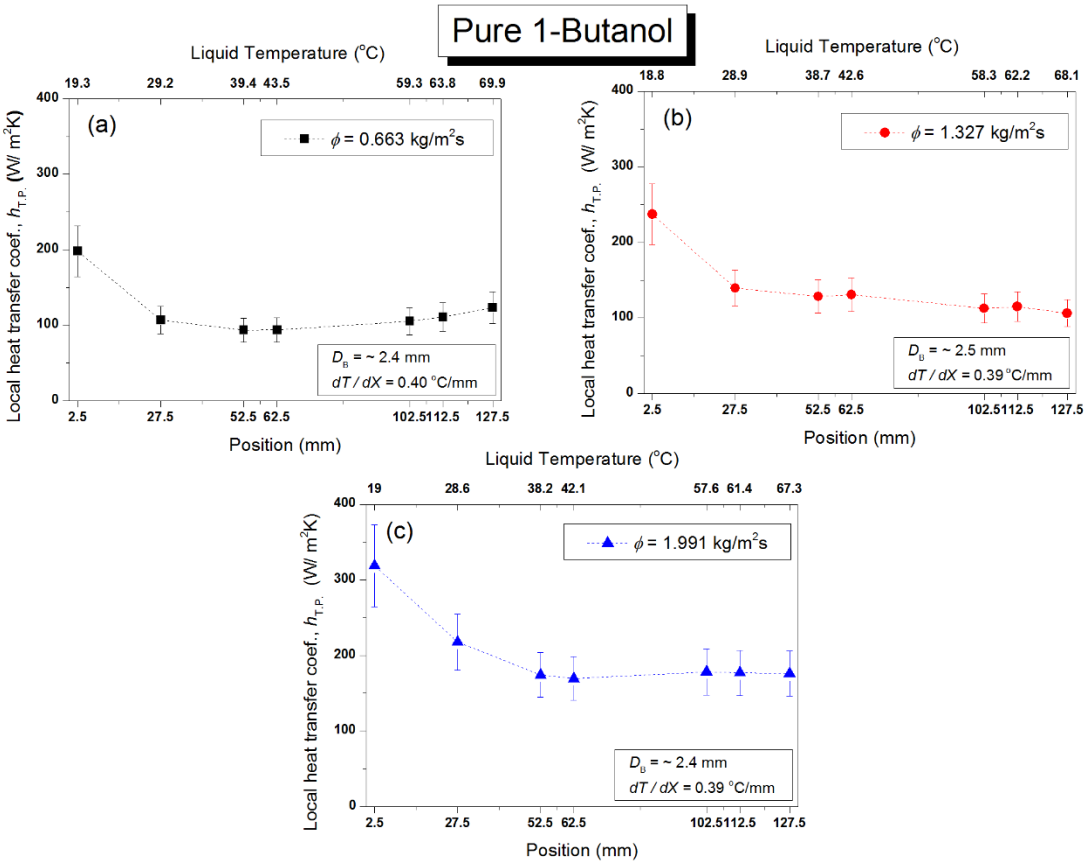
Pure 1-Butanol
Liquid Temperature (°C)
19.3 29.2 39.4 43.5 59.3 63.8 69.9
(a)
$\phi$ = 0.663 kg/m$^2$s
$D_B$ = ~ 2.4 mm
$dT/dX$ = 0.40 °C/mm
Local heat transfer coef., $h_{T.P.}$ (W/ m$^2$K)
Position (mm)
Liquid Temperature (°C)
18.8 28.9 38.7 42.6 58.3 62.2 68.1
(b)
$\phi$ = 1.327 kg/m$^2$s
$D_B$ = ~ 2.5 mm
$dT/dX$ = 0.39 °C/mm
Local heat transfer coef., $h_{T.P.}$ (W/ m$^2$K)
Position (mm)
Liquid Temperature (°C)
19 28.6 38.2 42.1 57.6 61.4 67.3
(c)
$\phi$ = 1.991 kg/m$^2$s
$D_B$ = ~ 2.4 mm
$dT/dX$ = 0.39 °C/mm
Local heat transfer coef., $h_{T.P.}$ (W/ m$^2$K)
Position (mm)

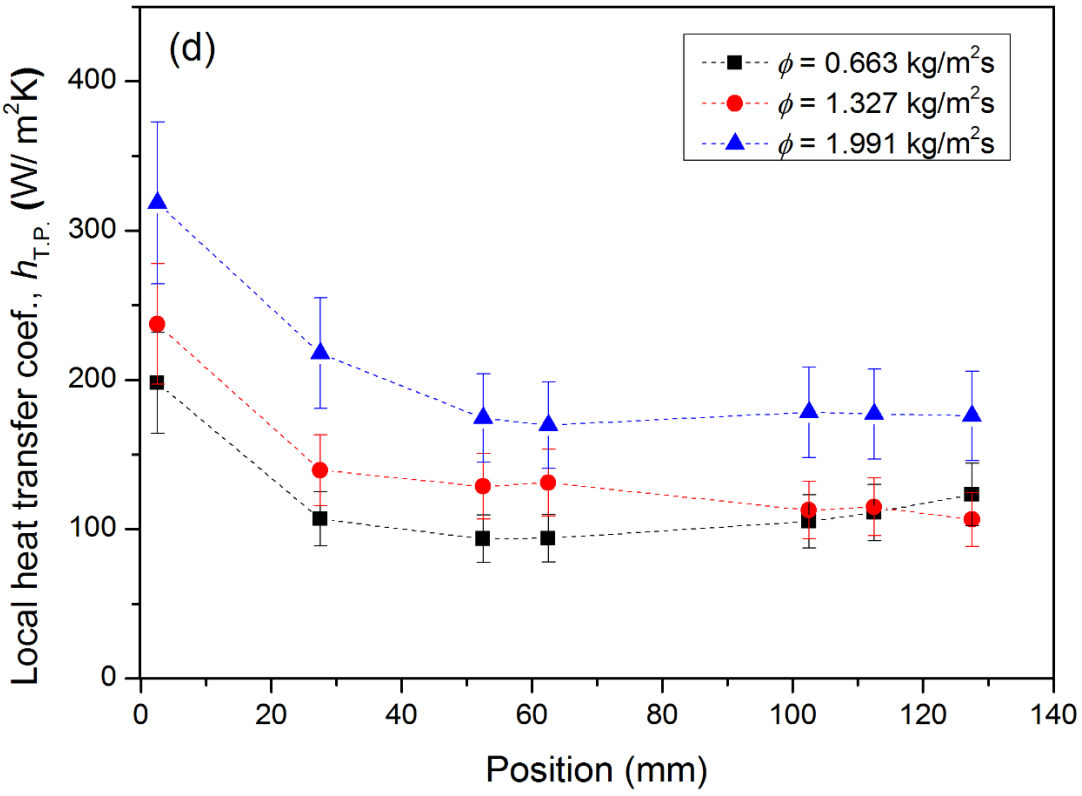


**Figure 6.2-3** Local heat transfer coefficients, $h_{T.P.,local}$, in the two phase flow versus the position, *x*, and the temperature, *T*, at three different mass fluxes, $\phi$, in the same temperature gradient field, from ~18ºC to ~75ºC (inlet-outlet liquid temperatures), containing pure 1-butanol as operating fluid. Absolute errors regarding two-phase heat transfer coefficient calculations are presented in the Table 3.1-2, error around 17%.

In this fashion, two phase flow curves of the local heat transfer coefficients, $h_{T.P.,local}$, of the induced travelling bubbles in water – 1-butanol 5% vol. mixture as a function of the position, *x*, and temperature, *T*, along the circular micro-channel, at four different mass fluxes, $\phi$, were calculated, as can be seen in Figure 6.2-4. More specifically, graph (a) presents local heat transfer coefficients obtained in the characteristic case where the flow mode was changed from bubbly to slug and back to bubbly flow in the vicinity of the outlet part of the channel, at $\dot{V} = 0.2$ mL/ min volumetric flow rate. Remarkably, in graph (a) the local heat transfer coefficients was significantly increased (highest $h_{T.P.,local}$), in the phase region where the slug flow occurred. In Figure 6.2-4 (b), it can be seen that the local heat transfer performance changed when the flow rate was increased in the system, at $\dot{V} = 0.5$ mL/ min. The characteristic bubble growth, as it was visually seen in Figure 6.1-3 and calculated in

Figure 6.1-11 (d), was accompanied by an increase in the local heat transfer coefficient values, at the higher positions of the channel. Similarly, in Figure 6.2-4 (c) the local heat transfer distribution along the heated channel was seen to follow the same tendency but with higher calculated values of $h_{T.P.,local}$, than in the previous case, at $\dot{V} = 0.5\ \mathrm{mL/min}$. One characteristic sharp jump in the heat transfer coefficient values at temperatures around 40°C occurred, at the highest volume flow rate at $\dot{V} = 1.5\ \mathrm{mL/min}$, in Figure 6.2-4 (d). Then the system was seen to follow same behaviour with the previous two cases but with higher obtained $h_{T.P.,local}$ values. Moreover, comparing the calculated $h_{T.P.,local}$ values of the four cases in the alcohol mixture, it was observed that the highest $h_{T.P.,local}$ values were achieved when the highest mass flux, $\phi$, was applied in the system.

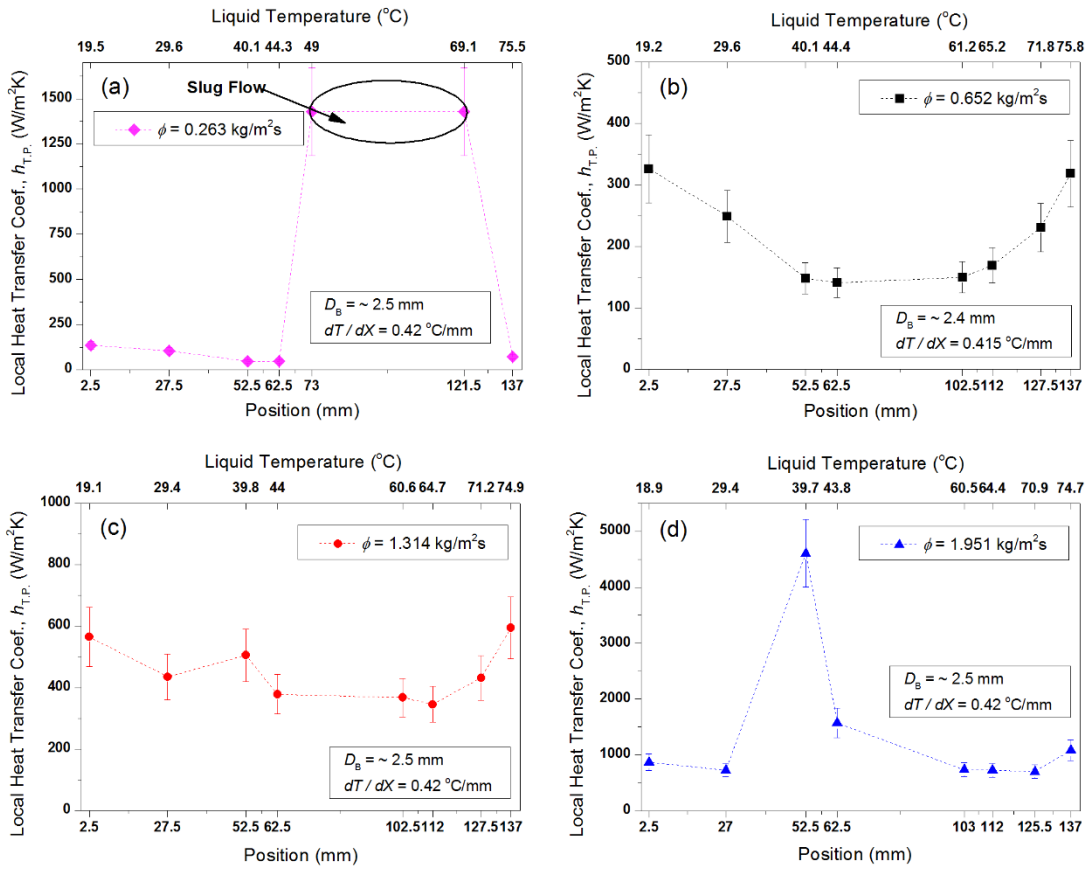

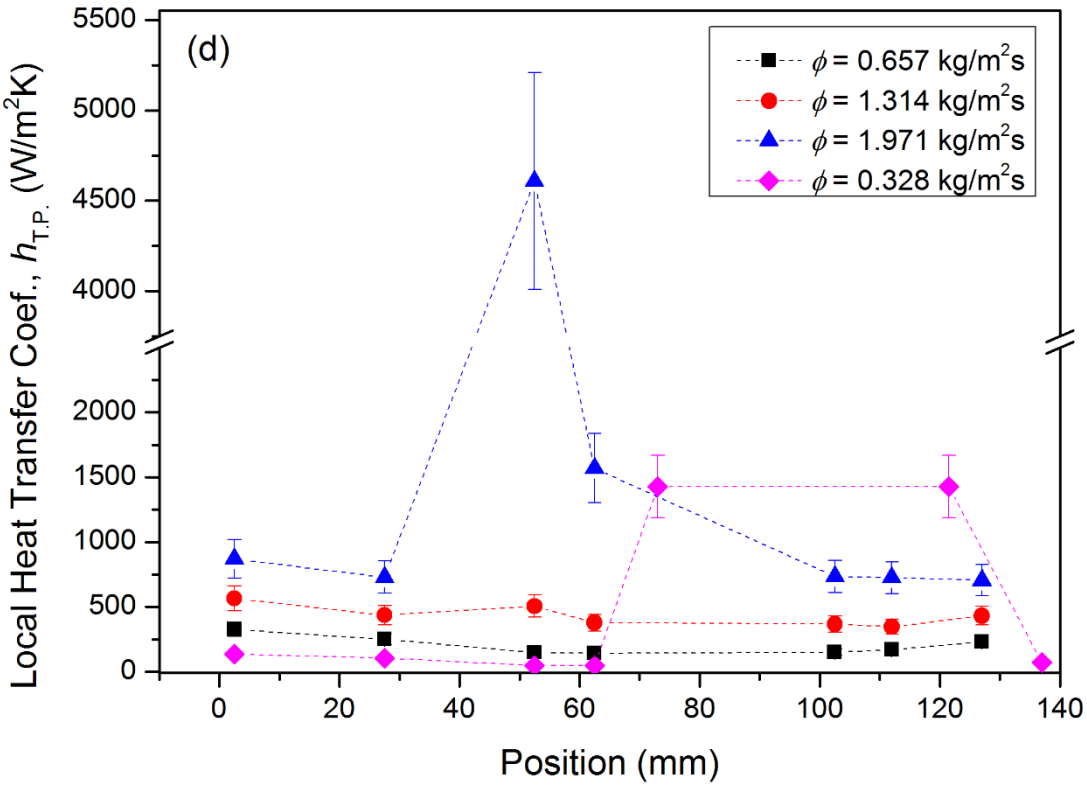


**Figure 6.2-4** Local heat transfer coefficient, $h_{T.P.,local}$, calculations in the two phase flow containing water – 1-butanol 5% vol. mixture (self-rewetting fluid) versus the position, *x*, and the temperature, *T*, at four different mass fluxes, $\phi$, in the same temperature gradient field, from ~18ºC to ~75ºC (inlet-outlet liquid temperatures), respectively. Absolute errors regarding two-phase heat transfer coefficient calculations are presented in the Table 3.1-2, error around 17%.

## 6.3 Discussion

From our experimental investigation and analytical calculations, it was shown that the motion of migrating spherical bubbles along the micro-channel depends strongly on the working fluids: pure liquids and binary alcohol mixture used, and the experimental conditions: isothermal and non-isothermal cases. More specifically, the rising bubbles in the pure liquids (Figure 6.1-6) followed a constant linear velocity profile for both the isothermal and the non-isothermal cases. Another clear feature, for the bubbles flowing in pure liquids was the presence of Marangoni stresses (temperature gradients) which was driving liquid towards the cold region of the channel and

therefore was enhancing the upward motion of the air bubble. The induced thermocapillary stresses in the linear temperature gradient field caused the bubbles to reach a higher rise velocity than in the isothermal ones, for all the mass fluxes used in this experimental study.

Using the water – 1-butanol 5% vol. mixture as the continuous bulk liquid in a heated glass micro-channel, it was observed that the behaviour of the induced travelling bubbles in the mixture (Figure 6.1-7) departs considerably from that of the pure liquids. The anomalous surface tension behaviour of the self-rewetting fluids with the temperature (Figure 5.1-2) and the position of surface tension minimum along the uniformly heated micro-channel drastically affected the induced Marangoni stresses. The migration of the bubbles towards the warmer zone (upstream) in the alcohol mixture within the applied temperature gradient field, induced a non-linear (algorithmic) behaviour at $\dot{V} = 0.5 \text{ and } 1 \text{ mL/ min}$, as presented in Figure 6.1-7. However, the air bubbles travelling in the mixture at volume flow rate of $\dot{V} = 1.5 \text{ mL/ min}$, (highest applied in this series of experiments) were followed a linear velocity profile (Figure 6.1-7), consistent with the observations in the pure liquid cases. Interestingly, the migrating (air) bubbles in the mixture at $\dot{V} = 0.2 \text{ mL/ min}$, (lowest used) resulted in a changing flow mode i.e. bubbly-slug-bubbly flow, adopting a highly non-linear behaviour, Figure 6.1-8. Along the micro-channel, bubbles were influenced by three factors: the buoyancy, the liquid flow and the thermocapillary (Marangoni) stresses. The bubbles were clearly affected or even changed the flow mode (e.g. when slug flow occurred) inside the channel, when thermocapillarity influenced strongly the system and drove flow in the vicinity of the liquid-gas interface, in the case of the non-isothermal binary alcohol mixture. The rising bubbles were subjected to (strong) interfacial forces depending on the immediate position in the channel connected with the parabolic curvature of the surface tension, in this applied temperature gradient field. Therefore, at positions in the channel that corresponded to higher values of surface tension than its minimum and with positive gradient ($d\gamma / dT > 0$), Figure 6.3-1, the induced Marangoni stresses drove liquid upwards, towards the hotter region of the channel, and inhibited the upward motion of the bubble. The reverse phenomenon occurred at positions corresponding to lower values of the surface tension minimum and with a negative gradient ($d\gamma / dT < 0$,

Figure 6.3-1), hence promoting the upward movement of the bubbles. This was evident in the non-isothermal cases for the mixture, where it was shown that the rise velocity of the bubbles was lower than of those in the isothermal ones (for the three applied different mass fluxes (Figure 6.1-6). The strong net capillary-surface force due to the temperature gradients caused the bubbles migration to retarded and deformed their shape. This was the reason behind the non-linear retardation of the bubbles until the outlet part of the channel for the two cases at volume flow rates of $\dot{V} = 0.5 \text{ and } 1 \text{ mL/ min}$, (Figure 6.1-7) in the non-isothermal mixture systems. However, the bubbles migrating in the alcohol mixture, at $\dot{V} = 1.5 \text{ mL/ min}$, were observed to follow a linear behaviour (Figure 6.1-7) along the heated channel as the increased liquid flow, combined with the buoyancy effect, dominated over thermocapillary Marangoni stresses in this case. Our results have demonstrated that the motion of the bubbles in a self-rewetting fluid can be more complex and deviations (from the usual behaviour in pure liquids) can be attributed to the generated thermocapillary stresses which oppose or promote the direction of the buoyancy-driven bubble rise and the imposed liquid flow.

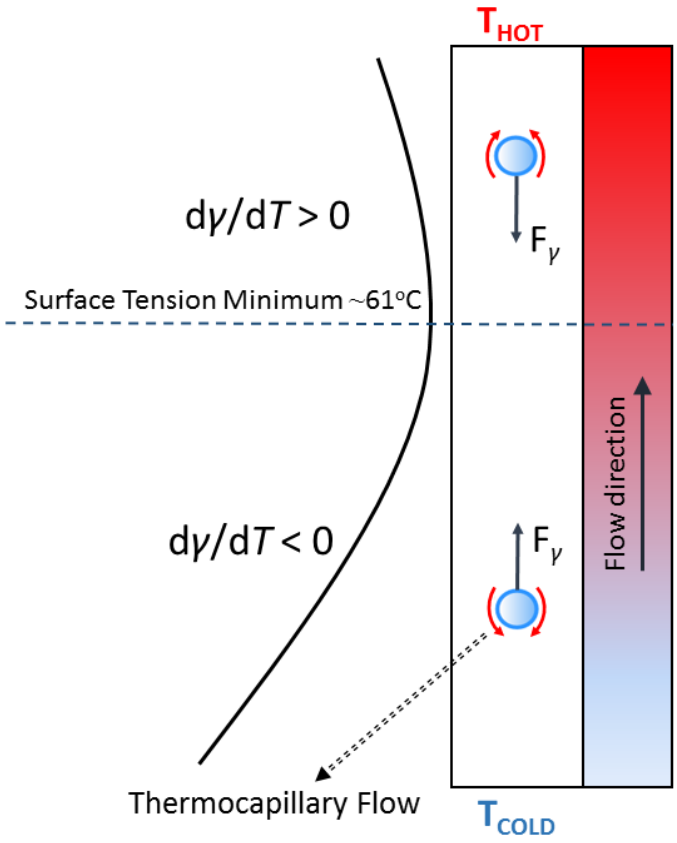


**Figure 6.3-1** Schematic drawing of the presence of Marangoni stresses acting at the interface of the migrating bubbles system. Note that at positions corresponding to lower values of the surface tension minimum, interfacial flows enhance the upward movement of the bubbles and the reverse phenomenon occurs at higher positions from the well-defined minimum (around 62°C).

Previous experimental and theoretical studies on the rising and deforming of a single bubble in a liquid flow have been reported in the literature [143, 147, 232-234]. The bubbles shape varies greatly in different flow regimes as a function of the non-dimensional parameters such as Reynolds (*Re*) number, Rayleigh number (*Ra*), Nusselt (*Nu*), Marangoni (*Ma*), Capillary number (*Ca*), Bond number (*Bo*) etc. Considering the importance and the competition between forces acting on our non-isothermal system, calculations of the dimensionless numbers for pure fluids and alcohol mixture were systematically carried out, as displayed in Table 6.3-1. Small bubbles ($r$ = ~1.25 mm) travelling in the system with small Reynolds and Bond numbers ($Re < 1$ and $Bo < 1$), were seen to rise in a steady fashion, sustain the spherical shape and increase in size due to surface tension forces variations along the uniformly

heated channel. The shape of larger bubbles, with intermediate Reynolds and Bond numbers ($1 < Re < 100$ and $1 < Bo < 100$), were affected significantly by the flow conditions. In our experiments the Reynolds numbers were characteristically low resulting in a smooth, constant fluid flow; laminar flow. Moreover, the calculated Rayleigh and Nusselt numbers demonstrated that the heat transfer was primarily in the form of heat convection with high *Ra* numbers and $Nu > 1$, in all cases, as can be seen in Table 6.3-1. For the pure water cases the dimensionless numbers showed that the migration of the bubbles was mainly driven by buoyancy, the imposed liquid flow and the Marangoni stresses. The presence of strong surface tension forces maintained the spherical shape of the bubbles ($Bo = 0.54$ and $Ca < 10^{-5}$, absence of viscous forces) and enhanced the upward movement along the heated channel. On the other hand, the rising bubbles in pure 1-butanol working fluid were influenced by strong body forces (buoyancy), the liquid flow and weak Marangoni stresses which was evidenced from the observations of bubble deformation ($Bo = 1.42$ and $Ca < 10^{-5}$, absence of viscous forces) and adopted a disk-like shape (Figure 6.1-1). However, the findings presented in the self-rewetting liquid flows brought to light a new phenomenon which was first reported in the latest work of Shanahan and Sefiane [155] in which the rising bubbles migrated against the liquid flow due to the strong thermocapillary stresses. In our study, the travelling bubbles in self-rewetting fluid were subjected to buoyancy, liquid flow and strong surface tension forces (Marangoni stresses). The bubbles kept spherical shape, $Bo = 0.45$, and were unaffected by the viscous forces, $Ca < 10^{-5}$. However, it was also clear that the bubbles motion within the channel was related significantly with the position *x*, the temperature *T* and the surface tension minimum, along the channel where either promoted or retarded the bubble movement resulting in a non-linear velocity profile (algorithmic), as reported previously and presented in Figure 6.3-1.

The aforementioned observations about bubbles motion in the non-isothermal liquid flows were consistent with the single phase and two phase flows local heat transfer coefficients, as presented in Figure 6.2-1 – 6.2-4. It was seen that for the pure liquids heat transfer coefficient curves were influenced by the mass flux in both single phase and two-phase regions. Moreover, heat transfer coefficients were sensitive to the applied heat flux in the single phase flows and an enhancement in the heat transfer

profile was calculated as the heat flux was increased, for all working fluids used. In the two-phase flows, the calculated local heat transfer coefficients were shown to follow a non-linear trend in terms of the position *x*, and the temperature *T*, along the channel, in each flow rate, for all operating fluids. Moreover, the anomalous property of the alcohol mixture which essentially influenced the motion of the rising bubbles was also revealed in the local heat transfer coefficient values in the two-phase flows regions. In the mixture cases, at flow rate of $\dot{V} = 0.2\ \mathrm{mL/min}$, and in the proximity of the surface tension minimum, bubble motion was apparently governed by strong thermocapillary stresses and slug flow occurred enhancing drastically the heat transfer profile of the system, as seen in Figure 6.2-2. However, at $\dot{V} = 0.5\ \mathrm{mL/min}$, the local heat transfer coefficient values started to increase (again) in the proximity of the surface tension minimum until the outlet of the channel, consistent with the observed bubble ratio growth (up to ~25%), as it was seen in Figure 6.1-11. Thus, the enhancement of the heat transfer mechanism occurred at the higher position of the channel where the bubble motion was influenced strongly by the thermocapillarity. The same feature but less intensive (bubble ratio growth up to ~10%, in Figure 6.1-11) was revealed at $\dot{V} = 1\ \mathrm{mL/min}$ mixture fluid flow, where the calculated local heat transfer coefficients increased as the bubble was flowing in the vicinity of the surface tension minimum (~62$^{o}$C) until the outlet of the channel. In this case, the competition between the liquid flow and buoyancy against the Marangoni stresses was more balanced and the bubbles followed an intermediate behaviour. Interestingly, at $\dot{V} = 1\ \mathrm{mL/min}$ flow rate, the highest local heat transfer coefficient values were obtained which were clearly associated with the highest mass flux (heat flux) applied and without bubble deformation to occur. It is worth noting that in all cases containing the alcohol mixture, different bubble motions were observed when we changed the mass flux (and so the heat flux) in the same temperature field, resulting in a different heat transfer profile. It is clear from all the above mentioned that the thermocapillarity played an important role in the energy transport mechanism and had a major impact in the heat transfer profile of the self-rewetting systems.

**Table 6.3-1** Calculated dimensionless groups for the pure liquids and alcohol mixture i.e. self-rewetting fluid (data reduction see also Chapters 2.6.1 and 3.1.5).

| Liquid | Mass flux $\varphi$ (kg/m$^2$s) | Reynolds number (***Re***) (inlet – outlet) | **Dimensionless numbers** | | | | |
|---|---|---|---|---|---|---|---|
| | | | Rayleigh (***Ra***) (inlet) | Nusselt (***Nu***) (inlet) | Marangoni (***Ma***) (inlet) | Capillary (***Ca***) (inlet) | Bond (***Bo***) |
| **Pure water** | 0.67 | 2.3 - 6.17 | 11191.7 | 5.14 | 16.01 | 9.07 x $10^{-6}$ | *0.54* (bubble flow, $r_b$ = ~1.25mm) |
| | 1.33 | 4.6 - 12.34 | 9359.8 | 4.91 | 32.02 | 1.81 x $10^{-5}$ | |
| | 1.99 | 6.9 - 15.92 | 8075.2 | 4.74 | 48.02 | 2.71 x $10^{-5}$ | |
| **Pure 1-butanol** | 0.54 | 0.7 - 2.41 | 38000.9 | 6.98 | 33.87 | 8.98 x $10^{-7}$ | *1.42* (bubble flow, $r_b$ = ~1.25mm) |
| | 1.07 | 1.42 - 4.82 | 34120.2 | 6.79 | 67.26 | 1.79 x $10^{-6}$ | |
| | 1.61 | 2.12 - 7.24 | 28640.1 | 6.50 | 101.12 | 2.71 x $10^{-6}$ | |
| **Water – 1-butanol 5% vol.** | 0.26 | 0.73 - 1.92 | 5987.7 | 4.39 | 5.63 | 1.10 x $10^{-5}$ | *0.45* (initially bubble flow, $r_b$ = ~1.25mm) *1.11* (slug flow occurred, $r_s$ = ~1.8 mm) |
| | 0.65 | 1.83 - 4.79 | 5091.5 | 4.22 | 11.27 | 2.75 x $10^{-5}$ | *0.45* (bubble case, $r_b$ = ~1.25mm) |
| | 1.30 | 3.67 - 9.63 | 4319.8 | 4.05 | 22.54 | 5.50 x $10^{-5}$ | |
| | 1.95 | 5.5 - 14.44 | 3857.2 | 3.94 | 33.81 | 8.24 x $10^{-5}$ | |

## 6.4 Conclusions

A systematic experimental investigation of an air bubble rising in isothermal and non-isothermal liquid flows whose walls have a linearly increasing temperature gradient, in vertical circular micro-channels, was conducted. Particular interest was paid to the development of thermocapillary stresses due to surface tension gradients in pure liquids flows (pure water and 1-butanol) and in self-rewetting fluid flows (water – 1-butanol 5% vol.), and in turn, the bubble dynamics. Our results indicate that the motion of the bubble in the binary alcohol solution can be drastically affected by the presence of strong surface tension forces (Marangoni effect) and its parabolic dependence on temperature with a well-defined minimum. The presence of Marangoni stresses found to promote or retard the upward movement of the buoyancy-driven bubble depending on the location associated with the surface tension minimum. We have also shown that in some cases of the self-rewetting fluid that the bubble experienced considerable elongation and the flow changed from bubbly to slug. This phenomenon is due to the interfacial flows acting on the travelling bubble (strong Marangoni tresses), and the characteristic slow liquid flow used in this case. These motions were absent in the case of pure liquids whose surface tension decreases linearly with temperature. The anomalous property of the self-rewetting fluids was also the key factor of the enhanced heat transfer performance compared to that of the linear liquids, within the same temperature gradient field and same applied mass fluxes.

# Chapter 7: Final Conclusions and Future Work

## 7.1 Conclusions

Given that comprehensive conclusions have been provided at the end of each chapter, only a review with the most important findings emerging from this experimental investigation is presented in this section. In this work, a study on the contact line dynamics and the underlying phenomena present during wetting, evaporation and internal flows of pure liquids, polymer solutions and alcohol mixtures, under different experimental conditions, has been conducted. Furthermore, the presence of thermocapillary instabilities and flows in drops and bubbles which were migrating in microchannels, was systematically examined. Different techniques, tools, approaches and methods have been used and explored pursuing to uncover the interplay mechanisms, under isothermal and non-isothermal conditions, of evaporating droplets and travelling bubbles in liquid flows. The main findings revealed during this research, attempting to shed more light on the fluid dynamics, role of interface, thermocapillary and heat transfer phenomena were extensively discussed.

The evaporative behaviour of aqueous polymer (PEO) solutions on real, smooth, solid substrates varying from hydrophilic to hydrophobic, has been investigated at macroscale, in Chapter 4. PEO solutions with different molecular weights have been used and complicated modes of evaporation have been identified. After complete of the characteristic four stage drying process on solid (glass) substrates, the shape of the final dried PEO deposits i.e. pillars or puddles, was found to depend strongly on the molecular weight of the polymer solution. More specifically, the duration of the pinning stage was crucial to the final morphology of the dried polymeric deposits and it was governed from the competition of the complicated phenomena taking place at the vicinity of the contact line connected with the flows and interactions in the bulk of the semidilute fluid. Diffusion-based arguments, namely the Péclet number, could not fully explain the results obtained (absence of pillars) for PEO droplets with the high molecular weights [39]. PEO solutions with high molecular weights showed that pillar formation mechanism was drastically affected by the interface phenomena (polymer/substrate) and could modify the four stage drying mechanism. In addition, the importance of substrate hydrophobicity or hydrophilicity on the pinning and depinning stages was evident, affecting by the interfacial phenomena and the polymer

chains (short and/or long) interactions. For high $M_w$ PEO droplets was seen that the intertwining between the long loops and tails of an adsorbed polymer layer (at contact line) and the polymer gel network within the bulk of the fluid resulted in the appearance of strong adhesion in the system during the evaporation process. It is worth noting that the presence of interfacial phenomenon at the contact line might be an important contribution to the physics of the overall behaviour in addition to the Péclet number arguments discussed in previous studies.

In Chapter 5, the contact line dynamics of pure liquids (pure water and pure 1-butanol) and binary alcohols mixtures (self-rewetting fluids) were investigated. The short-time spreading mechanism of the droplets was found to depend strongly on the temperatures of the substrates. The spreading exponents in the inertia-capillary regime were measured to vary with the temperature (substrate) and to follow a monotonic trend as the temperature was increased. However, in the cases of the evaporating self-rewetting droplets in different substrate temperatures, a non-monotonic behaviour was revealed, at the early times of the wetting process. This behaviour was consistent with the anomalous property of the surface tension with temperature, at some ranges of concentration for these alcohol solutions. Additionally, it has been shown that thermocapillary instabilities were present in the evaporation of these volatile liquids droplets under non-isothermal conditions using IR thermography. The nature of the observed thermal patterns was liquid dependent. In the cases of self-rewetting droplets spoke-like radial waves appeared which rotated around the droplet. The presence of these characteristic surface-tension-driven (Marangoni effect) thermal travelling waves were due to temperature and/or concentration gradients generated at the non-isothermal liquid interface. The thermal fluctuations were more intensive and appeared to rotate faster at higher substrate temperatures i.e. strong Marangoni effect. It was also observed that the magnitude of the temperature and concentration gradients varied as the evaporation progressed. At the early-times of the spreading, the generation of Marangoni stresses was drastically influenced the liquids' wetting mechanism and so the spreading exponents. To further verify the strong impact of the Marangoni effect on the contact line dynamics, experiments using self-rewetting droplets sliding on a uniformly heated inclined substrate covered with a silicone oil, were performed. It has been shown that the induced strong thermocapillary and solutal

Marangoni stresses acted at the non-isothermal liquid interface resulted in the enhancement of the spreading rates compared to the experiments conducted on solid glass substrates. Furthermore, by the time that gravity-capillary forces became subcritical and the Marangoni effect (surface-tension forces) dominated in the system, the self-rewetting droplet was remarkably observed to climb the inclined wall. The understanding of phenomena related to the contact line dynamics and subsequent generation of thermal travelling waves due to thermocapillary instabilities during wetting is useful for future research on this topic. In what follows, a further examination of the thermocapillary stresses (Marangoni effect) in the droplets with non-circular contact areas, under non-isothermal conditions, was carried out using infrared thermography. Pure liquid water droplets, with complex three-dimensional droplet geometries, have been found to exhibit sophisticated flows which was dictated by interface tension gradients. The strong thermocapillary instabilities presented during non-spherical (cold) droplet evaporation on heated substrates resulted in the generation of distinctive thermal patterns, namely *vortices*. The irregularity of the droplets' shape and the unsteady mass transfer combined with the interfacial tensions resulted in a complex dynamic behaviour of the internal flows within the liquid. The presence and formation of these characteristic thermal patterns appeared to be both geometrical (three dimensional profile) and substrate temperature dependent.

The last part of this thesis consisted of an extensive experimental investigation of air bubbles migrating in vertical circular microchannels, and it was conducted under controlled isothermal and non-isothermal conditions. The use of varying operating liquids i.e. pure liquids and binary alcohol mixtures, resulted in different flow patterns and bubbles motion which was drastically influenced by the presence of thermocapillary stresses acted at the vicinity of the bubble's interface. It has been found that the competition between the gravity, liquid flow and the Marangoni effect promoted or retarded the movement of the bubbles, in pure liquids and water-butanol mixture, under different applied liquid flow rates and temperature conditions. More specifically, in the cases of self-rewetting liquid flows, the bubbles exhibited an unusual behaviour associated with the non-monotonic dependence of the surface tension on temperature. Additionally, the heat transfer distribution of the pure liquids and the alcohol mixture, in the single and two-phase flows, was systematically

examined. The calculations showed that the self-rewetting fluid heat transfer performance was enhanced compared to pure liquids within the same temperature gradient field and same applied flow conditions. The latter may point out the significant contribution of the Marangoni effect in the single and two-phase flows systems. A possible consequence of this study is the application in cooling-heating technologies where more rapid cooling systems may be expected from innovative liquids such as binary alcohol mixtures, with the property to ‘‘self-rewet” by spreading rapidly towards the hotter regimes, hence preventing dry-out of hot surfaces.

## 7.2 Future Work

The physical richness and relevance of such fundamental topics investigated and discussed in this thesis make the space for further research for several attractive future applications. The complexity of the non-equilibrium phenomena observed during evaporation and spreading of polymer solutions and alcohol mixtures drops and bubble migration, certainly offers the possibility to study and to uncover new configurations and interactions.

Although, the evaporation mechanism and polymer-deposition of PEO solutions (10% wt.) with different molecular weights and other physical parameters were thoroughly investigated in this study (Chapter 4), numerous and various questions remain elusive and need to be addressed in future studies. Polymers can be varied in sizes, compositions, branching, architecture etc. affecting the underlying physical mechanisms, interactions at the vicinity of the contact line and the fluid dynamics during evaporation process. Of great importance would be the study of controlling the structure of the deposited polymer by investigating the crystallization forces acting at the contact line for different polymer molecular weights and also try to seize the interactions during pinning and depinning of these solutions. Electrowetting technique would be essential to study for these PEO solutions, as has been proposed one of the most promising techniques for the manipulation of the droplet interface and for the

control of the dried deposits after evaporation process. A more detailed research to uncover the mechanisms governing the interactions between polymer-polymer, polymer-fluid, polymer-substrate and fluid-substrate of these solutions triggered by voltage would of great interest. Moreover, coffee ring stain effect with the resulting dried polymer formation-patterns on various substrates or the polymer interactions on structured substrates could be other useful topics of further research to expand the knowledge regarding these phenomena. Furthermore, the effect of adding surfactants on the self-assembly mechanism of polymer solutions should be assessed. Potentially, all the above could lead into nano-micro-technological applications such as ink-jet printing, evaporative cooling technologies and micro-electronics.

The results presented in Chapter 5 provide an insight into the various and complex behaviour which occurs in the spreading and subsequent evaporation of both pure volatile liquids and binary alcohol mixtures i.e. self-rewetting fluids. Many interesting routes for future research have become apparent in terms of early-time spreading phenomena and the presence of thermocapillary instabilities within the spherical pure and water-alcohol droplets and also in the non-spherical pure water droplets, under non-isothermal conditions. Techniques such as PIV, combined with accurate high speed visualizations and IR thermography measurements may be able to show more conclusively how contact line dynamics and thermal behaviour affects the resulting internal flows and vice versa. Moreover, experimental configurations in which there are externally imposed convection currents in the fluid interface also become new and very interesting to investigate internal flows and manipulate the thermal imbalances of evaporating droplets. Another case to investigate is the behaviour of nanoparticles at the interface of the self-rewetting fluids and to observe how the addition of nanoparticles alters the behaviour. In particular, the effect of non-circular wetted area and the generated thermal patterns within the evaporating droplets is still new and poses many challenges for further investigation. The use of different substrates (from hydrophilic to hydrophobic, structured surfaces, varying thermal conductivities etc.) would be essential to understand the underlying fluid dynamics regarding surface interactions during evaporation and subsequent spreading behaviour. These studies could be useful in advanced heat transfer industrial applications e.g. column reactors,

heat pipes or terrestrial and space applications, avoiding sedimentation, erosion or clogging and aiming to enhance heat transfer performance.

Particular interest, in Chapter 6, was paid to the behaviour and control of the motion of bubbles travelling in microchannels. Exploring the thermocapillary migration of bubbles within different bulk liquids under varying applied flows and temperature conditions is of great importance with potential applications for cooling purposes where single and two phase flows are present. More specifically, the further understanding of heat transfer phenomena with the use of innovative self-rewetting fluids in multiphase flow systems and the subsequent Marangoni effect contribution would provide information in several mechanisms for extending and enhancing the performance of the single phase ones. The use of different channel geometries, surface coating or fluid additives would be crucial to enhance the heat transfer performance of these water-alcohol fluids. For example, hydrophobic channel surfaces may introduce more nucleation sites which enhance heat transfer performance, while the nucleated bubbles may coalesce easily to form a vapour layer on the heating surface to cause boiling crisis and severe heat transfer deterioration. On the other hand, the use of porous coatings on channels would provide more stable nucleation regions and capillary wetting phenomena which are favourable for heat transfer, but at the same time porous coatings pose a thermal resistance to heat transfer. There is scope for much further investigation into many aspects of these systems, extending the research into the interfacial phenomena connected with heat transfer distribution, including more liquids and channel geometries with potential applications ranging from drug delivery systems to chemical analysis processes.

# References


1. Young, T., *An Essay on the Cohesion of Fluids.* Philosophical Transactions of the Royal Society of London, 1805. **95**: p. 65-87.
2. Dussan V, E.B., *On the Spreading of Liquids on Solid Surfaces: Static and Dynamic Contact Lines.* Annual Review of Fluid Mechanics, 1979. **11**(1): p. 371-400.
3. de Gennes, P.G., *Wetting: statics and dynamics.* Reviews of Modern Physics, 1985. **57**(3): p. 827-863.
4. Joanny, J.F. and P.G. de Gennes, *A model for contact-angle hysteresis.* Journal of Chemical Physics, 1984. **81**(1): p. 552-562.
5. Squires, T.M. and S.R. Quake, *Microfluidics: Fluid physics at the nanoliter scale.* Reviews of Modern Physics, 2005. **77**(3): p. 977-1026.
6. Neinhuis, C. and W. Barthlott, *Characterization and Distribution of Water-repellent, Self-cleaning Plant Surfaces.* Annals of Botany, 1997. **79**(6): p. 667-677.
7. Reiter, G., *Dewetting of thin polymer films.* Physical Review Letters, 1992. **68**(1): p. 75-78.
8. Reiter, G., *Unstable thin polymer films: rupture and dewetting processes.* Langmuir, 1993. **9**(5): p. 1344-1351.
9. Bergeron, V., et al., *Controlling droplet deposition with polymer additives.* Nature, 2000. **405**(6788): p. 772-775.
10. Bourgès-Monnier, C. and M.E.R. Shanahan, *Influence of Evaporation on Contact Angle.* Langmuir, 1995. **11**(7): p. 2820-2829.
11. Picknett, R.G. and R. Bexon, *The evaporation of sessile or pendant drops in still air.* Journal of Colloid and Interface Science, 1977. **61**(2): p. 336-350.
12. Birdi, K.S., D.T. Vu, and A. Winter, *A study of the evaporation rates of small water drops placed on a solid surface.* The Journal of Physical Chemistry, 1989. **93**(9): p. 3702-3703.
13. Birdi, K.S. and D.T. Vu, *Wettability and the evaporation rates of fluids from solid surfaces.* Journal of Adhesion Science and Technology, 1993. **7**(6): p. 485-493.

14. Hu, H. and R.G. Larson, *Evaporation of a Sessile Droplet on a Substrate.* The Journal of Physical Chemistry B, 2002. **106**(6): p. 1334-1344.
15. Shanahan, M.E.R. and C. Bourgès-Monnier, *Effects of evaporation on contact angles on polymer surfaces.* International Journal of Adhesion and Adhesives, 1994. **14**(3): p. 201-205.
16. Erbil, H.Y. and R.A. Meric, *Evaporation of Sessile Drops on Polymer Surfaces: Ellipsoidal Cap Geometry.* The Journal of Physical Chemistry B, 1997. **101**(35): p. 6867-6873.
17. Mollaret, R., et al., *Experimental and Numerical Investigation of the Evaporation into Air of a Drop on a Heated Surface.* Chemical Engineering Research and Design, 2004. **82**(4): p. 471-480.
18. Hu, H. and R.G. Larson, *Analysis of the Effects of Marangoni Stresses on the Microflow in an Evaporating Sessile Droplet.* Langmuir, 2005. **21**(9): p. 3972-3980.
19. Paik, S.W., et al., *Spatially and Temporally Resolved Temperature Measurements for Slow Evaporating Sessile Drops Heated by a Microfabricated Heater Array.* Journal of Heat Transfer, 2006. **129**(8): p. 966-976.
20. Erbil, H.Y., G. McHale, and M.I. Newton, *Drop Evaporation on Solid Surfaces: Constant Contact Angle Mode.* Langmuir, 2002. **18**(7): p. 2636-2641.
21. Cachile, M., et al., *Evaporating Droplets.* Langmuir, 2002. **18**(21): p. 8070-8078.
22. Panwar, A.K., S.K. Barthwal, and S. Ray, *Effect of evaporation on the contact angle of a sessile drop on solid substrates.* Journal of Adhesion Science and Technology, 2003. **17**(10): p. 1321-1329.
23. Sefiane, K., L. Tadrist, and M. Douglas, *Experimental study of evaporating water–ethanol mixture sessile drop: influence of concentration.* International Journal of Heat and Mass Transfer, 2003. **46**(23): p. 4527-4534.
24. Zhang, X., et al., *Evaporation of Sessile Water Droplets on Superhydrophobic Natural Lotus and Biomimetic Polymer Surfaces.* ChemPhysChem, 2006. **7**(10): p. 2067-2070.
25. Deegan, R.D., *Pattern formation in drying drops.* Physical Review E, 2000. **61**(1): p. 475-485.

26. Deegan, R.D., et al., *Capillary flow as the cause of ring stains from dried liquid drops.* Nature, 1997. **389**(6653): p. 827-829.
27. Deegan, R.D., et al., *Contact line deposits in an evaporating drop.* Physical Review E, 2000. **62**(1): p. 756-765.
28. Erbil, H.Y., *Evaporation of pure liquid sessile and spherical suspended drops: A review.* Advances in Colloid and Interface Science, 2012. **170**(1–2): p. 67-86.
29. Hu, H. and R.G. Larson, *Marangoni Effect Reverses Coffee-Ring Depositions.* The Journal of Physical Chemistry B, 2006. **110**(14): p. 7090-7094.
30. Sefiane, K., et al., *On the effect of the atmosphere on the evaporation of sessile droplets of water.* Physics of Fluids, 2009. **21**(6): p. 062101.
31. Singh, M., et al., *Inkjet Printing—Process and Its Applications.* Advanced Materials, 2010. **22**(6): p. 673-685.
32. Man, W. and W.B. Russel, *Direct Measurements of Critical Stresses and Cracking in Thin Films of Colloid Dispersions.* Physical Review Letters, 2008. **100**(19): p. 198302.
33. Bigioni, T.P., et al., *Kinetically driven self assembly of highly ordered nanoparticle monolayers.* Nat Mater, 2006. **5**(4): p. 265-270.
34. Sefiane, K., *On the Formation of Regular Patterns from Drying Droplets and Their Potential Use for Bio-Medical Applications.* Journal of Bionic Engineering, 2010. **7**: p. S82-S93.
35. Brutin, D., et al., *Pattern formation in drying drops of blood.* Journal of Fluid Mechanics, 2011. **667**: p. 85-95.
36. Rowan, S.M., et al., *Evaporation of Microdroplets of Azeotropic Liquids.* The Journal of Physical Chemistry B, 2000. **104**(34): p. 8217-8220.
37. Li, G. and K. Graf, *Microstructures formation by deposition of toluene drops on polystyrene surface.* Physical Chemistry Chemical Physics, 2009. **11**(33): p. 7137-7144.
38. Baldwin, K.A., et al., *Drying and deposition of poly(ethylene oxide) droplets determined by Peclet number.* Soft Matter, 2011. **7**(17): p. 7819-7826.
39. Baldwin, K.A. and D.J. Fairhurst, *The effects of molecular weight, evaporation rate and polymer concentration on pillar formation in drying poly(ethylene oxide) droplets.* Colloids and Surfaces A: Physicochemical and Engineering Aspects, 2014. **441**: p. 867-871.

40. Okawa, T., *Boiling Heat Transfer Characteristics of Nanofluids.* JAPANESE JOURNAL OF MULTIPHASE FLOW, 2014. **28**(2): p. 167-174.
41. Degaleesan, S., M. Dudukovic, and Y. Pan, *Experimental study of gas-induced liquid-flow structures in bubble columns.* AIChE Journal, 2001. **47**(9): p. 1913-1931.
42. Ahmed, S. and V.P. Carey, *Effects of Surface Orientation on the Pool Boiling Heat Transfer in Water/2-Propanol Mixtures.* Journal of Heat Transfer, 1999. **121**(1): p. 80-88.
43. di Francescantonio, N., R. Savino, and Y. Abe, *New alcohol solutions for heat pipes: Marangoni effect and heat transfer enhancement.* International Journal of Heat and Mass Transfer, 2008. **51**(25–26): p. 6199-6207.
44. Hu, Y., et al., *Heat transfer enhancement of micro oscillating heat pipes with self-rewetting fluid.* International Journal of Heat and Mass Transfer, 2014. **70**(0): p. 496-503.
45. Savino, R., et al., *Heat pipes with binary mixtures and inverse Marangoni effects for microgravity applications.* Acta Astronautica, 2007. **61**(1–6): p. 16-26.
46. Savino, R. and R. Monti, *Heat Pipes for Space Applications.* Space Technology,, 2005. **25**: p. 59-61.
47. Tanaka, K., et al., *Low-Gravity Experiments of Lightweight Flexible Heat Pipe Panels with Self-Rewetting Fluids.* Annals of the New York Academy of Sciences, 2009. **1161**(1): p. 554-561.
48. Savino, R., A. Cecere, and R. Di Paola, *Surface tension-driven flow in wickless heat pipes with self-rewetting fluids.* International Journal of Heat and Fluid Flow, 2009. **30**(2): p. 380-388.
49. Sefiane, K., S. David, and M.E.R. Shanahan, *Wetting and Evaporation of Binary Mixture Drops.* The Journal of Physical Chemistry B, 2008. **112**(36): p. 11317-11323.
50. Bonn, D., et al., *Wetting and spreading.* Reviews of Modern Physics, 2009. **81**(2): p. 739-805.
51. de Gennes, P.G., F. Brochard-Wyart, and D. Quéré, *Capillarity and Wetting Phenomena*. 1 ed. Drops, Bubbles, Pearls, Waves. 2004: Springer-Verlag New York. 292.

52. Wong, K.V. and O. De Leon, *Applications of Nanofluids: Current and Future.* Advances in Mechanical Engineering, 2010. **2**.
53. Simpkins, P.G. and V. Kuck, *On air entrainment in coatings.* Journal of Colloid and Interface Science, 2003. **263**(2): p. 562-571.
54. Wall, S. and B. Black. *Drops of Spring*. 2007 [cited 2015 8/10]; Available from: http://pelfind.net/photo/140028p2718269/18-refreshing-water-droplet-photos.
55. Pearson, J.R.A., *On convection cells induced by surface tension.* Journal of Fluid Mechanics, 1958. **4**(05): p. 489-500.
56. Harkins, W.D. and H.F. Jordan, *Surface tension by the ring method.* Science, 1930. **72**: p. 73-75.
57. Barr, A. *Surface Tension* 2011 [cited 2015 20/12]; Available from: http://www.mrxstitch.com/arteries-surface-tension/.
58. Kyowa Interface Science Co., L. *Surface Tension* [cited 2015 20/12]; Available from: http://www.face-kyowa.co.jp/english/en_science/en_theory/en_what_Surface_tension/.
59. Dupré, P. and A. Dupré, *Théorie mécanique de la chaleur*. 1869, Paris: Gauthier-Villars.
60. Extrand, C.W., *A Thermodynamic Model for Contact Angle Hysteresis.* Journal of Colloid and Interface Science, 1998. **207**(1): p. 11-19.
61. Hyväluoma, J., et al., *Droplets on inclined rough surfaces.* The European Physical Journal E, 2007. **23**(3): p. 289-293.
62. Dussan V., E.B. and R.T.-P. Chow, *On the ability of drops or bubbles to stick to non-horizontal surfaces of solids.* Journal of Fluid Mechanics, 1983. **137**: p. 1-29.
63. Cassie, A.B.D. and S. Baxter, *Wettability of porous surfaces.* Transactions of the Faraday Society, 1944. **40**(0): p. 546-551.
64. Schwartz, L.W. and S. Garoff, *Contact angle hysteresis on heterogeneous surfaces.* Langmuir, 1985. **1**(2): p. 219-230.
65. Johnson, R.E. and R.H. Dettre, *Contact Angle Hysterisis. III. Study of an Idealized Heterogenous Surface.* Journal of Physical Chemistry, 1964. **68**(7): p. 1744-&.
66. Israelachvili, J.N. and M.L. Gee, *Contact angles on chemically heterogeneous surfaces.* Langmuir, 1989. **5**(1): p. 288-289.

67. Woodward, J.T., H. Gwin, and D.K. Schwartz, *Contact Angles on Surfaces with Mesoscopic Chemical Heterogeneity.* Langmuir, 2000. **16**(6): p. 2957-2961.
68. Nguyen, C.T., et al., *Viscosity data for Al2O3–water nanofluid—hysteresis: is heat transfer enhancement using nanofluids reliable?* International Journal of Thermal Sciences, 2008. **47**(2): p. 103-111.
69. Tabeling, P., *Microfluidics/Microfluidique - Foreword.* Comptes Rendus Physique, 2004. **5**(5): p. 519-520.
70. Soltman, D. and V. Subramanian, *Inkjet-Printed Line Morphologies and Temperature Control of the Coffee Ring Effect.* Langmuir, 2008. **24**(5): p. 2224-2231.
71. Wijshoff, H., *The dynamics of the piezo inkjet printhead operation.* Physics Reports, 2010. **491**(4–5): p. 77-177.
72. de Gans, B.J., P.C. Duineveld, and U.S. Schubert, *Inkjet printing of polymers: State of the art and future developments.* Advanced Materials, 2004. **16**(3): p. 203-213.
73. Bénard, H., *Les tourbillons cellulaires dans une nappe liquide. - Méthodes optiques d'observation et d'enregistrement.* J. Phys. Theor. Appl., 1901. **10**(1): p. 254-266.
74. Block, M.J., *Surface Tension as the Cause of Benard Cells and Surface Deformation in a Liquid Film.* Nature, 1956. **178**(4534): p. 650-651.
75. Scriven, L.E. and C.V. Sternling, *On cellular convection driven by surface-tension gradients: effects of mean surface tension and surface viscosity.* Journal of Fluid Mechanics, 1964. **19**(03): p. 321-340.
76. Ghasemi, H. and C.A. Ward, *Energy Transport by Thermocapillary Convection during Sessile-Water-Droplet Evaporation.* Physical Review Letters, 2010. **105**(13): p. 136102.
77. Ristenpart, W.D., et al., *Influence of Substrate Conductivity on Circulation Reversal in Evaporating Drops.* Physical Review Letters, 2007. **99**(23): p. 234502.
78. Cheng, A.K.H., D.M. Soolaman, and H.-Z. Yu, *Evaporation of Microdroplets of Ethanol−Water Mixtures on Gold Surfaces Modified with Self-Assembled Monolayers.* The Journal of Physical Chemistry B, 2006. **110**(23): p. 11267-11271.

79. Liu, C. and E. Bonaccurso, *Microcantilever sensors for monitoring the evaporation of microdrops of pure liquids and mixtures.* Review of Scientific Instruments, 2010. **81**(1): p. 013702.
80. Shi, L., et al., *Wetting and evaporation behaviors of water–ethanol sessile drops on PTFE surfaces.* Surface and Interface Analysis, 2009. **41**(12-13): p. 951-955.
81. Hamamoto, Y., J.R.E. Christy, and K. Sefiane, *The Flow Characteristics of an Evaporating Ethanol Water Mixture Droplet on a Glass Substrate.* Journal of Thermal Science and Technology, 2012. **7**(3): p. 425-436.
82. Bennacer, R. and K. Sefiane, *Vortices, dissipation and flow transition in volatile binary drops.* Journal of Fluid Mechanics, 2014. **749**: p. 649-665.
83. Schiaffino, S. and A.A. Sonin, *Molten droplet deposition and solidification at low Weber numbers.* Physics of Fluids, 1997. **9**(11): p. 3172-3187.
84. Biance, A.-L., C. Clanet, and D. Quéré, *First steps in the spreading of a liquid droplet.* Physical Review E, 2004. **69**(1): p. 016301.
85. Bird, J.C., S. Mandre, and H.A. Stone, *Short-Time Dynamics of Partial Wetting.* Physical Review Letters, 2008. **100**(23): p. 234501.
86. Soboleva, O.A., E.A. Raud, and B.D. Summ, *Initial-stage of the spreading of a drop over a solid-surface* Colloid Journal of the Russian Academy of Sciences, 1991. **53**(6): p. 920-923.
87. Soboleva, O.A., B.D. Summ, and E.A. Raud, *Transition from inertial to viscous spreading of a drop.* Colloid Journal of the Ussr, 1989. **51**(6): p. 1049-1052.
88. Eddi, A., K.G. Winkels, and J.H. Snoeijer, *Short time dynamics of viscous drop spreading.* Physics of Fluids, 2013. **25**(1): p. 013102.
89. Courbin, L., et al., *Dynamics of wetting: from inertial spreading to viscous imbibition.* Journal of Physics: Condensed Matter, 2009. **21**(46): p. 464127.
90. Winkels, K.G., et al., *Initial spreading of low-viscosity drops on partially wetting surfaces.* Physical Review E, 2012. **85**(5): p. 055301.
91. Rafaï, S., et al., *Superspreading: Aqueous Surfactant Drops Spreading on Hydrophobic Surfaces.* Langmuir, 2002. **18**(26): p. 10486-10488.
92. Tanner, L.H., *Spreading of silicone oil drops on horizontal surfaces* Journal of Physics D-Applied Physics, 1979. **12**(9): p. 1473-84.
93. Maxwell, J.C., *Collected scientific papers.* 1890. **2**: p. 625.

94. Rowan, S.M., M.I. Newton, and G. McHale, *Evaporation of Microdroplets and the Wetting of Solid Surfaces.* The Journal of Physical Chemistry, 1995. **99**(35): p. 13268-13271.
95. Shanahan, M.E.R., *Simple Theory of "Stick-Slip" Wetting Hysteresis.* Langmuir, 1995. **11**(3): p. 1041-1043.
96. Chandra, S., et al., *Effect of liquid-solid contact angle on droplet evaporation.* Fire Safety Journal, 1996. **27**(2): p. 141-158.
97. Rowan, S.M., et al., *Evaporation of Microdroplets of Three Alcohols.* The Journal of Physical Chemistry B, 1997. **101**(8): p. 1265-1267.
98. Moon, H., et al., *Low voltage electrowetting-on-dielectric.* Journal of Applied Physics, 2002. **92**(7): p. 4080-4087.
99. Hu, H. and R.G. Larson, *Analysis of the Microfluid Flow in an Evaporating Sessile Droplet.* Langmuir, 2005. **21**(9): p. 3963-3971.
100. Dugas, V., J. Broutin, and E. Souteyrand, *Droplet Evaporation Study Applied to DNA Chip Manufacturing.* Langmuir, 2005. **21**(20): p. 9130-9136.
101. Widjaja, E. and M.T. Harris, *Particle deposition study during sessile drop evaporation.* AIChE Journal, 2008. **54**(9): p. 2250-2260.
102. Moffat, J.R., K. Sefiane, and M.E.R. Shanahan, *Effect of TiO2 Nanoparticles on Contact Line Stick−Slip Behavior of Volatile Drops.* The Journal of Physical Chemistry B, 2009. **113**(26): p. 8860-8866.
103. Orejon, D., K. Sefiane, and M.E.R. Shanahan, *Evaporation of nanofluid droplets with applied DC potential.* Journal of Colloid and Interface Science, 2013. **407**: p. 29-38.
104. McHale, G., et al., *Evaporation and the Wetting of a Low-Energy Solid Surface.* The Journal of Physical Chemistry B, 1998. **102**(11): p. 1964-1967.
105. Maxwell, J.C., *Diffusion,* in *Encycolpedia Britannica (Ninth ed.)*. 1878a. p. 214-221.
106. Lee, H.H., K.S. Chou, and K.C. Huang, *Inkjet printing of nanosized silver colloids.* Nanotechnology, 2005. **16**(10): p. 2436-2441.
107. Sefiane, K. and R. Bennacher, *An expression for droplet evaporation incorporating thermal effects.* Journal of Fluid Mechanics, 2011. **667**: p. 260-271.

108. Park, J. and J. Moon, *Control of Colloidal Particle Deposit Patterns within Picoliter Droplets Ejected by Ink-Jet Printing.* Langmuir, 2006. **22**(8): p. 3506-3513.
109. Shen, X.Y., C.M. Ho, and T.S. Wong, *Minimal Size of Coffee Ring Structure* Journal of Physical Chemistry B, 2010. **114**(26): p. 8826-8826.
110. Crafton, E.F. and W.Z. Black, *Heat transfer and evaporation rates of small liquid droplets on heated horizontal surfaces.* International Journal of Heat and Mass Transfer, 2004. **47**(6–7): p. 1187-1200.
111. David, S., K. Sefiane, and L. Tadrist, *Experimental investigation of the effect of thermal properties of the substrate in the wetting and evaporation of sessile drops.* Colloids and Surfaces A: Physicochemical and Engineering Aspects, 2007. **298**(1–2): p. 108-114.
112. Sobac, B. and D. Brutin, *Thermal effects of the substrate on water droplet evaporation.* Physical Review E, 2012. **86**(2): p. 021602.
113. Shanahan, M.E.R., K. Sefiane, and J.R. Moffat, *Dependence of Volatile Droplet Lifetime on the Hydrophobicity of the Substrate.* Langmuir, 2011. **27**(8): p. 4572-4577.
114. Nguyen, T.A.H. and A.V. Nguyen, *Increased Evaporation Kinetics of Sessile Droplets by Using Nanoparticles.* Langmuir, 2012. **28**(49): p. 16725-16728.
115. Orejon, D., K. Sefiane, and M.E.R. Shanahan, *Stick–Slip of Evaporating Droplets: Substrate Hydrophobicity and Nanoparticle Concentration.* Langmuir, 2011. **27**(21): p. 12834-12843.
116. Askounis, A., et al., *Nanoparticle deposits near the contact line of pinned volatile droplets: size and shape revealed by atomic force microscopy.* Soft Matter, 2011. **7**(9): p. 4152-4155.
117. Marín, Á.G., et al., *Order-to-Disorder Transition in Ring-Shaped Colloidal Stains.* Physical Review Letters, 2011. **107**(8): p. 085502.
118. Yunker, P.J., et al., *Suppression of the coffee-ring effect by shape-dependent capillary interactions.* Nature, 2011. **476**(7360): p. 308-311.
119. Parisse, F. and C. Allain, *Drying of Colloidal Suspension Droplets: Experimental Study and Profile Renormalization.* Langmuir, 1997. **13**(14): p. 3598-3602.
120. Pauchard, L. and C. Allain, *Buckling instability induced by polymer solution drying.* EPL (Europhysics Letters), 2003. **62**(6): p. 897.

121. Andrew, S., *Dewetting-mediated pattern formation in nanoparticle assemblies.* Journal of Physics: Condensed Matter, 2011. **23**(8): p. 083001.
122. Pauchard, L. and C. Allain, *Stable and unstable surface evolution during the drying of a polymer solution drop.* Physical Review E, 2003. **68**(5): p. 052801.
123. Willmer, D., et al., *Growth of solid conical structures during multistage drying of sessile poly(ethylene oxide) droplets.* Physical Chemistry Chemical Physics, 2010. **12**(16): p. 3998-4004.
124. Baldwin, K.A., et al., *Monolith formation and ring-stain suppression in low-pressure evaporation of poly(ethylene oxide) droplets.* Journal of Fluid Mechanics, 2012. **695**: p. 321-329.
125. Fischer, B.J., *Particle Convection in an Evaporating Colloidal Droplet.* Langmuir, 2001. **18**(1): p. 60-67.
126. Freed-Brown, J., *Evaporative deposition in receding drops.* Soft Matter, 2014. **10**(47): p. 9506-9510.
127. Willmer, D., *Non-Equilibrium Polymeric Fluids*. 2011, Nottingham Trent University.
128. Cox, L.R., E.H. Dunlop, and A.M. North, *Role of molecular aggregates in liquid drag reduction by polymers.* Nature, 1974. **249**(5454): p. 243-245.
129. Hammouda, B., *Solvation characteristics of a model water-soluble polymer.* Journal of Polymer Science Part B: Polymer Physics, 2006. **44**(22): p. 3195-3199.
130. Hammouda, B., D.L. Ho, and S. Kline, *Insight into clustering in poly(ethylene oxide) solutions.* Macromolecules, 2004. **37**(18): p. 6932-6937.
131. Israelachvili, J., *The different faces of poly(ethylene glycol).* Proceedings of the National Academy of Sciences, 1997. **94**(16): p. 8378-8379.
132. Abuchowski, A., et al., *Effect of covalent attachment of polyethylene glycol on immunogenicity and circulating life of bovine liver catalase.* The Journal Of Biological Chemistry, 1977. **252**(11): p. 3582-3586.
133. André, C.D., et al., *Effects of Ammonium Sulfate and Sodium Chloride Concentration on PEG/Protein Liquid−Liquid Phase Separation.* Langmuir, 2008. **24**(18): p. 10345-10351.
134. Collyer, A.A., *Turbulence and Drag Reduction: A Macroscopic View*. Vol. 10. 1975: Physics Education.

135. Wallstrom, L. and K.A.H. Lindberg, *Wood Surface Stabilization with Polyethyleneglycol, Peg.* Wood Science and Technology, 1995. **29**(2): p. 109-119.

136. Mamalis, D., et al., *Effect of Poly(ethylene oxide) Molecular Weight on the Pinning and Pillar Formation of Evaporating Sessile Droplets: The Role of the Interface.* Langmuir, 2015. **31**(21): p. 5908-5918.

137. Subramanian, R.S., *Thermocapillary migration of bubbles and droplets.* Advances in Space Research, 1983. **3**(5): p. 145-153.

138. Subramanian, R.S., *The motion of bubbles and drops in reduced gravity*. In Transport Processes in Drops, Bubbles, and Particles 1992: Hemisphere, New YorK.

139. Subramanian, R.S., Balasubramaniam, R. & Wozniak, G. , *Fluid mechanics of bubbles and drops*. In Physics of Fluid in Microgravity 2002, London: Taylor and Francis 149-177.

140. Darhuber, A.A., et al., *Thermocapillary actuation of droplets on chemically patterned surfaces by programmable microheater arrays.* Journal of Microelectromechanical Systems, 2003. **12**(6): p. 873-879.

141. Chen, J.Z., et al., *Effect of contact angle hysteresis on thermocapillary droplet actuation.* Journal of Applied Physics, 2005. **97**(1): p. 014906.

142. Young, N.O., J.S. Goldstein, and M.J. Block, *The motion of bubbles in a vertical temperature gradient.* Journal of Fluid Mechanics, 1959. **6**(3): p. 350-356.

143. Balasubramaniam, R. and R.S. Subramaniam, *Thermocapillary bubble migration—thermal boundary layers for large Marangoni numbers.* International Journal of Multiphase Flow, 1996. **22**(3): p. 593-612.

144. Subramanian, R.S., *Slow migration of a gas bubble in a thermal gradient.* Aiche Journal, 1981. **27**(4): p. 646-654.

145. Crespo, A., E. Migoya, and F. Manuel, *Thermocapillary migration of bubbles at large Reynolds numbers.* International Journal of Multiphase Flow, 1998. **24**(4): p. 685-692.

146. Balasubramaniam, R. and R.S. Subramanian, *The migration of a drop in a uniform temperature gradient at large Marangoni numbers.* Physics of Fluids, 2000. **12**(4): p. 733-743.

147. Balasubramaniam, R. and A.-T. Chai, *Thermocapillary migration of droplets: An exact solution for small marangoni numbers.* Journal of Colloid and Interface Science, 1987. **119**(2): p. 531-538.

148. Merritt, R.M., D.S. Morton, and R.S. Subramanian, *Flow Structures in Bubble Migration under the Combined Action of Buoyancy and Thermocapillarity.* Journal of Colloid and Interface Science, 1993. **155**(1): p. 200-209.

149. Balasubramaniam, R., *Thermocapillary and buoyant bubble motion with variable viscosity.* International Journal of Multiphase Flow, 1998. **24**(4): p. 679-683.

150. Chen, J.C. and Y.T. Lee, *Effect of surface deformation on thermocapillary bubble migration.* AIAA Journal, 1992. **30**(4): p. 993-998.

151. Zhao, J.-F., et al., *Thermocapillary Migration of Deformable Bubbles at Moderate to Large Marangoni Number in Microgravity.* Microgravity Science and Technology, 2010. **22**(3): p. 295-303.

152. Haj-Hariri, H., Q. Shi, and A. Borhan, *Thermocapillary motion of deformable drops at finite Reynolds and Marangoni numbers.* Physics of Fluids, 1997. **9**(4): p. 845-855.

153. Ma, C. and D. Bothe, *Direct numerical simulation of thermocapillary flow based on the Volume of Fluid method.* International Journal of Multiphase Flow, 2011. **37**(9): p. 1045-1058.

154. Liu, H., et al., *Phase-field-based lattice Boltzmann finite-difference model for simulating thermocapillary flows.* Physical Review E, 2013. **87**(1): p. 013010.

155. Shanahan, M.E.R. and K. Sefiane, *Recalcitrant bubbles.* Scientific Reports, 2014. **4**: p. 4727.

156. Sobieszuk, P., P. Cygański, and R. Pohorecki, *Bubble lengths in the gas–liquid Taylor flow in microchannels.* Chemical Engineering Research and Design. **88**(3): p. 263-269.

157. Vochten, R. and G. Petre, *Study of the heat of reversible adsorption at the air-solution interface. II. Experimental determination of the heat of reversible adsorption of some alcohols.* Journal of Colloid and Interface Science, 1973. **42**(2): p. 320-327.

158. Limbourg-Fontaine, M.C., et al., *Thermocapillary movements around a surface tension minimum under microgravity conditions (part I. Technical*

*description of the stem experiments. D1 mission of spacelab).* Acta Astronautica, 1986. **13**(4): p. 197-208.

159. Oron, A. and P. Rosenau, *On a nonlinear thermocapillary effect in thin liquid layers.* Journal of Fluid Mechanics, 1994. **273**: p. 361-374.
160. Slavtchev, S.G. and S.P. Miladinova, *Thermocapillary flow in a liquid layer at minimum in surface tension.* Acta Mechanica, 1998. **127**(1-4): p. 209-224.
161. Abe, Y., A. Iwasaki, and K. Tanaka, *Microgravity Experiments on Phase Change of Self-Rewetting Fluids.* Annals of the New York Academy of Sciences, 2004. **1027**(1): p. 269-285.
162. Abe, Y., *Self-Rewetting Fluids.* Annals of the New York Academy of Sciences, 2006. **1077**(1): p. 650-667.
163. Savino, R. and D. Paterna, *Marangoni effect and heat pipe dry-out.* Physics of Fluids 2006. **18**(11): p. 118103.
164. McGillis, W.R. and V.P. Carey, *On the Role of Marangoni Effects on the Critical Heat Flux for Pool Boiling of Binary Mixtures.* Journal of Heat Transfer, 1996. **118**(1): p. 103-109.
165. Karapetsas, G., et al., *Thermocapillary-Driven Motion of a Sessile Drop: Effect of Non-Monotonic Dependence of Surface Tension on Temperature.* Langmuir, 2014. **30**(15): p. 4310-4321.
166. Olbricht, W.L., *Pore-Scale Prototypes of Multiphase Flow in Porous Media.* Annual Review of Fluid Mechanics, 1996. **28**(1): p. 187-213.
167. Delamarche, E., D. Juncker, and H. Schmid, *Microfluidics for Processing Surfaces and Miniaturizing Biological Assays.* Advanced Materials, 2005. **17**(24): p. 2911-2933.
168. El-Ali, J., et al., *Cell Stimulus and Lysis in a Microfluidic Device with Segmented Gas−Liquid Flow.* Analytical Chemistry, 2005. **77**(11): p. 3629-3636.
169. Fujioka, H. and J.B. Grotberg, *The steady propagation of a surfactant-laden liquid plug in a two-dimensional channel.* Physics of Fluids, 2005. **17**(8): p. 082102.
170. Sujoy Kumar Saha, Manvendra Tiwari, and Z.W. Bengt Sundén, *Advances in Heat Transfer Enhancement*. 1 ed. 2016: Springer International Publishing. VIII, 129.

171. Chung, P.M.-Y., *An experimental study of single -phase and two -phase flows in microchannels*. 2003, University of Toronto Canada. p. 179.
172. Nishio, S., *Single-Phase Laminar-Flow Heat Transfer and Two-Phase Oscillating-Flow Heat Transport in Microchannels.* Heat Transfer Engineering, 2004. **25**(3): p. 31-43.
173. Kandlikar, S.G. and P. Balasubramanian, *An Extension of the Flow Boiling Correlation to Transition, Laminar, and Deep Laminar Flows in Minichannels and Microchannels.* Heat Transfer Engineering, 2004. **25**(3): p. 86-93.
174. Wang, Y., *Liquid-vapour phase change and multiphase flow heat transfer in single micro-channels using pure liquids and nano-fluids*. 2011, University of Edinburgh. p. 255.
175. Morini, G.L., *Single-phase convective heat transfer in microchannels: a review of experimental results.* International Journal of Thermal Sciences, 2004. **43**(7): p. 631-651.
176. Buhlmann, A.A., *Decompression: Decompression Sickness*. 1984: Springer-Verlag Berlin New York.
177. Kantarci, N., F. Borak, and K.O. Ulgen, *Bubble column reactors.* Process Biochemistry, 2005. **40**(7): p. 2263-2283.
178. Nowadzky, T., A. Pantoja, and J.R. Britton, *Bubble continuous positive airway pressure, a potentially better practice, reduces the use of mechanical ventilation among very low birth weight infants with respiratory distress syndrome.* Pediatrics, 2009. **123**(6): p. 1534-40.
179. Burns, M.A., et al., *An Integrated Nanoliter DNA Analysis Device.* Science, 1998. **282**(5388): p. 484-487.
180. Gunther, A. and K.F. Jensen, *Multiphase microfluidics: from flow characteristics to chemical and materials synthesis.* Lab on a Chip, 2006. **6**(12): p. 1487-1503.
181. Tran, T.N., M.W. Wambsganss, and D.M. France, *Small circular- and rectangular-channel boiling with two refrigerants.* International Journal of Multiphase Flow, 1996. **22**(3): p. 485-498.
182. Cubaud, T. and C.-M. Ho, *Transport of bubbles in square microchannels.* Physics of Fluids, 2004. **16**(12): p. 4575-4585.

183. Saisorn, S. and S. Wongwises, *The effects of channel diameter on flow pattern, void fraction and pressure drop of two-phase air–water flow in circular micro-channels.* Experimental Thermal and Fluid Science, 2010. **34**(4): p. 454-462.

184. Sitar, A. and I. Golobic, *Heat transfer enhancement of self-rewetting aqueous n-butanol solutions boiling in microchannels.* International Journal of Heat and Mass Transfer, 2015. **81**: p. 198-206.

185. Sur, A. and D. Liu, *Adiabatic air–water two-phase flow in circular microchannels.* International Journal of Thermal Sciences, 2012. **53**: p. 18-34.

186. Wang, Y. and K. Sefiane, *Effects of heat flux, vapour quality, channel hydraulic diameter on flow boiling heat transfer in variable aspect ratio micro-channels using transparent heating.* International Journal of Heat and Mass Transfer, 2012. **55**(9–10): p. 2235-2243.

187. Hewitt, G.F., C.J. Martin, and N.S. Wilkes, *Experimental and modelling studies of annular flow in the region between flow reversal and the pressure drop minimum.* Physicochemical Hydrodynamics, 1985. **6**(1-2): p. 69-86.

188. Nedderman, R.M., *Boiling, Condensation Gas-Liquid Flows. By P. B. Whalley. Oxford Science Publication, 1987. 291* Journal of Fluid Mechanics, 1988. **191**: p. 598-599.

189. Dukler, A.E. and Y. Taitel, *Flow Pattern Transitions in Gas-Liquid Systems: Measurement and Modeling*, in *Multiphase Science and Technology*, G.F. Hewitt, J.M. Delhaye, and N. Zuber, Editors. 1986, Springer Berlin Heidelberg. p. 1-94.

190. Malter, L. and D.B. Langmuir, *Resistance, Emissivities and Melting Point of Tantalum.* Physical Review, 1939. **55**(8): p. 743-747.

191. Allen, R.D., L.F. Glasier, and P.L. Jordan, *Spectral Emissivity, Total Emissivity, and Thermal Conductivity of Molybdenum, Tantalum, and Tungsten above 2300°K.* Journal of Applied Physics, 1960. **31**(8): p. 1382-1387.

192. Milošević, N.D., et al., *Thermal Properties of Tantalum Between 300 and 2300 K.* International Journal of Thermophysics, 1999. **20**(4): p. 1129-1136.

193. Madding, R.P. *Emissivity measurement and temperature correction accuracy considerations*. 1999.

194. Shah, R.K. and A.L. London, *Laminar flow forced convection in ducts: a source book for compact heat exchanger analytical data*. 1978: Academic Press.

195. M.Thirumaleshwar, *Fundamentals of Heat and Mass Transfer, Includes mathcad-based solutions to problems*. 2006: Dorling Kindersley (India) Pvt. Ltd., licenses of Pearson Education in South Asia, .

196. Taylor, J.R., *An Introduction to Error Analysis: The Study of Uncertainties in Physical Measurements* Second ed. 1997: University Science Books,.

197. Rotenberg, Y., L. Boruvka, and A.W. Neumann, *Determination of Surface-Tension and Contact-Angle from the Shapes of Axisymmetric Fluid Interfaces.* Journal of Colloid And Interface Science, 1983. **93**(1): p. 169-183.

198. Nečas, D. and P. Klapetek, *Gwyddion: an open-source software for SPM data analysis.* Central European Journal of Physics, 2012. **10**(1): p. 181-188.

199. Shanahan, M.E.R., *Contact Angle Equilibrium on Thin Elastic Solids.* Journal of Adhesion, 1985. **18**(4): p. 247-267.

200. Shanahan, M.E.R., *Equilibrium of Liquid Drops on Thin Plates; Plate Rigidity and Stability Considerations.* Journal of Adhesion, 1987. **20**(4): p. 261-274.

201. Francis, L.F., et al., *Development and measurement of stress in polymer coatings.* Journal of Materials Science, 2002. **37**(22): p. 4717-4731.

202. Cheng, X., Y. Xue, and C. Xie, *Tribological investigation of PTFE composite filled with lead and rare earths-modified glass fiber.* Materials Letters, 2003. **57**(16–17): p. 2553-2557.

203. Ebnesajjad, S., *Discovery and History of Fluoropolymers*, in *Introduction to Fluoropolymers*. 2013, William Andrew Publishing: Oxford. p. 17-35.

204. Rubinstein, M. and R.H. Colby, *Polymer Physics*. 2003, Oxford: Oxford University Press.

205. Ramiasa, M., et al., *Contact Line Friction in Liquid–Liquid Displacement on Hydrophobic Surfaces.* The Journal of Physical Chemistry C, 2011. **115**(50): p. 24975-24986.

206. Chremos, A., et al., *Adsorption and self-assembly of linear polymers on surfaces: a computer simulation study.* Soft Matter, 2009. **5**(3): p. 637-645.

207. Braithwaite, G.J.C., A. Howe, and P.F. Luckham, *Interactions between Poly(ethylene oxide) Layers Adsorbed to Glass Surfaces Probed by Using a Modified Atomic Force Microscope.* Langmuir, 1996. **12**(17): p. 4224-4237.

208. Fu, Z. and M.M. Santore, *Poly(ethylene oxide) adsorption onto chemically etched silicates by Brewster angle reflectivity.* Colloids and Surfaces A: Physicochemical and Engineering Aspects, 1998. **135**(1–3): p. 63-75.
209. J. C. Braithwaite, G. and P. F. Luckham, *Effect of molecular weight on the interactions between poly(ethylene oxide) layers adsorbed to glass surfaces.* Journal of the Chemical Society, Faraday Transactions, 1997. **93**(7): p. 1409-1415.
210. Kalloudis, M., et al., *Thin Films of Poly(isoprene-b-ethylene Oxide) Diblock Copolymers on Mica: An Atomic Force Microscopy Study.* Langmuir, 2013. **29**(7): p. 2339-2349.
211. Cosgrove, T., et al., *Polymer at Interfaces*. 1993, London Chapman and Hall.
212. Galliano, A., S. Bistac, and J. Schultz, *Adhesion and friction of PDMS networks: molecular weight effects.* Journal of Colloid and Interface Science, 2003. **265**: p. 372-379.
213. Jones, R.L. and R.J. Spontak, *Effect of chain length and surface density on looped polymers grafted to an impenetrable surface.* The Journal of Chemical Physics, 1995. **103**(12): p. 5137-5143.
214. Semenov, A.N. and J.F. Joanny, *Structure of Adsorbed Polymer Layers: Loops and Tails.* EPL (Europhysics Letters), 1995. **29**(4): p. 279.
215. Deruelle, M., et al., *Adhesion energy between polymer networks and solid surfaces modified by polymer attachment.* Faraday Discussions, 1994. **98**(0): p. 55-65.
216. Deruelle, M., L. Léger, and M. Tirrell, *Adhesion at the Solid-Elastomer Interface: Influence of the Interfacial Chains.* Macromolecules, 1995. **28**(22): p. 7419-7428.
217. Bureau, L. and L. Léger, *Sliding Friction at a Rubber/Brush Interface.* Langmuir, 2004. **20**(11): p. 4523-4529.
218. Cohen, C., et al., *Incidence of the molecular organization on friction at soft polymer interfaces.* Soft Matter, 2011. **7**(18): p. 8535-8541.
219. Léger, L. and C. Creton, *Adhesion mechanisms at soft polymer interfaces.* Philosophical Transactions of the Royal Society A: Mathematical, Physical and Engineering Sciences, 2008. **366**(1869): p. 1425-1442.

220. Léger, L., et al., *The stick–slip transition in highly entangled poly(styrene-butadiene) melts.* Advances in Colloid and Interface Science, 2001. **94**(1–3): p. 39-52.

221. Léger, L., H. Hervet, and E. Raphael, *Surface-anchored polymer chains: Their role in adhesion and friction.*, in *Advances in Polymer Science* 1999. p. 185-225

222. Lasance, C.J.M. *The thermal conductivity of ceramics*. 1999; Available from: http://www.electronics-cooling.com/1999/09/the-thermal-conductivity-of-ceramics/.

223. Yeh, M.-C., P.-C. Lin, and L.-J. Chen, *Effect of Molecular Structure on Wetting Behavior at the Air−Liquid Interface of Water + Alcohol Mixtures.* The Journal of Physical Chemistry B, 2004. **108**(28): p. 9955-9961.

224. Brunet, P., J. Eggers, and R.D. Deegan, *Motion of a drop driven by substrate vibrations.* European Physical Journal-Special Topics, 2009. **166**: p. 11-14.

225. Paolo, S., et al., *Drop motion induced by vertical vibrations.* New Journal of Physics, 2015. **17**(11): p. 113017.

226. Puthenveettil, B.A., V.K. Senthilkumar, and E.J. Hopfinger, *Motion of drops on inclined surfaces in the inertial regime.* Journal of Fluid Mechanics, 2013. **726**: p. 26-61.

227. Karapetsas, G., K.C. Sahu, and O.K. Matar, *Effect of Contact Line Dynamics on the Thermocapillary Motion of a Droplet on an Inclined Plate.* Langmuir, 2013. **29**(28): p. 8892-8906.

228. Sáenz, P.J., et al., *Evaporation of sessile drops: a three-dimensional approach.* Journal of Fluid Mechanics, 2015. **772**: p. 705-739.

229. Kumar, V., M. Paraschivoiu, and K.D.P. Nigam, *Single-phase fluid flow and mixing in microchannels.* Chemical Engineering Science, 2011. **66**(7): p. 1329-1373.

230. Guo, Z.-Y. and Z.-X. Li, *Size effect on single-phase channel flow and heat transfer at microscale.* International Journal of Heat and Fluid Flow, 2003. **24**(3): p. 284-298.

231. Owhaib, W. and B. Palm, *Experimental investigation of single-phase convective heat transfer in circular microchannels.* Experimental Thermal and Fluid Science, 2004. **28**(2–3): p. 105-110.

232. Bhaga, D. and M.E. Weber, *Bubbles in viscous liquids: shapes, wakes and velocities.* Journal of Fluid Mechanics, 1981. **105**: p. 61-85.

233. Raymond, F. and J.M. Rosant, *A numerical and experimental study of the terminal velocity and shape of bubbles in viscous liquids.* Chemical Engineering Science, 2000. **55**(5): p. 943-955.

234. Balasubramaniam, R., et al., *Thermocapillary migration of bubbles and drops at moderate values of the Marangoni number in reduced gravity.* Physics of Fluids, 1996. **8**(4): p. 872-880.